UNIVERSITY OF SOUTHAMPTON

FACULTY OF ENGINEERING AND PHYSICAL SCIENCES

Aeronautical and Astronautical Department

Theory and modelling of dual-fuel combustion

by

Bruno Souza Soriano

Thesis for the degree of Doctor of Philosophy

July 2019

UNIVERSITY OF SOUTHAMPTON

ABSTRACT

FACULTY OF ENGINEERING AND PHYSICAL SCIENCES
Aeronautical and Astronautical Department

Doctor of Philosophy

THEORY AND MODELLING OF DUAL-FUEL COMBUSTION

by Bruno Souza Soriano

Dual-fuel combustion is an attractive strategy for utilising lean mixtures of alternative fuels such as natural gas in internal combustion engines. In pilot ignited dual-fuel, a pilot injection of a more reactive fuel such as diesel provides the source of ignition for the fuel-lean mixture, resulting in high thermal efficiency and low emissions. The dual-fuel combustion process involves competition between deflagration, diffusion and autoignition combustion modes, presenting a challenge for established turbulent combustion models commonly tailored to model a single combustion mode. The present study addresses three key challenges that arise in dual-fuel engines, in addition to the challenges of the better-understood single fuel diesel engine: (a) the chemical interaction of the fuels on the ignition process; (b) the effect of the inhomogeneous and reactive conditions on the flame structure; (c) and the effect of both fuels on flame propagation speed.

Chemical Explosive Mode Analysis of dual-fuel combustion reveals a complex process in which the majority of the inhomogeneous mixture is consumed by deflagration. Thus, the description of the effect of dual-fuel conditions on the propagation process is critical to the understanding and modelling of dual-fuel combustion. Flame propagation speed is analysed in detail using both laminar and turbulent conditions. The results reveal that the flame speed depends on chemical contribution of both fuels, and also depends significantly on the release of heat and pre-ignition chemical species ahead of the flame. A new model is developed to accurately capture these effects. The effects of dual-fuel composition on the ignition process are studied through laminar and turbulent simulations using methane as surrogate for natural gas. In order to isolate the thermal and chemical contributions of methane, the ignition process is compared with a simulation in which methane is treated as inert. Methane is known to retard ignition of higher-hydrocarbons. However, the analysis provided in this thesis reveals that the combination of the chemical effects of methane with the molecular transport makes an additional contribution to the retardation of ignition.

A combination of different approaches is identified for modelling the premixed and non-premixed phases of dual-fuel combustion. Two different modelling approaches are developed: a hybrid mixture fraction Conditional Moment Closure/G-equation approach; and a mixture fraction-progress variable Double Conditional Moment Closure (DCMC). The predictions are assessed by comparison to previous experimental data for a dual-fuel Rapid Compression-Expansion Machine. The hybrid model can adequately describe ignition and the transition to premixed flame propagation, and ignition of the premixed end gas. However, the hybrid approach is sensitive to the criteria used to couple the models, and these criteria are avoided with the DCMC approach. The DCMC model is applied as a tabulated flamelet solution assuming statistical homogeneity in space and time. The novel application of DCMC in dual-fuel showed good prediction of heat release rate compared with the experimental data and highlights the potential of the model to predict dual-fuel combustion.

Contents

Abstract iii

Declaration of Authorship xvii

Acknowledgements xix

Nomenclature xxi

1 Introduction 1
- 1.1 Outline . . . 4
- 1.2 Publications . . . 4
  - 1.2.1 2016 . . . 4
  - 1.2.2 2017 . . . 4
  - 1.2.3 2019 . . . 5

2 Background 7
- 2.1 Dual-fuel engines . . . 7
- 2.2 Physics of dual-fuel combustion . . . 11
  - 2.2.1 Dual-fuel ignition . . . 12
  - 2.2.2 Dual-fuel flames . . . 13
- 2.3 Modelling of turbulent combustion . . . 15
  - 2.3.1 Turbulent combustion modelling strategies . . . 15
  - 2.3.2 Application of turbulent combustion modelling to dual-fuel . . . 16
  - 2.3.3 The Conditional Moment Closure framework . . . 19
    - 2.3.3.1 The joint-PDF . . . 22
  - 2.3.4 Objectives for model development . . . 24

3 Formulation 27
- 3.1 Governing equations for reactive flow . . . 27
  - 3.1.1 Mass conservation equation . . . 27
  - 3.1.2 Species conservation equation . . . 28
  - 3.1.3 Momentum conservation equation . . . 30
  - 3.1.4 Energy conservation equation . . . 30
- 3.2 Combustion . . . 31
  - 3.2.1 Premixed flames . . . 32
  - 3.2.2 Non-premixed combustion . . . 36
  - 3.2.3 Partially premixed combustion . . . 38

3.3 Conditional Moment Closure . . . 39
3.3.1 First-order conditional moment closure . . . 39
3.3.2 Conditioning variables . . . 40
3.3.3 Double Conditional Moment Closure transport equations . . . 42
Single-conditioning: . . . 44
Double-conditioning: . . . 44
3.3.4 Presumed probability density function modelling . . . 45
3.3.5 Moment equations for conditioning variables . . . 46
Mixture Fraction: . . . 46
3.3.6 Numerical implementation of the CMC equations . . . 46
3.4 The G-Equation model . . . 47

4 Investigation of flame propagation in autoignitive blends of n-heptane and methane fuel 49
4.1 Introduction . . . 49
4.1.1 Laminar flame speed . . . 50
4.1.2 Laminar flame thickness . . . 51
4.2 Methodology . . . 52
4.3 Results and Discussion . . . 54
4.3.1 Validation of chemical kinetics mechanisms . . . 54
4.3.1.1 Ignition delay . . . 55
4.3.1.2 Flame speed . . . 55
4.3.2 Effects of pre-ignition chemistry on flame speed . . . 56
4.3.3 Effects of pre-ignition chemistry on flame thickness . . . 59
4.3.4 Flame speeds at autoignitive conditions . . . 62
4.3.4.1 Additional data comparing alternative mixing-rules . . . 64
4.3.5 Effects of pre-ignition chemistry . . . 65
4.4 Conclusions . . . 68

5 Analysis of dual-fuel combustion initiation in turbulent flow 71
5.1 Introduction . . . 71
5.2 Formulation . . . 71
5.2.1 Numerical simulation . . . 71
5.2.2 Combustion mode analysis . . . 73
5.3 Assessment of numerical accuracy . . . 76
5.4 Results . . . 77
5.4.1 Evolution of the combustion process . . . 77
5.4.2 Ignition analysis . . . 81
5.4.3 CEMA analysis . . . 85
5.4.4 Displacement Speed Analysis . . . 88
5.5 Conclusion . . . 95

6 DCMC-based modelling for the joint mixture fraction-progress variable pdf in partially-premixed combustion 97
6.1 Introduction . . . 98
6.2 Analysis . . . 100
6.2.1 DNS data . . . 100
6.2.2 Reaction rate closure . . . 101

6.2.3 Reference flame solutions . . . 101
6.3 Fluid-age solution . . . 102
6.3.1 Age-generated joint-pdfs . . . 105
6.4 Results . . . 105
6.4.1 Stratified flame . . . 106
6.4.2 Non-premixed temporal jet . . . 107
6.4.3 Non-premixed autoignitive lifted flame . . . 109
6.5 Conclusion . . . 113

7 Hybrid modelling of dual-fuel combustion 115
7.1 Introduction . . . 115
7.2 Formulation . . . 118
7.2.1 Flow field solver . . . 118
7.2.2 G-equation model . . . 119
7.2.2.1 Turbulent flame speed correlations . . . 120
7.2.2.2 Methane/n-heptane laminar flame speed model for dual-fuel engines . . . 121
7.2.3 Conditional Moment Closure Ignition Model . . . 124
7.2.4 Numerical implementation of CMC . . . 125
7.2.5 CMC sub-models . . . 128
7.2.6 Ignition chemistry . . . 129
7.2.7 Ignition criteria . . . 130
7.2.8 Model coupling . . . 131
7.3 Assessment of numerical accuracy . . . 132
7.3.0.1 Reference solutions . . . 133
7.3.0.2 Time step sensitivity . . . 134
7.3.0.3 Mixture fraction grid-dependence . . . 135
7.4 Summary of cases . . . 135
7.5 Results . . . 137
7.5.1 Ignition criteria . . . 139
7.5.2 Laminar flame speed modelling . . . 141
7.5.3 Turbulent flame speed correlations . . . 143
7.5.4 Further discussion about the hybrid modelling . . . 144
7.6 Conclusion . . . 145

8 Double Conditional Moment Closure modelling of dual-fuel combustion 147
8.1 Introduction . . . 148
8.2 Formulation . . . 149
8.2.1 Double Conditional Moment Closure . . . 150
8.2.2 Computational Fluid Dynamics . . . 151
8.2.3 Numerical setup . . . 154
8.3 Results . . . 155
8.4 Conclusion . . . 159

9 Conclusion 161
9.1 Dual-fuel flame propagation in laminar flow . . . 161
9.2 Ignition processes, flame propagation and flame structure in turbulent flow 162

9.3 Duel-fuel combustion modelling 163
Hybrid modelling: 163
DCMC modelling for partially premixed combustion: 164
Application of DCMC modelling to duel-fuel combustion: . 165
9.4 Future work 165

A Procedure for removing intermediate species ahead of the flame 167

B Validation of the DME/CH4 chemical mechanism 171

References 173

List of Figures

1.1 Contributions to the world temperature change [73]. 2
1.2 World energy consumption over the years 1990-2015 [26]. 2

2.1 Schematic representation of a dual-fuel engine [219]. 8
2.2 Schematic representation of dual-fuel combustion. 12
2.3 Scatter of intermediate mass fraction at a fixed time. Large filled circles are the conditional mean. Plot on the left corresponds mass fraction conditioned on mixture fraction $\langle Y_i|\eta\rangle$; whereas on the right mass fraction is conditioned on η close to stoichiometric and ζ: $\langle Y_i|\xi = 1/3, \zeta\rangle$ [111]. . . 20

3.1 Laminar premixed flame structure [160]. 33
3.2 Premixed turbulent combustion diagram [160]. 35
3.3 Counter-flow configuration of a nonpremixed flame [160]. 37
3.4 Illustration of a propagating triple flame [59]. 38
3.5 Flame front computed by G-equation model [160]. 47

4.1 The temperature profile in several steady freely-propagating stoichiometric n-heptane–air flames with different residence times at 850 K and 40 bar. The location of the cool flame front is indicated. 53
4.2 The temperature-dependence of ignition delay time for stoichiometric methane/n-heptane–air blends at 40 bar with $\phi_{CH_4}/\phi_{tot} = 0.0, 0.5, 0.8, 1.0$ computed with POLIMI-106 [171] and POLIMI-451 [170] mechanisms. . . 54
4.3 Constant-volume ignition delay times for stoichiometric methaneair at 30 atm and n-heptane/air at 55 atm. Shock-tube data: ◯ [78], □ [63]. . . . 56
4.4 Constant-volume ignition delay times for stoichiometric n-heptane-air at 42atm for Polimi-451, Mehl et al., Polimi-106, Liu et al. and Lu et al. (refer to Figure S1 for legend). Shock-tube data ▲ [44]. 56
4.5 Constant-volume ignition delay times for stoichiometric methane/n-heptaneair mixtures at 30 bar with 80%$_{vol}$ CH4 (left axis) and 95%$_{vol}$ CH4 (right axis) in the fuel blend. 57
4.6 Laminar flame speed of methaneair flames versus equivalence ratio for 360 K (lower speeds) and 400 K (higher speeds) at 10 bar. ◀ experimental data [69]. 57
4.7 Laminar flame of methane-air flames versus equivalence ratio at 300K, 1.01bar. Refer to Fig. 4.6 for legend. 58
4.8 Laminar flame speeds of stoichiometric methane/n-heptane blends versus residence time at 40 bar: simulations (symbols); model Eq. 4.8 (solid). . . 59

4.9 Laminar flame speed and temperature versus residence time for stoichiometric n-heptane–air at 40 bar and 850 K: Unmodified flame in the full domain (white circles); 0.2 mm domain with inlet composition from the unmodified flame (grey circles); 0.2 mm domain with intermediate species removed from the inlet composition (black circles). 60
4.10 Normalised high-temperature reaction front speed $s_f/s_{r,0,fuel}$ versus $\alpha/(\delta_f s_{r,0,fuel})$ for short residence time ($\tau_f \longrightarrow 0$) stoichiometric methane–air and n-heptane–air flames with unburnt temperatures 700, 775, 850, 925 and 1000 K (symbols), and data for n-heptane–air combustion with residence times up to 98% of the ignition delay time at 775, 850, and 925 K (various dashed lines as labelled). Square symbols indicate the conditions where the progress variable ahead of the flame equals 0.15. 61
4.11 Cool-flame reaction front speed s_f versus thermal thickness δ_f for stoichiometric n-heptane–air flames normalised by reference flame properties at 850 K and 40 bar for a range of residence times (symbols). Data range from $\tau_f = 1.6 \cdot 10^{-04}$ s to $\tau_f = 7.1 \cdot 10^{-04}$ s. Dashed lines correspond to Eq. 4.3. 62
4.12 Transport budgets and mass fraction profiles for stoichiometric n-heptane–air at 850 K and 40 bar for Y_{QOOH} (left column) and Y_{OH} (right column). The residence times at the flame front are 85% (top row), and 95% (bottom row) of the overall ignition delay time. The data are plotted versus the distance from the inlet. 63
4.13 Variation of flame speed with equivalence ratio for methane/n-heptane fuel blends at 850 K and 40 bar for $\phi_{CH4}/\phi_{tot} = 0$, 0.5 and 1.0; and linear [244], Hirasawa *et al.* [77], and Di Sarli *et al.* [58] mixing-rules. Closed square and circular symbols correspond to flame speeds from simulatins and from Eq. 4.8 respectively for residence times between 40 and 60% of the ignition delay time 64
4.14 Variation of flame speed with equivalence ratio for methane/n-heptane fuel blends at 850K and 40bar: Polimi-106 simulations for $\phi_{CH4}/\phi_{tot} = 0$ (•), 0.8 (◊) and 1.0 (★); Fitted flame speeds from a Gaussian function (dashed line); and Eq. 4.5 (solid line) [244] and Hirasawa et al. [77] (dash-dot-dot line) mixing-rules 65
4.15 Normalised flame speed versus the progress variable upstream of the flame front: Round symbols show $s_f/s_{r,fuel}$ at $\phi_{CH_4}/\phi_{tot} = 0$, 0.5, 0.8 and 1.0 for $T_u = 850$ K and 1000 K; Square symbols show $s_f/s_{f,therm}$ based on data from Fig. 4.9. Solid lines show $s_f/s_r = 2.4c$ and $s_f/s_{f,therm} = 1.18c$. 66

5.1 Two-dimensional initial conditions with mixture fraction distribution in y-direction. White shade represents the non-premixed DME and green shade the premixed oxidiser. Grey shade represents the initial vorticity. . 72
5.2 Temperature evolution in a 1D domain for two Δy: Symbols correspond to 0.9375 μm and lines 0.46875 μm. The time evolution goes from green to red lines. 76
5.3 Temperature evolution in a 1D domain for two Δy: lines correspond to 0.9375 μm and symbols 1.25 μm. The time evolution goes from green to red lines. 77
5.4 Detailed investigation of the three discretizations tested. Lines correspond to 0.46875 μm, circles to 0.9375 μm and stars to 1.25 μm. The time evolution goes from green to red lines. 78

5.5 Heat release colour maps for cases DF2D (left) and SF2D (right) for three times (as indicated on subfigures). The solid black line corresponds to the stoichiometric mixture fraction. 79
5.6 Time-space contour map the heat release rate in DF1D (left) and SF1D (right). The solid black line corresponds to the stoichiometric mixture fraction. Solid grey line correspond to methane-air homogeneous reactor ignition delay time. 79
5.7 OH species mass fraction conditioned on mixture fraction at different times. 81
5.8 Temperature conditioned on mixture fraction at different times. 82
5.9 Distribution of Y_{CH_2O} in mixture fraction space at t = 0.62 ms. 83
5.10 Overall ignition delay time τ_{0D} (solid lines) and first-stage ignition delay time (dashed lines) as a function of mixture fraction for cases SF0D (crosses) and DF0D (circles). Overall ignition delay times τ_{2D} for every independent ignition kernel in cases SF2D and DF2D are indicated by large symbols. 84
5.11 Overall ignition delay time for single- and dual-fuel counterflow configurations as a function of mixture fraction scalar dissipation rate. Dashed-lines correspond to the ignition location in mixture fraction space. 85
5.12 Temperature and λ_e profile for a freely-propagating flame at different mixture fractions: $\xi = 0.01$; $\xi = 0.03$. 86
5.13 Temperature profile coloured by α and projected source terms λ_e distribution for the 1D mixing layer. Black region correspond to $\lambda_e < 0$. 88
5.14 Contours of temperature, CEM eigenvalue (λ_e) and local combustion mode. 89
5.15 Effect of residence time on premixed laminar displacement speed for various mixtures from case DF2D. 90
5.16 Evolution of displacement speed in the one-dimensional mixing layer. Mixture fraction at the flame is represented by the solid blue line. 93
5.17 Displacement speed conditioned on mixture fraction. 94
5.18 Location with $s_d > 1.3 s_l$ 95

6.1 Colour maps of correlation (left) and instantaneous OH mass fraction (right) for a lifted autoigniting jet flame [247]. 99
6.2 A scatter plot of data from the position indicated by a star at $x = 7H, y = -1H$ in Fig. 6.1 in a lifted autoigniting jet flame from Ref. [247]. 99
6.3 Examples of Plackett copula distribution with the given odds parameter θ and uniform marginal distributions. Plots range from perfectly negative correlation (far left) to perfectly positive correlation (far right) [137]. . . . 99
6.4 Illustration of the three partially-premixed DNS data sets examined in this study: Left: Equivalence ratio-stratified slot Bunsen flame (volume rendering of heat release coloured); Centre: non-premixed temporal planar jet, (temperature field and stoichiometric iso-surface); Right: lifted autoigniting slot jet (volume rendering of OH mass fraction field). 101
6.5 The progress variable in an unsteady flamelet solution for an autoigniting non-premixed flame at regular time intervals. A single-time solution is highlighted in red, and a constant c line corresponding to taking a delta-function for c is shown as a blue horizontal line. 103
6.6 Structure of a laminar freely-propagating flame. Distribution of progress variable c; age a; and first derivative of progress variable in red. 104

6.7 Multi-dimensional flamelet solution for the stratified C4 conditions. (a) Q_a isolines; (b)$\langle N_c \mid \eta, \zeta\rangle$ given by Eq. 6.4. 106
6.8 Stratified case C4 x=6H, y=0.5H. Main plot: joint ξ-c distribution (black scatter), progress variable reaction rate (coloured contours), mean progress variable (horizontal blue line), $Q_{\hat{a}} = \hat{a}_{iso}$ (red line). Sub-plots: empirical marginal pdfs (black curves) and fitted β distributions (red) for ξ (top) and c (right). 107
6.9 Stratified case $x = 6H$: prediction of mean progress variable reaction rate for various c-pdf models. 108
6.10 $\langle Q_a \mid \eta, \zeta\rangle$ multi-dimensional flamelet solution for the non-premixed temporal jet. 108
6.11 Prediction of mean progress variable reaction rate for various c-pdf models. 109
6.12 Non-premixed temporal jet. Main plot: joint ξ-c distribution (black scatter), progress variable reaction rate (coloured contours), mean progress variable (horizontal blue line), $Q_{\hat{a}} = \hat{a}_{iso}$ (red line). Sub-plots: empirical marginal pdfs (black curves) and fitted β distributions (red) for ξ (top) and c (right). 110
6.13 Prediction of mean progress variable reaction rate for various c-pdf models at two different cross-planes. 111
6.14 Non-premixed lifted flame at iy = 251. Main plot: joint ξ-c distribution (black scatter), progress variable reaction rate (coloured contours), mean progress variable (horizontal blue line), $Q_{\hat{a}} = \hat{a}_{iso}$ (red line). Sub-plots: empirical marginal pdfs (black curves) and fitted β distributions (red) for ξ (top) and c (right). 112
6.15 Prediction of mean progress variable reaction rate for various c-pdf models at two different cross-planes. 112
6.16 Non-premixed lifted flame at iy = 151 and 12H. Main plot: joint ξ-c distribution (black scatter), progress variable reaction rate (coloured contours), mean progress variable (horizontal blue line), $Q_{\hat{a}} = \hat{a}_{iso}$ (red line). Sub-plots: empirical marginal pdfs (black curves) and fitted β distributions (red) for ξ (top) and c (right). 113

7.1 ETH Rapid Compression Machine [194]. 117
7.2 Three-dimensional grid in the section plane for a given time close to TDC with contours indicating the pilot injection 119
7.3 Laminar flame speed prediction from POLIMI_106 [171], GRI 3.0[206] and the flame speed correlation for 40 bar and 850 K (upper curve) and comparison against experimental data [69] at 10 bar and 360 K and 400 K (lower two curves). 123
7.4 Initial profiles in conditional space. 124
7.5 Profiles in mixture fraction space during ignition using different solution methods and timesteps as per the legend [237] 127
7.6 Comparison of CPU time using different solution methods [237]. 127
7.7 Evolution in mixture fraction space of conditional average (a) OH mass fraction; (b) temperature. 131
7.8 Scalar dissipation rate effect on ignition delay time. 134
7.9 Sensitivity of ignition delay to OS time step for the overall ignition delay τ, and the ignition delays at $\eta = \xi_{stoich}/2$ and $\eta = 3\xi_{stoich}/2$. 134
7.10 Solution dependence on the number of grid points in conditional space. . 136

7.11 Temperature evolution for different grid tested. The plot is the instant which $T_{\xi_{stoich}-\xi_{stoich}/2}$ reaches 1500 K for the first time for 301 points and low scalar dissipation rate. . . . 136
7.12 $\widetilde{Y}_{OH}$ (left) and mean temperature (right) for Case E at 1.3 ms (top) and 2.3 ms (bottom) after SOI. . . . 138
7.13 Heat release rate (left) and cumulative heat release (right) for experiment and Cases A and E for OP2 (top) and OP3 (bottom). Vertical grey line corresponds to TDC. . . . 139
7.14 Heat release rate (left) and cumulative heat release (right) for Cases A, B, E and experiment for OP2 (top) and OP3 (bottom). Vertical grey line corresponds to TDC. . . . 140
7.15 $\widetilde{Y}_{OH,CMC}$ contour with $\widetilde{C}_G = 0.5$ iso-line at 1.7 and 1.8ms after SOI in case OP2: left column uses $\widetilde{T} \geqslant 1200$ K as threshold and right column uses $\widetilde{Y}_{OH} \geqslant 4 \cdot 10^{-04}$. . . . 141
7.16 Temperature field of OP2 at 3.7 ms after start of injection. Simulation A (left) and B (right). . . . 142
7.17 Iso-surfaces from simulations A (left) and B (right) of OP2 at 3.7 ms after start of injection. On the top: $\widetilde{\xi} = 0.02$ and $\widetilde{\xi} = 0.002$ on the bottom: $\widetilde{C}_G = 0.5$. . . . 142
7.18 Comparison of simulationsA, C and E with experiment for OP2 (top) and OP3 (bottom): (left) Heat release rate; (right) Cumulative heat release. Vertical grey line corresponds to TDC. . . . 143
7.19 Comparison of simulation Cases A, D, and E with experiment for OP2 (top) and OP3 (bottom), showing heat release rate (left), cumulative heat release (right). Vertical grey line corresponds to TDC. . . . 144

8.1 Schematic illustration of the RCEM [213]. . . . 149
8.2 Schematic illustration of the coupling between CFD and turbulent combustion model [198]. . . . 154
8.3 Predictions of conditional mean progress variable reaction rate for various scalar dissipation rates. . . . 156
8.4 Comparison of measured heat release rate with DCMC prediction. . . . 157
8.5 Combustion evolution in physical space: Mixture fraction on the left; and temperature on the right . . . 157
8.6 Multi-dimensional flamelet solution of relative age. (a) conditional distribution of relative age: LTI corresponds to Low-Temperature Ignition, and HTI to High-Temperature Ignition ; (b) progress variable scalar dissipation rate using model from Eq. 6.4. . . . 159

A.1 Illustration of the reduced-domain simulation procedure: temperature field from a full-domain simulation of a stoichiometric n-heptane–air flame with $\tau_f = 0.95\tau_{ign}$ (top); temperature field from the reduced-domain simulation. . . . 167

B.1 Ignition delay times using reduced and detailed mechanisms. Dashed-line corresponds to first-stage ignition; Solid line to ignition delay time. . . . 171
B.2 Laminar flame speed predictions using reduced and detailed mechanisms . 172

List of Tables

2.1 Structural modelling approaches for dual-fuel combustion 24

4.1 Summary of chemical models. 55

5.1 Overall ignition delay times for single-fuel and dual fuel cases. 83

7.1 Operating conditions 118
7.2 Numerical test cases 136

8.1 Peak scalar dissipation rates used in the DCMC solutions. 155

Declaration of Authorship

I, Bruno Souza Soriano, declare that the thesis entitled *Theory and modelling of dual-fuel combustion* and the work presented in the thesis are both my own, and have been generated by me as the result of my own original research. I confirm that:

- this work was done wholly or mainly while in candidature for a research degree at this University;
- where any part of this thesis has previously been submitted for a degree or any other qualification at this University or any other institution, this has been clearly stated;
- where I have consulted the published work of others, this is always clearly attributed;
- where I have quoted from the work of others, the source is always given. With the exception of such quotations, this thesis is entirely my own work;
- I have acknowledged all main sources of help;
- where the thesis is based on work done by myself jointly with others, I have made clear exactly what was done by others and what I have contributed myself;
- Either none of this work has been published before submission, or parts of this work have been published as:

  Soriano, B. S., Richardson, E. S. Investigation of flame propagation in autoignitive blends of n-heptane and methane fuel. Combustion Theory and Modelling, 2019. DOI:10.1080/13647830.2019.1614228.

Signed:.....

Date:29/07/19.....

Acknowledgements

The accomplishment of the PhD can only be achieved with the contribution of special people. The first person I would like to acknowledge is my supervisor, Edward Richardson. His knowledge, passion for scientific research and commitment inspired me thorughout the PhD. I will be always thankful to his support and for providing me the opportunity to learn him.

To Larissa Marioni, who was always supportive and helped me through the worst moments and kept me sane. I could not have asked for someone better to be along side me. To my friends from the original unofficial combustion office - Mark, Tom and Nabil - it was a pleasure to share the office with you. The discussions and the fantastic working environment had a significant impact on my PhD. To all the other friends I have made during my stay Southampton, thank you for contributing to the great experience of living the the UK.

I would like to thank my family for all the support during my entire life. This thesis would not exist without all of you.

Finally, to the Brazilian National Council for Scientific and Technological Development (CNPq) and the program *Science without Border* for the financial support with grant number 207250/2014-6. It was a great opportunity to improve my skills which, hopefully, will help on the development of the country.

...

Nomenclature

TDC	**T**op **D**ead **C**entre
ATDC	**A**fter **T**op **D**ead **C**entre
CI	**C**ompression **I**gnition
PDF	**P**robability **D**ensity **F**unction
AMC	**A**mplitude **M**apping **C**losure
SI	**S**park **I**gnition
CMC	**C**onditional **M**oment **C**losure
DCMC	ouble **C**onditional **M**oment **C**losure
HPDI	**H**igh **P**ressure **D**irect **I**njection
RCEM	**R**apid **C**ompression **E**expansion **M**achine

Chapter 1

Introduction

Energy generation by means of combustion has become a concern for the global environment. The year of 2016 was marked by breaking the world temperature record, almost 1°C above the initial measurements made during the 1880s [148]. The temperature increase is attributed to the industrial revolution and human activities, with two-thirds of this global warming occurring since 1975. Even if 1°C seems to be a small amount, studies have shown that during the Ice Age the average world temperature was around 5°C lower than in the 1880s [34]. According to Hansen et al. [74], the main contribution to global warming comes from greenhouse gases emitted by human activities. Figure 1.1 shows the various contributions to the world temperature change predicted with the GISS modelE atmospheric model [196]. The results are presented in terms of effective forcing, defined as the perturbation on Earth's energy balance, as a function of time. The predominant forcing for temperature rise comes unquestionably from the increase in greenhouse gases in the atmosphere. If emissions continue to increase at the same rate as nowadays, the predicted temperature increase for 2100 is 2.7°C. The authors conclude that CO_2 emissions are the critical issue for global temperature change. Increasing energy efficiency and the usage of renewable fuels is a mid-term approach to tackle the issues concerning global warming. Also, efforts should be made to efficiently use the remaining gas and oil resources until acceptable energy alternatives are available.

The increasing global demand for energy makes the reduction of total greenhouse gases emissions a challenging task. Figure 1.2 shows the global energy consumption in terms of

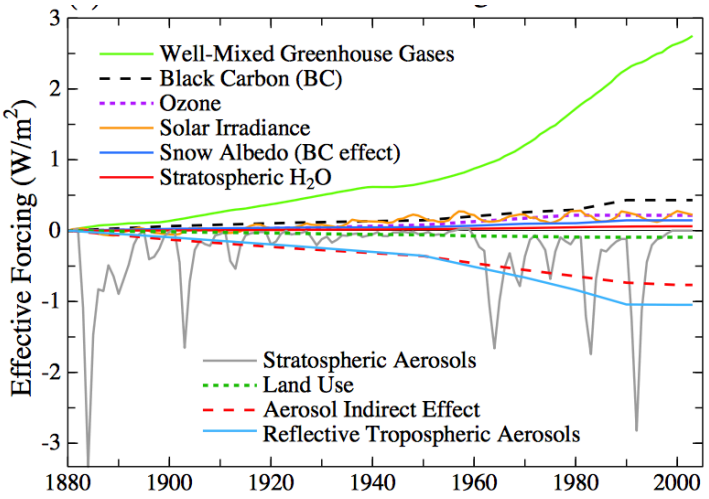

Figure 1.1: Contributions to the world temperature change [73].

million tonnes oil equivalent from 1990 until 2015. The hydroelectricity, nuclear energy and renewables still make a small contribution compared to the main sources: coal, oil and natural gas. Between the last three fuels, natural gas can offer life cycle greenhouse gas emissions benefits when applied to internal combustion engines [144].

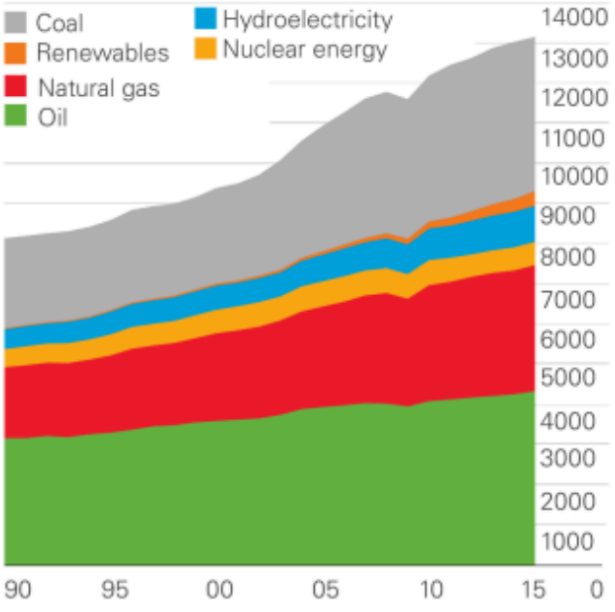

Figure 1.2: World energy consumption over the years 1990-2015 [26].

Natural gas is an attractive alternative to conventional fuels due to its high carbon-to-hydrogen ratio and because its resistance to knock enables higher compression ratios.

When burned under fuel-lean conditions, natural gas engines can achieve low fuel consumption and NO_x emissions [43, 102]. However, the simple change in fuel on an engine may not produce a significant reduction of harmful emissions. The low reactivity of natural gas makes its use in direct-injection compression-ignition engines challenging, since the long ignition delay may result in over-mixing before autoignition occurs. Spark-ignition (SI) of ultra-lean natural gas mixtures increase the engine cycle variability due to low flame speeds and ignition unreliability. It becomes necessary to improve the engine efficiency by changing its characteristics and developing new combustion strategies.

Low temperature combustion arises as a novel low-emission concept to meet the stringent pollutant and CO_2 regulations. The concept involves combustion of highly-diluted mixtures in order to reduce the peak temperature and consequent NOx formation. Low temperature technologies include Homogeneous Charge Compression Ignition (HCCI) and Reactivity Controlled Compression Ignition (RCCI), both potentially achieving thermal efficiencies above 50% and meeting emissions regulation [173], with the RCCI concept achieving greater operational flexibility. The reactivity-controlled compression ignition (RCCI) approach seeks to control ignition timing and location for less reactive fuels, such as natural gas, through addition of a more reactive fuel, such as diesel [114, 173]. In pilot-ignited dual-fuel engines, an example of the RCCI approach, pilot injection of a more reactive fuel produces multiple ignition sites for the premixed natural gas/air. The overall performance combines the high efficiency of a compression-ignition engine with the relatively low emissions associated with lean-premixed natural gas combustion [232].

The challenges associated with the development of a dual-fuel engine comes in part from the complex physics involved. Pilot-ignited dual-fuel combustion combines autoignition of the more reactive fuel and transition from an autoigniting diffusion flame to a premixed flame propagation. In terms the computational modelling of the problem, the combustion complexity renders established turbulent combustion models, usually tailored to CI or SI engines, inadequate to capture all the physics in a dual-fuel engine.

In summary, new combustion strategies are needed in order to reduce emissions of carbon dioxide and harmful gases. However, new types of engine operation often introduce additional complex phenomena. The objective of this thesis is to contribute to the

fundamental understanding of dual-fuel combustion and the development predictive approaches relevant to internal combustion engine applications.

1.1 Outline

Given the objective, this thesis proceeds in three parts: (1) reviewing the current state of knowledge and modelling for dual-fuel combustion technology; (2) numerical investigation of fundamental aspects of dual-fuel combustion, as required for model development; and (3) development of dual-fuel combustion models for internal combustion engine application.

1.2 Publications

This section lists the journal publications, submissions, and conferences papers produced in this thesis. Planned submissions are also included.

1.2.1 2016

Soriano, B. S., Matheson, T., Richardson, E. S. (2016). Flame speed model for autoignitive mixtures of methane and n-heptane. Conference paper presented at 16th Brazilian Congress of Thermal Sciences and Engineering, Vitoria, Brazil.

1.2.2 2017

Soriano, B. S., Richardson, E. S., Wright, Y., Schlatter, S. (2017). Conditional moment closure and G-equation hybrid modelling For dual-fuel methane/N-heptane combustion. Conference paper presented at European Combustion Meeting, Dubrovnik, Croatia.

Soriano, B. S., Richardson, E. S., Schlatter, S., Wright, Y. (2017). Conditional Moment Closure modelling for dual-fuel combustion engines with pilot-assisted compression ignition. Paper presented at SAE 2017 Powertrains, Fuels and Lubricants, Beijing, China.DOI: 10.4271/2017-01-2188.

Soriano, B. S., Richardson, E. S. (2017). Advanced hybrid modelling for pilot ignited dual-fuel combustion. Conference paper presented at the 24th ABCM International Congress of Mechanical Engineering, Curitiba, Brazil.

1.2.3 2019

Soriano, B. S., Richardson, E. S. (2019). Investigation of flame propagation in autoignitive blends of n-heptane and methane fuel. Combustion Theory and Modelling. *Accepted*. https://doi.org/10.1080/13647830.2019.1614228.

Soriano, B. S., Richardson, E. S. Numerical investigation of dual-fuel combustion-initiation in a turbulent mixing layer between DME and methane/air. *In preparation. Submission to Combustion and Flame* (Based on Chapter 5).

Richardson E.S., Soriano B.S. Statistical dependence of mixture fraction and progress variable in partially-premixed combustion. *In preparation. Submission to Combustion and Flame*. (Based on input from Chapter 6).

Soriano, B. S., Richardson, E. S., Seddik O., Pandurangi S., Wright Y. Investigation of Double-Conditional Moment Closure approach for dual-fuel combustion. *In preparation.* (Based on input from Chapter 8)

Chapter 2

Background

This chapter analyses and reviews current understanding and modelling for dual-fuel combustion processes. The review highlights fundamental questions concerning combustion physics and limitations in the established dual-fuel modelling addressed in later chapters.

2.1 Dual-fuel engines

The main technical requirements for successful implementation of lean combustion in internal combustion engines (ICE), with minimum exhaust emissions and high thermal efficiency are: high compression ratio, a highly effective ignition system, thorough mixing, e.g. achieved by high turbulence levels and swirl at the end of compression, and potentially catalytic coating on the combustion chamber [128]. Catalytic contributions and investigation of different techniques to enhance turbulence are outside the scope of this research. The advantage of high compression ratio effect can be realised by adopting natural gas in an existing CI engine without serious mechanical modifications [232]. However, the low reactivity of natural gas imposes a challenge for the ignition of the mixture.

Different types of ignition systems have been tested in natural gas SI engines, ranging from inductive and capacitive discharge systems to a plasma jets [49]. The use of another more ignitable mixture to start the combustion of a main mixture has extensively been studied in the past and seems to be a promising concept. Some techniques initiate

combustion by addition of heat while some others generate radical species that enhance ignition and broaden the flammability limits [70, 242].

According to Wei and Geng [232], there are three main methods to apply natural gas in diesel engines. The first is called *dual-fuel*, where the gas is injected in the intake manifold to generate a well-mixed charge that is ignited by a pilot jet of a more reactive fuel. This method reduces the engine volumetric efficiency generally by about 1-4% due to the fuel gas volume and the lack of latent heat of vaporization [90, 104]. In the second, called *High Pressure Direct Injection (HPDI)*, the gas is directly injected in the cylinder during the compression stroke along with a pilot jet of a reactive fuel providing the ignition [56]. The third method consists of direct injection of gas in a region with a hot externally-heated surface to enhance ignition. It is worth emphasizing that the present study is focused in the dual-fuel combustion method. A multiple hole fuel injector can distribute the reactive pilot fuel in different regions of the combustion chamber, and that fuel can increase the burn rate and reduce combustion duration of the background lean natural gas mixtures [139, 195]. Combustion initiation in dual fuel engines is fundamentally different compared to premixed systems ignited by a spark plug since an additional fuel is present and ignition is determined by the reaction kinetics and the pilot spray interaction with turbulence.

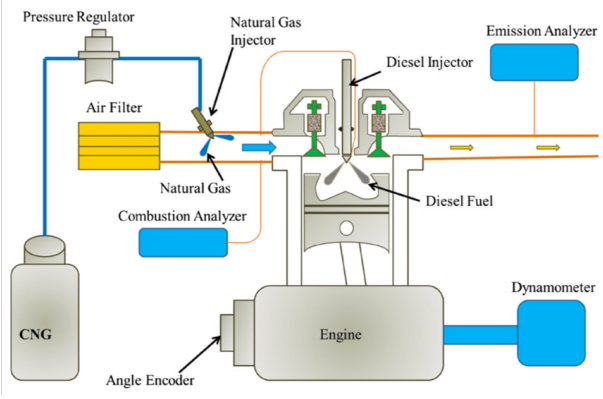

Figure 2.1: Schematic representation of a dual-fuel engine [219].

Reports about dual-fuel applications utilizing natural gas in large diesel engines date from 1950, when about 300,000 horsepower had been installed, mainly in mineral extraction in the USA [61]. In dual-fuel applied to CI engines, the amount of diesel injection should be modified in order to achieve comparable or higher values of pressure inside the cylinder during combustion. Some experiments show a decrease in the peak pressure for higher natural gas concentrations attributed to a longer ignition delay and

combustion duration [82, 152, 153]. On the other hand, other results reveal an increase in both pressure rise rate and pressure peak which is explained by the fast heat release by the premixed mixture when ignited close to TDC [123]. Among other parameters, the inlet temperature significantly affects the peak pressure resulting from the NG oxidation whereas the pilot jet ignition delay time remains approximately constant [231]. The small change in ignition delay time with respect to temperature can be explained by the Negative Temperature Coefficient (NTC) behaviour of diesel-like fuels, whereas the propagation speed increases non-linearly with unburnt temperature. The NTC usually occurs for higher hydrocarbon molecules, like diesel, and corresponds to an increase in ignition delay time for a certain range of unburnt temperature due to chemical effects. Additional explanation for the n-heptane NTC behaviour is given in Ref. [121].

A range of evidence suggests that chemical interaction between the two fuels results in differences during autoignition and flame propagation. Several studies have reported that the ignition delay time and ignition location of the pilot spray change considerably with the amount of premixed methane in the combustion chamber [7, 87, 88, 115, 117, 186, 195, 215]. An increase of ignition delay time may be expected because methane/air mixtures have ignition delay time orders of magnitude greater than that for n-heptane/air mixtures at similar conditions. However, it is not well established to what extent the effect of NG addition is only due to chemical kinetics interaction between the two fuels. Moreover, natural gas can interact differently depending on the fuel used in the pilot injection.

In practice, the amount of diesel fuel utilised to ignite the premixed charge varies, with 1 to 30% of energy coming from the pilot fuel [104, 184, 195]. In dual-fuel combustion, the pilot region is the major contributor to NO_x formation due to high temperatures [87]. Considering the Zeld'ovich thermal mechanism of formation of NOx, high temperature is necessary to provide the high activation energy for the oxygen atom to break the nitrogen molecule, and this reaction time scale is slow compared to the fuel oxidation process [217]. According to Kitamura et al. [98], temperatures above 2200K enhance NO_x formation and hence lower NOx emissions are obtained by using smaller pilot spray in a lean homogeneous natural gas-air mixture [106, 118]. In fact, the oxides of nitrogen can be lower than in SI engines under comparable conditions [87]. The injection timing also affects the NO_x formation when keeping the mass of pilot fuel constant. Peak NO_x production is observed for pilot injection around -35 ATDC, depending on the

inlet temperature [184]. For earlier injections, higher values of heat release are observed and the combustion has shorter duration. On the other hand, in a later injection, the combustion takes place in the expansion stroke resulting in low heat release rate and temperature. Intermediate injection timings may be required in order to give satisfactory combustion performance, even if the NO_x production is relative high due to a longer combustion duration and high pilot heat release.

Particulate matter and soot are considerably lower in dual-fuel than than diesel engines mainly due to the properties of NG. The high hydrogen to carbon ratio and the lack of carbon-carbon bonds lower the tendency to soot production. The majority of soot formation then comes from the pilot injection.

The main pollutant of concern in dual-fuel engines is unburned hydrocarbons (HC) produced at low and part load operations [118, 152, 185, 243, 249]. Liu et al. [118] measured the HC emissions composition for three different engine speeds and loads and concluded that around 90% of the total amount of unburned hydrocarbon consists of unreacted methane. At high engine load the unburned hydrocarbon emissions are reduced considerably, but did not achieve the same level as a CI engine operating only with diesel [185]. The low flame speed of natural gas combined with a lean mixture and a flame propagation occurring in the expansion stroke contribute to possible flame quenching. The flame heat transfer to the combustion chamber wall can also lead to flame quenching, leaving a layer of unburned mixture which can go out of the engine during the exhaust stroke [118]. According to Korakianitis et al. [104], an equivalence ratio of 0.4 is the threshold where the HC emissions considerably increase. For such conditions, the correct prediction of the flammability limits are important to assess the engine performance and emissions. The incomplete combustion of natural gas also helps to increase the CO emissions [118]. Usually, high CO emissions occur in a fuel-rich mixture due to the lack of oxygen to react with the fuel [76]. However, the carbon monoxide is also a result of low combustion temperature slowing the oxidation process [152].

A way to overcome the high production of CO and HC is to operate in *HPDI* mode, described before, or to increase the amount of pilot fuel injected. The second option increases the volume of the ignition region and contributes to a higher cylinder temperature for NG combustion. However, high pressures and temperatures can lead to the

autoignition of the end-gas [55, 194]. Moreover, as mentioned before, the increase in diesel injection increases the NOx formation. The trade-off between CO/HC and NOx emissions should be considered in the engine development. Nonetheless, premixed combustion of a homogeneous natural gas/air mixture ignited by injection of a small diesel pilot spray has been applied in many marine and stationary large-bore engines. Due to the especially high cost of prototyping and testing large-bore engines, it is particularly valuable to have reliable computational models for dual fuel combustion that can reduce the need for development through trial and error testing of engine hardware.

2.2 Physics of dual-fuel combustion

The combustion process in pilot-assisted compression ignition engines is fundamentally different from either spark-ignition or conventional diesel engines. Different ratios of pilot fuel and lean-premixed fuel lead to different combustion characteristics. The equivalence ratio of the premixed charge and injection parameters of the pilot fuel, such as start of injection, are the leading order parameters affecting the heat release rate profile [102]. Figure 2.2 presents a schematic representation of combustion process in dual-fuel engines. Pilot fuel is injected in the combustion chamber containing a lean premixed charge of natural gas/air. Similar to single-fuel direction-injection systems, the ignition occurs in mixture conditions favourable for autoignition [55]. Following formation of one or more ignition kernels, combustion transitions into a turbulent flame in a process involving competing phenomena, including autoignition, premixed and non-premixed flames. In the purely premixed combustion mode, fuel and oxidizer are mixed at the molecular level prior to oxidation, whereas in the non-premixed mode the fuel and oxidizer mix within the reaction zone. The case where fuel and oxidiser come from different streams but are partially mixed prior oxidation has been traditionally called partially premixed combustion [160]. The low reactivity of fuel lean natural gas mixture results in slow flame propagation and flame quenching can occur if volumetric expansion in the engine cylinder causes excessive cooling before the charge is fully burned.

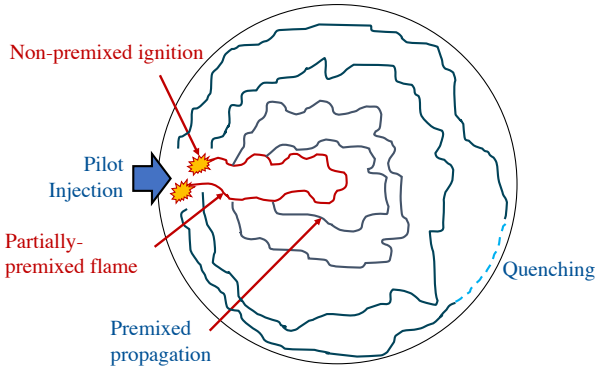

Figure 2.2: Schematic representation of dual-fuel combustion.

2.2.1 Dual-fuel ignition

The ignition process of a single-fuel direct-injection systems is relatively well-established in the literature [54, 136]. The main factors influencing the ignition process in single-fuel compression-ignition engines include thermochemical variables such as the ambient temperature, pressure and oxygen concentration, and spray parameters such as the nozzle geometry and the injection pressure and duration [112, 126, 155, 157, 158, 163]. Ignition of a single fuel occurs at a preferential composition given the thermochemical state of oxidiser and fuel, the so-called *most reactive mixture fraction* (ξ_{MR}) [136]. Mixture fraction is a conserved scalar that discribes the fraction of mass that originated from the fuel stream. The low-temperature combustion employed in diesel engines to limit NO_x emission can exhibit two-stage ignition [48] and a strong sensitivity to the fluid dynamic straining caused by the spray injection [112]. The fluid straining is often measured in terms of scalar dissipation rate. It enhances the transport of radicals away from the reaction zone and can accelerate, retard or preclude ignition depending on scalar dissipation rate and thermochemical conditions [175].

In the dual-fuel context, the ignition process is affected by the reaction kinetics of both fuels and by the turbulent mixing in the spray. The addition of premixed natural gas delays the ignition of the pilot fuel and changes its location in the more reactive fuel spray [193, 214]. The retarded autoignition process is related both to the reduced oxygen concentration and due to radical consumption by the methane molecule [214]. Nonetheless, the concept of most reactive mixture fraction is observed to be valid for dual-fuel combustion [55]. The mixing rate of the fuel is characterized by the mixture fraction

scalar dissipation rate. The response of fuel blends to different levels of scalar dissipation rate prior to ignition can also contribute to the increased ignition delays observed in experiments in dual-fuel combustion [194, 215], however it is not clear how significantly the presence of two different fuels affect the response to scalar dissipation. The effects of fuel addition in the oxidiser stream of a partially-premixed single-fuel counter-flow autoignition configuration were investigated in Ref. [175] using dimethyl-ether. Increasing amounts of DME in the oxidiser lead to a greater resilience to scalar dissipation rate due to transport of radicals from the lean premixed side to the rich fuel stream. Nonetheless, the findings cannot be extrapolated for dual-fuel conditions. Dimethyl ether autoignition characteristics and chemical kinetics are considerably different from methane which inhibit low temperature chemistry in large hydrocarbon fuels [214]. DME/CH4 fuel blends have been tested in an atmospheric counterflow burner showing that the methane addition increases the resilience to fluid dynamics strain, increasing the scalar dissipation rate extinction limits of the hot flame, but that it reduces the resilience of the cool-flame [176].

The ignition of the premixed charge happens via transfer of heat and of radical and intermediate species from a region of ignition kernels [55]. However, the ignition of the pilot fuel involves ignition in inhomogeneous mixture leading to complex flame structures that can affect the ignition of the premixed fuel. Hydrocarbons exhibiting two-stage ignition can present a poly-brachial flame structure during ignition in low-temperature combustion conditions [109]. The poly-brachial structure corresponds to a cool-flame branch related to the first-stage ignition and a high-temperature diffusion, lean-premixed and rich-premixed branches. In a study by Jin et al [84], performed simultaneously but independent from the similar work in Chapter 5, it was observed that the poly-brachial flames also occur during the ignition of a dual-fuel mixture. The effects of the premixed fuel chemical kinetics, however, have not been analysed directly and therefore further investigations are required.

2.2.2 Dual-fuel flames

Flame speed is critical in dual-fuel engines. Slow flame propagation may result in unburned hydrocarbons and carbon monoxide emissions [105], whereas excessively fast propagation may lead to autoignition of the end gas and consequent engine damage.

The displacement speed in the pilot-fuel region can be affected by mixture inhomogeneity [177, 180] and the heat and intermediate chemical species released by pre-ignition chemical reactions [207], in addition to the usual complexities of turbulence. The consumption of the premixed charge can transition from a flame propagation to an ignition front depending on the equivalence ratio, temperature and amount of pilot injection [55].

Classification of the different combustion modes (e.g. deflagration, ignition of diffusion fronts) involved in dual-fuel combustion is not trivial, however it provides valuable information regarding which strategy should be used to model the combustion process in dual-fuel engines. Since the rate of fuel consumption can change significantly depending on the operating conditions of the engine [102], the turbulent combustion model should not be tailored to just one specific combustion mode. Many attempts have been made to model dual-fuel combustion but there is still little knowledge regarding the combustion modes involved in the inhomogeneous dual-fuel pilot region. A well-established methodology to identify ignition from deflagration fronts is to compare the diffusion/reaction budgets using species mass fractions or energy transport equations [71, 109, 207]. The comparisons are limited to one-dimensional analyses and therefore are not attractive to understand the overall combustion process. The Chemical Explosive Mode Analysis (CEMA) has been used to detect different flame features such as ignition, extinction and premixed flames [124, 246]. CEMA is based on the eigen-analysis of the Jacobian involving the source terms in the species and energy equations therefore it is able to characterize the chemical dynamics of the combustion process. The chemical explosive mode is associated with a positive eigenvalue and indicates whether the thermochemical state leads to ignition when isolated. The identification of the different combustion modes was obtained for specific applications by defining a Damkhöler number based on the timescale of the chemical explosive mode and scalar dissipation rate. More recently, Xu et al [241] used CEMA to compute the ratio between the projected chemical and diffusion source terms to identify different local combustion modes. The methodology presents a systematic tool to distinguish between ignition, extinction and flame propagation, however so far it has not been applied to dual-fuel conditions.

2.3 Modelling of turbulent combustion

The solution of the system of equations for turbulent flows using the finite volumes approximation requires great computational effort. In general, three techniques are used to simulate a turbulent flow: Direct Numerical Simulation (DNS), which solves all turbulent scales; Large Eddy Simulation (LES), where the most energetic turbulent scales are solved and models are applied for the smaller ones; and Reynolds Averaged Navier-Stokes (RANS), most utilized by industry, applies models for the turbulent kinetic energy spectrum. Due to its computational cost, the application of DNS in turbulent reactive flows remains limited to fundamental studies using simplified configurations. Apart from the challenges of DNS related to accurate numerical integration of the governing equations in turbulent non-reactive flows, additional requirements need to be considered in the Direct Numerical Simulation of turbulent combustion. The main contributors to the excessive computational effort required to apply DNS in real engine problems are: the additional transport equations required for each chemical species considered; the thin reaction layers encountered at high temperatures and pressures; and the small chemical timescales of the chemical kinetics. The LES and RANS techniques involve the spatial filtering or ensemble averaging of the terms in the transport equations leading to unclosed terms for which additional modelling must be provided, for example involving the turbulent fluxes and reaction rates. In particular, the high non-linearity of the reaction rate with respect to the thermochemical state implies that the mean or filtered reaction rate required in RANS or LES is significantly different to the reaction source term evaluated based on the mean or filtered temperature and chemical composition available in RANS or LES, so that

$$\overline{\dot{\omega}}(\mathbf{Y}, T) \neq \dot{\omega}(\overline{\mathbf{Y}}, \overline{T}). \tag{2.1}$$

2.3.1 Turbulent combustion modelling strategies

Numerical modelling of turbulent combustion can be divided in two main types of approaches considering the assumptions regarding the combustion mode, i.e. mode-dependent and mode-independent. Even though turbulent combustion models can be classified without a prior assumption regarding the combustion mode [227], in reality

the well-established models are often tailored to premixed or non-premixed combustion modes. Simply speaking, premixed flame models [8, 23, 45, 131, 221, 233] fail to describe the diffusion-controlled and auto-ignition processes in diesel-like combustion, whereas non-premixed combustion models [99, 160, 237] cannot account for flame propagation in the gaseous premixed fuel/air mixture. Examples of mode-independent approaches are the well-mixed or first moment approach, where effects of sub-grid fluctuation are ignored. The key mode-independent method is the transported PDF approach, where a modelled transport equation is solved for joint probability density function of a set of variables in order to account for turbulent fluctuations [75]. Although, in principle, applicable to combustion in any mode it has proven difficult to formulate PDF modelling that wors accurately in premixed combustion applications. Despite the restrictions attached to the mode-dependent approaches, they can provide a good description (in specific situations) of the reaction-diffusion coupling with computational efficiency superior to transported PDF methods.

In this thesis, the focus is on the application of mode-dependent approaches for dual-fuel combustion. However, the complexity of the ignition due to the simultaneous occurrence of liquid fuel evaporation and chemical reactions of both fuels, and the later development of different combustion modes present a challenge for the established mode-dependent models [55, 230]. Two different approaches are considered here: a hybrid approach, where two different mode-dependent models are coupled to account for the premixed and non-premixed combustion; and a generalized model called Double Conditional Moment Closure (DCMC), where the problem is described by two conditioning parameters that account for the two different combustion modes.

This section proceeds with (a) a review of dual-fuel modelling efforts in light of the classification presented; (b) introduction to Conditional Moment Closure, a mode-dependent approach that is the main modelling approach used in this thesis; and (c) summary of the modelling strategies pursued in this study.

2.3.2 Application of turbulent combustion modelling to dual-fuel

Some attempts have been made to model dual-fuel combustion using phenomenological models, where empirical expressions are coupled with the thermodynamic energy conservation equation [6, 129, 138, 139, 164], or using quasi-two zone [6] and multi-zone

[117] models. These types of models demand relatively little computational effort and can give an overall description of the engine behaviour. The limitations arise from the fact that such models are not totally predictive and they require calibration with experimental data. Also, they do not consider the three-dimensionality of the combustion process, and this may cause errors in the emissions predictions.

Multi-dimensional Computational Fluid Dynamics (CFD) approaches promise greater predictivity. The most used method is to combined two models; one to compute the non-premixed combustion of diesel and another for premixed flame propagation [3, 32, 119, 143, 194]. In this approach, the pilot fuel ignition model acts as a trigger to start a separate model for combustion of the premixed charge. The limitation of this approach results from the poor consideration of the thermo-chemical interaction between the fuels which may cause deviations in the heat release rate predictions. In Cameretti et al. [32], for example, a challenging problem was the criterion for the ignition of methane. The model constants were adjusted differently for each of the two test cases in order to match the experiment. Schlatter [194] utilized a radical mass fraction as a tracer for the methane ignition as suggested in some DNS cases [14, 55, 56]. In order to account for the influence of the gaseous fuel on the ignition processes of the pilot fuel, an approach with detailed reaction mechanisms has been proposed for natural gas pilot ignition engines [127]. This Reynolds Averaged Navier Stokes-based approaches employ the so-called direct integration (DI) of the chemical kinetics, which considers that the turbulent fluid is locally well-mixed within the CFD cell, neglecting turbulence-chemistry interaction entirely. Direct integration methods cannot describe premixed flame propagation or the substantial influence of mixture fraction and temperature fluctuations during autoignition and combustion of fuel sprays [19, 136]. Hence this approach is restricted to cases where it is accurate to neglect turbulence-chemistry interactions both during the premixed combustion phase and during the pilot combustion phase.

In Refs. [250] and [203], dual fuel combustion was modelled by an adaptation of the characteristic timescale model (CTC), originally developed for diffusion-controlled combustion, and an extension of the model to account for addition of natural gas. Diesel and natural gas were lumped together to represent the fuel scalar in the combustion model according to their mass fractions in the respective cell of the computational domain. It was assumed that both the diesel and methane react at the same reaction rates.

Ignition was then modelled using the Shell ignition model [72, 192] which can successfully capture the auto-ignition of hydrocarbons in high-temperature and high-pressure environments. In this formulation the Shell model cannot account for the influence of the gaseous fuel on the ignition process of the pilot fuel despite the fact that, as presented in Chapter 4 and in Ref. [138, 195], the addition of methane has a substantial impact on the autoignition kinetics of diesel-like fuels. The model predictions for heat release rates, pressure evolutions and emissions were in good agreement with experimental results for natural gas substitution rates up to 90% (i.e. 10% diesel fuel pilot quantity). However, with substitution rates above 90%, where pilot masses are small, the agreement deteriorated rapidly due to the CTC models inability to accurately track the flame propagation processes which become prevalent with small pilot amounts and high natural gas substitution rates.

In order to account for the premixed flame propagation process of dual fuel combustion, a hybrid model was proposed in Ref. [202]. A level-set approach (G-equation) was chosen for the modelling of the premixed turbulent flame, which was extended with a new formulation for the determination of the laminar flame speed by chemistry tabulation. Due to the application of multiple models to cater for different stages in the dual fuel combustion process, a careful implementation of the coupling between those models is needed [202]. The extension to the G-equation model for the premixed combustion phase resulted in close agreement with experimental heat release profiles for natural gas substitution rates up to 98%. Furthermore it was highlighted that accurate laminar flame speed data for engine-like conditions is required to predict flame propagation rates and flame-wall interactions affecting emission of unburned hydrocarbons. A similar hybrid approach was presented by Cordiner et al. [46], combining the Shell ignition model with the coherent flame model.

The flame speeds of a wide range of two-component blends have been modelled to acceptable accuracy under non-autoignitive conditions using flame speed mixing-rules [58, 77, 244] as a function of the flame speeds of the individual fuel components. The success of these simple mixing rules indicates that the kinetic couplings between different fuels have a minor effect on the flame propagation under non-autoignitive conditions. Under autoignitive conditions however, the laminar flame speed increases due to the local accumulation of radical species and of the heat released prior to combustion [71]. It has not been established whether this effect is significant in dual-fuel engines. In

Chapter 4 it is found that thermochemical conditions of the fuel blends that result in a two-stage autoignition also result in a two-stage increase in flame speed by as much as 15%.

Recently, in Ref. [198] a hybrid flamelet generated manifold (FGM) hybrid model was developed to capture the auto-ignition and flame propagation of lean premixed methane-air mixtures. The different combustion modes were represented by flamelet tables generated by either a non-premixed counter-flow configuration (Conditional Moment Closure) or a purely premixed flame for different mixture fraction compositions. The model presented good agreement with a limited set of experimental data for a Rapid Compression Machine (RCEM), however it neglects stratification effects in the premixed flames close to the spray and still requires a user-specified criterion to decide when each table is used.

The well-mixed LES approach has been applied to dual-fuel combustion at conditions based on the Engine Combustion Network (ECN) Spray A [86]. Previous studies have reported small sensitivity to sub-grid scales during the autoignition process for the grid resolution used. The study provided valuable information regarding the early stages of dual-fuel combustion, however the used approach for the premixed phase of combustion has not been validated and DNS-like resolution may be required.

2.3.3 The Conditional Moment Closure framework

The Conditional Moment Closure (CMC) is an advanced predictive model originally developed by Klimenko [100] and Bilger [16]. The CMC model is a more refined description of turbulent combustion [222], where the mean thermochemical state of the mixture is conditioned to a variable which it depends on. Conditional Moment Closure (CMC) modelling seeks to relate turbulent fluctuations of composition and temperature to fluctuations of a smaller number of conditioning variables. The correct choice of the conditional variable reduces the fluctuations of the scalars and in various cases allows the closure of the reaction rates using first-order approximation as in Eq. 2.2, where the unconditional mean reaction rate is obtained from the conditional mean reaction rate evaluated using the conditional mean thermochemical state and the probability of finding conditioning variable in a given spatial location.

$$\overline{\dot{\omega}}(\underline{\mathbf{Y}},T) = \int_0^1 \langle \dot{\omega}(\underline{\mathbf{Y}},T)|\underline{\boldsymbol{\xi}} = \underline{\boldsymbol{\eta}}\rangle \, P(\underline{\boldsymbol{\eta}}) d\underline{\boldsymbol{\eta}} \tag{2.2}$$

Higher levels of fluctuation require second-order closure, using variances and covariances, or using an additional conditioning variable [38]. Figure 2.3 presents situation where the conditional fluctuations around the conditional mean are significantly reduced when two conditioning variables were used.

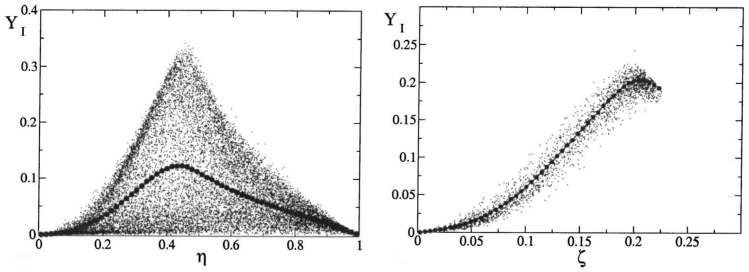

Figure 2.3: Scatter of intermediate mass fraction at a fixed time. Large filled circles are the conditional mean. Plot on the left corresponds mass fraction conditioned on mixture fraction $\langle Y_i|\eta\rangle$; whereas on the right mass fraction is conditioned on η close to stoichiometric and ζ: $\langle Y_i|\xi = 1/3, \zeta\rangle$ [111].

CMC has been successfully applied to nonpremixed combustion such as bluff body flames [96, 145, 178, 210] and jet flames [29, 57, 62, 146, 191, 224, 237] and also developed for premixed flames in Refs. [9, 10, 130, 187–189, 220, 223]. A simple approach for implementing CMC method is to assume spatial homogeneity of the conditional space leading to a zero-dimensional CMC as presented in [33, 53, 211]. In spray autoignition, spatial variations of single conditional moments are not negligible and spatial CMC or DCMC should be used. Studies with one-dimensional CMC are presented in [57, 97, 145, 146, 178, 191], whereas two-dimensional CMC was used in Refs. [22, 29, 52, 53, 146, 210, 224] and three-dimensional in Refs. [52, 62, 179, 188, 238]. Conditional moments often show smaller dependence on physical location than the unconditional means, therefore the spatial CMC can adopt a coarser grid or a lower dimension than that used in the CFD. Most of these studies are for non-premixed combustion and among these, all use the mixture fraction as conditioning variable. The mixture fraction characterizes mixing of the fuel and oxidiser and is the natural choice for this combustion mode [99]. The conditioning variable in premixed CMC is a progress variable whose definition maybe case dependent. The progress variable is often a function of species mass fractions [9, 10] and/or temperature [130] such that it equals zero in the unburnt state and unity in the fully reacted mixture [99]. In Ref. [187–189] the authors used the

total enthalpy (a conserved scalar given bysensible plus chemical enthalpy) to define a conditioning quantity in order to capture the fluctuations of the unburnt temperature seen in Homogeneous Charge Compression Ignition (HCCI) engines.

The spatial discretization of the conditional averages result in a considerable increase in computational time depending on the number of CMC cells used. Navarro-Martinez and Kronenburg [146] reported a factor of five increase in CPU time changing from a spatial one-dimensional CMC solution to a two-dimensional discretization. A possible approach to avoid this cost is to introduce n additional conditioning variable that is carefully chosen in order to reduce the fluctuations around the conditional mean. The conditional scatter during the ignition phase of a dual-fuel combustion motivates double-conditioning on mixture fraction and progress variable [55]. However, by conditioning on both on two variables the spatial variation of the conditional moments is reduced, possibly justifying a 'zero-dimensional' DCMC approach.

Few studies are found in the literature using DCMC. In Ref. [39], DCMC based on mixture fraction and scalar dissipation rate was developed to capture extinction and reignition in non-premixed combustion. Kronenburg [111] used DNS data to show the feasibility of using DCMC conditioned on mixture fraction and progress variable for modelling extinction and reignition. In Ref. [33], the authors have shown that the addition of a second conserved scalar conditioning variable in the CMC approach to account for fluctuactions in the unburnt state is reasonable for the prediction of autoignition in thermally and fuel-stratified mixtures. The use of mixture fraction and total enthalpy presented good predictions compared with the DNS results of autoignition in thermally inhomogeneous mixtures [187]. The importance of the cross-dissipation term was evaluated and found to have a small effect in the prediction of heat release rate in that case.

In the dual-fuel context, the mixture fraction and progress variable conditioning parameters is necessary capture both the non-premixed autoignition and the fully premixed flame propagation. The mixture fraction-progress variable methodology presented good results has been applied for a partially-premixed spray flame giving good agreement with experimental data in terms of lift-off height and overall flame structure [205]. Nonetheless, the assumptions made to close all terms in the DCMC model is a topic of ongoing research and requires further investigation for dual-fuel combustion. Both nonpremixed

CMC and DCMC based on mixture fraction and progress variable are mathematically presented in Chapter 3.

2.3.3.1 The joint-PDF

The unconditional Favre-averaged or Favre-filtered quantity ϕ required for RANS or LES is obtained, in the context of double conditioning, by integration with the mixture fraction and progress variable joint-PDF

$$\widetilde{\phi} = \int_0^1 \int_0^1 \langle \phi | \xi = \eta, c = \zeta \rangle \ \widetilde{P}\left(\xi = \eta, c = \zeta\right) d\eta d\zeta. \tag{2.3}$$

The transported PDF approach is a possible method to simulate the joint-PDF [11]. The computational cost of transported PDF methods are generally high due to the need to simulate the evolution of several realisations of the chemical composition in each CFD cell and result in a computationally expensive approach to apply in practical simulations. In addition, transported-PDF modelling for the premixed phase of combustion is not well-developed and therefore presumed PDF modelling has been developed. The presumed PDF approach employs algebraic functions to represent P as a function of a number of moments of the joint distribution [50].

The modelling of the joint mixture fraction ξ and progress variable c distribution is a topic of ongoing research. The statistical independence of ξ-c is often assumed in turbulent combustion modelling [21, 79, 113, 197], hence the joint-PDF is expressed as the product of the marginal distributions as

$$\widetilde{P}\left(\eta, \zeta\right) \approx \widetilde{P}\left(\eta\right) \widetilde{P}\left(\zeta\right). \tag{2.4}$$

DNS investigations of partially-premixed flames have shown that the assumption may not be appropriate [229]. Although the predictions of the turbulent combustion models previously mentioned [21, 79, 113, 197] presented satisfactory agreement with the reference data, it remains difficult to access the real impact of the statistical independence assumption. A direct comparison of the joint-PDF shapes is presented in Ref. [182] for a lifted-jet flame. The authors used the model for the joint distribution presented in Ref. [50], where the Plackett copula introduces the statistical dependence into the marginal

PDFs used for mixture fraction and progress variable. The statistical independence assumption showed good predictions of the ensemble-averaged reaction rate close to the flame base but over estimates at downstream positions. Therefore, the influence of the assumptions regarding the joint-PDF can be dependent on the case considered since the statistical independence is more likely to occur in flames with significant variance for mixture fraction and progress variable.

The presumed β distribution is the common choice for modelling the PDF of mixture fraction in non-premixed calculations using Conditional Moment Closure [22, 51, 66, 237, 239]. It presented better predictions than the clipped Gaussian distribution during the mixing process of a non-premixed gaseous n-heptane experiment [51, 132]. In multiphase simulations involving a fuel liquid spray, the mixture fraction β-PDF should be corrected for the mixture fraction at saturation due to the low estimate of the probability at those conditions [22].

The marginal PDF of progress variable has been modelled in a number of different ways. Cha & Pitsch [40] tested the β-PDF for progress variable in the context of extinction and reignition using the second order closure for the chemical source term in conditional moment closure modelling. Even though the results present a good agreement with DNS data in terms of the conditional average temperature at stoichiometric mixture fraction, the presumed PDF does not predict correctly the shape of the unimodal and bimodal distributions. The good predictions are obtained with a cancellation of errors between the presumed distribution and the nonlinear source term. In fact, the β distribution does not incorporate information regarding the reaction-diffusion process and the effects of different fuels that affect the distribution of progress variable within the flame. A laminar flamelet based PDF is presented in Ref. [25] for the thin flamelet regime, i.e. when the Kolmogorov scale is larger than the characteristic time scale of the laminar flame. The interior PDF is assumed to be inversely proportional to the progress variable gradient computed in a one-dimensional planar flame. The results showed good agreement with DNS data and revealed improved predictions for the shape of the PDF in comparison with the presumed β-PDF and delta function proposed in [24]. An improved version of the laminar based PDF for all range of c mean and variance can be found in Ref. [83]. Acknowledging the fact that the modified laminar based PDF can present an over prediction of the probability followed by a sharp cut-off in the region of $c \approx 1$, a new modelling for the progress variable PDF was proposed in Ref. [225] based on the

solution of a modelled turbulent flame representation obtained using the Linear Eddy Model. The new approach presented a better agreement with DNS results in comparison with β-PDF, laminar PDF [25] and modified laminar PDF [83]. These findings suggest that incorporating information about the reaction-diffusion dynamics associated with the specific combustion process can give improved modelling for a given set of input moments. Despite the good predictions of the model proposed by [225], the generation of the PDFs rely on one-dimensional premixed solutions that neglect fuel stratification as present in dual-fuel combustion and modern combustion devices.

The marginal distribution of progress variable in the context of dual-fuel combustion has not been investigated so far. The interaction between different combustion modes with different fuel blends can have a significant impact on the distribution and therefore requires further investigation.

2.3.4 Objectives for model development

Dual-fuel combustion can be modelled in different ways considering the computational time available or the degree of accuracy required in the results. Table 2.1 presents four possible combinations of mode-dependent models. From the left to the right and from the top to the bottom the models increase in complexity. The simplest method τ_{ign} & G-eq, uses an algebraic model, here named τ_{ign}, to capture ignition timing and a G-equation premixed flamelet model for the flame propagation. For a better description of the ignition phase, the non-premixed CMC approach can be used with the G-equation flamelet model: CMC (ξ) & G-eq. A different approach is to combine the simple τ_{ign} model with the more advanced a premixed model, called CMC (c). Ultimately, the most advanced (and costly) approach combines the two CMC models generating a double conditioned model, therefore avoiding the need for the user to specify the criteria for switching between the ignition and premixed models.

Table 2.1: Structural modelling approaches for dual-fuel combustion

τ_{ign} & G-eq	CMC (ξ) & G-eq
τ_{ign} & CMC (c)	DCMC (ξ, c)

Application of these possible model combinations raises a number of questions covered in *Theory and modelling of dual-fuel combustion*, including the dependence of the ignition time and location on dual-fuel conditions required for τ_{ign} (Ch. 4 & 5); the behaviour and modelling of the laminar and turbulent flame speed under dual-fuel conditions, as required for the G-equation model (Ch. 4 & 5 & 7); the structure of the dual-fuel combustion and the consequent suitability of CMC or DCMC approaches (Ch. 7 & 8); modelling of the conditional scalar dissipation rates and (joint) PDFs associated with these models (Ch. 5 & 6).

Chapter 3

Formulation

This chapter first sets out the governing equations and properties of turbulent flows used for DNS-based fundamental investigations of dual-fuel combustion in Chapters 4 and 5. Subsequently the formulation is set out for the Conditional Moment Closure modelling developed in Chapters 6, 7 and 8.

3.1 Governing equations for reactive flow

Combustion involves chemical reactions taking place within a fluid flow. Fuel is provided either as a solid, liquid or gas, and heat may be provided or removed by conduction, convection or radiation. The governing equations for reactive gaseous flow are set out below including source terms accounting for supply of fuel from a second phase, molecular transport and chemical production of different species, heat and thermal radiation.

3.1.1 Mass conservation equation

The mass conservation equation for a single-phase fluid is

$$\frac{\partial \rho}{\partial t} + \nabla \cdot (\rho \mathbf{u}) = \rho \Pi \tag{3.1}$$

where ρ is the density of the fluid, t is time, $\mathbf{u}$ is the velocity vector. The source term Π represents mass addition, for example the evaporated liquid mass per unit volume and

time.

3.1.2 Species conservation equation

The mass conservation equation for species k is defined as

$$\frac{\partial \rho Y_k}{\partial t} + \nabla \cdot \left(\rho \left(\mathbf{u} + \mathbf{V}_k\right) Y_k\right) = \rho \dot{\omega}_k + \rho \Pi_k \tag{3.2}$$

where $\mathbf{V}_k$ is the diffusion velocity vector and $\dot{\omega}_k$ is the reaction rate of species k. The term Π_k is the source term due to inter-phase mass transfer for species k. Different methods are used to obtain the diffusion velocity, the most complex one considers a binary diffusion matrix specifying different transport properties for each pair of species in the mixture [234]. The result is a system of equations of size N^2, where N is the number of species, which must be solved for each direction and at every instant in unsteady flows. In multi-dimensional CFD applications this formulation is usually avoided due to its computational cost. Considering a mixture that contains only two species k and p, in which the pressure gradients due to body forces make a negligible contribution to the molecular transport the diffusion velocity can be modelled by Fick's Law [222]

$$V_k Y_k = -D_{kp} \nabla Y_k \tag{3.3}$$

where D_{kp} is the diffusion coefficient of species k in p. Fick's Law may be applied to multi component mixture by adopting the mixture-averaged approach of Hirschfelder and Curtiss where D_{kp} in Eq. 3.3 is replaced by an equivalent diffusion coefficient D_k of species k in the remaining mixture, with

$$D_k = \frac{1 - Y_k}{\sum_{j \neq k} X_j / D_{jk}}. \tag{3.4}$$

where X_j is the mole fraction of species j.

Equation 3.3 is recovered when only two species are considered in Eq. 3.4. The diffusion coefficient D_k can alternatively be expressed in terms of a Lewis number $Le_k = D_{th}/D_k$, where D_{th} is the thermal diffusivity [222]. The Lewis number differs among species,

with small molecules such as H_2 or H diffusing faster than heat. Values of about 0.3 are encountered for H_2, whereas the Lewis number of CO_2 is about 1.4. When the Hirschfelder and Curtiss approximation is directly applied in Eq. 3.2, the mass is not conserved and a correction velocity V^c should be applied in the convection term. Equation 3.2 then becomes

$$\frac{\partial \rho Y_k}{\partial t} + \nabla \cdot (\rho(\mathbf{u} + \mathbf{V}_k^c)Y_k) = \nabla \cdot \left(\rho D_k \frac{W_k}{W_{mix}} \nabla X_k\right) + \rho\dot{\omega}_k + \rho\Pi_k \tag{3.5}$$

where W_k and W_{mix} are species k and the mixture's mean molecular weights, respectively. The correction velocity vector $\mathbf{V}_k^c$ is modelled as

$$\mathbf{V}_k^c = \sum_{k=1}^{N} D_k \frac{W_k}{W} \nabla X_k \tag{3.6}$$

The reaction source term $\dot{\omega}_k$ depends on the net contribution of all the elementary chemical reactions, producing or consuming species k. The net production rate of species k due to all N reactions can be expressed as

$$\dot{\omega}_k = \sum_{i=1}^{N} \nu_{ki} Q_i \tag{3.7}$$

where $\nu_{ki} = \nu''_{ki} - \nu'_{ki}$, with ν'_{ki} and ν''_{ki} being the stoichiometric coefficients of the reactants and products. The progress rate Q_i is written as

$$Q_i = K_{fk} \prod_{i=1}^{N} [X_k]^{\nu'_{ki}} - K_{rk} \prod_{i=1}^{N} [X_k]^{\nu''_{ki}} . \tag{3.8}$$

The coefficients K_{fk} and K_{bk} are the rates of forward and backward reactions, respectively. The rate coefficients in kinetic models for combustion chemistry are generally well characterized by an Arrhenius (exponential) dependence on temperature in the form

$$K = AT^{\beta} \exp\left(\frac{E_A}{R_u T}\right), \tag{3.9}$$

where A is a pre-exponential factor that relates to the likelihood of molecules colliding in orientations leading to reaction. The term $\exp(E_A/R_uT)$ accounts for the fraction

of molecular collision that occur with energy above the activation energy threshold E_A that will lead to a reaction [217].

3.1.3 Momentum conservation equation

The momentum conservation equation is derived from Newton's Second Law, considering Newtonian viscous forces and pressure forces, giving

$$\frac{\partial\left(\rho u_i\right)}{\partial t}+\frac{\partial}{\partial x_i}\left(\rho u_i u_j\right)=-\nabla p+\frac{\partial \sigma_{ij}}{\partial x_i}+\rho F_i+S_{,u}, \tag{3.10}$$

where p is the static pressure, σ is the viscous stress tensor, $\mathbf{F}$ is the vector of body forces acting on the flow field and $\mathbf{S}_u$ is the exchange of momentum from any dispersed phase to the gas. The viscous stress tensor is given by

$$\sigma_{ij}=2\mu\left[S_{ij}-\frac{1}{3}S_{kk}\delta_{ij}\right], \tag{3.11}$$

where δ_{ij} is the Kronecker delta, e.g. 0 if $i \neq j$ and 1 if $i = j$. The viscosity μ is a property of the fluid which depends on temperature and chemical composition. S_{ij} is the instantaneous strain rate tensor, defined as

$$S_{ij}\equiv\frac{1}{2}\left[\frac{\partial u_i}{\partial x_j}+\frac{\partial u_j}{\partial x_i}\right]. \tag{3.12}$$

3.1.4 Energy conservation equation

The total enthalpy of the chemical species h_k is the sum of the sensible and chemical enthalpies

$$h_k=h_{k,ref}+\int_{T_{ref}}^{T}c_{p,k}dT, \tag{3.13}$$

and the total enthalpy of the mixture is obtained with

$$h=\sum_{i=1}^{n}Y_k h_k. \tag{3.14}$$

The energy balance equation in terms of total enthalpy can be derived from the First Law of Thermodynamics

$$\frac{\partial}{\partial t}(\rho h) + \frac{\partial}{\partial x_i}(\rho u_i h) = \frac{\partial p}{\partial t} + \sigma_{ij}\frac{\partial u_i}{\partial x_i} + u_i\frac{\partial p}{\partial x_i} - \frac{\partial j_q}{x_i} + q_R + S_h, \tag{3.15}$$

where q_R is the source term for the radiation heat transfer. The first term on the RHS accounts for the pressure change and must be retained for internal combustion engine calculations. The second term accounts for viscous heating. The third term in the RHS is important for acoustic interaction and pressure waves. The term S_h accounts for the change in enthalpy of the gas phase due to heat exchange with the dispersed phase. The term j_q is the heat flux due to enthalpy transport by diffusional fluxes j_k,

$$j_q = -\lambda\nabla T + \sum_{i=1}^{n} h_k j_k, \tag{3.16}$$

where λ is the thermal conductivity and j_k is given by Eq. 3.3.

The static pressure is computed assuming the ideal gas law as

$$p = \rho R_u T / W_{mix}, \tag{3.17}$$

where R_u is the Universal Gas Constant and W_{mix} is the mean molar mass of the mixture.

3.2 Combustion

The combustion equations set out above describe reacting flow in a very general way. In practical combustion systems involving fast chemical kinetics and high Reynolds numbers, very rich physical behaviours emerge from this mathematical description, including turbulence, flames and various interactions between the two. A basic description of these emergent turbulent combustion behaviours is presented below in order to introduce a number of essential parameters used to characterise combustion processes throughout this thesis.

Combustion can be defined as a rapid oxidation generating heat or both heat and light [217]. Because of the high temperatures involved, combustion chemical kinetics are relatively fast, so that combustion tends to occur within thin sheets called flames. Flames maybe categorized according to how fuel and oxidizer are mixed. For example, predominantly premixed flames are seen in spark ignition engines, whereas predominantly non-premixed flames can be seen in compression ignition engines. Both types of flames can occur in either turbulent or laminar flows. In practice, combustion systems can display a wide range of partially-premixed combustion modes, potentially with premixed and non-premixed flames coexisting. However, in order to formulate modelling that may apply across the multiple modes found in dual-fuel engines it is first necessary to introduce theoretical descriptions of the limiting premixed and non-premixed cases.

3.2.1 Premixed flames

Premixed flames have fuel and oxidizer mixed at the molecular level prior to oxidation and involve a thin reaction front propagating with a burning velocity. Figure 3.1 shows a planar freely-propagating laminar premixed flame with fuel-lean reactants. The flame front propagates into the oncoming fluid at speed S_L. The chemical reaction forms products Y_P and heat which diffuse ahead of the reaction zone to form a preheat zone. Products mass fraction increases toward the burnt side of the flame until a certain level where all fuel is consumed and a burnt temperature T_b is reached. In a steady state flame, the diffusion of heat and products is balanced by the heat release rate.

The numerical solution of one-dimensional steady-state flames, such as presented in Fig. 3.1, is usually performed by prescribing the thermochemical state at the cold boundary and fixing the location of the flame within the domain. This is the so-called freely-propagating flame solution, where the mass flow rate at the inlet is part of the solution of the system of equations. In order to avoid heat transfer to the cold boundary, the flame should be positioned in the domain such that the temperature and species gradients are negligible at the boundary [91]. The simulation of flames at elevated pressure and temperature can be problematic in the case of highly reactive fuels since the zero gradient assumption for the cold boundary may not be satisfied.

The premixed flame has a characteristic thermal thickness δ computed as [222]

$$\delta_{th} = \frac{\Delta T}{\left|\frac{dT}{dx}\right|_{max}}, \tag{3.18}$$

where ΔT is the difference between the burnt and unburnt temperatures. Based on the observations that the reaction layer is thin compared to the preheat layer, Spalding [209] derived a model for flame thickness as

$$\delta_{th} \approx 2\frac{D_{th}}{S_L}, \tag{3.19}$$

and the same form of relation $\delta_{th} \sim D_{th}/S_L$ can be obtained purely on dimensional grounds [222]. A characteristic flame time scale, equal to the time taken to burn through one flame thickness is given by

$$\tau_c = \delta_{th}/S_L. \tag{3.20}$$

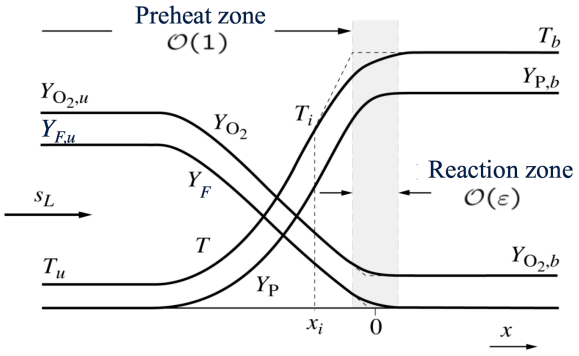

Figure 3.1: Laminar premixed flame structure [160].

Because premixed flames are naturally thin, the structure observed in laminar flames can persist even in turbulent flow, provided that the flame length scales are relatively short compared to the length scales of the turbulence. The flame scales may be compared with the integral turbulence scales, or the Kolmogorov scales of turbulence by considering the Damköhler number Da or Karlovitz number Ka, respectively.

$$Da = \frac{\tau_t}{\tau_c} = \frac{l_t/u'(l_t)}{\delta/S_L} \tag{3.21}$$

where l_t is the integral scale and $u'(l_t)$ is the integral RMS velocity. The Karlovitz number Ka relates a time scale τ_k defined as the velocity fluctuation and eddy size evaluated at the Kolmogorov scale (smallest eddy) to τ_c

$$Ka = \frac{\tau_c}{\tau_k} = \frac{u'(\eta)/\eta}{S_L/\delta}. \tag{3.22}$$

When $Ka < 1$, the shortest turbulent time scale is greater than the chemical scale and turbulence is not able to affect the flame inner structure which remains similar to the laminar structure presented in Fig. 3.1. The flame can be wrinkled by turbulent motions and the turbulent flame speed has been modelled as the laminar flame speed multiplied by factor related to the increase in flame surface area caused by the wrinkling. For $Da << 1$ the turbulence is faster than the chemical time scale. The reactants and products are then mixed by turbulent motions faster than they react and the reaction rate is controlled by chemistry defining a perfectly stirred reactor regime [222].

Various combustion regimes can be identified considering the Karlovitz numbers in Fig. 3.2. For $Ka < 1$, the smallest eddy has a greater time scale than the flame chemical scale. In this "thin flame regime" or "flamelet regime" the flame structure remains laminar and turbulent motions can only wrinkle the propagation front. Two additional regimes are identified for $Ka < 1$ [222]:

- $u' < S_L$: the turbulent fluid motion is too low to interact with the flame front. This condition is named "wrinkled flamelet regime".
- $u' > S_L$: in this case the velocity fluctuation is able to wrinkle the flame and the interaction can lead to pockets of burnt and unburnt mixtures. This regime is described as the "corrugated flamelet" regime.

For the case where the flame time scale is in between the integral and Kolmogorov time scales, i.e. $\tau_\eta < \tau_c < \tau_t$ or $Ka > 1$ and $Da > 1$, the small eddies modify the flame structure at the same time as it is wrinkled. The flame can no longer be treated as a laminar flame front. This regime, called "thickened flame" or "distributed reaction zones", can lead to flame quenching depending on the intensity of the flame stretch. A "well-stirred reactor" limit can be reached when the integral scale turbulent motions have a shorter time scale than the flame ($Da < 1$) [222].

Peters [160] defines an additional Karlovitz number Ka_δ as a function of the reaction zone thickness δ_R,

$$Ka_\delta = \frac{\delta_R^2}{\eta^2}. \tag{3.23}$$

This quantity characterizes the extent to which turbulence can affect not only the preheat zone but also the inner reaction zone of the flame. At atmospheric conditions, the reaction zone corresponds to approximately one tenth of the preheat zone thickness leading to $Ka_\delta = Ka/100$. Figure 3.2 the premixed regime diagram plotted as the non-dimensional velocity v'/S_L versus the length scale l_t/δ_{th} proposed by Peters [160]. The Reynolds number presented in the diagram relates turbulent quantities: $Re = v'l_t/S_L\delta_{th}$. The line $v'/S_L = 1$ corresponds to the boundary between wrinkled and corrugated flamelets, i.e. when turbulent motion is fast enough to compete with the propagation speed. The boundary $Ka = 1$, also called the Klimov-Williams criterion, represents the case where the Kolmogorov length scale is equal to the flame thickness. For $1 < Ka < Ka_\delta$ the eddies can penetrate the preheat zone not affecting the reaction layer. In the broken reaction zones, or well-stirred reactor [222], the eddies increase the heat loss and intermediate species transport from the reaction zone quenching the flame locally. This regime is not classified as a so-called flamelet regime, defined according to Poinsot and Veynant as: *a turbulent premixed reacting flow is in a flamelet regime when a line connecting any point A in fresh gases to another point B in burnt products crosses (at least) one active flame front.* In other words, the authors define the flamelet regime as a continuous flame without quenching.

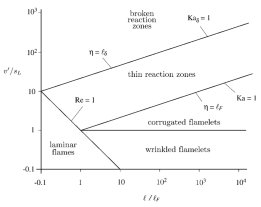

Figure 3.2: Premixed turbulent combustion diagram [160].

3.2.2 Non-premixed combustion

Non-premixed combustion is characterized by the fuel and oxidizer coming from different streams, as illustrated in Fig. 3.3 for a counter-flow configuration. Non-premixed combustion can also be described as a diffusion flame because, once ignited, the reaction rate is generally limited by the rate of diffusion of the fuel and oxidizer into the flame. Both terminologies are used in this text. The mixture fraction ξ, defined as the fraction of the mass at a point in the flow that originated from the fuel stream, is a natural choice of parameter for use in analysis and modelling of non-premixed flames. The rate of molecular mixing within a non-premixed flame can then be characterised by the mixture fraction scalar dissipation rate, χ_ξ,

$$\chi_\xi \equiv 2D_\xi \left(\nabla\xi\right)^2, \tag{3.24}$$

where D_ξ is the effective diffusivity of the mixture fraction variable. Following convention for the Conditional Moment Closure modelling approach [99] used in Chapters 7 and 8, the scalar dissipation rate can alternatively be described using the parameter N_ξ, defined as $N_\xi \equiv \chi_\xi/2$. Confusingly, both χ_ξ and N_ξ get described as scalar dissipation rate.

The counterflow configuration presented in Fig. 3.3 has been used extensively to study autoignition in diffusion flames and their response to fluid dynamic strain, as characterised by the scalar dissipation rate. Increasing the scalar dissipation rate for an initially-burning non-premixed counterflow flame increases diffusion of heat and product species out of the reaction zone, eventually leading to extinction at a critical scalar dissipation rate, χ_{ext}.

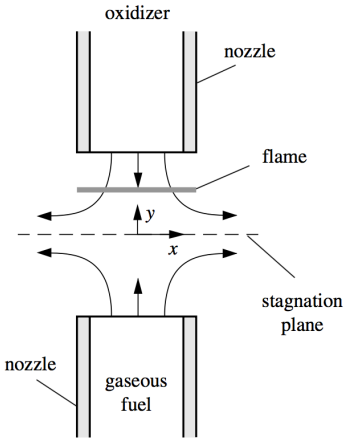

Figure 3.3: Counter-flow configuration of a nonpremixed flame [160].

Autoignition of non-premixed flames is of particular relevance to combustion in dual-fuel engines. Excessive scalar dissipation can prevent accumulation of heat and radical species needed for autoignition. The ignition delay time generally increases with scalar dissipation rate as observed in Refs. [81, 120, 134] and autoignition is only possible below a critical scalar dissipation rate, χ_{ign}, which is necessarily less than the critical scalar dissipation rate for extinction. The values of χ_{ext} and χ_{ign} depend on the state of the fuel and oxidiser streams and the ratios χ/χ_{ext} or χ/χ_{ign} can be used to characterise the influence of fluid dynamic strain on the non-premixed reaction processes.

In an autoigniting non-premixed flame, ignition first occurs at a preferential value for the mixture, called *most reactive mixture fraction* ξ_{MR}, which is usually different from the stoichiometric value [136]. The most reactive mixture fraction varies depending on the fuel and boundary conditions. It is shown in Ref. [136], comparing different DNS simulations, that ignition kernels appear in a preferred mixture fraction and in regions with low scalar dissipation rates. In turbulent flow, the ignition delay time is usually greater than the corresponding value with no mixing. Fluctuations in the scalar dissipation rate can allow the mixture to autoignite even if the time-averaged quantity is above the critical value [136].

3.2.3 Partially premixed combustion

Practical combustion devices often try to benefit from the advantages of premixed and non-premixed combustion modes by burning the fuel in a stratified medium that is partially premixed. The partially premixed combustion mode comprehends all the conditions where the flame cannot be classified as purely premixed or non-premixed. The partially premixed situation is likely to happen in systems where fuel and oxidiser are allowed to mix prior to reaction [59]. Examples of partially premixed combustion comprehend: lifted flames in gas turbines, direct injection spark ignition engines and the early combustion stages of a compression ignition engine [160].

The autoignition process in a partially premixed medium leads to subsequent flame propagation into mixture with different equivalence ratios and can result on the formation of a triple flames structure as illustrated in Fig. 3.4. The rich and lean partially premixed flames connect around the stoichiometric equivalence ratio and a non-premixed flame is established downstream as a result of the excess of oxygen in the lean side and fuel on the rich side. The curvature of the flame is related to the decrease in the propagation speed away from the stoichiometric region.

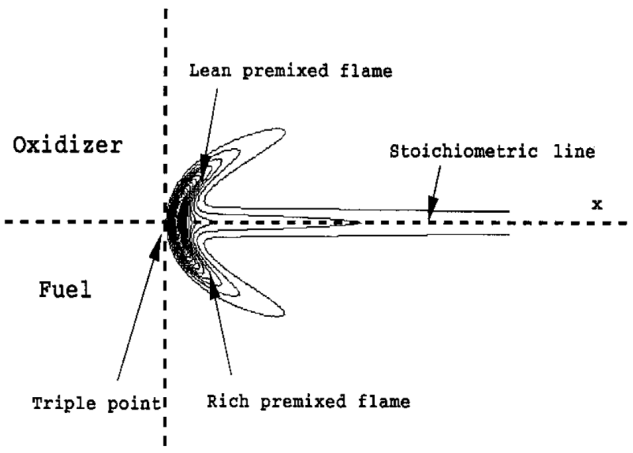

Figure 3.4: Illustration of a propagating triple flame [59].

In dual-fuel combustion, partially premixed combustion is likely to occur in the region close to the pilot fuel. As shown in Chapter 5, the appearance of triple flames during the ignition process of the dual-fuel mixture contribute to the ignition of the purely premixed charge.

3.3 Conditional Moment Closure

3.3.1 First-order conditional moment closure

Reaction rates have highly non-linear dependence on the thermochemical state in combustion, and turbulence can cause large fluctuations of the thermochemical state. Therefore evaluating reaction rates based on the unconditionally-averaged thermochemical state can give large errors:

$$\widetilde{\dot{\omega}\left(\mathbf{Y}\right)} \neq \dot{\omega}\left(\tilde{\mathbf{Y}}\right). \tag{3.25}$$

$\dot{\omega}$ is the vector of reaction rates corresponding to the vector of thermochemical state variables $\mathbf{Y}$. The Conditional Moment Closure approach seeks to achieve improved modelling of turbulent reacting flows by evaluating the mean or filtered reaction rates appearing in RANS or LES in terms of conditional moments, rather than unconditional moments.

Due to inherent reaction-diffusion dynamics of combustion processes [168], the thermochemical state tends to fluctuate along a low-dimensional manifold, such that the fluctuations of the numerous thermochemical state variables can be related to the variation of a much smaller number of 'conditioning' thermochemical variables. By choosing a set of conditioning variables ϕ that accounts for the majority of turbulent fluctuations, the conditionally-averaged reaction rate can be accurately approximated with first-order conditional moment closure:

$$\langle \dot{\omega}\left(\mathbf{Y}\right) \mid \phi = \psi \rangle \approx \dot{\omega}\left(\langle Y \mid \phi = \psi \rangle\right). \tag{3.26}$$

$\langle \cdot \mid \psi \rangle$ denotes density-weighted ensemble-averaging subject to the vector of conditioning variables ϕ being equal to a vector of sample-space variables ψ. Having modelled the conditionally-averaged reaction rate, the unconditionally-average reaction rate can be obtained by convolution of the conditional reaction rates with a model for the joint-probability density function (pdf) of the conditioning variables:

$$\widetilde{\dot{\omega}\left(\mathbf{Y}\right)} \approx \int \langle \dot{\omega} \mid \phi = \psi \rangle \tilde{P}_{\phi}\left(\phi = \psi\right) d\psi \tag{3.27}$$

where $\tilde{P}_{\phi}(\psi)$ is the density-weighted joint-pdf for the vector of conditioning variables.

Application of conditional moment closure therefore requires (i) selection of suitable conditioning variables; (ii) modelling for the evolution of the conditionally-averaged thermochemical state; and (iii) modelling for the joint-pdf of the conditioning variables, as formulated below.

3.3.2 Conditioning variables

In many practical combustion problems it is found that as few as one or two conditioning variables can be sufficient to close the conditional reaction rates accurately: In non-premixed combustion, it is found that the majority of the thermochemical variation can be related to fluctuations of the mixture fraction; in premixed combustion it is found that the majority of the thermochemical variation can be related to fluctuations of a reaction progress variable; and in partially-premixed combustion, for example in dual-fuel engines, it is found that the majority of the thermochemical variation can be related to the combined fluctuations of mixture fraction and reaction progress variable.

Mixture fraction: The mixture fraction is defined as the local fraction of mass originating from a particular stream of fluid. In two-stream non-premixed combustion, the mixture fraction is conventionally used to represent the fraction of mass originating from the fuel stream. If all chemical species diffuse equally, then the mixture fraction is uniquely defined and can be evaluated by considering atom conservation of any element present in the system. If preferential diffusion occurs, mixture fraction is not uniquely determined by the atomic mass fractions and it is common to use a weighted combination of the carbon, hydrogen and oxygen atoms proposed by Bilger [15]. The mixture fraction can be computed as

$$\xi = \frac{\beta - \beta_1}{\beta_2 - \beta_1}, \tag{3.28}$$

where the subscripts 1 and 2 are the oxidizer and fuel streams, respectively. When $\beta = 0$, $\xi = \xi_{stoich}$. The β values are a function of the reactive elemental mass fractions Z_i

$$\beta = \sum_{i=1}^{elements} \gamma_i Z_i. \tag{3.29}$$

The coefficients γ_i for hydrocarbon fuels proposed by Bilger [15] are $2/W_C$, $1/(2W_H)$, and $-1/W_O$ for carbon, hydrogen and oxygen. W_i is the atomic weight of element i.

The elemental mass fraction is obtained with the expression

$$Z_i = \sum_{i=1}^{elements} \sum_{j=1}^{nspec} \frac{W_i Y_j}{MW_j} \nu_i \tag{3.30}$$

where Y_j is the mass fraction of species j, MW_j is the molecular weight of the species, and ν_i is the number of moles of element i in the molecule.

Progress variable: A progress variable is a reactive scalar quantity selected in order to measure the evolution from the unburnt to the fully-burnt state: it should therefore increase monotonically through an ignition or deflagration reaction front. Progress variables have been defined in terms of temperature, sensible enthalpy, mass fractions or mole fractions [99, 160, 228]. By convention the progress variable is normalised to vary between zero in the reactants and unity in the products [160]. In this study, it is assumed that a well-defined progress variable can be constructed as a linear sum of species mass fractions,

$$Y_c = \alpha \cdot \mathbf{Y} \tag{3.31}$$

where α is the vector of weighting coefficients for the species mass fractions. A normalised progress variable c can then be obtained using the unburnt $Y_{c,u}$ and burnt chemical equilibrium $Y_{c,eq}$ limits of Y_c based on the local mixture fraction value:

$$c(x_i, t) = \frac{Y_c(x_i, t) - Y_{c,u}(\xi(x_i, t))}{Y_{c,eq}(\xi(x_i, t)) - Y_{c,u}(\xi(x_i, t))}. \tag{3.32}$$

It is desirable that the choice of α should provides good resolution of the thermochemical variation through the reaction front, and methods have been proposed for optimising the progress variable specification, for example Ref. [80]. However it has also been found that relatively simple summation of four main product species mass fractions, $Y_c = Y_{H_2O} + Y_{CO_2} + Y_{CO} + Y_{H_2}$ gives satisfactory behaviour across a broad spectrum of combustion modes and a wide range of hydrocarbon fuels (i.e. excluding hydrogen and synthesis-gas). Assuming all of these four species are not present in the unburnt mixture, the expression for progress variable simplifies to

$$c(x_i, t) = \frac{Y_c(x_i, t)}{Y_{c,eq}(\xi(x_i, t))}. \tag{3.33}$$

The governing equation for Y_c is obtained as a linear combination of the species mass fraction equations. If all species have equal diffusivities D and assuming there is no condensation or evaporation of the species used to define Y_c, Y_c evolves according to

$$\frac{\partial \rho Y_c}{\partial t} + \nabla \cdot (\rho \mathbf{u} Y_c) = \nabla (\rho D \nabla Y_c) + \rho \dot{\omega}_{Y_c} \tag{3.34}$$

where $\dot{\omega_{Y_c}}$ is the progress variable reaction rate. Substituting the normalised progress variable definition from Eq. 3.33 into Eq. 3.34 yields a transport equation for c,

$$\frac{\partial \rho c}{\partial t} + \nabla \cdot (\rho \mathbf{u} c) = \nabla (\rho D \nabla c) + \rho \dot{\omega}_{c^*} + \rho c \Pi. \tag{3.35}$$

The effective chemical source term for normalised progress variable $\dot{\omega}_{c^*}$ takes account of the effect of mixture fraction diffusion on the progress variable normalisation,

$$\dot{\omega}_{c^*} = \frac{1}{\partial Y_c / \partial c} \left[\dot{\omega}_{Yc} + N_\xi \frac{\partial^2 Y_c}{\partial \xi^2} + 2 N_{\xi,c} \frac{\partial^2 Y_c}{\partial \xi \partial c} + N_c \frac{\partial^2 Y_c}{\partial c^2} \right] \tag{3.36}$$

The progress variable scalar dissipation rate and the cross-mixture fraction-progress variable scalar dissipation rates are defined similarly to the mixture fraction scalar dissipation rate:

$$\begin{aligned} N_\xi \equiv & \frac{1}{2} \chi_\xi \equiv \langle D (\nabla \xi)^2 \mid \eta, \zeta \rangle \\ N_{\xi,c} \equiv & \frac{1}{2} \chi_{\xi,c} \equiv \langle D \nabla \xi \cdot \nabla c \mid \eta, \zeta \rangle \\ N_c \equiv & \frac{1}{2} \chi_c \equiv \langle D (\nabla c)^2 \mid \eta, \zeta \rangle. \end{aligned} \tag{3.37}$$

3.3.3 Double Conditional Moment Closure transport equations

Transport equations describing the evolution of the conditionally-averaged thermochemical state can be derived using techniques set out by Klimenko and Bilger [99]. Since partially-premixed combustion processes arising in dual-fuel engines may benefit from use of mixture fraction and progress variable conditioning, the double-conditional moment closure (DCMC) transport equations are introduced here. Sitte and Mastorakos [205] present the DCMC equations for the conditional average mass fraction of species k,

$$Q_k(\eta, \zeta; \mathbf{x}, t) = \langle Y_k(\mathbf{x}, t) \mid \xi(\mathbf{x}, t) = \eta, c(\mathbf{x}, t) = \zeta \rangle \tag{3.38}$$

where η is the sample space variable for mixture fraction and ζ is the sample space variable for progress variable. Assuming unity Lewis number, applying the primary closure hypothesis set out in Ref. [99], and extending Mortensen and Bilger's treatment of spray terms for double conditioning, the transport equation for Q_k is [204, 205]

$$\begin{aligned}\frac{\partial Q_k}{\partial t} + \nabla\cdot(Q_k\langle\mathbf{u}\mid\eta,\zeta\rangle) = Q_k\nabla\cdot(\langle\mathbf{u}\mid\eta,\zeta\rangle) - \frac{1}{\bar\rho\widetilde{P}}\nabla\cdot\left(\bar\rho\widetilde{P}\left[\langle\mathbf{u}Y_k\mid\eta,\zeta\rangle - Q_k\langle\mathbf{u}\mid\eta,\zeta\rangle\right]\right)\\ + \frac{1}{\bar\rho\widetilde{P}}\nabla\cdot\left(\bar\rho\widetilde{P}\langle D\nabla Y_k\mid\eta,\zeta\rangle\right) + \langle N_\xi\mid\eta,\zeta\rangle\frac{\partial^2 Q_k}{\partial\eta^2}\\ + 2\langle N_{\xi,c}\mid\eta,\zeta\rangle\frac{\partial^2 Q_k}{\partial\eta\partial\zeta} + \langle N_c\mid\eta,\zeta\rangle\frac{\partial^2 Q_k}{\partial\zeta^2} + \langle\dot\omega_k\mid\eta,\zeta\rangle\\ - \langle\dot\omega_c^*\mid\eta,\zeta\rangle\frac{\partial Q_k}{\partial\zeta} + (\delta_{kf}-Q_k)\langle\mathit{\Pi}\mid\eta,\zeta\rangle - \langle S_\xi^-\mid\eta,\zeta\rangle\frac{\partial Q_k}{\partial\eta}\\ - \langle S_c^-\mid\eta,\zeta\rangle\frac{\partial Q_k}{\partial\zeta}\end{aligned} \tag{3.39}$$

where $\langle\dot\omega_c^*\mid\eta,\zeta\rangle$ corresponds to the conditionally average apparent reaction rate in the transport equation of progress variable. The terms $\langle S_\xi^-\mid\eta,\zeta\rangle$ and $\langle S_c^-\mid\eta,\zeta\rangle$ are the conditionally average spray source term of mixture fraction and progress variable respectively. The apparent reaction rate and spray source terms are written as

$$\begin{aligned}\langle\dot\omega_c^*\mid\eta,\zeta\rangle &= \frac{1}{\partial Q_{Y_c}/\partial\zeta}\left[\langle\dot\omega_{Y_c}\mid\eta,\zeta\rangle + \langle N_\xi\mid\eta,\zeta\rangle\frac{\partial^2 Q_{Y_c}}{\partial\eta^2}\right.\\ &\quad\left. + 2\langle N_{\xi,c}\mid\eta,\zeta\rangle\frac{\partial^2 Q_{Y_c}}{\partial\eta\partial\zeta} + \langle N_c\mid\eta,\zeta\rangle\frac{\partial^2 Q_{Y_c}}{\partial\zeta^2}\right],\\ \langle S_\xi^-\mid\eta,\zeta\rangle &= (1-\eta)\langle\mathit{\Pi}\mid\eta,\zeta\rangle,\\ \langle S_c^-\mid\eta,\zeta\rangle &= \frac{1}{\partial Q_{Y_c}/\partial\zeta}\left[\delta_{Y_cF} - Q_{Y_c} - (1-\eta)\frac{\partial Q_{Y_c}}{\partial\eta}\right]\langle\mathit{\Pi}\mid\eta,\zeta\rangle.\end{aligned} \tag{3.40}$$

The corresponding DCMC equation for total enthalpy is given by [204, 205]

$$\begin{aligned}\frac{\partial Q_h}{\partial t} + \nabla\cdot(Q_h\langle\mathbf{u}\mid\eta,\zeta\rangle) = Q_h\nabla\cdot(\langle\mathbf{u}\mid\eta,\zeta\rangle) - \frac{1}{\bar\rho\widetilde{P}}\nabla\cdot\left(\bar\rho\widetilde{P}\left[\langle\mathbf{u}h\mid\eta,\zeta\rangle - Q_h\langle\mathbf{u}\mid\eta,\zeta\rangle\right]\right)\\ + \frac{1}{\bar\rho\widetilde{P}}\nabla\cdot\left(\bar\rho\widetilde{P}\langle D_{th}\nabla h\mid\eta,\zeta\rangle\right) + \langle N_\xi\mid\eta,\zeta\rangle\frac{\partial^2 Q_h}{\partial\eta^2}\\ + 2\langle N_{\xi,c}\mid\eta,\zeta\rangle\frac{\partial^2 Q_h}{\partial\eta\partial\zeta} + \langle N_c\mid\eta,\zeta\rangle\frac{\partial^2 Q_h}{\partial\zeta^2}\\ - \langle\dot\omega_c^*\mid\eta,\zeta\rangle\frac{\partial Q_h}{\partial\zeta} + +\langle S_h\mid\eta,\zeta\rangle - Q_h\langle\mathit{\Pi}\mid\eta,\zeta\rangle\\ - \langle S_\xi^-\mid\eta,\zeta\rangle\frac{\partial Q_h}{\partial\eta} - \langle S_c^-\mid\eta,\zeta\rangle\frac{\partial Q_h}{\partial\zeta} + \langle S_w\mid\eta,\zeta\rangle.\end{aligned} \tag{3.41}$$

Equations 3.39 and 3.41 contain numerous unclosed terms for which sub-models need to be provided. In general the conditionally-averaged chemical source term is closed with the first-order closure set out in Section 3.3.1. Other models and approximations may be case specific. Two different CMC approaches are employed in this thesis.

Single-conditioning: Chapter 7 employs spatially-two-dimensional CMC, singly conditioned on mixture fraction. This removes dependence on ζ. Further simplification is obtained in Chapter 7 by neglecting spray source terms in the CMC transport equations and, since the equation is applied in the RANS context, by neglecting spatial molecular transport of conditional mean quantities, leading to the simplified 2D-CMC equations:

$$\begin{aligned}\frac{\partial Q_k}{\partial t} + \nabla\cdot(Q_k\langle\mathbf{u}\mid\eta\rangle) = Q_k\nabla\cdot(\langle\mathbf{u}\mid\eta\rangle) - \frac{1}{\bar{\rho}\widetilde{P}}\nabla\cdot\left(\bar{\rho}\widetilde{P}\left[\langle\mathbf{u}Y_k\mid\eta\rangle - Q_k\langle\mathbf{u}\mid\eta\rangle\right]\right)\\ + \langle N_\xi\mid\eta\rangle\frac{\partial^2 Q_k}{\partial\eta^2} + \langle\dot{\omega}_k\mid\eta\rangle,\end{aligned} \tag{3.42}$$

and

$$\begin{aligned}\frac{\partial Q_h}{\partial t} + \nabla\cdot(Q_h\langle\mathbf{u}\mid\eta\rangle) = Q_h\nabla\cdot(\langle\mathbf{u}\mid\eta\rangle) - \frac{1}{\bar{\rho}\widetilde{P}}\nabla\cdot\left(\bar{\rho}\widetilde{P}\left[\langle\mathbf{u}h\mid\eta\rangle - Q_h\langle\mathbf{u}\mid\eta\rangle\right]\right)\\ + \langle N_\xi\mid\eta\rangle\frac{\partial^2 Q_h}{\partial\eta^2} + \langle S_w\mid\eta\rangle.\end{aligned} \tag{3.43}$$

The final term in S_w is introduced (rather than derived) in order to model convective wall heat transfer that is not otherwise resolved by the spatial grid of the CMC solution. Sub-models for $\langle\mathbf{u}\mid\eta\rangle$, $[\langle\mathbf{u}Y_k\mid\eta\rangle - Q_k\langle\mathbf{u}\mid\eta\rangle]$, $\langle N_\xi\mid\eta\rangle$ and $\langle S_w\mid\eta\rangle$ are presented in Chapter 7.

Double-conditioning: Chapter 8 employs spatially-zero-dimensional DCMC, conditioned on mixture fraction and progress variable. This removes terms involving spatial derivatives of averaged quantities. Again, spray source terms are neglected in the DCMC transport equations leading to a simplified 0D-DCMC equation set:

$$\begin{aligned}\frac{\partial Q_k}{\partial t} = \langle N_\xi\mid\eta,\zeta\rangle\frac{\partial^2 Q_k}{\partial\eta^2} + 2\langle N_{\xi,c}\mid\eta,\zeta\rangle\frac{\partial^2 Q_k}{\partial\eta\partial\zeta} + \langle N_c\mid\eta,\zeta\rangle\frac{\partial^2 Q_k}{\partial\zeta^2}\\ + \langle\dot{\omega}_k\mid\eta,\zeta\rangle - \langle\dot{\omega}_c^*\mid\eta,\zeta\rangle\frac{\partial Q_k}{\partial\zeta}.\end{aligned} \tag{3.44}$$

Neglecting wall-heat transfer, pressure variation, spray source terms and preferential transport, the conditionally-averaged total enthalpy is conserved by the remaining linear

mixing process and therefore the DCMC equation for enthalpy need not be solved. Sub-models requried for the conditional scalar dissipation rates are set out in Chapters 6 and 8.

3.3.4 Presumed probability density function modelling

Application of the CMC approach requires a model for the (joint-)pdf of the conditioning variables: Mixture fraction-conditioned CMC requires a model for the mixture fraction pdf $\tilde{P}_\xi(\eta)$, and mixture fraction-progress variable DCMC requires a model for the joint ξ-c pdf, $\tilde{P}_{\xi,c}(\eta,\zeta)$. The simplest and most common approach for modelling the joint ξ-c pdf is to assume that mixture fraction and progress variable are statistically-independent, as in Ref. [205], so that the joint-pdf can be expressed as the product of the marginal pdfs of mixture fraction and progress variable,

$$\widetilde{P}_{\xi,c}\left(\eta,\zeta\right) = \widetilde{P}_\xi\left(\eta\right)\widetilde{P}_c\left(\zeta\right). \tag{3.45}$$

Limitations of assuming statistical independence and improved modelling for the joint-pdf is developed in Chapter 6.

Initially the marginal pdfs $\tilde{P}_\phi$ of mixture fraction and progress variable are each modelled by the beta-distribution as a function of the respective mean $\tilde{\phi}$ and variance $\widetilde{\phi''^2}$,

$$\begin{aligned}
\widetilde{P}_\phi\left(\psi\right) =& \frac{\psi^{r-1}\left(1-\psi\right)^{s-1}}{\int_0^1 \psi^{r-1}\left(1-\psi\right)^{1-s}\,d\psi} \\
r =& \widetilde{\phi}\left(\frac{\widetilde{1-\phi}}{\widetilde{\phi''^2}} - 1\right) \\
s =& r\frac{\widetilde{1-\phi}}{\widetilde{\phi}}.
\end{aligned} \tag{3.46}$$

The mean and variances required to evaluate the beta-pdf are obtained by solving moment transport equations given below.

3.3.5 Moment equations for conditioning variables

Mixture Fraction: Moment transport equations for the Favre-mean and variance of mixture fraction and progress variable are given in Ref. [222]. These moment equations can be interpreted either in a RANS context, or as Favre-filtered moments in the LES (provided that the filter kernel is spatially homogenous such that it commutes with differentiation). Assuming equal diffusivities for all species and modelling turbulent transport as a diffusion process with turbulent diffusivity D_t, the first and second moment equations for mixture fraction are,

$$\frac{\partial \bar{\rho}\widetilde{\xi}}{\partial t} + \nabla \cdot \left(\bar{\rho}\widetilde{\mathbf{u}}\widetilde{\xi}\right) = \nabla \left(\bar{\rho}\left(\bar{D} + D_t\right)\nabla\widetilde{\xi}\right) + \bar{\rho}\tilde{\Pi}_{\xi}, \tag{3.47}$$

and

$$\frac{\partial \bar{\rho}\widetilde{\xi''^2}}{\partial t} + \nabla \cdot \left(\bar{\rho}\widetilde{\mathbf{u}}\widetilde{\xi''^2}\right) = \nabla \cdot \left(\bar{\rho}\left(\bar{D} + D_t\right)\nabla\widetilde{\xi''^2}\right) - 2\bar{\rho}\widetilde{N}_{\xi} + 2\bar{\rho}\left(\bar{D} + D_t\right)\nabla\tilde{\xi}\cdot\nabla\tilde{\xi}. \tag{3.48}$$

Here, the spray source term in the variance equation has been neglected, assuming that scalar variance production is dominated by turbulent mixing.

The corresponding progress variable moment equations are,

$$\frac{\partial \bar{\rho}\widetilde{c}}{\partial t} + \nabla \cdot \left(\bar{\rho}\widetilde{\mathbf{u}}\widetilde{c}\right) = \nabla \left(\bar{\rho}\left(\bar{D} + D_t\right)\nabla\widetilde{c}\right) + \bar{\rho}\widetilde{\dot{\omega}_{c^*}} + \bar{\rho}\widetilde{c}\widetilde{\Pi}, \tag{3.49}$$

and

$$\begin{aligned}\frac{\partial \bar{\rho}\widetilde{c''^2}}{\partial t} + \nabla \cdot \left(\bar{\rho}\widetilde{\mathbf{u}}\widetilde{c''^2}\right) = \nabla \cdot \left(\bar{\rho}\left(\bar{D} + D_t\right)\nabla\widetilde{c''^2}\right) - 2\bar{\rho}\widetilde{N}_c \\ + 2\bar{\rho}\left(\hat{D} + D_t\right)\nabla\tilde{c}\cdot\nabla\tilde{c} + 2\bar{\rho}\left(\widetilde{c\dot{\omega}_{c^*}} - \widetilde{c}\widetilde{\dot{\omega}}_{c^*}\right).\end{aligned} \tag{3.50}$$

3.3.6 Numerical implementation of the CMC equations

The spatially-zero-dimensional DCMC equations are implemented in an in-house solver. The spatial-CMC solutions are implemented by coupling the in-house solver with the STAR-CD engine simulation code as set out in Chapter 7. The DCMC equations are solved using a finite difference approach on a non-uniform Cartesian grid spanning the unit-square solution domain. Since the DCMC solutions in this thesis assume adiabatic constant-pressure combustion, the burnt and unburnt states do not change with time and

Dirichlet boundary conditions are employed. A more general time-varying set of boundary conditions is available in the DCMC code, as set out in Ref. [140]. First derivatives in conditioning space are evaluated using first-order accurate upwind differences and second derivatives are evaluated using second-order accurate central differencing. The DCMC equations are integrated either by the method of lines approach using the stiff VODPK ODE solver [27] in Chapter 6 or, in order to achieve greater computational efficiency for stiffer chemical mechanisms, using a fractional step approach set out in Chapter 8 in which the chemistry is solved point-wise using the SpeedCHEM library [159]. Further details regarding numerical setup are provided in the relevant results chapters.

3.4 The G-Equation model

The model presented here is used in the G-eq/CMC (ξ) hybrid approach presented in Chapter 7 with futher details regarding the implementation and tests performed.

The G-equation approach treats premixed flames in the flamelet regime as an infinitely thin surface separating reactants and products where the progress variable changes between 1 or 0. Williams [234] introduced a level-set variable G to locate the flame surface at $G = G_0$, as seen in Fig. 3.5. The level-set propagates normal to $G = G_0$ iso-surface with a modelled flame speed. The level-set approach simplifies the problem counter-gradient diffusion and source term closure. The modelling is applicable to flames with $Ka < 1$, i.e. corrugated and wrinkled flamelets.

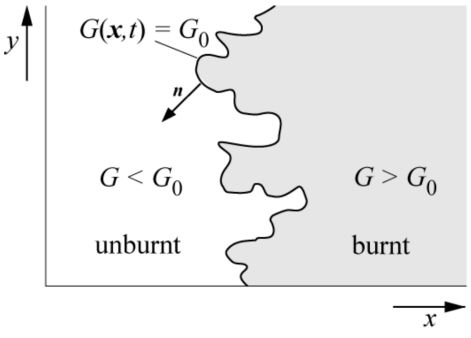

Figure 3.5: Flame front computed by G-equation model [160].

The temporal evolution of the G field is described by advection and propagation speed. In RANS or LES no all turbulent motions of the flow are resolved and therefore an

averaged or filtered level-set variable $\widetilde{G}$ is employed, which propagates with a turbulent flame speed S_T. The transport equation of $\widetilde{G}$is defined in [222] as

$$\frac{\partial \rho \widetilde{G}}{\partial t} + \frac{\partial \rho \widetilde{u_i} \widetilde{G}}{\partial x_i} = \rho S_T \left| \frac{\partial \widetilde{G}}{\partial x_i} \right| \tag{3.51}$$

Different closures for S_T are presented in the literature. However a common feature is that S_T is modelled a function of laminar flame speed and local turbulence properties [37, 160]. S_L can be tabulated based on one-dimensional premixed flame calculations or described by algebraic functions as presented in Ref. [244].

Chapter 4

Investigation of flame propagation in autoignitive blends of n-heptane and methane fuel

Natural gas is used to power compression-ignition engines via the dual-fuel mode, where a more reactive fuel such as diesel is also injected in order to provide a source of ignition. Following ignition, flame propagates through a partially-reacted inhomogeneous mixture of the two fuels, and the objective of this chapter is to develop understanding and modelling concerning the laminar flame speed under dual-fuel compression-ignition engine conditions. Flame propagation through methane–n-heptane fuel blends is studied using numerical simulations at engine-relevant conditions. The effects of pre-ignition chemistry on flame speed are investigated, and a new model is developed to account for these effects.

4.1 Introduction

Hydrogen and light hydrocarbon fuels such as methane exhibit single-stage high-temperature ignition behaviour. Pre-ignition reactions have limited effect on flame propagation through single-stage ignition mixtures until the mixture is close to the point of autoignition [71, 107, 133]. In contrast, some heavier hydrocarbons relevant to real transport fuels, such as n-heptane, exhibit low temperature chemistry (LTC) [12] and *cool flames*

[68]. The chemical kinetics controlling cool flames arise at high pressure and moderate temperatures, and are closely related to those of two-stage ignition and Negative Temperature Coefficient (NTC) behaviour [44, 60]. Following much of the literature, the term 'cool flame' is used indiscriminately here to refer both to deflagrative and to ignitive reaction fronts involving low temperature chemistry. Low temperature chemistry can significantly modify the chemical and transport properties of a mixture [236], thereby affecting the laminar flame speed in mixtures well before the onset of high-temperature ignition [107, 150]. The response of laminar flame properties to blending of fuels with dissimilar ignition behaviours, such as methane and n-heptane, has not been characterised fully at autoignitive conditions. Methane/n-heptane mixtures are of particular interest because these have been used in research studies as surrogate fuels for the natural gas/diesel mixtures arising in pilot-ignited dual fuel engines, (e.g., [7, 55, 195]).

The laminar flame speed and laminar flame thickness are centrally important in characterisation and modelling of turbulent combustion in engines because they directly affect the turbulent flame speed [161]. The dependence of the turbulent flame speed on laminar flame properties persists for flames affected by LTC [235, 236]. Knowledge of the laminar flame speed and laminar flame thickness are therefore key to understanding and modelling turbulent combustion processes under the autoignitive conditions that predominate in practical combustion systems. However established empirical models for the variation of flame speeds with temperature, pressure, equivalence ratio and dilution, such as in Ref. [142], do not account for the effect of pre-ignition chemical processes on flame speed.

4.1.1 Laminar flame speed

Pre-ignition chemical reactions ahead of a flame affect the propagation speed. As such, there is not a unique freely-propagating laminar flame speed (s_l) at autoignitive conditions. Rather, the flame speed depends on the extent of the pre-ignition reactions ahead of the flame [71, 107, 150], which can be related to the residence time τ_f [199, 201] between the reactants mixing and arriving at the flame front. The propagation speed of the flame front can be evaluated in a general way from the density-corrected displacement speed s_f [234]. Evaluating s_f in any unstrained one-dimensional stationary flame

configuration yields a well-defined residence time-dependent flame speed, provided that diffusive fluxes through the inlet of the flow domain are negligible [107].

A non-autoignitive freely-propagating laminar flame corresponds to the limit where the residence time is much less than the ignition delay time τ_{ign}, i.e. $\tau_f \ll \tau_{ign}$. Conversely, the limit $\tau_f \to \tau_{ign}$ corresponds to the transition from a deflagrative flame to a pure ignition front [248]. Hereafter we refer to the flame speed in the short residence time limit $\tau_f \ll \tau_{ign}$ as *reference flame speed* s_r [107].

4.1.2 Laminar flame thickness

In the case of diffusion-limited flame propagation with negligible chemical reaction upstream of and within the preheat layer, the thermal thickness of the flame front δ_f scales with the thermal diffusivity α and laminar flame speed as [226]

$$\delta_f \sim \frac{\alpha}{s_f}. \tag{4.1}$$

The thermal thickness is $\delta_f = \Delta T/(dT/dx)_{max}$, where ΔT is the temperature rise across the front and $(dT/dx)_{max}$ is the maximum temperature gradient within the flame. Since the variation of thermal diffusivity and flame speed with reactant properties are typically well-modelled by established empirical relations, (e.g., [142]), this scaling relationship provides a simple means for estimating how the reaction front thickness varies across a range of combustion conditions for which the flame front behaviour is deflagrative. This scaling relationship breaks down as the flame transitions into an ignition front. The transport equation for progress variable c within a stationary ignition front is

$$u\frac{\partial c}{\partial x} = \frac{\omega_c}{\rho}, \tag{4.2}$$

where x and u are the displacement and velocity normal to the flame and ω_c is the reaction source term for progress variable. The thermal thickness of the reaction front can be approximated using the progress variable gradient: $\delta_f \sim (\partial c/\partial x)^{-1}_{max}$, giving the relationship

$$\delta_f \sim \frac{\rho_u}{\omega_{c,max}} s_f, \tag{4.3}$$

in which the factor $\rho_u/\omega_{c,max}$ is positive, with magnitude dependent on the thermo-chemical state of the reactants. The relationship between δ_f and s_f therefore provides an indication of whether a flame front is *deflagrative* ($\sim$ Eq. 4.1) or *ignitive* ($\sim$ Eq. 4.3).

The objectives of this study are to investigate and to model the effects of different methane/n-heptane fuel blends and their pre-ignition chemistry on the speed of reaction fronts under dual-fuel compression-ignition engine conditions. The following section sets out the physical modelling and numerical approach adopted. The results are then analysed in order (1) to assess the effects on flame speed and structure due to thermal and chemical contributions of the different fuels; and (2) to develop a new modelling approach for reaction front speeds under autoignitive conditions.

4.2 Methodology

Simulations of adiabatic un-stretched steady one-dimensional laminar flames are used to investigate the combined effects of methane/n-heptane ratios and pre-ignition chemistry at engine-relevant temperatures. The effect of the pre-ignition chemistry is assessed by varying the residence time upstream of the flame front. The residence time is changed by varying the position specified for the flame relative to the inlet of the solution domain, as illustrated in Fig. 4.1. The residence time τ_f at the flame front is evaluated as

$$\tau_f = \int_{x_i}^{x_f} \frac{1}{u(x)} dx, \tag{4.4}$$

where x_i is the $x-$location of the inlet to the solution domain, x_f is the location of the upstream edge of the flame, here defined as being half of one thermal thickness upstream of the maximum temperature gradient location.

Reactant mixtures are described in terms of their total-equivalence ratio, ϕ_{tot}, evaluated in the conventional manner by considering the stoichiometric oxygen-fuel ratio for the fuel mixture, and fuel-equivalence ratios ϕ_{CH_4} and $\phi_{C_7H_{16}}$ [89]. The fuel equivalence ratios are defined by $\phi_{CH_4} = \nu_{CH_4} Y_{(CH_4,u)}/Y_{(O_2,u)}$ and $\phi_{C_7H_{16}} = \nu_{C_7H_{16}} Y_{(C_7H_{16},u)}/Y_{(O_2,u)}$, where subscript u denotes the unburnt composition and ν_{fuel} is the stoichiometric oxygen-to-fuel mass ratio for each fuel. These definitions of the fuel equivalence ratio can be added to obtain the total equivalence ratio, $\phi_{tot} = \phi_{CH_4} + \phi_{C_7H_{16}}$.

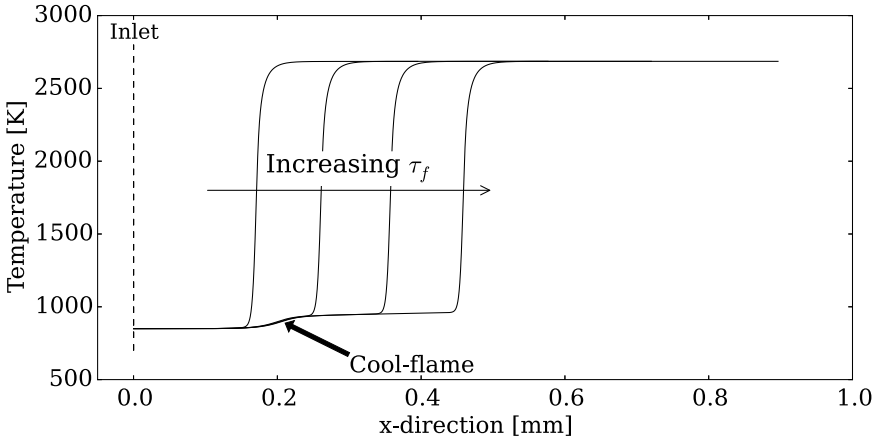

Figure 4.1: The temperature profile in several steady freely-propagating stoichiometric n-heptane–air flames with different residence times at 850 K and 40 bar. The location of the cool flame front is indicated.

The flames are simulated using the COSILAB one-dimensional flame solver [2] with multi-component molecular transport, ideal gas models with seven-coefficient polynomials for the temperature-dependence of thermodynamic properties. The methane/n-heptane chemistry is modelled using a 106 species mechanism for n-heptane combustion [171], presenting a good compromise between accuracy and computational time. There are few experimental data available for autoignition and flame propagation in methane/n-heptane fuel blends at engine-relevant conditions. Therefore the chemical model has been selected on the basis of satisfactory autoignition and flame propagation predictions of experimental data for pure methane–air and n-heptane–air mixtures, and satisfactory agreement with more detailed models for autoignition and flame propagation in methane/n-heptane fuel blends. Validation data for the 106 species mechanism used are providedon Section 4.3.1. Figure 4.2 presents the variation of ignition delay time with temperature for four stoichiometric methane/n-heptane fuel blends (ϕ_{CH4}/ϕ_{tot} =0, 0.5, 0.8, and 1.0) in air at 40 bar, with results for the 106 species skeletal mechanism in reasonably close agreement with its 451 species parent detailed mechanism [170]. Fuel blends are mixed with air throughout this study, and air is modelled as 79% N_2 and 21% O_2 by volume.The predictions show significant NTC behaviour at the conditions investigated in this study, with the NTC behaviour reducing as the proportion of methane in the fuel is increased.

The COSILAB software employs adaptive grid refinement and a stationary flame solution is obtained using a modified-Newton method [2]. The grid-independence of the solution

data presented in this paper has been established by incrementally tightening the adaptive grid error tolerances until numerical convergence is achieved, requiring between one hundred and four hundred grid points, depending on the simulation conditions.

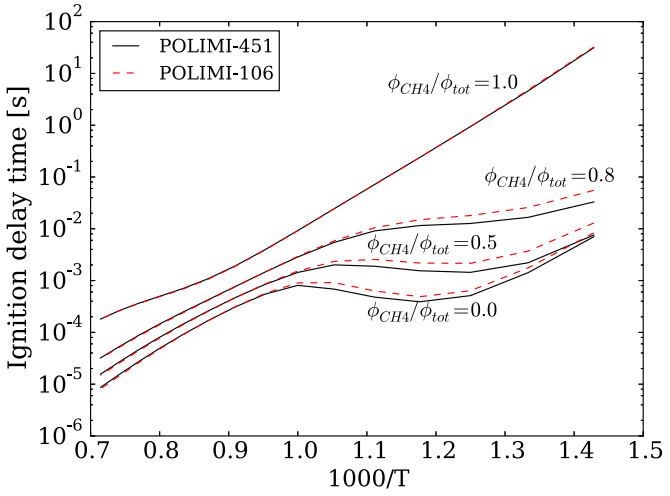

Figure 4.2: The temperature-dependence of ignition delay time for stoichiometric methane/n-heptane–air blends at 40 bar with $\phi_{CH_4}/\phi_{tot} = 0.0, 0.5, 0.8, 1.0$ computed with POLIMI-106 [171] and POLIMI-451 [170] mechanisms.

4.3 Results and Discussion

4.3.1 Validation of chemical kinetics mechanisms

The 106 species Polimi-106 skeletal mechanism is selected for this study based on comparison against experimental ignition delay time and flame speed data for combustion of pure methane and pure n-heptane. Since ignition delay and flame speed measurements for combustion of methane/n-heptane blends are not generally available, the Polimi-106 model predictions for methane/n-heptane blends are also compared with predictions of more detailed chemical mechanisms. Data are presented for the chemical models summarised in Table 4.1.

The Polimi-106 skeletal scheme [171] is a sub-set of the Polimi-451 scheme [170]. The 44-species reduced mechanism by Liu et al. [121] is considered because it gives an adequate compromise between predictive accuracy and computational expense for engine calculations, and the 42-species Chalmers mechanism is considered because it performed best out of the mechanisms compared in a previous study of methane/n-heptane dual fuel

Table 4.1: Summary of chemical models.

Mechanism name	Reference	Main fuel	Number of species	Type
Polimi-451	[170]	n-heptane	451	detailed
Mehl et al.	[141]	n-heptane	658	detailed
Polimi-106	[171]	n-heptane	106	skeletal
Liu et al.	[121]	n-heptane	44	reduced
Lu et al.	[125]	n-heptane	52	reduced
Chalmers	[7]	n-heptane	42	reduced
GRI3.0	[206]	methane	53	detailed
San Diego	[1]	methane	50	detailed

combustion [7]. The 52-species reduced mechanism developed by Lu et al. [125] employs dynamic stiffness removal in order to achieve low computational cost, and it has been validated against its parent detailed mechanism in a perfectly-stirred reactor at ambient temperatures and for homogeneous autoignition at engine-relevant temperatures.

4.3.1.1 Ignition delay

Constant volume ignition delay predictions are presented for pure methane and n-heptane in Figs. 4.3 and 4.4, in comparison with shock-tube measurements for stoichiometric methane-air at 30 atm [78], n-heptaneair at 55 atm [63] and n-heptaneair at 42 atm [44]. Ignition delay time predictions for the reduced n-heptane mechanisms are compared with the detailed n-heptane mechanisms for ignition of methane/n-heptane blends in Fig. 4.5.

4.3.1.2 Flame speed

Figure 4.6 presents stoichiometric methaneair flame speeds at 10 bar for equivalence ratios spanning 0.7 to 1.2 at 360 and 400 K, comparing experimental measurements [69] and numerical predictions of methane-air flame speeds for the detailed methane mechanisms and the reduced n-heptane mechanisms. Similar data for ambient pressure are presented in Figure 4.7.

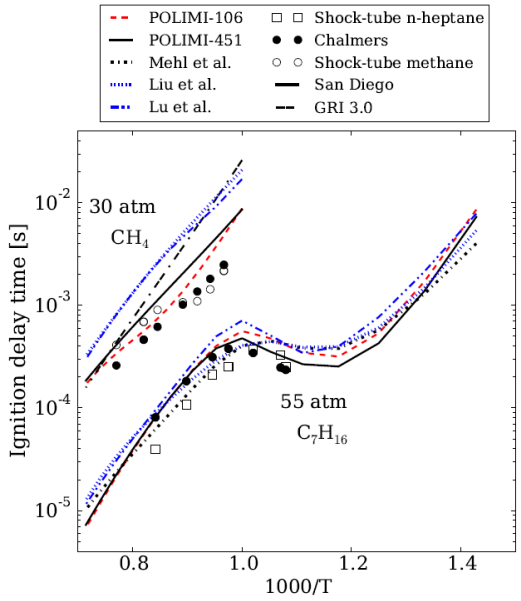

Figure 4.3: Constant-volume ignition delay times for stoichiometric methaneair at 30 atm and n-heptane/air at 55 atm. Shock-tube data: ◯ [78], □ [63].

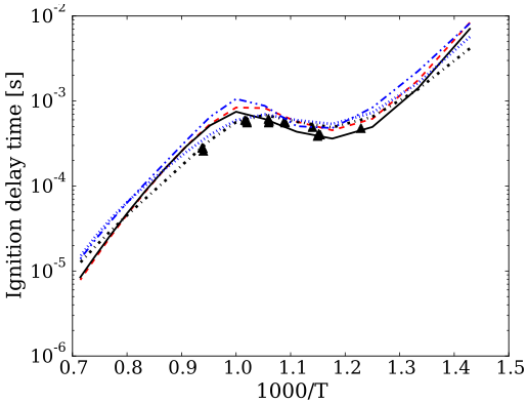

Figure 4.4: Constant-volume ignition delay times for stoichiometric n-heptane-air at 42atm for Polimi-451, Mehl et al., Polimi-106, Liu et al. and Lu et al. (refer to Figure S1 for legend). Shock-tube data ▲ [44].

4.3.2 Effects of pre-ignition chemistry on flame speed

Figure 4.8 shows the variation of flame speed with residence time for pure methane, pure n-heptane and two methane/n-heptane fuel blends with global stoichiometric equivalence ratio ($\phi_{tot} = 1$) at 40 bar and 850 or 1000 K. The results are presented in terms of residence time, rather than in terms of the flame positions reported in Refs. [71, 107], since, for autoignitive conditions, the chemical evolution upstream of the flame can be related to residence time, as shown below. The residence time may serve as a useful parameter for accounting for chemical evolution in a range of flows [199], whereas interpretation of

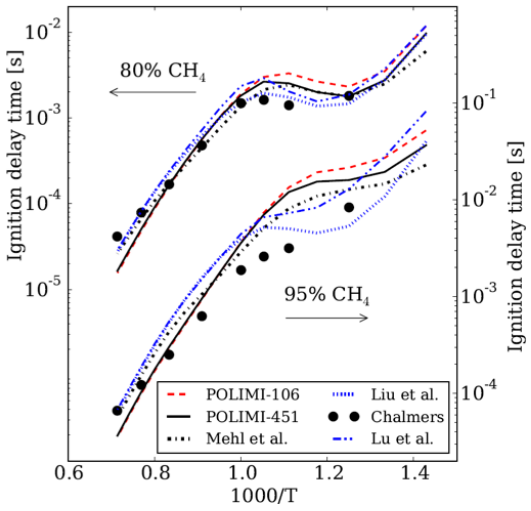

Figure 4.5: Constant-volume ignition delay times for stoichiometric methane/n-heptaneair mixtures at 30 bar with 80%$_{vol}$ CH4 (left axis) and 95%$_{vol}$ CH4 (right axis) in the fuel blend.

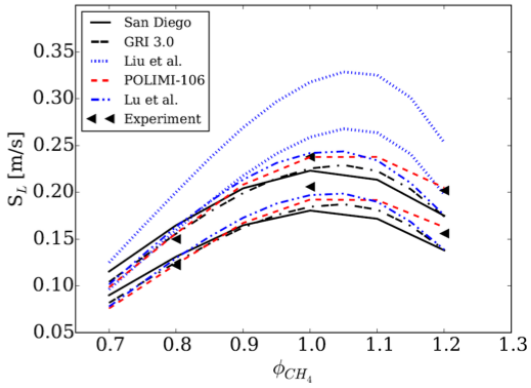

Figure 4.6: Laminar flame speed of methaneair flames versus equivalence ratio for 360 K (lower speeds) and 400 K (higher speeds) at 10 bar. ◀ experimental data [69].

the flame position is configuration specific. Nonetheless, the residence time and flame position are closely related in the present one-dimensional configuration using to Eq. 4.4. The flame speed of the methane–air mixture remains approximately constant until the residence time approaches the ignition delay time, when it increases indefinitely, as observed previously in Refs. [71, 133]. For an unburned temperature of 1000 K where n-heptane–air mixtures exhibit single-stage ignition, the evolution of the flame speed of the n-heptane–air mixture is qualitatively similar to the pure methane case. However, for an unburned temperature of 850 K where n-heptane–air mixtures exhibit two-stage ignition, the flame speed also increases in two distinct stages: the flame speed increases

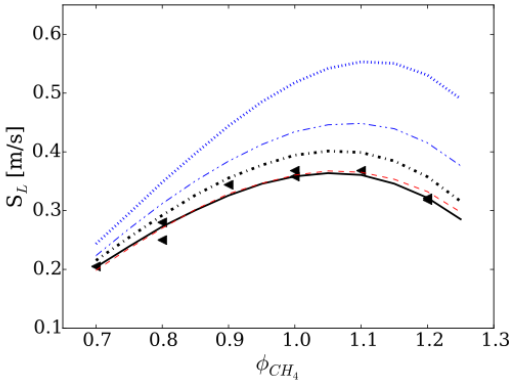

Figure 4.7: Laminar flame of methane-air flames versus equivalence ratio at 300K, 1.01bar. Refer to Fig. 4.6 for legend.

by 15 % when the residence time reaches the first-stage ignition delay time, then increases gradually during the second-stage ignition-delay, before increasing indefinitely as the residence time approaches final ignition delay time. The same two-stage increase in flame speed is observed for methane/n-heptane blends that show two-stage ignition behaviour, and the two-stage effect is stronger as the proportion of n-heptane increases.

Figure 4.9 shows that the first-stage increase in flame speed coincides with the first-stage increase in temperature, occurring between 0.13-0.18 ms residence time for 40 bar 850 K stoichiometric n-heptane–air flames. The flame speed is expected to be affected by the temperature increase, however consumption of major reactants and production of intermediate species by the pre-ignition chemical reactions ahead of the flame also affect flame speed. We conduct a numerical experiment in order to quantify the relative influence that the thermal and chemical changes have on the flame speed during first-stage ignition. The experiment isolates the effect of the intermediate species from the thermal effects by performing modified flame simulations in which we remove all intermediate species a short distance upstream of the flame while keeping the temperature and mixture enthalpy unchanged following the procedure set out in the Appendix, resulting in a modified flame speed $s_{f,therm}$. Since the intermediate species have been removed from the modified flame, the variation of $s_{f,therm}$ shown in Fig. 4.9 is entirely due to the temperature rise and the consumption of major reactants ahead of the flame front. The results of the modified flame experiment indicate that the first stage increase in flame speed is due to both thermal and chemical influences in approximately equal measure. Modelling for the flame speed should take each of these effects into account.

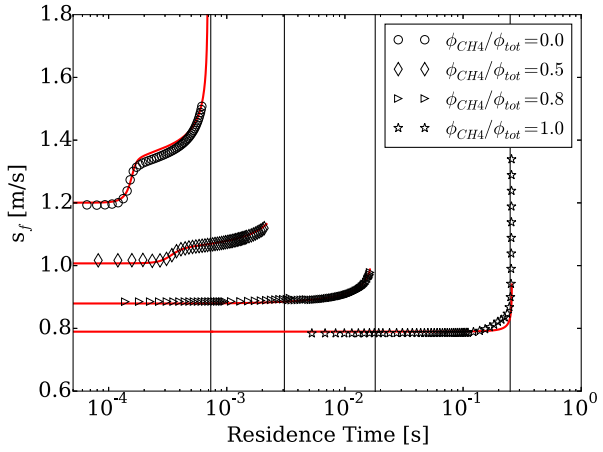

(a) 850 K

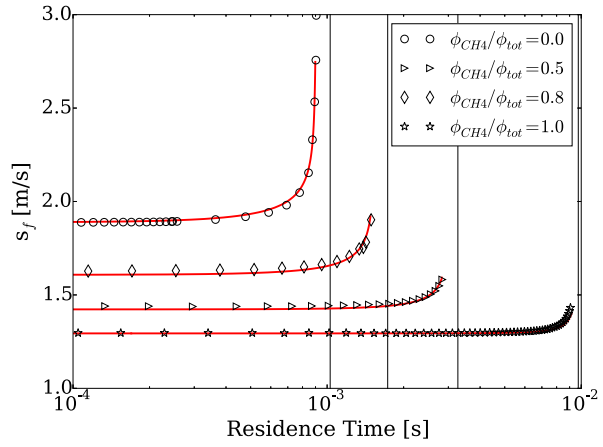

(b) 1000 K

Figure 4.8: Laminar flame speeds of stoichiometric methane/n-heptane blends versus residence time at 40 bar: simulations (symbols); model Eq. 4.8 (solid).

4.3.3 Effects of pre-ignition chemistry on flame thickness

Diffusion-limited (i.e. deflagrative) flame propagation is expected to exhibit a scaling relationship between flame thickness and flame speed given by Eq. 4.1. Figure 4.10 shows the variation of the high-temperature flame's speed with α/δ_f for premixed combustion of stoichiometric methane–air and n-heptane–air over a range of reactant temperature (T_u = 700 to 1000 K). Data are normalised by the reference laminar flame speeds of methane ($s_{r,0CH_4} = 0.79ms^{-1}$) and n-heptane ($s_{r,0C_7H_16} = 1.20ms^{-1}$) at T_0 = 850 K and p_0 = 40 bar, where subscript '0' refers to datum conditions. Reference properties for flames with short residence times (shown as symbols) follow the deflagrative scaling relationship as T_u is increased from 700 to 1000 K. The gradient of s_r with respect to α/δ_r is greater for n-heptane–air flames due to the greater reactivity of n-heptane

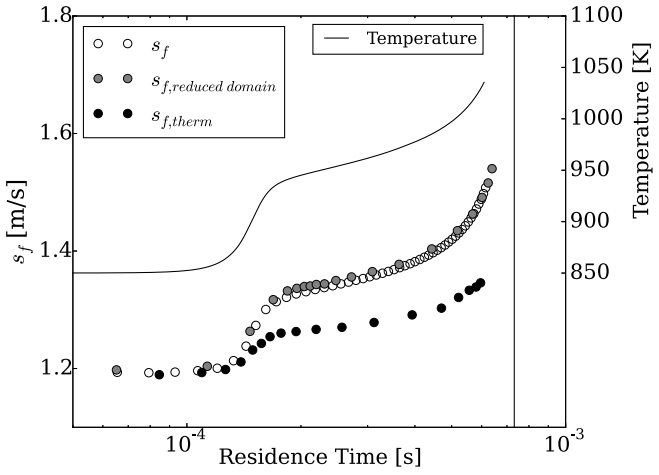

Figure 4.9: Laminar flame speed and temperature versus residence time for stoichiometric n-heptane–air at 40 bar and 850 K: Unmodified flame in the full domain (white circles); 0.2 mm domain with inlet composition from the unmodified flame (grey circles); 0.2 mm domain with intermediate species removed from the inlet composition (black circles).

compared to methane. As residence time increases (dashed lines), the flame speed of the n-heptane–air mixture remains largely unchanged until the mixture undergoes first-stage ignition. Subsequently the reaction front speed increases, and the reaction front thickness initially reduces in accordance with the deflagrative scaling given in Eq. 4.1. Finally, as the temperature-based progress variable ($c \equiv (T-T_u)/(T_b-T_u)$) ahead of the flame reaches around 0.15 , at the locations indicated by square symbols in Fig. 4.10, the deflagrative scaling breaks down and the front thickness starts to increase (α/δ_f reduces) because the residence time ahead of the flame approaches the ignition delay time – marking the transition from deflagrative to ignitive scaling of the front thickness.

Figure 4.11 presents the variation of the cool-flame's speed and thickness for the 850 K 40 bar stoichiometric n-heptane–air flame as the residence time increases. The thickness of the cool-flame follows the linear scaling behaviour given for ignition fronts in Eq. 4.3. Despite its name, the cool-flame exhibits ignitive rather than deflagrative behaviour across all of the conditions in this study: the data flow a linear relationship between cool-flame speed and thickness as indicated by the dashed lines in Fig. 4.11. The absence of deflagrative cool-flames is consistent with Ref. [251], where steady deflagrative cool-flames could only be stabilised when aerodynamic straining was used to prevent the development of a high-temperature flame. Ju *et al.* [85], in contrast, showed that steady deflagrative double-flame structures, involving a cool-flame and a hot-flame, can arise

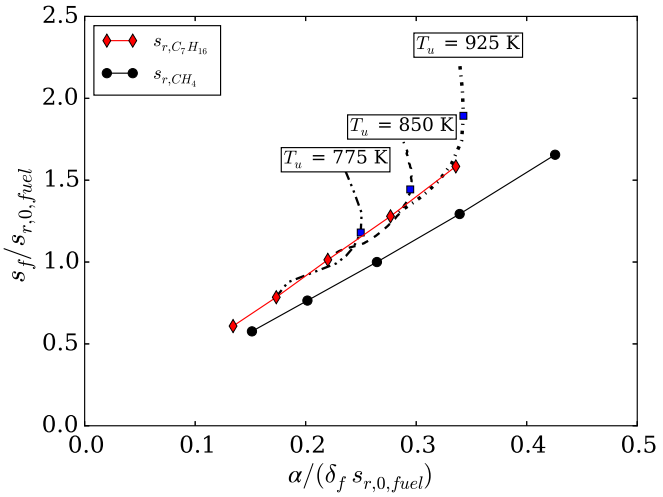

Figure 4.10: Normalised high-temperature reaction front speed $s_f/s_{r,0,fuel}$ versus $\alpha/(\delta_f s_{r,0,fuel})$ for short residence time ($\tau_f \longrightarrow 0$) stoichiometric methane–air and n-heptane–air flames with unburnt temperatures 700, 775, 850, 925 and 1000 K (symbols), and data for n-heptane–air combustion with residence times up to 98% of the ignition delay time at 775, 850, and 925 K (various dashed lines as labelled). Square symbols indicate the conditions where the progress variable ahead of the flame equals 0.15.

under very lean low-temperature combustion conditions (e.g. ϕ=0.1, T_u = 530 K). The combustion conditions investigated by Ju *et al.* are unlike the conditions in most engines since the magnitude of heat release in the cool-flame is similar to the magnitude of heat release in the hot flame. At richer, higher-temperature conditions typical of current engines, it may be that the magnitude of heat release in the hot-flame is greater, such that its flame speed would cause it to over-take any cool-flame, should a cool-flame arise, preventing observation of steady deflagrative cool-flames.

The transition between deflagrative and ignitive scaling of the flame thickness is accompanied by diminishing importance of diffusive transport within the flame fronts. Figure 4.12 shows mass fraction transport budgets for stoichiometric n-heptane flames at 850 K and 40 bar for two residence times τ_f/τ_{ign} = 0.85 and 0.95. The reaction (R), convection (C) and diffusion (D) terms [107] are presented for the alkyl hydroperoxy radical (C_7H_15OOH, abbreviated to QOOH) within the cool-flame and for OH within the high-temperature flame front. The convection term arises because the simulated flames are stationary. The budgets indicate that diffusive transport in the high-temperature reaction front becomes gradually less important as the residence time increases, and is generally less important in the cool-flame front. The magnitude of the diffusion term in the high-temperature flame is lower at τ_f/τ_{ign} = 0.95, at which point the flame thickness

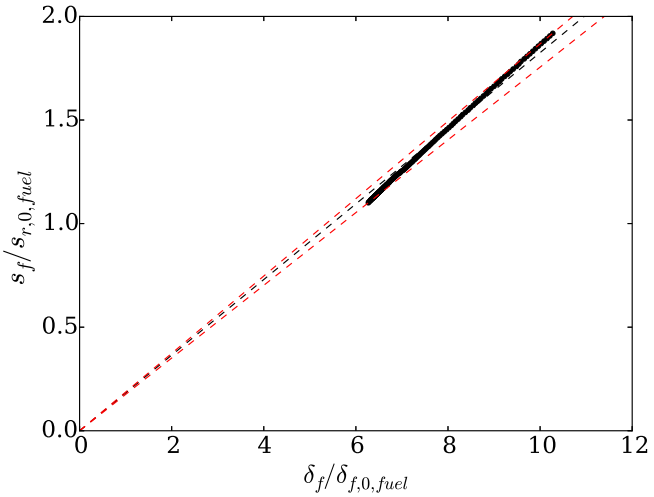

Figure 4.11: Cool-flame reaction front speed s_f versus thermal thickness δ_f for stoichiometric n-heptane–air flames normalised by reference flame properties at 850 K and 40 bar for a range of residence times (symbols). Data range from $\tau_f = 1.6 \cdot 10^{-04}$ s to $\tau_f = 7.1 \cdot 10^{-04}$ s. Dashed lines correspond to Eq. 4.3.

is increasing with flame speed, than at $\tau_f/\tau_{ign} = 0.85$, at which point the flame thickness is reducing in accordance with the deflagrative scaling (Eq. 4.1). However the gradual reduction of the diffusive transport contribution does not provide as clear a delineation of the transition between deflagrative and ignitive behaviours as the changes in the s_f – δ_f dependence shown in Figs. 4.10 and 4.11.

Analysis of the flame thickness indicates that the deflagrative scaling in Eq. 4.1 applies to the high-temperature flame front across a wide range of autoignitive conditions and, given models for s_f and α, provides a useful means of modelling the variation of δ_f in a flow up to the transition to ignitive behaviour.

4.3.4 Flame speeds at autoignitive conditions

The laminar flame speed is a key input for a number of turbulent combustion models [161]. For a given set of conditions the reference laminar flame speed may be evaluated from experimental measurements or, if suitable chemical and thermodynamic models are available, from a laminar flame simulation. The laminar flame speed may be provided to a turbulent combustion model by means of a data table or some form of algebraic fit to the data. Several empirically-derived algebraic models for laminar flame speed have been developed and used widely for combustion of individual fuels at non-autoignitive conditions [142]. Furthermore, due to the effort required to obtain flame speed data

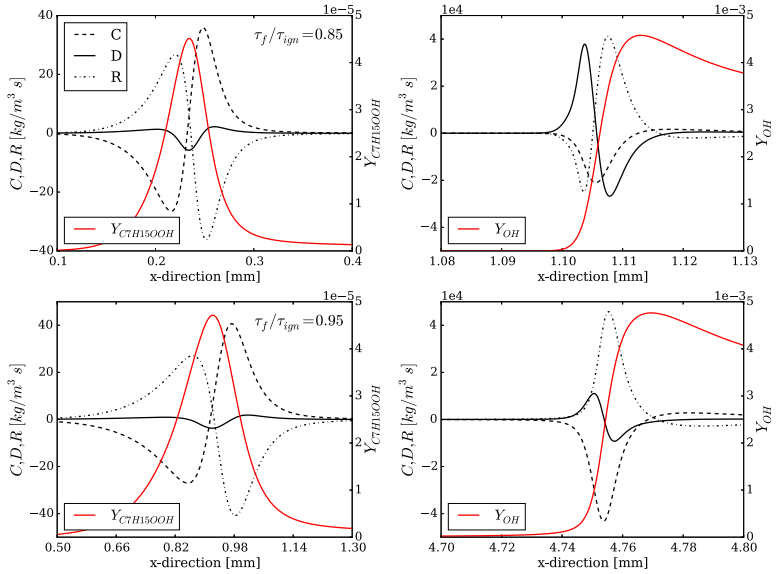

Figure 4.12: Transport budgets and mass fraction profiles for stoichiometric n-heptane–air at 850 K and 40 bar for Y_{QOOH} (left column) and Y_{OH} (right column). The residence times at the flame front are 85% (top row), and 95% (bottom row) of the overall ignition delay time. The data are plotted versus the distance from the inlet.

across a wide range of operating conditions as well as for different blends of fuels, mixing rules have been proposed in order to estimate the reference laminar flame speed of blends of individual fuels for which reference flame speeds are available [58, 77, 244]. For combustion under autoignitive conditions, however, the preceding analysis indicates that it is necessary also to account for the effect of pre-ignition chemistry on the flame speed, including the distinct contributions of heat release, reactant consumption and enhanced reactivity ahead of the flame. Due to the large domain size needed for the simulations required to generate the data presented in Fig. 4.8 it is not practical to compute the flame speed directly for the full range of residence times, fuel blends and mixture conditions that arise during operation of a dual-fuel engine. The objective of this section therefore is to develop a method for estimating the effects of pre-ignition chemistry on flame speed taking the reference flame speed as an input. This novel method can be applied to reference flame speeds obtained by any means.

In order to evaluate reference flame speeds efficiently and accurately in this study, well-established algebraic models are used to account for the dependence on equivalence ratio and the blending between fuels [244].

Yang and Reitz [244] modelled the dependence of reference flame speed s_r on equivalence

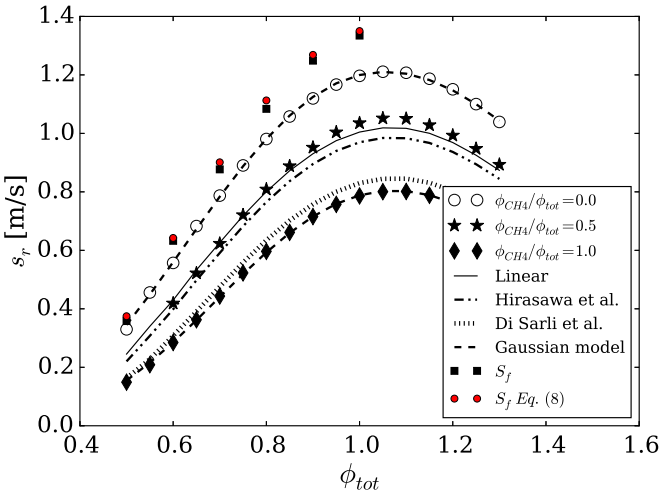

Figure 4.13: Variation of flame speed with equivalence ratio for methane/n-heptane fuel blends at 850 K and 40 bar for ϕ_{CH4}/ϕ_{tot} = 0, 0.5 and 1.0; and linear [244], Hirasawa *et al.* [77], and Di Sarli *et al.* [58] mixing-rules. Closed square and circular symbols correspond to flame speeds from simulatins and from Eq. 4.8 respectively for residence times between 40 and 60% of the ignition delay time

ratio using a four-parameter Gaussian function and accounted for fuel blending using a linear mixing rule which, for blends of methane and n-heptane, takes the form,

$$s_{r,mix} = Z_{CH_4} s_{r,CH_4} + (1 - Z_{CH_4}) s_{r,C_7H_{16}}, \tag{4.5}$$

where $Z_{CH_4} = Y_{CH_4,u}/(Y_{CH_4,u} + Y_{C_7H_{16},u})$ is the local mass fraction of methane in the fuel blend. The Gaussian fit for methane and n-heptane flame speeds, and the flame speeds of methane/n-heptane blends given by Eq. 4.5 are validated for a range of equivalence ratio in Fig. 4.13, showing a close fit to the numerically-obtained flame speeds. Alternative mixing rules by Hirasawa *et al.* [77] and Di Sarli *et al.* [58] are also tested in Fig. 4.13. The Di Sarli *et al.* model tends to over-emphasise the contribution of methane. The linear model is adopted here as it is simpler and marginally more accurate than the Hirasawa *et al.* model for methane/n-heptane combustion cases considered.

4.3.4.1 Additional data comparing alternative mixing-rules

Figure 4.14 presents the performance of the linear [244] and Hirasawa et al. [77] flame speed mixing rules for the case of ϕ_{CH4}/ϕ_{tot} = 0.8, showing that both models are satisfactory also for this condition.

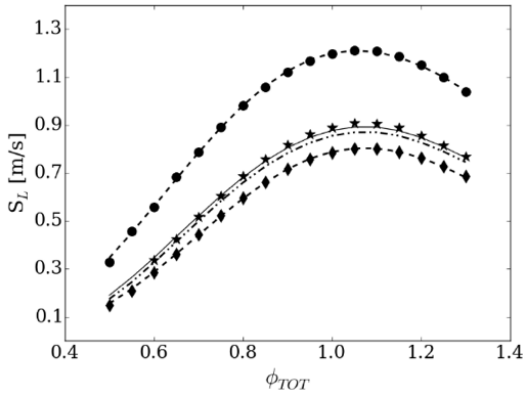

Figure 4.14: Variation of flame speed with equivalence ratio for methane/n-heptane fuel blends at 850K and 40bar: Polimi-106 simulations for $\phi_{CH4}/\phi_{tot} =$ 0 (•), 0.8 (◊) and 1.0 (★); Fitted flame speeds from a Gaussian function (dashed line); and Eq. 4.5 (solid line) [244] and Hirasawa et al. [77] (dash-dot-dot line) mixing-rules

4.3.5 Effects of pre-ignition chemistry

The form of the Metghalchi and Keck model [142] suggests how one can account for the effects of the temperature rise and reactant consumption arising ahead of the flame at autoignitive conditions, providing the first two factors on the right hand side of the following equation:

$$s_{f,fuel} = s_{r,fuel} \cdot \left(\frac{T}{T_u}\right)^{\alpha_{fuel}} \cdot (1 - \beta_{fuel}\xi_b) \cdot \mathcal{F}(c) \cdot \left(\frac{\rho}{\rho_u}\right). \tag{4.6}$$

Eq. 4.6 accounts for the flame speed increase due to the temperature increasing by the factor T/T_u ahead of the flame. The flame speed decreases by the factor $(1 - \beta_{fuel}\xi_b)$ because some of the fuel and oxidiser are consumed by the pre-ignition reactions, diluting the mixture with mass fraction ξ_b of burned products. α_{fuel} and β_{fuel} are fuel-dependent model coefficients. Accounting for the thermal expansion upstream of a one-dimensional planar flame, the flame speed is multiplied by the density ratio ρ/ρ_u, where ρ is the density just ahead of the flame. A further factor $\mathcal{F}(c)$ is introduced to account for the increase in flame speed due to the chemical influence of intermediate species produced upstream of the flame; this influence is shown by the difference between s_f and $s_{f,therm}$ in Fig. 4.9. Fig. 4.15 shows that $s_f/s_{f,therm}$ has an approximately linear dependence on progress variable. This suggests a simple model:

$$\mathcal{F}(c) = 1 + \gamma_{fuel}.c, \tag{4.7}$$

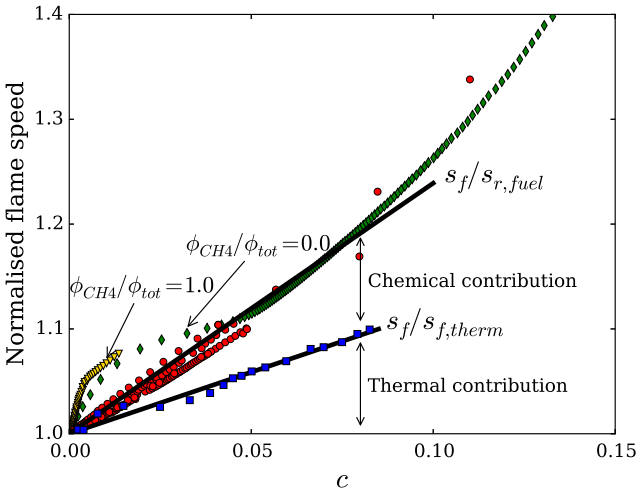

Figure 4.15: Normalised flame speed versus the progress variable upstream of the flame front: Round symbols show $s_f/s_{r,fuel}$ at $\phi_{CH_4}/\phi_{tot} = 0$, 0.5, 0.8 and 1.0 for $T_u = 850$ K and 1000 K; Square symbols show $s_f/s_{f,therm}$ based on data from Fig. 4.9. Solid lines show $s_f/s_r = 2.4c$ and $s_f/s_{f,therm} = 1.18c$.

with $\gamma_{C_7H_{16}} \approx 1.18$ for n-heptane. Equation 4.6 thus provides a breakdown of the contributions to the increase of the flame speed under autoignitive conditions.

Figure 4.15 shows that, for small values of progress variable, the laminar flame speed at autoignitive conditions increases approximately linearly with the value of progress variable c just ahead of the flame for the full range of methane/n-heptane fuel blends investigated, suggesting that Eq. 4.6 may be linearised into the form

$$s_{f,fuel} = s_{r,fuel}\,(1 + \epsilon_{fuel}.c)\,. \tag{4.8}$$

where ϵ_{fuel} is a model coefficient. The data presented in Fig. 4.15 suggests that ϵ_{fuel} is in the range 2.4 ± 0.5 for the blends considered ($\phi_{CH_4}/\phi_{tot} = 0, 0.5, 0.8, 1.0$) for progress variable less than 0.1. The linear model applies well to mixtures of methane and n-heptane, with pure n-heptane-air and methane-air blends some deviation from the linear model at 850 K for small values of progress variable, for which the increase in flame speed is anyway relatively small (shown by diamond and triangular symbols in Fig. 4.15). The value is potentially fuel specific and significantly higher values are obtained for example with dimethyl ether blends (not shown). From Eq. 4.6, the temperature-dependence leads to super-linear behaviour as the residence time approaches the ignition delay and the flame transitions into an ignition front, however this is of limited concern in the modelling of flame speed as flamelet-based turbulent combustion models that require

flame speed as an input would not be applicable to flames with ignitive, rather than deflagrative behaviour. Therefore the linear modelling approach remains valid for the deflagrative combustion conditions at which the flamelet approach is applicable.

The model has been developed with respect to numerically-simulated flame speed data, therefore the model coefficient ϵ_{fuel} is subject to uncertainty associated with the accuracy of the chemical mechanism employed. However the broad validity of the relatively detailed 106 species mechanism used in this study suggests that the approximately-linear response of flame speed indicated in Fig. 4.15 is at least qualitatively correct. In principle, ϵ_{fuel} could be evaluated directly from experimental measurement rather than by computation, however experimental measurements of flame speeds in partially-reacted mixtures are likely to be very challenging and will also involve significant, possibly greater, uncertainty.

The specification of progress variable may also affect the value of the model coefficient ϵ_{fuel}. Linear combinations of species mass fractions may be used as a basis for progress variable as an alternative to temperature, however it is important to employ a progress variable specification that resolves the evolution of the low-temperature combustion processes. For example, it is found that a progress variable specification based on the sum of carbon dioxide and carbon monoxide mass fractions also yields a linear flame-speed relationship, whereas use of carbon dioxide alone would not be appropriate since relatively little carbon dioxide is produced by the low-temperature chemistry. Due to the weak non-linearity between alternative definitions of progress variable, small differences in the value of ϵ_{fuel} can arise depending on the progress variable specification.

In order to linearise Eq. 4.6, each of the factors in Eq. 4.6 can be expressed as a function of progress variable: rearranging the definition of progress variable gives $T/T_u = 1+c(T_b/T_u-1)$; approximating the fraction of reactants that have been consumed by the progress variable gives $\xi_{pr} \approx c$; and, neglecting changes in pressure and molar mass, the ideal gas equation gives $\rho/\rho_u \approx [1 + c(T_b/T_u - 1)]^{-1}$. Since the model is only required to be valid for small values of progress variable, a first-order Taylor expansion of Eq. 4.6 yields the linear relationship

$$s_{f,fuel} = s_{r,fuel}\left(1 + \left[(\alpha_{fuel} - 1) \times \left(\frac{T_u}{T_b} - 1\right) - \beta_{fuel} + \gamma_{fuel}\right].c\right). \tag{4.9}$$

The coefficients $\alpha_{C_7H_{16}} = 2.79$, $T_u/T_b = 3.18$, $\beta_{C_7H_{16}} = 3.02$ are obtained by least-squares fitting to a data set containing reference flame speeds for n-heptane flames with $700 < T_u < 1000$ K, $20 < p < 60$ bar, $0.8 < \phi < 1.2$ and $0 < \xi < 0.15$. These coefficients and $\gamma_{C_7H_{16}} = 1.18$ lead to a prediction that $\epsilon_{C_7H_{16}} = 2.1$, which is reasonably close to the value of $\epsilon \approx 2.4$ obtained from Fig. 4.15. Since the difference in ϵ_{fuel} between the methane/n-heptane fuel blends considered is relatively small it is convenient to adopt a single value $\epsilon = 2.4$ for the full range of fuel blends.

The flame speed model given by Eq. 4.8 is tested in Fig. 4.8, providing a good prediction of the variation of reference flame speed with residence time for all of the fuel blends and temperatures investigated. The model is tested across a range of lean equivalence ratios in Fig. 4.13, showing that the simple linear model correctly describes the reducing magnitude of the pre-ignition chemistry effect reduces under lean conditions. In order to apply the flame speed model in engine simulations, the progress variable in the mixture ahead of the flame then needs to be modelled, either by simulating the evolution of the chemical composition during ignition as in Ref. [**?**], or potentially by modelling the progress variable as a function of the Livengood-Wu integral [122].

4.4 Conclusions

The effects of pre-ignition chemistry on laminar flame speed in autoignitive methane/n-heptane fuel blends are investigated using premixed laminar flame simulations. Pre-ignition reactions cause the speed of the flame to increase. Fuels that exhibit two-stage ignition behaviour, such as n-heptane, also exhibit a two-stage increase in the speed of the reaction front as the reactant residence time increases. The increase in flame speed is due to distinct contributions of heat release, reactant consumption, and enhanced reactivity ahead of the flame. Addition of methane to n-heptane-air mixtures retards and reduces the first-stage increase in flame speed, in part due to dilution of the more-reactive n-heptane fuel, and in part due to consumption of radical species by the methane chemistry. As the residence time of the reactants approaches the ignition delay time, the reaction front transitions into a pure ignition front, in which diffusive transport is negligible.

Prior to transitioning into a pure ignition front, the behaviour of the flame can be classified as deflagrative or ignitive depending whether the flame thickness and flame speed obey the deflagrative scaling $\delta_f \sim \alpha/s_f$. The thickness of cool-flames exhibits ignitive scaling with flame speed, $\delta_f \sim s_f$, for all conditions simulated. The transition between deflagrative and ignitive scaling is also associated with a reduction in the relative magnitude of diffusive transport within the flame front, however examination of the transport budget alone does not provide a sharp delineation between deflagrative and ignitive behaviours.

Modelling for flame speed in dual-fuel blends at autoignitive conditions should account for the local composition of the fuel blend, and for the effects of pre-ignition chemistry. Modelling is introduced to account for the effects of pre-ignition chemistry on the flame speed. The model is a simple linear function of the progress variable ahead of the flame – accounting for the distinct contributions of heat release, reactant consumption, and enhanced reactivity ahead of the flame. The flame speed model accurately describes the variation of flame speed and hence flame thickness for the full range of methane/n-heptane blends at engine-relevant conditions, up to the deflagration/ignition transition.

This flame speed is applied in G-equation modelling in Ch. 7, and the modelling approach is extended to methane-DME blends in Ch. 5 in order to capture contributions of pre-ignition chemistry in turbulent flows.

Chapter 5

Analysis of dual-fuel combustion initiation in turbulent flow

5.1 Introduction

This chapter presents analysis of the processes involved in dual-fuel turbulent combustion under engine conditions using detailed chemistry DNS of a pseudo-turbulent DME/methane–air mixing layer. The objectives are to establish the role of methane chemistry in the dual-fuel ignition and flame propagation processes, and how it affects the response of the processes to turbulent mixing.

5.2 Formulation

5.2.1 Numerical simulation

Dual-fuel combustion is investigated in a two-dimensional (2D) DNS configuration, illustrated in Fig. 5.1, adapted from the single-fuel study of Krisman et al. [110]. Additional homogeneous (0D) and laminar flame (1D) simulations are performed under corresponding thermochemical conditions in order to provide reference data for analysis of the 2D DNS. The 2D DNS involves a mixing layer with pilot fuel (70%$_{vol}$ DME, 30%$_{vol}$ nitrogen) at 400 K on one side, defined as unity mixture fraction, and oxidiser at 900 K on the other, defined as zero mixture fraction, and a uniform pressure of 40 bar. The profile

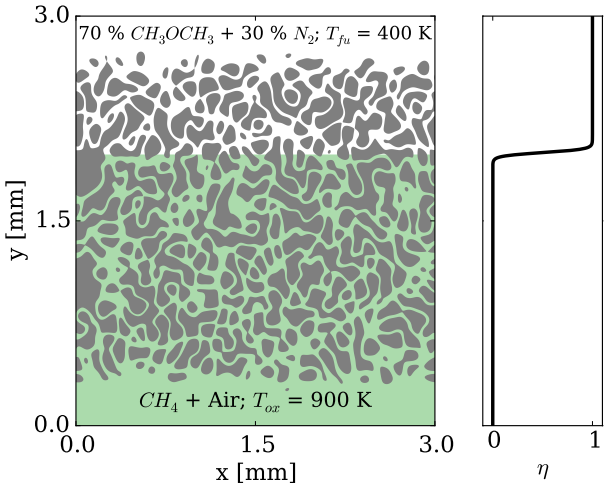

Figure 5.1: Two-dimensional initial conditions with mixture fraction distribution in y-direction. White shade represents the non-premixed DME and green shade the premixed oxidiser. Grey shade represents the initial vorticity.

of mixture fraction ξ is initialised as a function of the y-coordinate according to

$$\xi(y) = \frac{1}{2}\left(1.0 + tanh\left(\frac{(y - y_0)}{L_\xi}\right)\right) \tag{5.1}$$

where $y_0 = 2$ mm and $L_\xi = 25\mu m$ determine the position and thickness of the mixing layer. The 2D simulation domain is a 3×3 mm square, with periodic boundary conditions in the x-direction and partially non-reflecting outflow boundaries in the y-direction.

The oxidiser stream for the dual-fuel Case DF2D contains a mixture of methane and air ($21\%_{vol}$ oxygen, $79\%_{vol}$ nitrogen) with equivalence ratio 0.4. A further 2D single-fuel simulation, Case SF2D, is performed for reference, replacing the methane with a non-reactive diluent with the same thermodynamic properties as methane in order to help distinguish the effects of dilution and of chemical reactions associated with addition of methane.

Following Krisman et al. [110], the initial velocity field has zero mean, plus fluctuations generated according to a model turbulence spectrum [154] with $u' = 0.49$ ms^{-1} and integral length scale $L_t = 0.1$ mm. Defining Damkholer number as $Da = \tau_t/\tau_{\eta_{MR}}$, where τ_t is the turbulence time scale defined as $\tau_t = L_t/u'$, and $\tau_{\eta_{MR}}$ is the ignition delay time of the most reactive mixture fraction obtained in a homogeneous reactor, one obtains $Da = 0.38$. This Da number is similar to those recorded in simulations [156] at the ignition location for the engine-relevant Spray A configuration of the Engine Combustion Network (ECN) [162]. The initial velocity field is set to zero close to the

y-direction boundaries, as illustrated in Fig. 5.1 to avoid inflow early in the simulation which could lead to numerical instability of the boundary conditions.

Chemical reaction is modelled by a new 25-species reduced mechanism produced by the group of Prof. Tianfeng Lu, derived from a detailed DME/methane combustion mechanism (Mech_56.54) [30]. The detailed Mech_56.54 mechanism has been validated extensively against experimental results for ignition delay times for the full range of DME/methane blends, including for conditions relevant to dual-fuel engine operation [30]. A particular feature of the reduced mechanism derivation is the application of techniques [13] to obtain a mechanism with low numerical stiffness, enabling explicit time integration with a time step of 1ns at the present DNS conditions. The new mechanism correctly predicts first- and second-stage ignition delay and laminar flame speeds in close agreement with the parent detailed mechanism for the conditions used in the DNS calculation. Comparisons between the reduced and detailed mechanisms are presented on Appendix B. Temperature-dependent heat capacities and mixture-averaged molecular transport models are employed [92, 93].

The compressible NavierStokes, species continuity, and total energy equations were solved using the Sandia DNS code, S3D [41]. A fourth-order explicit Runge-Kutta method for time integration [94] and an eighth-order central differencing scheme for spatial discretization [95] were used with a tenth-order filter applied every 50 time steps to remove spurious high-frequency oscillations. NavierStokes characteristic boundary conditions (NSCBC) were used to provide partially non-reflecting boundaries in the y-direction [167], employing the improvements reported in Ref. [245]. Various homogeneous reactor, freely-propagating laminar flame and unsteady counter-flow simulations referred to in the study are performed using the COSILAB solver and identical thermochemical models [47].

5.2.2 Combustion mode analysis

The dual-fuel combustion process involves a range of combustion modes, such as autoignition, diffusion flame and deflagration, depending on the relative contributions of chemical source terms and diffusive fluxes for relevant chemical species. A variety of techniques have been employed previously in order to distinguish these combustion modes,

typically considering empirically-selected chemical species and arbitrary threshold values (e.g. Refs. [42, 107, 108, 207, 246]). Inhomogeneous dual-fuel combustion presents a particular challenge for these analysis methods since it is difficult to identify a single set of chemical species that adequately characterise the whole combustion process.

Chemical Explosive Mode Analysis (CEMA) has been developed as a basis for systematic characterisation of combustion processes, in which the most relevant sets of chemical species or *chemical modes* are identified locally as eigenvectors of the Jacobian matrix of the chemical source term [**?**]. Eigenvectors with positive real part eigenvalues indicate 'explosive' chemical modes (CEMs), since the associated rates grow exponentially, whereas negative real part eigenvalues indicate 'exhausted' modes that decay over time. The sign of the most-positive eigenvalue λ_e (i.e. excluding the zero eigenvalues associated with conservation modes), has been used in numerous studies to distinguish where reactive mixtures are in an explosive pre-ignition state ($\lambda_e > 0$) or in an exhausted post-ignition state ($\lambda_e < 0$) [246**?** **?**]. However λ_e is a purely chemical property of the mixture and does not, by itself, describe effects of molecular transport on the mode of combustion.

In order to characterise combustion mode systematically, Xu *et al.* [241] recently developed a combustion mode indicator based on the relative contributions of chemistry and molecular transport in the evolution of the CEMs. This new approach is employed in this study as a means of identifying the various combustion modes arising in the complex dual-fuel combustion environment, as set out below.

The Jacobian matrix $\mathbf{J}_\omega = \partial\omega/\partial\mathbf{y}$ describes the dynamics of the chemical evolution:

$$\frac{D\omega(\mathbf{y})}{Dt} = \mathbf{J}_\omega \frac{D\mathbf{y}}{Dt} = \mathbf{J}_\omega \left(\omega + \mathbf{s}\right), \tag{5.2}$$

where D/Dt is the material derivative, $\mathbf{y}$ is the thermochemical state vector, ω is the corresponding vector of chemical source terms and $\mathbf{s}$ is the vector of diffusion source terms. The eigenvalue λ_e is related to the Jacobian by

$$\lambda_e = \mathbf{b}_e \cdot \mathbf{J}_\omega \cdot \mathbf{a}_e, \tag{5.3}$$

where $\mathbf{a}_e$ and $\mathbf{b}_e$ are the right and left eigenvectors of the CEM. The contributions of reaction and diffusion to the evolution of the CEM are given by projecting Eq. 5.2 onto

the CEM. The projected chemical and diffusion source terms are denoted respectively by

$$\phi_\omega \equiv \mathbf{b}_e \cdot \omega \tag{5.4}$$

and

$$\phi_s \equiv \mathbf{b}_e \cdot \mathbf{s}. \tag{5.5}$$

ϕ_ω and ϕ_s are defined for preignition mixture only ($\lambda_e > 0$) and the direction of $\mathbf{b}_e$ is chosen such that ϕ_ω is always non-negative.

The local combustion mode indicator α is defined in the pre-ignition mixture by

$$\alpha = \phi_s/\phi_\omega. \tag{5.6}$$

Xu *et al.* [241] demonstrated that the value of α can be used to delineate three modes of premixed combustion: (i) Diffusion-supported ($\alpha > 1$): chemical evolution is reinforced by molecular transport, as in the preheat layer of a deflagration wave; (ii) Autoignition ($|\alpha| < 1$): molecular transport plays a minor role in the chemical evolution; (iii) Local extinction mode ($\alpha < -1$): the chemical evolution is counteracted and overwhelmed by molecular transport.

The combustion mode indicator refers to the evolution of a single chemical mode. In complex combustion processes, such as inhomogeneous dual-fuel combustion, a secondary combustion mode may become faster than the previously most-explosive chemical mode. In order to characterise the rotation of or switching between chemical modes, the alignment of each thermochemical variable with the CEM is quantified by the explosion index (EI) [**?**]

$$\mathbf{EI} = \frac{diag|\mathbf{a}_e\mathbf{b}_e|}{sum(diag|\mathbf{a}_e\mathbf{b}_e|)}, \tag{5.7}$$

where "||" denotes the element-wise absolute values. **EI** is a normalised vector with each element lying within $[0, 1]$, and the magnitude of each element indicating the size of the contribution of the corresponding thermochemical variable within the CEM [**?**].

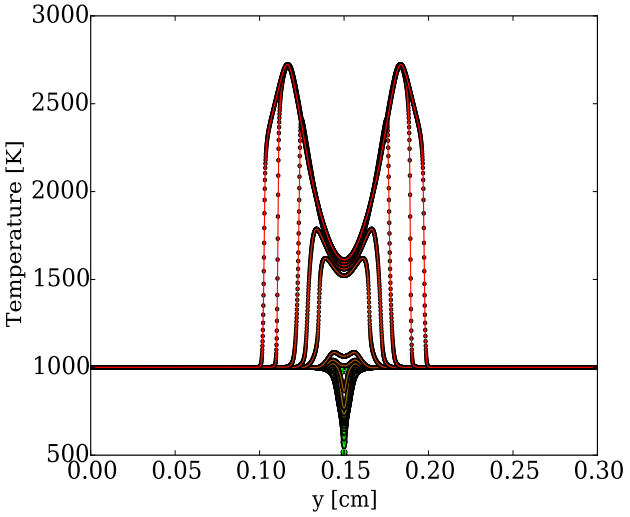

Figure 5.2: Temperature evolution in a 1D domain for two Δy: Symbols correspond to 0.9375 μm and lines 0.46875 μm. The time evolution goes from green to red lines.

5.3 Assessment of numerical accuracy

The thermal thickness δ_{th} and reaction thickness δ_r of a premixed flame are computed using the 1D freely propagating configuration with the 25-species chemistry at the following conditions: 40 bar; 1000 K; $\phi_{CH4} = 0.5$ and $\phi_{DME} = 0.0$. δ_{th} in such conditions is 20 μm, whereas δ_r is 5 times smaller, $\delta_r = 3.9\mu m$. The flame speed predicted by the 25-species scheme was 0.4 m/s. In Krisman *et al.* [109] the grid resolution was 1 μm, which corresponds to 4 points inside the obtained δ_r.

The spatial resolution requirements for the dual-fuel case is assessed using the S3D code to simulate ignition in a 1D laminar mixing layer in a 3 mm wide domain at the same thermochemical conditions as the DF2D case. Figure 5.2 shows the temperature evolution for two different discretizations: 0.9375 μm and 0.46875 μm. In both cases the time-step was 1 ns. According to the results in Fig. 5.2, 1 μm is enough to capture the autoignition and transition to the premixed flame propagation. Further analysis with coarser resolution shows a good prediction of the premixed flame propagation phase. Figure 5.3 compares refined results (0.46875 μm) with a 1.25 μm resolution in terms of temperature evolution. However, looking at the details of the ignition event for the three different discretizations one can see the deviations of temperature and peak of OH mass fraction for $\Delta y = 1.25\mu$m. The 0.9375 μm and 0.46875 μm present the same results and support use of grid spacing around 1 μm.

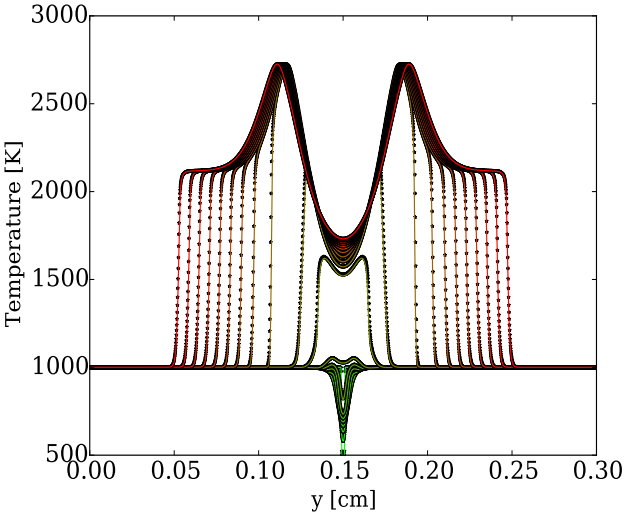

Figure 5.3: Temperature evolution in a 1D domain for two Δy: lines correspond to 0.9375 μm and symbols 1.25 μm. The time evolution goes from green to red lines.

5.4 Results

5.4.1 Evolution of the combustion process

The evolution of the combustion processes for two-dimensional quasi-turbulent cases DF2D and SF2D is illustrated in Fig. 5.5 by heat release colour maps at three different times. Both simulation cases have identical initial velocity fields and the mixture fraction field evolves similarly in both cases, as shown by the black line indicating the stoichiometric contour. However there are significant differences in the flame structures observed between the dual-fuel case and the single-fuel case, as indicated by the heat release patterns.

Laminar flow simulations of a 1D mixing layer with the same initial mixture fraction distributions as the 2D cases are shown in Fig. 5.6 in order to illustrate the various flame structures identified in the pseudo-turbulent 2D simulations. The corresponding single- and dual-fuel 1D cases are denoted by DF1D and SF1D. The 1D mixing layer simulations share many features with previous poly-brachial 2D laminar flow simulations of lifted DME-air flames [110], and this poly-brachial flame structure explains many of the features observed in the pseudo-turbulent 2D simulations in the present study. The heat release rate profiles in the 1D simulations are plotted as a colour map over time, revealing the inception of low-temperature combustion under slightly lean conditions (to

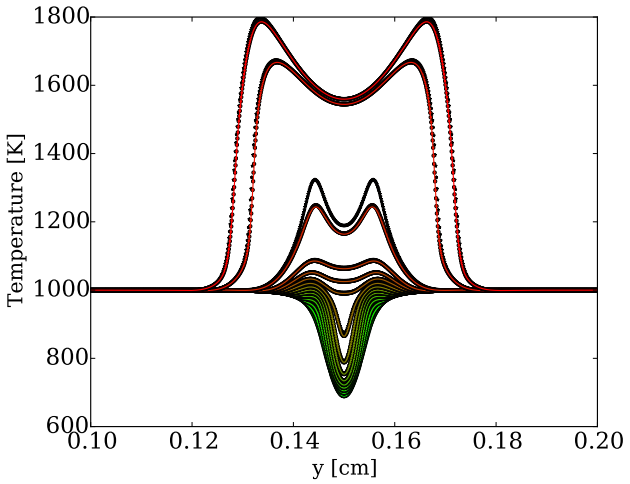

(a) Temperature evolution

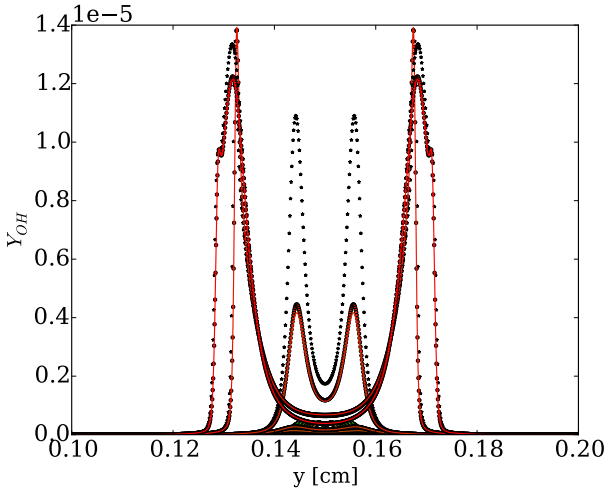

(b) OH mass fraction evolution

Figure 5.4: Detailed investigation of the three discretizations tested. Lines correspond to 0.46875 μm, circles to 0.9375 μm and stars to 1.25 μm. The time evolution goes from green to red lines.

the left of the black line indicating the locus of the stoichiometric mixture fraction). Subsequently the low-temperature branch migrates to the rich side of the mixing layer over time. The presence of reactive methane in the oxidiser (case DF2D) more than doubles the delay time for onset of the low-temperature combustion compared to the single-fuel case (case SF2D). The heat release patterns corresponding to the low-temperature combustion are seen in the 2D simulations in Figs. 5.5a,b, predominantly on the rich side of the stoichiometric iso-line (i.e. towards the top of the image).

The first high-temperature ignition kernels appear in the 1D laminar and 2D pseudo-turbulent flames in rich mixture, labelled HTI in Figs. 5.6 and 5.5a,b. For the present

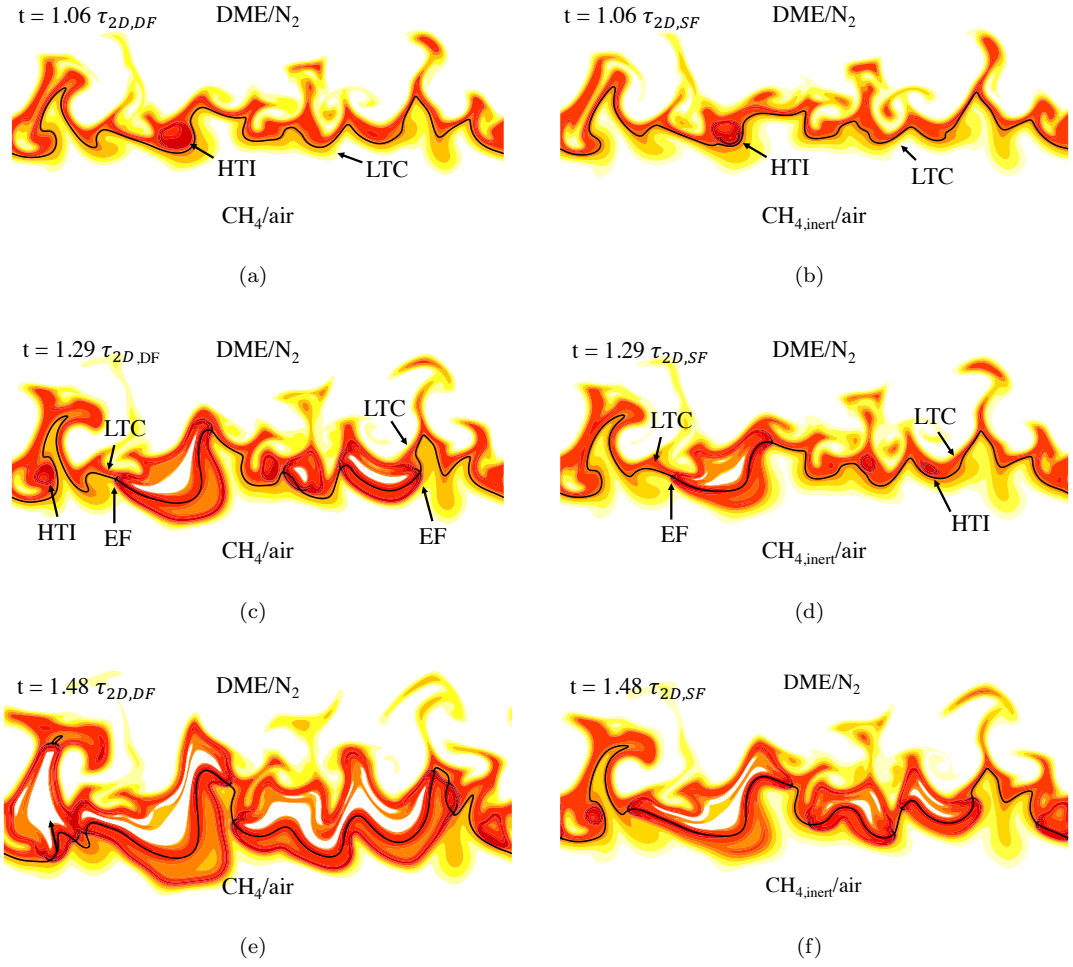

Figure 5.5: Heat release colour maps for cases DF2D (left) and SF2D (right) for three times (as indicated on subfigures). The solid black line corresponds to the stoichiometric mixture fraction.

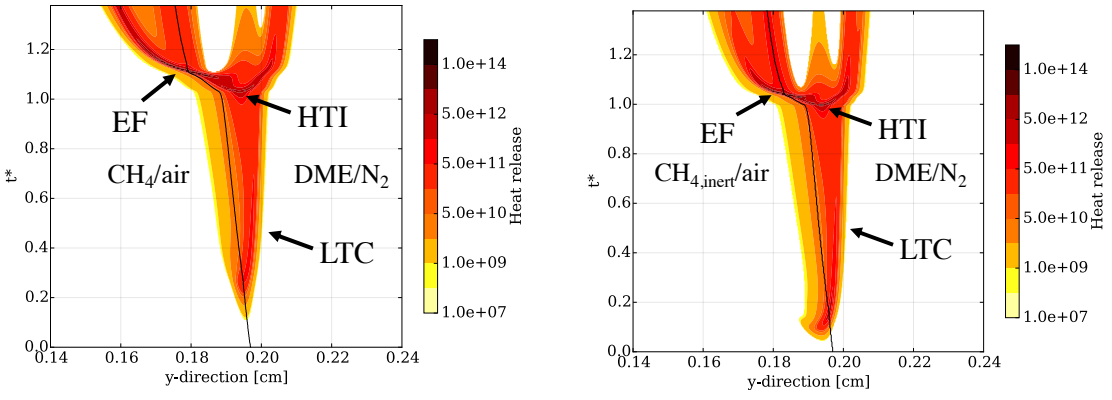

Figure 5.6: Time-space contour map the heat release rate in DF1D (left) and SF1D (right). The solid black line corresponds to the stoichiometric mixture fraction. Solid grey line correspond to methane-air homogeneous reactor ignition delay time.

DME fuel, methane addition has only a weak influence on the overall ignition delay time. High-temperature ignition occurs within the same 'eddy' in both cases SF2D and DF2D, indicating that the flow and mixing conditions at this location are somehow favourable for early ignition. Over time, the high-temperature combustion spreads from the ignition kernels across the stoichiometric line, whereupon edge flames are established, labelled as 'EF' in Figs 5.5 and 5.6. In the single-fuel cases (SF1D and SF2D) the edge flame takes a form resembling a classical triple flame [183] with fuel-lean and fuel-rich deflagration branches meeting with a stoichiometric diffusion flame at the flame's leading edge. In the dual-fuel cases (DF1D and DF2D), the diffusion flame is relatively weak and diffuse, while the deflagrative branches are thinner and more intense. The lean-branch of the dual-fuel edge flame eventually propagates into the lean-premixed oxidiser, completing the ignition process. Figure 5.7 shows a well-defined structure for the OH mass fraction distribution in mixture fraction space. The similarities of OH distribution for the single- and dual-fuel cases suggest that the major influence of methane chemistry is in the lean premixed branch of the edge flame, where it is the broadened towards zero mixture fraction.

The evolution of temperature conditioned on mixture fraction space, presented in Fig. 5.8, shows that the entire mixing layer in the range $0 < \xi < 0.6$ is affected by low-temperature chemistry. After the appearance of the first ignition kernel, two distinctive regions are observed: one corresponding to the cool-flame; and another related to the hot-flame.

Numerous ignition kernels appear during the course of the 2D simulations leading to additional edge flames. The simultaneous appearance of ignition kernels and edge flames is consistent with observations in optical dual-fuel engines [181]. In both single- and dual-fuel cases, the majority of the mixture in the vicinity of the stoichiometric iso-line appears to be consumed by the passage of thin edge flames rather than spontaneous ignition. The character and speed of the edge flame structures are therefore of significant interest for understanding and modelling the transition from dual-fuel ignition to deflagrative premixed combustion. The subsequent analysis therefore comprises three sections focussing in turn on the influence of methane addition on the ignition behaviour, the structure of the reaction fronts arising during the ignition-to-flame transition, and the propagation speeds associated with these reaction fronts.

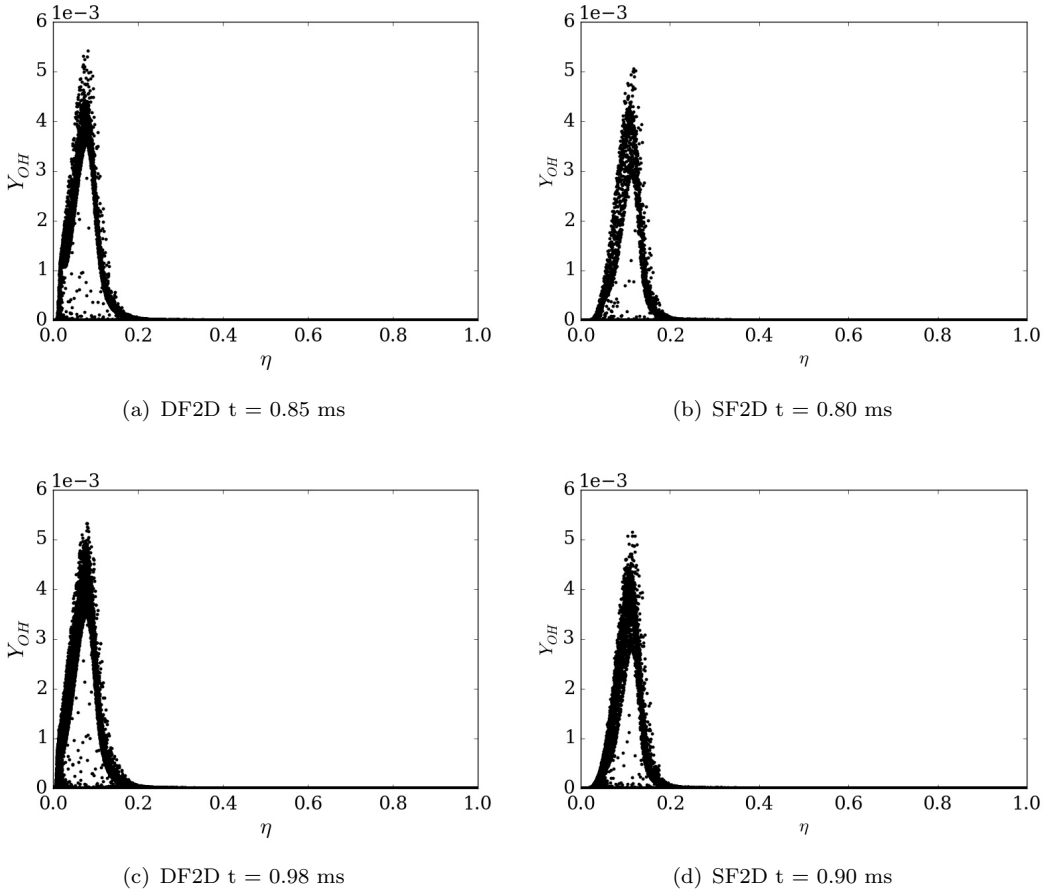

(a) DF2D t = 0.85 ms

(b) SF2D t = 0.80 ms

(c) DF2D t = 0.98 ms

(d) SF2D t = 0.90 ms

Figure 5.7: OH species mass fraction conditioned on mixture fraction at different times.

5.4.2 Ignition analysis

Figure 5.10 presents the ignition time and mixture fraction-location of all independent ignition kernels identified in the two-dimensional cases. The dependence of homogeneous ignition delay time on mixture fraction is also shown for the single-fuel and dual-fuel cases, based on sets of constant-pressure 'zero-dimensional' homogeneous-reactor calculations, SF0D and DF0D respectively. The overall ignition delay time τ_{ign} is recorded when the temperature exceeds 1500 K and the first-stage ignition is recorded when the mass fraction of $CH_3OCH_2O_2$ exceeds 20% of the maximum value [110].

In comparison with the homogeneous ignition delay curve, molecular transport effects in the 2D cases cause the mixture fraction location of the earliest ignition to move to significantly richer values, from around 0.13 in the homogeneous reactor to 0.22-0.4 in the 2D cases. The earliest ignition events in the two-dimensional DNS occur at $\xi = 0.268$ and

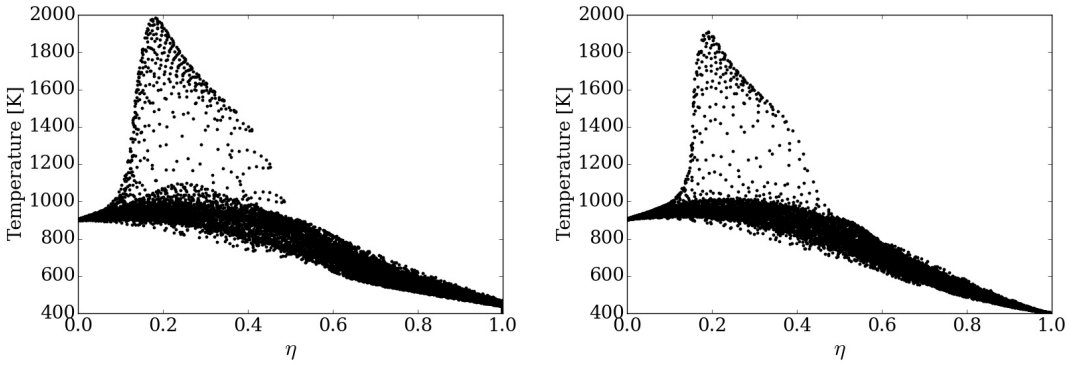

(a) DF2D t = 0.70 ms

(b) SF2D t = 0.62 ms

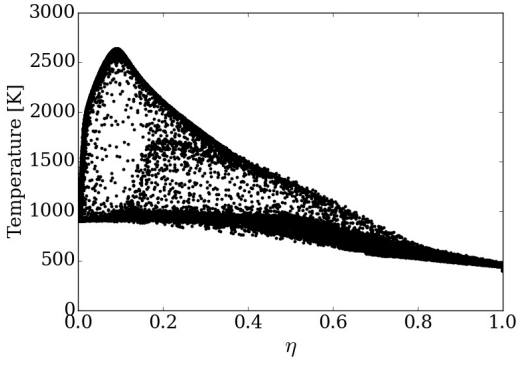

(c) DF2D t = 0.85 ms

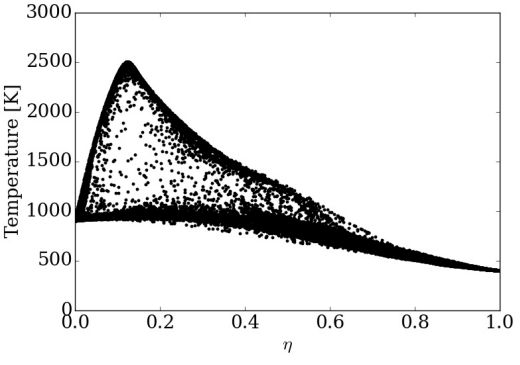

(d) SF2D t = 0.80 ms

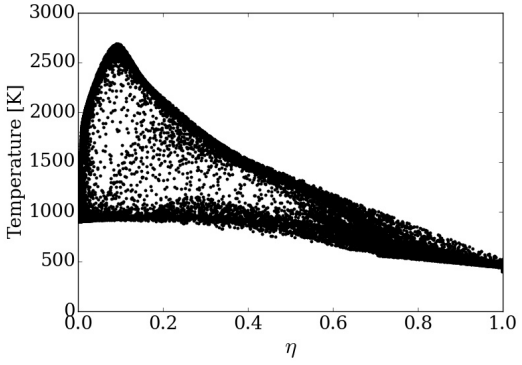

(e) DF2D t = 0.98 ms

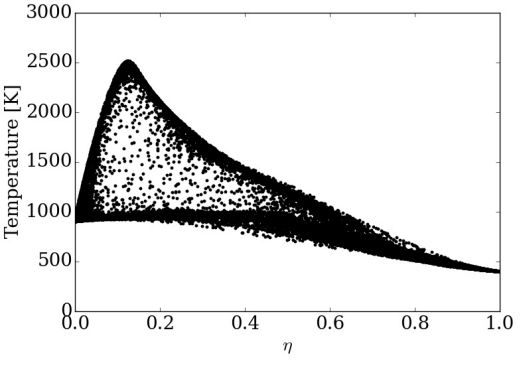

(f) SF2D t = 0.90 ms

Figure 5.8: Temperature conditioned on mixture fraction at different times.

Table 5.1: Overall ignition delay times for single-fuel and dual fuel cases.

Case	**SF**	**DF**
τ_{0D} [ms]	0.426	0.445
τ_{2D} [ms]	0.593	0.658

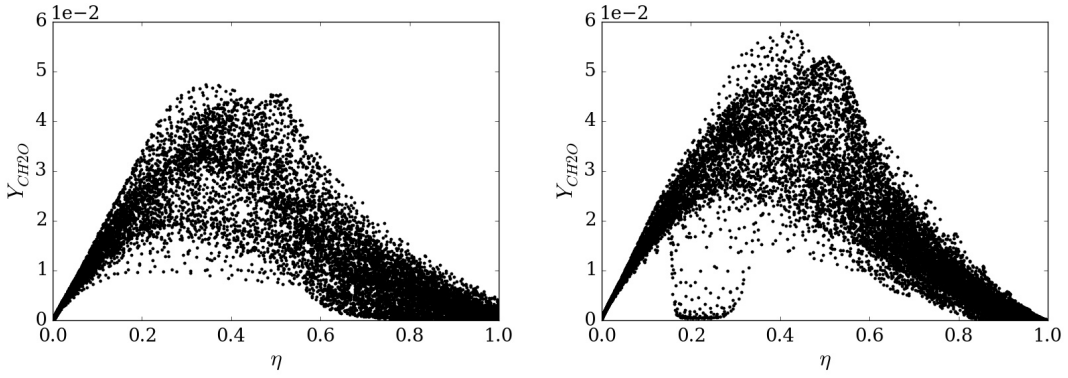

(a) DF2D (b) SF2D

Figure 5.9: Distribution of Y_{CH_2O} in mixture fraction space at t = 0.62 ms.

$\xi = 0.270$ with stoichiometric scalar dissipation rates of $\chi_{stoich} = 41.9s^{-1}$ and $\chi_{stoich} = 49.2s^{1}$ for cases DF2D and SF2D respectively. The stoichiometric scalar dissipation rate of the first ignition kernels is lower than for subsequent ignition events (which involve scalar dissipation rates up to $120s^{-1}$), in agreement with previous observations that ignition occurs preferentially in regions with lower scalar dissipation rate [135].

Previous single-fuel DNS studies have shown that propagation of cool flames towards richer mixture fraction promotes high-temperature ignition of fuel-rich mixture ahead of its homogeneous ignition delay time [109, 110], as observed here also for the dual-fuel case. In addition, chemical kinetic coupling between DME and methane fuels influences the ignition process: previous experimental investigation of a laminar non-premixed counterflow show that blending methane into DME fuel makes cool flames more susceptible to extinction [176]. The distribution of formaldehyde (CH_2O) in mixture fraction space presented in Fig. 5.9 shows a smaller contribution of low-temperature chemistry during the ignition process. This weakening of the low-temperature chemistry effect in the dual-fuel case appears to be a factor contributing to the 11% extension of the overall ignition delay time for the dual-fuel case DF2D, compared to SF2D, as reported in Table 5.1.

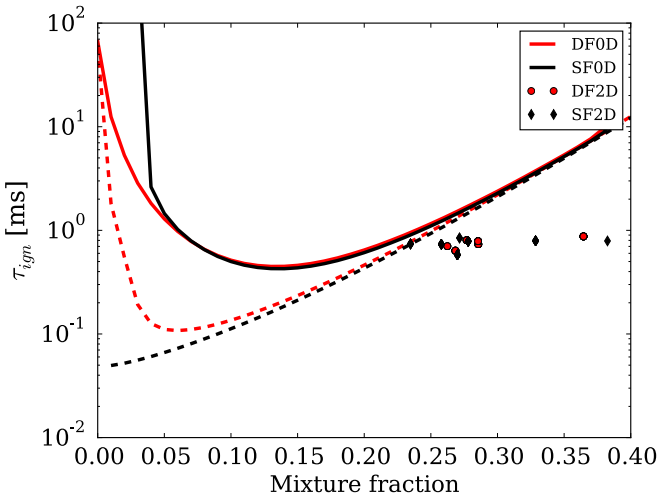

Figure 5.10: Overall ignition delay time τ_{0D} (solid lines) and first-stage ignition delay time (dashed lines) as a function of mixture fraction for cases SF0D (crosses) and DF0D (circles). Overall ignition delay times τ_{2D} for every independent ignition kernel in cases SF2D and DF2D are indicated by large symbols.

In contrast, the reactive methane present in the dual-fuel mixture does not significantly affect homogeneous reactor calculations of the most reactive mixture fraction value ($\xi_{MR} \approx 0.13$) or the minimum overall ignition delay time τ_{0D} compared to the single-fuel case. At leaner conditions the SF0D and DF0D homogeneous ignition delay times eventually diverge, since the oxidiser stream in the single-fuel case contains no fuel and therefore never ignites. The insensitivity of the homogeneous-reactor ignition delay time τ_{0D} to the presence of reactive methane is a peculiar feature of the DME fuel that contrasts with the significant increase of ignition delay caused by methane addition for diesel-like fuels such as dodecane [64]. DME differs from hydrocarbon fuels such as dodecane in that methane is a main intermediate product of low-temperature combustion processes of DME, reducing sensitivity to the presence of background methane.

The sensitivity of the dual-fuel ignition process to molecular mixing is investigated further through sets of single-fuel and dual-fuel one-dimensional laminar counterflow autoignition simulations, SFCF and DFCF, for a range of different global strain rates. The strain rate of the counterflow simulations is parametrised in terms of the stoichiometric mixture fraction dissipation rate in the initial unreacted flow. Ignition delay times for SFCF and DFCF simulations are reported in Fig. 5.11 for a range of scalar dissipation rates extending up to the critical value ($\chi_{st,crit}$=64 s^{-1}) beyond which no ignition was recorded in the SFCF case. The ignition delay for the DFCF case tends to a finite value

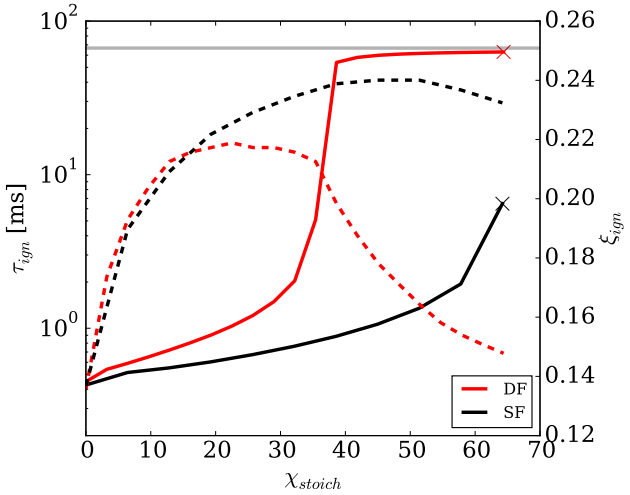

Figure 5.11: Overall ignition delay time for single- and dual-fuel counterflow configurations as a function of mixture fraction scalar dissipation rate. Dashed-lines correspond to the ignition location in mixture fraction space.

at high scalar dissipation rate since the adiabatic methane-air mixture in the oxidiser must ignite eventually, even for very large scalar dissipation rate values.

Figure 5.11 shows that the combination of methane chemical kinetics and molecular transport in the dual-fuel case acts to retard overall ignition, with the retarding effect of methane chemistry becoming greater as the scalar dissipation rate increases. Given the similar homogeneous ignition delay times for single-fuel DME and dual-fuel DME/CH_4 mixtures, the increased sensitivity of the dual-fuel ignition process to fluid dynamic strain caused by chemical interactions involving methane appears to be the leading cause of the increased ignition delay in the quasi-turbulent DF2D case, compared to SF2D.

5.4.3 CEMA analysis

Chemical Explosive Mode Analysis has not been applied to dual-fuel combustion previously. To aid interpretation of the CEMA results for the dual-fuel DF2D case, the variety of combustion modes arising in dual-fuel combustion is first illustrated in one-dimensional laminar premixed and non-premixed dual-fuel combustion examples. Figure 5.12 presents the CEMA analysis for two one-dimensional premixed combustion cases: the first case (given by conditions at $\xi = 0.01$ from the DF2D case) displays little chemical activity ahead of the flame and the second case (given by $\xi = 0.03$ from the

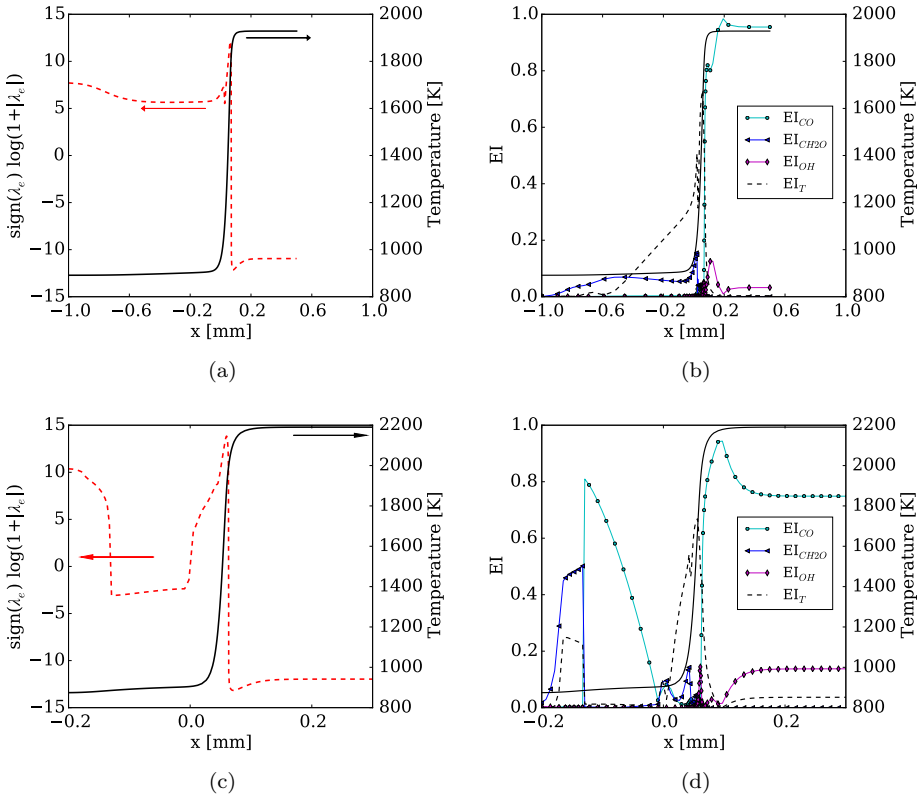

Figure 5.12: Temperature and λ_e profile for a freely-propagating flame at different mixture fractions: $\xi = 0.01$; $\xi = 0.03$.

DF2D case) exhibits a distinct low-temperature combustion front ahead of the high-temperature combustion front. The presence of the low-temperature combustion front is indicated by the first transition of λ_e from positive (explosive) to negative (exhausted) in Fig. 5.12c. Further downstream, a different CEM emerges (positive λ_e) before finally being exhausted in the high-temperature reaction front. This change of the chemical mode can arise either by a continuous rotation of the previous CEM, or by a distinct lower-ranked mode evolving to become the most explosive mode. The different makeups of the low-temperature CEM and the high-temperature CEMs are illustrated by the explosion indices **EI** shown for OH, CH_2O, OH, and temperature T in Fig. 5.12d: the low-temperature explosive mode is most closely aligned with CH_2O with a secondary contribution from temperature, whereas the high-temperature explosive mode is most closely aligned with temperature, with CO, CH_2O and OH contributing variously as the high-temperature explosive mode evolves.

Figure 5.13 presents CEM analysis of autoignition in the laminar mixing layer DF1D. The variation through the flame of ϕ_ω and ϕ_s, and their ratio α, is compared with the

balance of reaction and diffusion source terms for OH mass fraction. At the instant of high-temperature ignition (maximum temperature $\approx$ 1500 K at $t = 0.75$ ms in Fig. 5.13a), reaction source terms are dominant $|\alpha| < 1$. Analysing the lean reaction front after ignition at $t = 1ms$ in Fig. 5.13b shows distinct low- and high-temperature fronts of autoignitive mixture $|\alpha| < 1$, separated by a region of chemically-exhausted mixture. The 'preheat' layer of the low-temperature reaction front is diffusively-supported, $\alpha > 1$. In contrast, the preheat layer of the high-temperature reaction front is identified as a local extinction region, $\alpha < -1$, however this label may be misleading since the region also corresponds to the change over between low-temperature and high-temperature chemical modes. The distinct band of autoignitive low-temperature reaction disappears as the reaction front propagates into the lean methane-air mixture at $t = 2ms$, although the presence of an $\alpha < -1$ region that is not present in classical deflagrations [241] suggests that there is still a switch between two different CEM as the temperature rises in the preheat layer.

The identification of the different combustion modes in DF2D provides valuable information about the contribution of autoigniting and delagration processes on the pilot-ignited methane-air combustion. Figure 5.14 presents contours of temperature (first column), λ_e (second column) and α (third column) for different times during ignition. The first row, corresponding to ignition delay time, presents several pockets along the rich side of the mixing layer where the projected chemical source term is dominant. Some of the pockets extend to lean mixtures where diffusion reverses the ignition process. Combustion starts with one ignition kernel observed in the temperature field and identified by the dark-red eigenvalue contours (most explosive). The other red pockets observed on the combustion mode plot (first row) will eventually lead to autoignition as chemistry evolves and mixture fraction scalar dissipation rate diminishes.

On the combustion mode indicator plot, one can see that the flame presents an autoignition behaviour until it reaches the stoichiometric mixture fraction where an edge-flame is established with deflagrative characteristics. The propagation of the rich branch of the edge-flame into ignition-dominated regions can affect the local displacement. An interaction between pre-ignition chemistry and flame propagation into lean mixtures can be identified by the double zero-crossing of λ_e indicated by the yellow isoline at $\lambda_e = 0$ (last row for the combustion mode contours). To summarize, the combustion process is dominated by ignition in the rich side of the mixing layer, where the ignition kernel

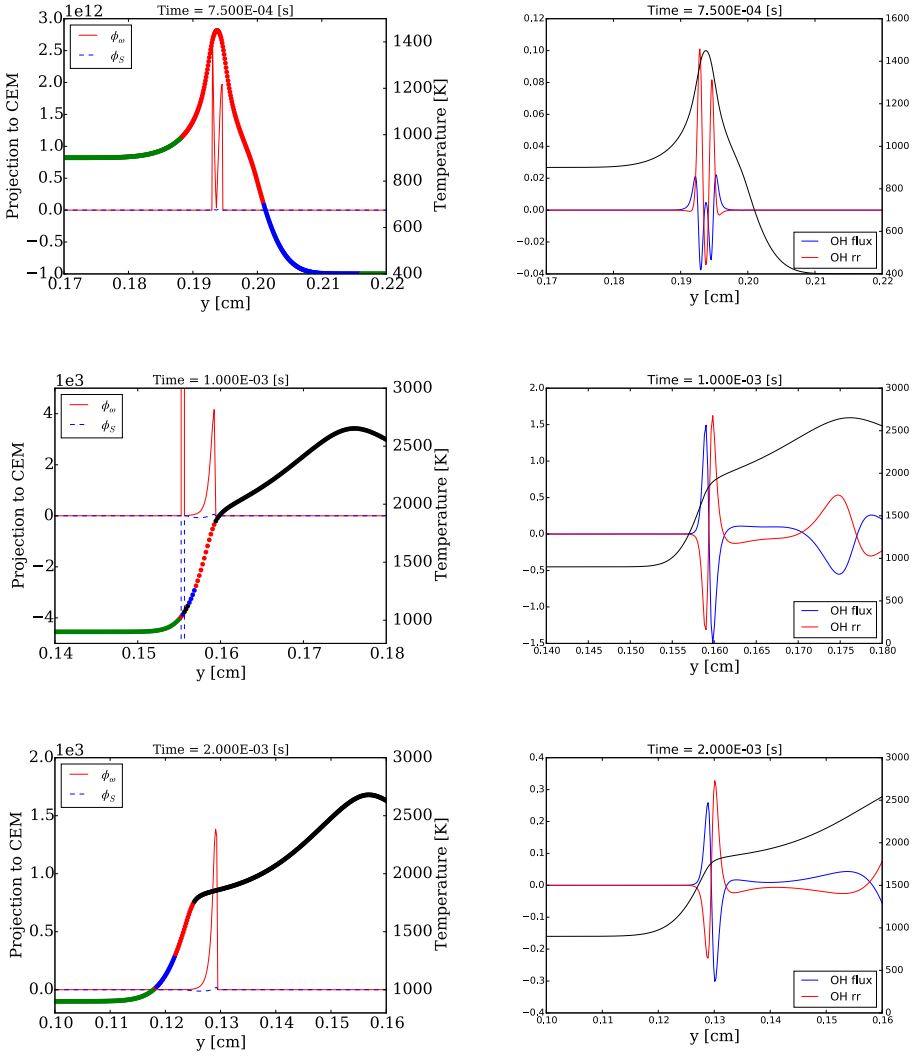

Figure 5.13: Temperature profile coloured by α and projected source terms λ_e distribution for the 1D mixing layer. Black region correspond to $\lambda_e < 0$.

are formed. Some of those ignition regions cross the stoichiometric isosurface towards lean mixtures but are extinguished by diffusion. The flame propagation is affected by partially reacted fuel but overall the edge-flame and lean premixed branch present a deflagrative structure.

5.4.4 Displacement Speed Analysis

The effects of pre-ignition chemistry on flame speed are first analysed for purely premixed compositions at different thermochemical states corresponding to different mixture fractions from the initial condition of the DF2D case. The composition was partially-reacted

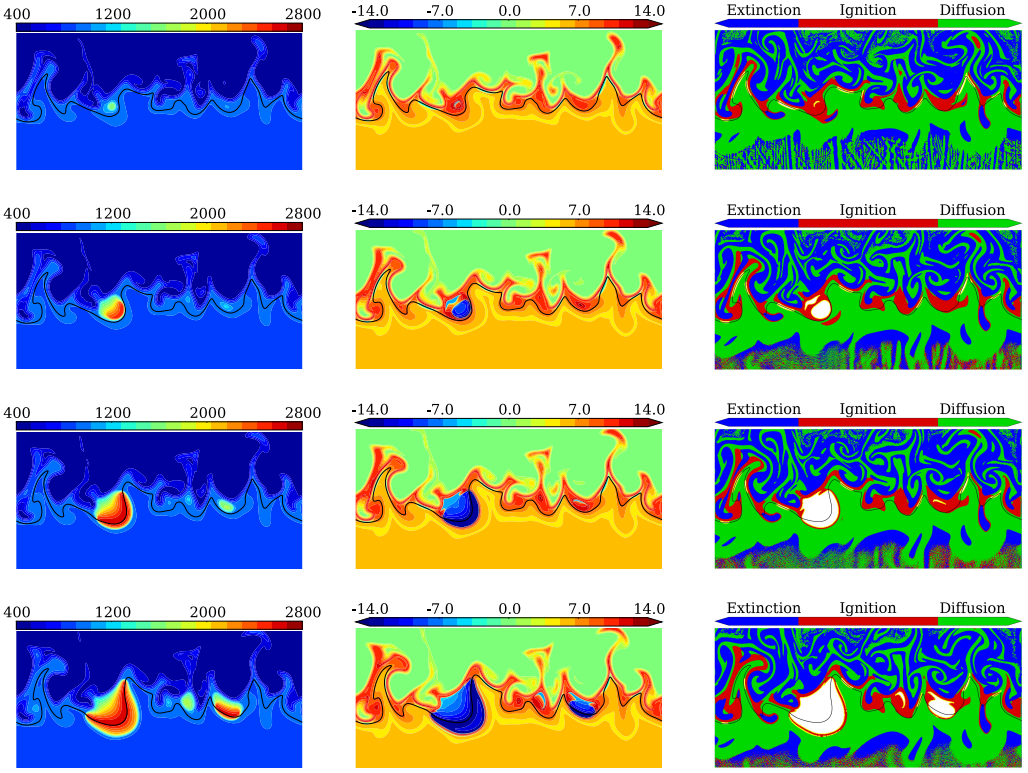

Figure 5.14: Contours of temperature, CEM eigenvalue (λ_e) and local combustion mode.

in a constant pressure reactor for a range of different residence times, and the composition from the constant pressure reactor used as inlet boundary condition in a 1D laminar freely-propagating flame. The methodology neglects spatial transport during the period that the mixture is in the constant pressure reactor. Nonetheless, analysis in Chapter 4 demonstrates that this simplification has minimal effect on the resulting flame speed. The total residence time τ_f is recorded as the sum of the time spent in the constant pressure reactor and the residence time upstream of the flame front in the one-dimensional laminar flame calculation.

Figure 5.15a presents the effects of residence time on displacement speed of mixtures in the range $0.0 \leq \xi \leq 0.8$. Propagation speeds of mixture close to the stoichiometric mixture fraction are highly affected by low-temperature chemistry ahead of the flame. Those effects are reduced with the increase of methane content in the mixture due to a weaker first-stage ignition as in Fig. 4.8. Figure 5.15b shows a linear dependence of flame speed on the progress variable ahead of the flame is observed for DME/methane blends, as it was also for n-heptane/methane mixtures in Chapter 4. Progress variable in this

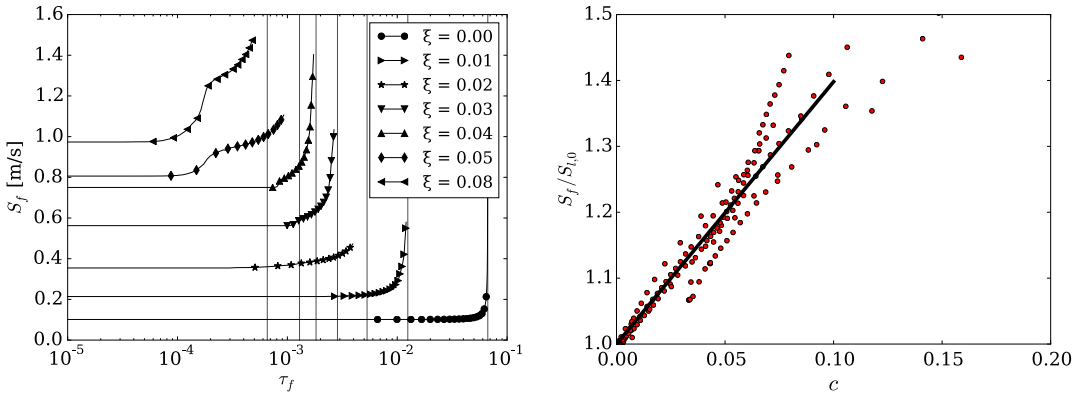

Figure 5.15: Effect of residence time on premixed laminar displacement speed for various mixtures from case DF2D.

case is defined in terms of temperature and $S_{l,0}$ in Fig. 5.15b corresponds to the reference flame as residence time τ_f tends to zero. The linear least-square fitting for a total of 467 flames predicted a slope equal to $\gamma = 3.981$. The linear model presented in Eq. 4.8 provides valuable information with which to quantify the effect of low temperature chemistry on propagation speed in the 1D mixing layer.

The flame propagation speed is evaluated in the turbulent case in terms of the displacement speed of a scalar iso-surface representing the flame front. Due to mixture inhomogeneity in dual-fuel combustion, a single iso-value of an individual species mass fraction or temperature cannot adequately characterize the flame front location and its displacement speed. Instead, the flame is tracked using an iso-surface of progress variable defined as a function of mixture fraction by

$$c = \frac{Y_c - Y_{c,u}(\xi)}{Y_{c,b}(\xi) - Y_{c,u}(\xi)}. \tag{5.8}$$

Subscripts u and b denote the burned and unburned states. In general Y_c is a weighted sum of species mass fractions. In this chapter Y_c is defined by the oxygen mass fraction, $Y_c = Y_{O_2}$. This definition gives a monotonic variation of progress variable through ignition and deflagaration processes for all mixture fractions of case DF2D. The progress variable displacement speed is given by,

$$s_d = \frac{1}{\rho|\nabla c|}\frac{D\rho c}{Dt}, \tag{5.9}$$

where D/Dt represents the substantial derivative. Noting the dependence of c on ξ, the progress variable displacement speed can be evaluated as

$$s_d = \frac{1}{\rho|\nabla c|}\left[\frac{1}{(Y_{c,b}-Y_{c,u})}\left(\frac{D\rho Y_c}{Dt} - \frac{\partial Y_{c,u}}{\partial \xi}\frac{D\rho\xi}{Dt}\right)\right. \tag{5.10}$$

$$\left. -\frac{Y_c - Y_{c,u}}{(Y_{c,b}-Y_{c,u})^2}\frac{D\rho\xi}{Dt}\left(\frac{\partial Y_{c,b}}{\partial \xi} - \frac{\partial Y_{c,u}}{\partial \xi}\right).\right] \tag{5.11}$$

Defining $Y_{c,\Delta} = Y_{O2,b}(\xi) - Y_{O2,u}(\xi)$, Eq. 5.10 can be rewritten as

$$s_d = \frac{1}{\rho Y_{c,\Delta}|\nabla c|}\left(\frac{D}{Dt}\left(\rho Y_c\right) - \frac{\partial Y_{c,u}}{\partial \xi}\frac{D\left(\rho\xi\right)}{Dt} - c\frac{\partial Y_{c,\Delta}}{\partial \xi}\frac{D\left(\rho\xi\right)}{Dt}\right). \tag{5.12}$$

The mixture fraction is defined in terms of the elemental mass fractions as in Eq. 3.28. The density-corrected displacement speed is then evaluated as

$$\overline{s_d^*}\left(y\right) = \frac{\rho s_d}{\rho_u(\xi)}\,\Big|\, c = c^*, \tag{5.13}$$

where $\rho_u(\xi)$ is the density of unburnt mixture corresponding to the local mixture fraction and c^* is the progress variable value used to track the flame front. In DNS analysis the choice of c^* is usually based on the location of maximum heat release rate in a laminar flame. The progress variable at the location of peak heat release in laminar flames across the range of flammable mixture fractions for case DF2D lies in the narrow range between $0.7 < \xi < 0.85$. In this Chapter displacement speed is reported for a particular progress variable value, $C^* = 0.8$.

Equation 5.13 has been verified by comparing its predictions with a finite difference evaluation of the flame speed calculated by tracking the position of the c^* iso-surface and the local velocity over time in a one-dimensional case (DF1D). To validate the decision to track a c^* iso-surface, displacement speed has also been calculated for a $1500K$ iso-surface, which is a common choice for analysis in premixed flames. A limitation of using a constant temperature value is that the reference point moves within the flame as it propagates through mixture fraction gradients. In contrast, use of a progress variable threshold reduces this movement and, given that the flame is typically very thin, results are not sensitive to the exact value of c^*.

Figure 5.16 presents the evolution of displacement speed using different methodologies to compute s_d. No flame speed is recorded until the progress variable or temperature reach

the respective tracking values (0.8 and 1500K respectively). At the location where these tracking values are first reached, the progress variable gradient is zero, giving an infinite flame speed at the centre of the ignition kernel. The flame speed subsequently reduces to a value on the order of the reference laminar flame speed, as expected for deflagrative combustion fronts. Based on the temperature ignition threshold of 1500K, ignition occurs first in rich mixture. The displacement speed passes through a local maximum as it propagates through stoichiometric before reducing again as the flame propagates through increasingly lean mixture. There is reasonably close agreement between the temperature and progress variable-based displacement speeds, possibly because the flame remains relatively thin during the combustion process. However the flame speed deviates from the reference laminar flame speeds expected based on the local mixture fraction values. Three main mechanisms for this difference in flame speed are considered:

1. Pre-ignition chemistry: The flame propagates into a partially reacted pre-ignition mixture and heat and radicals produced by first stage ignition enhance the propagation speed;

2. Unsteadiness: The flame develops over time and its flame speed is affected by its history (e.g. due to being thinner or thicker than the steady-state laminar flame thickness); and

3. Stratification: The equivalence ratio varies across the flame and the radical and thermal pool diffusing into the flame from the product side may offer enhanced 'back-support', as analysed by Richardson *et al.* [177, 180].

In order to evaluate the effects of pre-ignition chemistry, unsteadiness and stratification, the flame speeds given by the reference laminar premixed flame speed $s_l(\xi)$ (i.e. without pre-ignition chemistry) and the laminar premixed flame speed based on the thermochemical state one thermal thickness ahead of the flame s_f (as given by Eq. 4.8) are presented in Fig. 5.16. $s_l(\xi)$ is evaluated based on the mixture fraction value where temperature reaches 1500 K in the flame front. For richer mixtures ($\xi > 0.1$) the flame speed is significantly affected by ignition reactions upstream of the flame, even where the domain length upstream of the flame is a matter of a few flame thicknesses, therefore there is no well-defined freely-propagating flame for the richer mixtures and these laminar flame speed values should be treated only as indicative values. While these richer mixtures

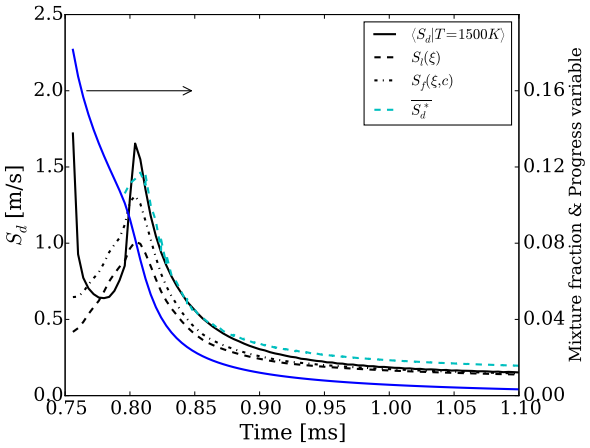

Figure 5.16: Evolution of displacement speed in the one-dimensional mixing layer. Mixture fraction at the flame is represented by the solid blue line.

are primarily of interest due to their role in ignition, rather than flame propagation, the observed dependence on residence time highlights the role of pre-ignition chemistry in the enhancement of flame speed under the present conditions. The differences between $s_l(\xi)$ and s_f for lean mixtures are due to low temperature chemistry, whereas the stratification and unsteadiness effects are quantified by the difference between s_f and $\overline{s_d^*}$. Stratification and unsteadiness effects during the early stages of flame propagation have a significant effect on displacement speed, with $\overline{s_d^*}$ assuming values below $s_l(\xi)$ even though the propagation is in a partially reacted region. The difference between $s_l(\xi)$ and s_f reaches its maximum around the stoichiometric mixture fraction and decreases as the total equivalence ratio is reduced. The constant in Eq. 4.8 goes up to 4.8 if only the stoichiometric flame was considered. However, a significant enhancement is observed until $\xi \approx 0.005$, the differences between s_l and s_f at 1 ms for the 1D mixing layer are still substantial: $s_l = 15.7m/s$ and $s_d = 22.2cm/s$.

Figure 5.17 presents the displacement speed conditioned on mixture fraction at the flame for all simulation time after ignition in case DF2D. The displacement speeds are generally of the same order of magnitude as the laminar flame speed, indicating that fuel consumption during pilot burn out ($\xi > 0.0$) is dominated by deflagrative propagation, as observed in the CEMA analysis. However, the displacement speeds are typically 30% or more greater than the laminar flame speed values. The flame front in this simulation is weakly turbulent and there are no instances where strain or curvature cause the displacement speed to fall below the laminar value. The conditionally averaged displacement speed $\overline{\langle s_d^*|\eta, c = c^*\rangle}$ is comparable to the displacement speed obtained from

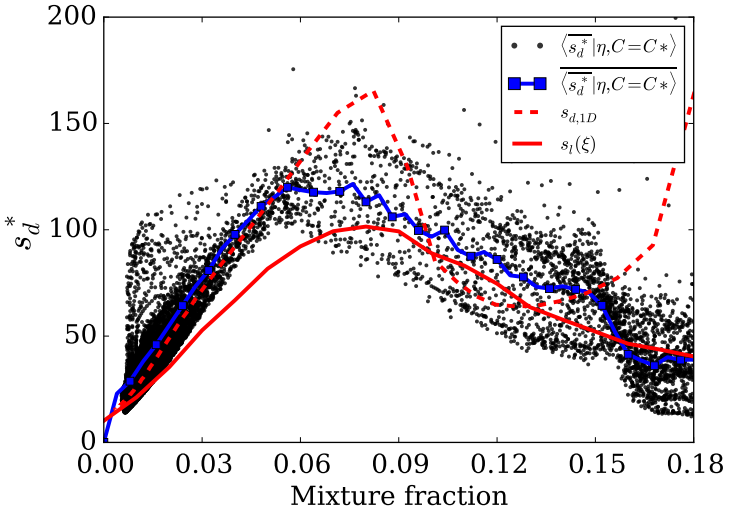

Figure 5.17: Displacement speed conditioned on mixture fraction.

the one-dimensional mixing layer $s_{d,1D}$. Thus, on average displacement speed is not affected by turbulent effects (strain or curvature).

In lean mixtures, the maximum flame speed that would be expected to arise due to back-support would be the stoichiometric flame speed. Since the flame speeds in lean mixtures here exceed the stoichiometric laminar value, back support is not a sufficient explanation for the increased flame speed. The data therefore suggest that the displacement speed is significantly affected by release of heat and radicals by from pre-ignition reactions of the pilot fuel.

Figure 5.18 presents contours of heat release rate at four times. Red dots indicate locations where the local displacement speed exceeds the reference laminar flame speed by at least 30%, i.e. $s_d > 1.3 s_l$. Flame curvature is observed to be important in some regions where the mixing layer is distorted by turbulence. However, a great number of lean flames propagating with 30% above the laminar flame speed are located in regions with negligible curvature and therefore their increased propagation speed is attributed to pre-ignition chemistry and unsteadiness/stratification. The folding of the stoichiometric mixture fraction surface, similar to observations in Sripakagorn et al. [212], contributes to the increased displacement speed predicted for $\xi \approx 0.08$ at t = 0.90 ms (Fig. 5.18b). Flame-flame interaction, generally occurring when two different edge flames connect, is also observed to contribute to an increase in flame speed at 0.95ms (Fig. 5.18c).

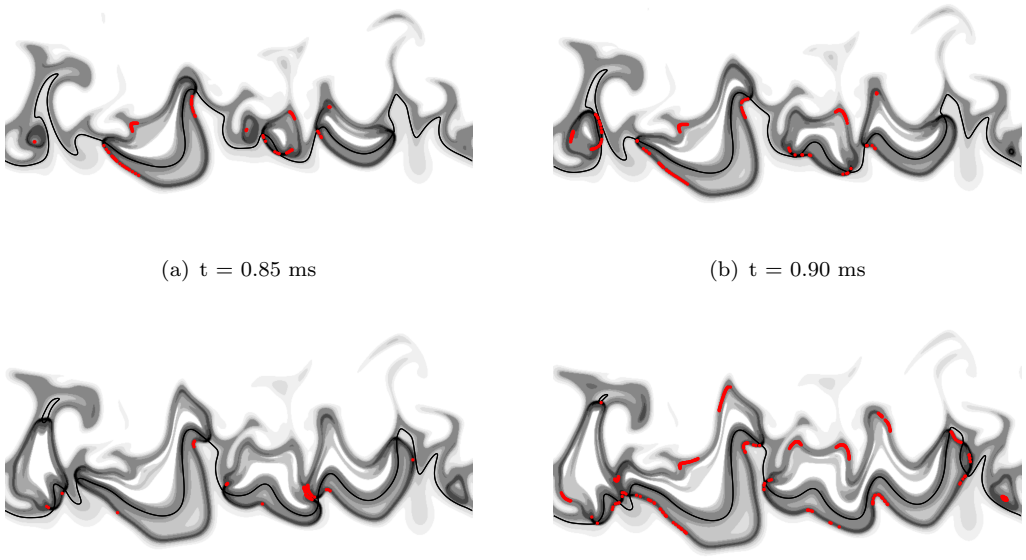

(a) t = 0.85 ms (b) t = 0.90 ms

(c) t = 0.95 ms (d) t = 0.98 ms

Figure 5.18: Location with $s_d > 1.3 s_l$

Examination of the CEMA results (right column of Fig. 5.14) at locations where elevated displacement speeds are indicated in Fig. 5.18 shows numerous instances where the elevate propagation speed of lean reaction fronts is associated with a band of 'exhausted' fluid ahead of the flame (the boundary between explosive and exhausted fluid is indicated by thick yellow lines). The occurrence of a band of exhausted fluid ahead of the high-temperature reaction front is characteristics of flame propagation into the products of a cool flame for $\xi = 0.03$ in Fig. 5.12. This connection between enhance flame speed and the presence of pre-ignition chemistry effects emphasises the importance of pre-ignition chemistry in the deflagrative combustion of the pilot fuel region.

5.5 Conclusion

Dual-fuel methane-DME combustion is analysed using DNS with realistic multi-step chemistry at relevant engine conditions. The contributions of methane chemistry on the ignition process were identified by replacing CH_4 by an inert chemical species with the same thermochemical properties. Methane addition has limited chemical effect on the ignition of homogeneous mixtures, but it substantially increases the mixture sensitivity to molecular transport, so that turbulent mixing significantly retards the DME ignition process. This phenomenon has not been identified in previous studies considering the

effect of methane addition on ignition of typical diesel surrogates, such as dodecane, possibly because ignition of non-oxygenated hydrocarbons already shows a strong sensitivity to methane addition in homogeneous reactors. This effect is captured qualitatively by counter-flow flamelet calculations with fixed scalar dissipation rates, however unsteady scalar dissipation rate solutions or other models may be required in order to obtain quantitatively accurate predictions of the ignition process.

Following the formation of ignition kernels, the combustion process transitions into poly-brachial flame structure with low temperature chemistry, diffusion and deflagration branches. The projected chemical and diffusion source terms analysis revealed a complex combustion process in which most of the inhomogeneous mixture is consumed by deflagration.

The analysis of displacement speed revealed a large scatter in the two-dimensional simulation. The different aspects of flame speed enhancement were analysed with the aid of simpler one-dimensional laminar mixing layer calculation. A strong influence of pre-ignition chemistry for all range of inhomogeneous mixtures is observed. Stratification effects can also have a significant impact on regions with large gradients of mixture fraction. Considering the turbulence levels used, curvature had a minor effect on the overall displacement speed of the flame.

From the modelling perspective, the DME/methane-air dual-fuel combustion requirements are: detailed chemistry to predict the kinetic interaction between the different fuels; the turbulence-chemistry interaction during ignition in order to capture the response of the fuel blends to scalar dissipation rate; a general approach that is not tailored to premixed or non-premixed combustion; the capability to capture the different mechanisms affecting displacement speed, in particular stratification and pre-ignition chemistry.

Chapter 6

DCMC-based modelling for the joint mixture fraction-progress variable pdf in partially-premixed combustion

The joint-probability density function is a key ingredient for Double Conditional Moment Closure modelling. There is no theoretical support for the common assumption that mixture fraction and progress variable are statistically-independent. This chapter investigates a new 'age-based' method proposed by Dr E.S. Richardson for modelling the statistical dependence of mixture fraction and progress variable in partially premixed combustion systems, such as dual-fuel engines. The new approach is motivated by the insight that the evolution of the chemical state and hence the form of the scalar pdf is shaped by the reaction-diffusion dynamics in the combustion system. The Double Conditional Moment Closure solution for a combustion system contains information about the reaction-diffusion dynamics for that system, and the new method provides improved modelling by making use of this information. In this chapter, Direct Numerical Simulation data provided by Sandia National Laboratories for three very different partially-premixed combustion modes are used in order to investigate the validity of the new modelling approach.

6.1 Introduction

Partially-premixed combustion is commonly modelled with reference to the mixture fraction ξ and progress variable c. Information about the joint probability density function (pdf) of ξ and c may be used to improve modelling of average or filtered reaction rates needed in Reynolds Averaged or Large Eddy Simulations (LES) of turbulent combustion. In the absence of more accurate simple models for the statistical dependence of mixture fraction and progress variable, a common approach in presumed-pdf modelling is to assume statistical independence, even though the hypothesis of statistical independence cannot be strictly exact [229]. For example, DNS of a lifted autoigniting jet flame shown in Fig. 6.1 displays clear bands of correlation between mixture fraction and progress variable. The presence of correlation proves that mixture fraction and progress variable cannot be statistically independent. Even in locations where there is no correlation, for example at the location indicated by the star in Fig. 6.1, scatter plots of mixture fraction and progress variable, for example Fig. 6.2, exhibit structure that is indicative of statistical dependence. Previous attempts to incorporate information about correlation into modelling for the joint ξ-c pdf, for example using the Plackett copula [50], have not seen any significant uptake. This may be because use of approaches like the Plackett copula have no physical justification and typically increases complexity significantly – Darbyshire and Swaminathan [50] advocate a copula approach requiring five input moments (i.e. two means, two variances and one correlation) – and improved accuracy has not been demonstrated adequately. Moreover, the Plackett copula describes diagonal dependence structures as seen in Fig. 6.3, which is a limitation when compared to the complex distributions such as presented in Fig. 6.2. The goal of this chapter therefore is to test a new physics-based concept for modelling the joint-pdf with an equal or lower number of input moments, compared to common independent joint-pdf approaches (e.g. requiring two means and two variances).

Mixing of fuel and oxidiser is characterised in terms of the fuel mixture fraction ξ, as defined by [15]. Reaction progress is characterised by progress variable c defined as

$$c = \frac{Y_c - Y_{c,u}(\xi)}{Y_{c,b}(\xi) - Y_{c,u}(\xi)}. \tag{6.1}$$

Here, the simple specification $Y_c = Y_{CO2} + Y_{H2O} + Y_{CO} + Y_{H2}$ is adopted consistently across the different combustion cases investigated, noting that this combination

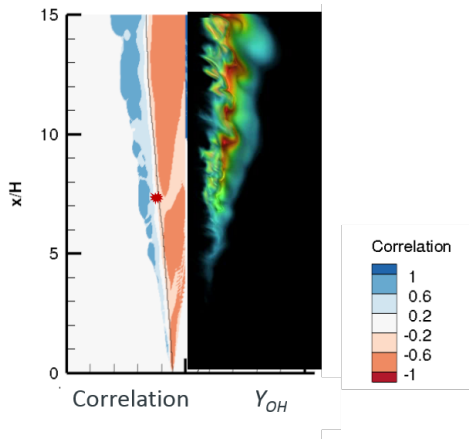

Figure 6.1: Colour maps of correlation (left) and instantaneous OH mass fraction (right) for a lifted autoigniting jet flame [247].

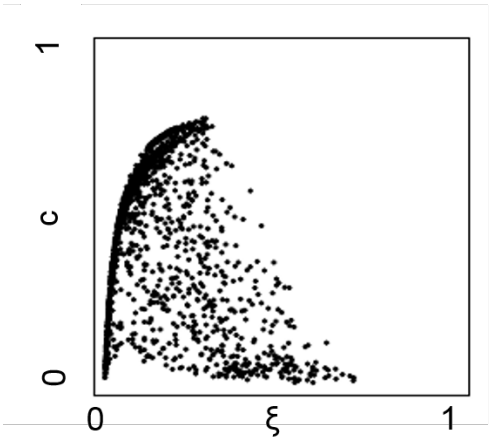

Figure 6.2: A scatter plot of data from the position indicated by a star at $x = 7H, y = -1H$ in Fig. 6.1 in a lifted autoigniting jet flame from Ref. [247].

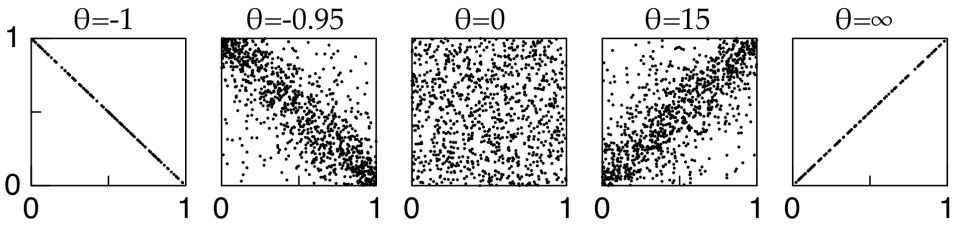

Figure 6.3: Examples of Plackett copula distribution with the given odds parameter θ and uniform marginal distributions. Plots range from perfectly negative correlation (far left) to perfectly positive correlation (far right) [137].

of species, or the subset $Y_{CO2} + Y_{CO}$, have proven satisfactory in previous analyses of these and similar combustion cases [101, 116, 147].

In this chapter differences in the joint-pdf modelling are assessed by evaluating their impact on evaluation of the unconditional reaction rate source term of progress variable.

$$\widetilde{\dot{\omega}}_c = \int_0^1 \int_0^1 \langle \dot{\omega}_c \mid \eta, \zeta \rangle \widetilde{P}_{\xi,c}\left(\eta, \zeta\right) d\eta d\zeta \tag{6.2}$$

where η and ζ are the sample-space variables for mixture fraction and progress variable respectively, and $\langle . \mid \eta, \zeta \rangle$ is the double-conditional Favre average.

6.2 Analysis

6.2.1 DNS data

Three DNS data sets illustrated in Fig. 6.4 are analysed involving: (1) equivalence ratio-stratified flame propagation [180], (2) non-premixed autoignition [247], and (3) partially-premixed extinction and reignition [116]. All cases were simulated with the Sandia DNS code S3D [41]. Full details of the respective DNS datasets are provided in the articles referenced.

Equivalence ratio-stratified flame propagation data from two turbulent slot Bunsen flame configurations are analysed. The first configuration (case C4 in Ref. [180]) has a stoichiometric jet issuing into an infinite coflow of $\phi = 0.41$ products and the second configuration (case C4 in Ref. [180]) has a $\phi = 0.41$ jet issuing into an infinite stoichiometric coflow. Data are presented on a cross-plane at one half of the domain height. Non-premixed autoignition data for a diluted ethylene slot jet issuing into a highly-heated coflow of air [247] are presented on a cross-plane at three different heights: 6H, 7H and 12H. Data for the temporally-evolving jet of Lignell et al. [116] at two times: at t = 0.11 and 0.26 ms , representing instants during extinction and re-ignition, respectively, with approximately 50% of the stoichiometric flame surface extinct [116]. For the planes or times analysed, data are presented versus the statistically inhomogeneous cross-stream y-direction.

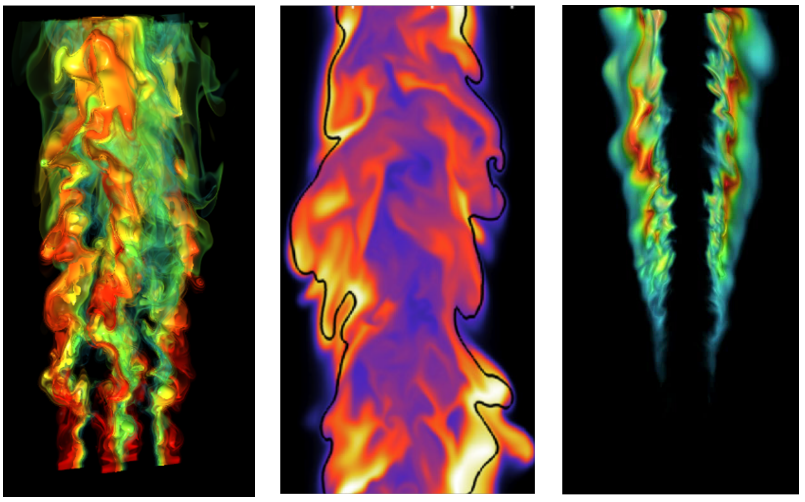

Figure 6.4: Illustration of the three partially-premixed DNS data sets examined in this study: Left: Equivalence ratio-stratified slot Bunsen flame (volume rendering of heat release coloured); Centre: non-premixed temporal planar jet, (temperature field and stoichiometric iso-surface); Right: lifted autoigniting slot jet (volume rendering of OH mass fraction field).

6.2.2 Reaction rate closure

The practical impact of the statistical dependence between mixture fraction and progress variable is assessed a priori based on Direct Numerical Simulation data by evaluating the Favre-mean reaction rate $\widetilde{\dot{\omega}}_c$ using the first-order double-conditional moment closure (DCMC) approach, given in Eq. 6.2, testing different models for the joint-pdf $\widetilde{P}_{\xi,c}(\eta,\zeta)$. The joint-pdf is modelled (i) using the empirical pdf from the DNS; and combining the empirical mixture fraction pdf with (ii) a δ-function pdf for progress variable; (iii) an independent β-pdf for progress variable; and (iv) with progress variable dependence given by the new age-generated joint-pdf, Eq. 6.6.

6.2.3 Reference flame solutions

The empirical data provided by the various DNS does not span the full ξ-c space and therefore cannot be used to evaluate all of the different joint-pdf models compared in this work. In order to obtain reaction source terms across the full ξ-c space, DCMC solutions are calculated for each DNS case. It is emphasised that the objective of this analysis is to assess the validity of the joint-pdf models rather than the accuracy of DCMC modelling, or of any other model for reaction rates, however the DCMC solution does yield close agreement with conditionally-averaged reaction rates in each DNS case.

Since the same double-conditional reaction rates are used to compare all of the different joint-pdfs (including the empirical joint-pdf), this approach provides a direct measure of the influence of the different joint-pdf models.

The stand-alone DCMC approach set out in Chapter 3 is employed to generate the reference flame solutions. The unburnt conditions at $\zeta = 0$ are specified according to linear mixing of species mass fractions and enthalpy between two reactant streams at $\eta = 0$ and 1. The burnt condition is defined in this study as the chemical equilibrium state for a given mixture fraction in the absence of transport effects. The composition of the two reactant streams corresponds to the various DNS cases introduced in 6.2.1. Thermochemical models are identical to the DNS cases. Due to the absence of radiative heat losses or differential diffusion in the DCMC equation, total enthalpy remains a constant linear function of mixture fraction for all ζ, therefore conditional enthalpy is not solved in the DCMC calculation. Modelling for the conditional scalar dissipation rates is introduced in the following sub-section.

The DCMC equations are implemented in an in-house Fortran code and solved by time marching to a steady state solution using the DVODE stiff ordinary differential equation solver [27]. The computation uses a structured Cartesian grid. In order to achieve grid-independent solutions, 101 uniformly-space grid points are used in the η and ζ directions, with the η grid clustered around the stoichiometric mixture fraction for non-premixed cases and is uniform for the stratified Bunsen flame case [180].

6.3 Fluid-age solution

The concept underlying the age-generated joint-pdf may be understood by first considering the established Lagrangian-flamelet approach [165] applied to autoigniting non-premixed systems illustrated in Fig. 6.5: As the initially-unburnt flamelet undergoes autoignition the progress variable evolves at a different rate at each value of mixture fraction, thereby providing a model for the dependence of progress variable on mixture fraction at each point in time. The progress variable-mixture fraction dependence reflects the reaction and scalar dissipation dynamics of the flamelet. The joint ξ-c distribution implied by the Lagrangian flamelet corresponds to a single flamelet residence time or

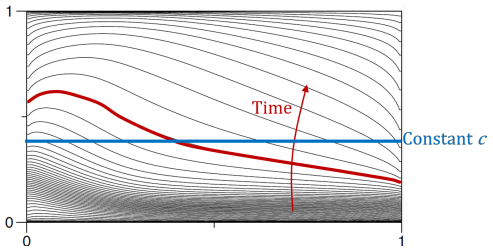

Figure 6.5: The progress variable in an unsteady flamelet solution for an autoigniting non-premixed flame at regular time intervals. A single-time solution is highlighted in red, and a constant c line corresponding to taking a delta-function for c is shown as a blue horizontal line.

Lagrangian flamelet *age* [200]. This contrasts with the unrealistic ξ-c distribution that would be given by taking a single value for c (i.e. the blue line in Fig. 6.5).

The Lagrangian-flamelet approach is not immediately applicable to partially-premixed combustion involving, for example, flame propagation. Instead, the age-generated joint-pdf approach is constructed using two-dimensional flamelet solutions or DCMC solutions in ξ-c space. Instead of tracking flamelet age in a Lagrangian manner, a fluid age variable is solved within the DCMC calculation. The fluid age is defined by the transport equation [65]

$$\frac{\partial a}{\partial t} + \mathbf{u}.\nabla a = \frac{1}{\rho}\nabla\left(\rho\mathcal{D}\nabla a\right) + 1. \tag{6.3}$$

While the DCMC solution for thermochemical state evolves towards a steady state if the dissipation rate models are constant, the conditionally-averaged age $Q_a = \langle a \mid \eta, \zeta \rangle$ given by solving Eq. 3.44 with $\omega_a = 1$ (as per the source term in Eq. 6.3) is not steady, since the combustion wave propagates through the age field of the underlying mixture. However, if the combustion wave itself is steady, the relative age field taken in a frame of reference attached to the steady-state flamelet, given by $Q_{\hat{a}} = Q_a - Q_a\left(\eta_{ref}, \zeta_{ref}\right)$, does evolve towards a steady state. Therefore the $Q_{\hat{a}}$ solution field is used as the basis for modelling the joint-pdf.

For a system with strictly zero reaction rate in the unburned mixture (as required in the classical description of a freely-propagating deflagration) the relative age value tends to inf at $\zeta = 0$ and +inf at chemical equilibrium, $\zeta = 1$. For an autoignitive system with non-zero reaction rate at $\zeta = 0$ the relative age remains finite at $\zeta = 0$. The numerically discretised DCMC equation for $Q_{\hat{a}}$ (Eq. 3.44) is solved at the ζ boundaries and zero-gradient boundary conditions are applied to $Q_{\hat{a}}$ at $\eta = 0$ and

1. While the mathematical solution for $Q_{\hat{a}}$ is indefinite at at least one ζ boundary, the discretised approximation to the equation, with appropriate modelling for $\langle N_c \mid \eta, \zeta \rangle$ and appropriate numerical discretisation of the diffusive transport at the boundary, remains finite and shows convergence (the relative age field over the majority of progress variable space is converged with a relatively course grid spacing (e.g. $\Delta\zeta \approx 0.01$), while the age gradients and boundary values move further from zero as the near-boundary grid spacing is reduced therefore the age iso-lines used to construct the age-generated pdf are not affected by incomplete resolution at $c \longrightarrow 0$ and $c \longrightarrow 1$). A one-sided second order approximation for the second derivative with respect to progress variable is employed at the ζ boundaries.

In this study, the model for $\langle N_c \mid \eta, \zeta \rangle$ is based on the combustion structure of a freely-propagating laminar flame. The evolution of progress variable c and age a in a laminar premixed flame is presented in Fig. 6.6. The first derivative of progress variable is illustrated by the red shade in the figure. In the age distribution it is assumed a constant density throughout the flame, therefore a constant slope for a and consequently a constant age dissipation rate N_a. Assuming that $N_{\xi a} = 0$, the progress variable dissipation rate can then be modelled in terms of age as

$$\langle N_c \mid \eta, \zeta \rangle = N_a \left(\frac{\partial Q_{\hat{a}}}{\partial \zeta} \right)^{-2} \tag{6.4}$$

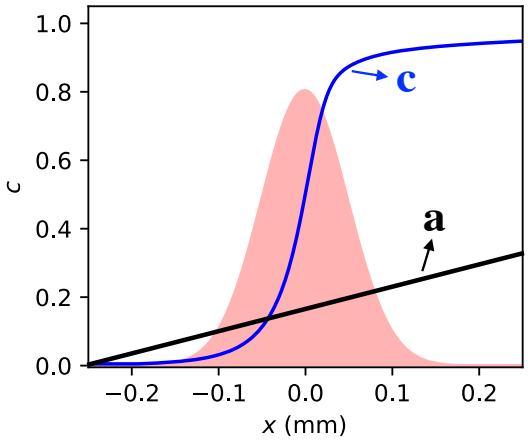

Figure 6.6: Structure of a laminar freely-propagating flame. Distribution of progress variable c; age a; and first derivative of progress variable in red.

Due to the finite difference approximations employed, $\partial Q_{\hat{a}}/\partial\zeta$ and hence $\langle N_c \mid \eta, \zeta \rangle$ are non-zero and finite at the ζ boundaries. The Modelling for the mixture fraction

dissipation is less critical and the simple Amplitude Mapping Closure [149] approach is adopted in each case.

The values N_a and $N_{\xi,0}$ are chosen in order to obtain $\langle N_c \mid \eta, \zeta \rangle$ and $\langle N_\xi \mid \eta, \zeta \rangle$ profiles approximately matching the peak conditionally-averaged scalar dissipation rates observed at the relevant time or cross-stream plane of the various DNS data sets. Results presented here employ a simple model for cross dissipation based on limiting possible scenarios for the alignment between mixture fraction and progress variable gradients: $\langle N_{\xi,c} \mid \eta, \zeta \rangle = 0$. More advanced specifications are possible for the conditional scalar dissipation rates. However the focus of the present Chapter is on demonstrating a new overall methodology for modelling joint-pdf shapes, rather than development of predictive conditional scalar dissipation rate modelling.

6.3.1 Age-generated joint-pdfs

The simplest age-generated joint-pdf assumes that the joint ξ-c pdf corresponds to a single $Q_{\hat{a}} = \hat{a}_{iso}$ iso-surface in the DCMC solution. Providing a value for the mean progress variable and a model for the ξ marginal pdf, the value of a_{iso} is determined iteratively from the relation

$$\tilde{c} = \int_0^1 \int_0^1 \zeta . \delta \left(Q_a - a_{iso} \right) \tilde{P}_\xi \left(\eta \right) d\eta . d\zeta . \tag{6.5}$$

Having determined $\hat{a}_{iso}$, mean reaction rates and other moments can be generated using

$$\tilde{P}_{\xi,c}(\eta, \zeta) = \delta \left(Q_{\hat{a}} - \hat{a}_{iso} \right) \tilde{P}_\xi . \tag{6.6}$$

Employing a β-function for the ξ marginal pdf, the age-generated joint-pdf requires a minimum input of only three moments: mean and variance of mixture fraction and mean progress variable.

6.4 Results

The age-generated joint-pdf is presented and predictions of the unconditional reaction rate given by Eq. 6.2 are compared to against those from the empirical ξ-c distribution, the delta-function progress variable distribution, and β-function marginal distribution.

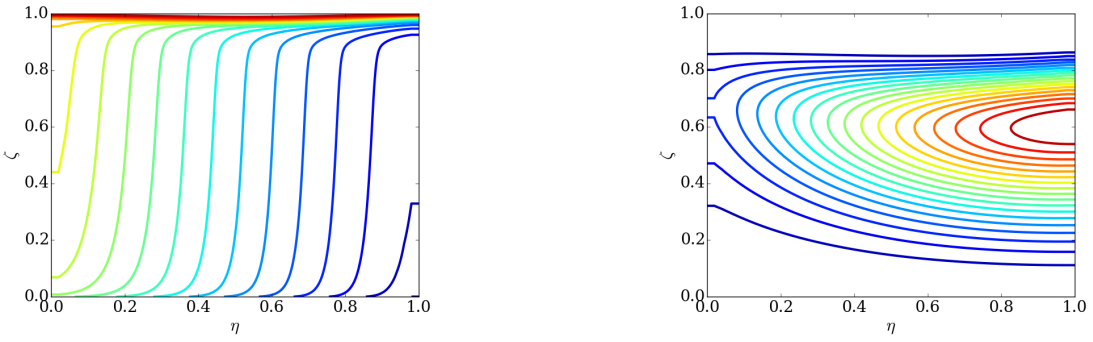

(a) (b)

Figure 6.7: Multi-dimensional flamelet solution for the stratified C4 conditions. (a) Q_a isolines; (b)$\langle N_c \mid \eta, \zeta \rangle$ given by Eq. 6.4.

The results indicate that the empirical ξ-c distributions in these diverse partially premixed turbulent flames evolve approximately in line with iso-contours of the relative age variable. While the β-function provides an acceptable model for the mixture fraction marginal distribution, it is a poor model for the range of different progress variable pdf shapes observed. The delta-function also gives a poor approximation to the progress variable marginal pdf. The implication is that the simple 3-parameter model for the joint pdf given by a presumed β-function pdf mapped onto a single value of conditional age provides an improved description of the joint-pdf compared to the 4-parameter independent β-function approach, or the 3-parameter β-mixture fraction and delta-progress variable approaches.

6.4.1 Stratified flame

Figure 6.7 illustrates the multi-dimentional flamelet solution of Q_a and N_c for the stratified flame, with N_c modelled using Eq. 6.4 . Typically, the maximum gradient of a premixed stoichiometric flame occurs at $c \approx 0.6$ ($\xi = 1.0$ in the figure) and moves to greater c values with smaller magnitude as the flame gets leaner, as is correctly captured by the new model for N_c.

The use of the age solution to model the joint-pdf is illustrated for two different points in the cross-stream y-direction, shown in Fig. 6.8. The empirical joint-pdf is illustrated by ξ-c scatter showing a definite statistical dependence between ξ and c that can be described as 's'-shaped, similar to the shapes predicted in Fig. 6.7a. The δ-pdf corresponding to the local mean progress variable is shown as a horizontal blue line. The

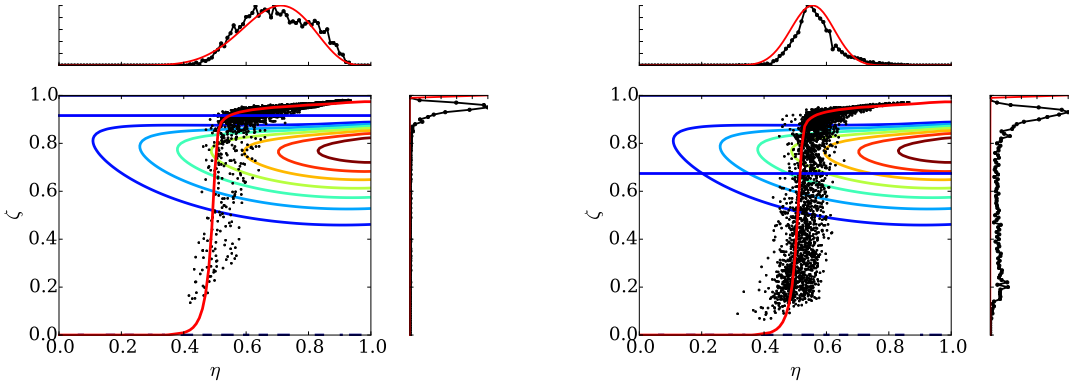

(a) iy = 81 (b) iy = 151

Figure 6.8: Stratified case C4 x=6H, y=0.5H. Main plot: joint ξ-c distribution (black scatter), progress variable reaction rate (coloured contours), mean progress variable (horizontal blue line), $Q_{\hat{a}} = \hat{a}_{iso}$ (red line). Sub-plots: empirical marginal pdfs (black curves) and fitted β distributions (red) for ξ (top) and c (right).

age-generated-pdf given by Eq. 6.6 is shown as a red curve. Marginal pdfs for mixture fraction and progress variable are also shown at the top and side of the plot. It is clear that the age-generated pdf captures the shape of the empirical pdf accurately, passing through the middle of the scatter. In contrast, the δ-pdf completely fails to describe the shape of the joint-distribution and instead attributes probability to regions of composition space that are not present in the DNS data.

The correct modelling of the DNS empirical distribution given by the age-generated approach is further demonstrated by the prediction of the mean progress variable reaction rate in Fig. 6.9, where the approximations for the c-pdf are compared with the empirical pdf obtained from the DNS. The age-based pdf clearly presents the closest agreement with the empirical-pdf.

6.4.2 Non-premixed temporal jet

The extinction and reignition case involves complex flame physics where partially-premixed flame propagation and/or non-premixed flames interact depending on the degree of extinction [116]. The results presented here correspond to two different times from Case 2 in Lignell et al. [116]: initially the percentage of the stoichiometric flame surface that is burning decreases due to localised extinction and at 0.11 ms the percentage of the stoichiometric isosurface that is burning drops below 50 %; the flame

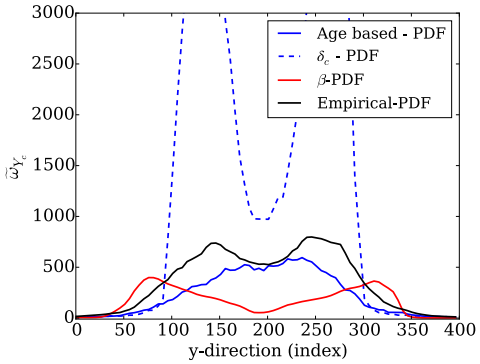

Figure 6.9: Stratified case $x = 6H$: prediction of mean progress variable reaction rate for various c-pdf models.

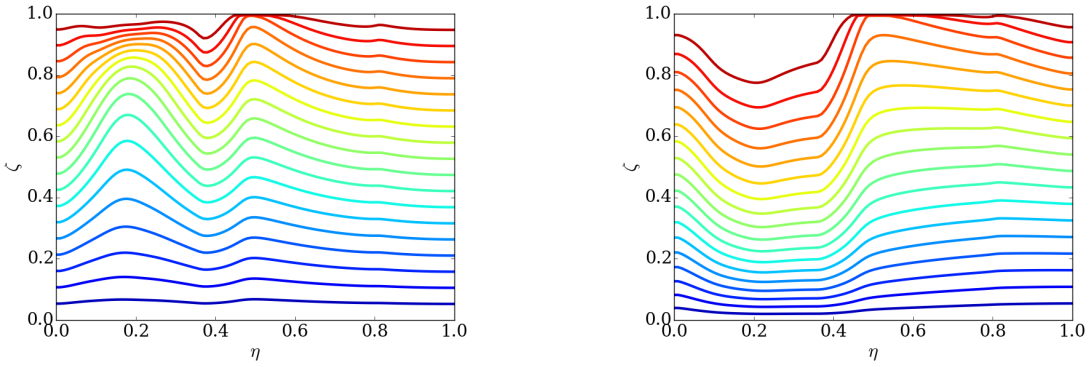

(a) t = 0.26 ms (reignition)

(b) t = 0.11 ms (extinction)

Figure 6.10: $\langle Q_a \mid \eta, \zeta \rangle$ multi-dimensional flamelet solution for the non-premixed temporal jet.

reaches the minimum burning rate of 34% of the stoichiometric surface area before recovering and passing through 50% again at 0.26 ms. The times 0.11 ms and 0.26 ms therefore are representative of the extinction and reignition processes respectively. At 0.11 ms the stoichiometric mixture experiences scalar dissipation rate above the critical extinction value, $\langle N_\xi \mid \eta = 0.5 \rangle_{ext} = 3587 s^{-1}$, whereas, as expected, the during reignition $\langle N_\xi \mid \eta = 0.5 \rangle < \langle N_\xi \mid \eta = 0.5 \rangle_{ext}$. The DCMC solutions were performed with $\langle N_\xi \mid \eta = 0.5 \rangle = 2 \langle N_\xi \mid \eta = 0.5 \rangle_{ext}$ and $\langle N_\xi \mid \eta = 0.5 \rangle = \langle N_\xi \mid \eta = 0.5 \rangle_{ext}/2$ in order to illustrate how extinction and reignition conditions respectively affect the shape of the solution for $Q_{\hat{a}}$. Figure 6.10 presents the conditional age distribution $\langle Q_a \mid \eta, \zeta \rangle$ for the two scalar dissipation rates used. The age contours for the extinction case exhibit a broadly 'v'-shaped dependence, since the initially burning mixture undergoes extinction first in the region of the stoichiometric mixture fraction (due to the high diffusion rates near to the reaction front).

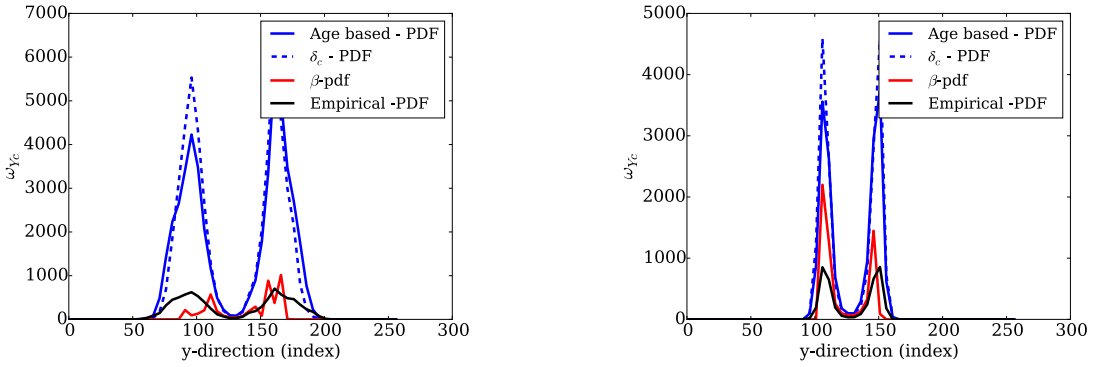

(a) t = 0.26 ms (reignition)

(b) t = 0.11 ms (extinction)

Figure 6.11: Prediction of mean progress variable reaction rate for various c-pdf models.

The prediction of the mean progress variable reaction rate presented in Fig. 6.11 shows a minor improvement of the age-based pdf compared to the delta function for c. However, the independent β-pdf for progress variable gives overall a better agreement with the empirical joint-pdf. Figure 6.12 shows that $\hat{a}_{iso}$ gives a good description of the DNS joint ξ-c distribution, nonetheless the assumption of a delta function for relative age $\delta\left(Q_{\hat{a}} - \hat{a}_{iso}\right)$ does not capture the large fluctuations around $\hat{a}_{iso}$.

6.4.3 Non-premixed autoignitive lifted flame

The ethylene slot jet presented in Ref. [247] corresponds to a lifted flame stabilised by autoignition at 5.8 jet widths (H) from the inlet, as illustrated in Fig. 6.1. The first ignition kernels occur on the lean side of the mixing layer at low scalar dissipation rate and are followed by a stable flame downstream. Lean mixtures present a positive correlation whereas rich mixtures have negative correlation and the stoichiometric mixture fraction, represented by the black solid line in figure, clearly separating the transition between negative to positive correlations. This correlation structure derives from the fact that, in this case, the progress variable increases fastest close to the stoichiometric composition, resulting in an 'n'-shaped dependence structure, as seen in Fig. 6.2.

The DCMC reference solutions were computed using cross-stream conditionally-averaged scalar dissipation rate amplitudes equal based on the DNS data at 6, 7 and 12H from the inlet.

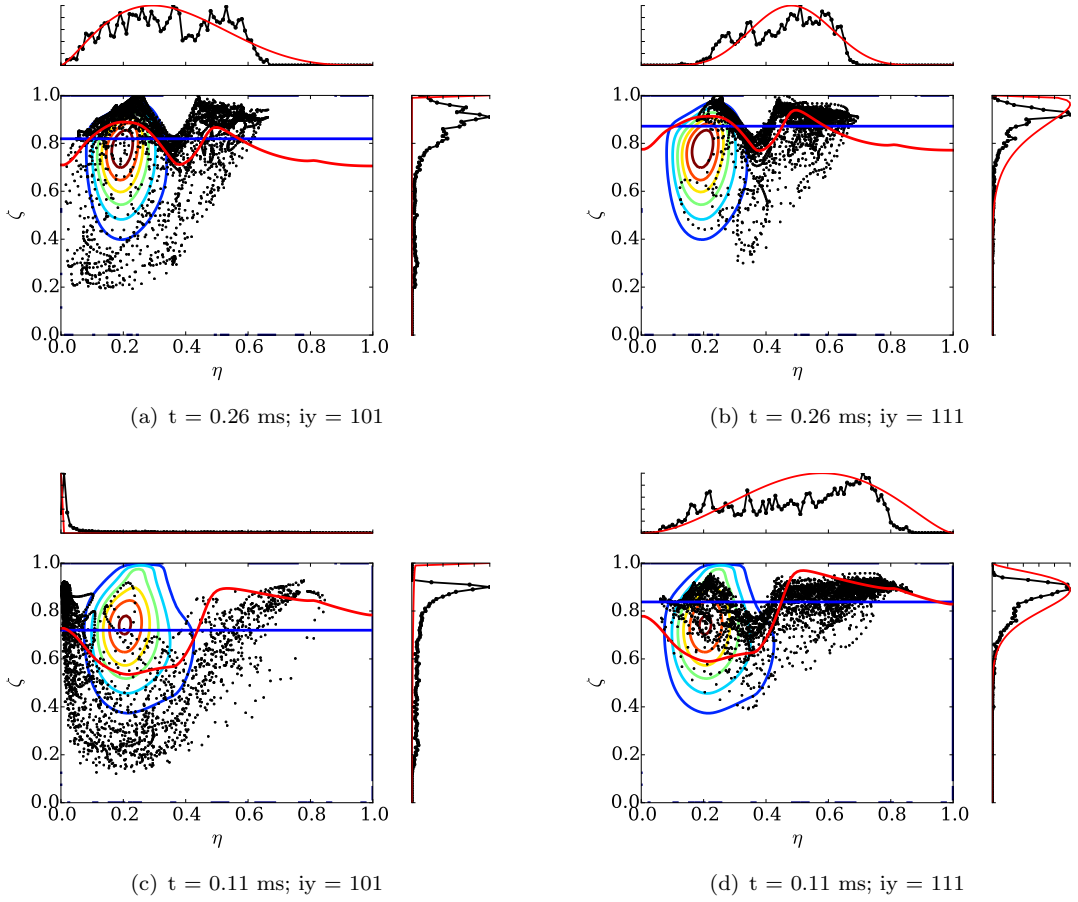

(a) t = 0.26 ms; iy = 101

(b) t = 0.26 ms; iy = 111

(c) t = 0.11 ms; iy = 101

(d) t = 0.11 ms; iy = 111

Figure 6.12: Non-premixed temporal jet. Main plot: joint ξ-c distribution (black scatter), progress variable reaction rate (coloured contours), mean progress variable (horizontal blue line), $Q_{\hat{a}} = \hat{a}_{iso}$ (red line). Sub-plots: empirical marginal pdfs (black curves) and fitted β distributions (red) for ξ (top) and c (right).

were approximated to be the same for the heights close to the stabilization point 6H and 7H. The third cross-plane 12H corresponds to a location far from the stabilization point where mixture fraction dissipation rates are lower, therefore the DCMC solution was obtained for lower mixture fraction scalar dissipation rate. The three modelling options for the conditional cross-dissipation are considered here: $\langle N_{\xi,c} \mid \eta, \zeta \rangle = [-1; 0; 1] s^{-1}$. Figure 6.13 presents the prediction of mean progress variable reaction rate for various c-pdf models and two different domain heights: 6H and 7H. The delta function for c and the age-based pdf computed with negative and zero cross-dissipation tend to over predict the reaction source term for both heights. A significant improvement on the predictions of reaction rate is observed for 6H (Fig. 6.15a) when the age-based pdf is obtained using positive cross-dissipation $\langle N_{\xi,c} \mid \eta, \zeta \rangle = 1$. The better agreement with the empirical pdf is in accordance with the positive ξ-c correlation for the lean mixture in

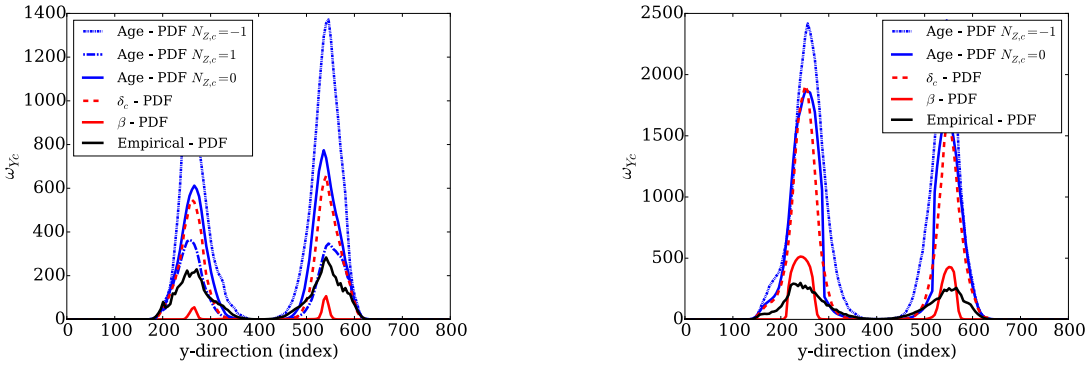

(a) 6H (b) 7H

Figure 6.13: Prediction of mean progress variable reaction rate for various c-pdf models at two different cross-planes.

the stabilization point presented in Fig. 6.1. The flamelet solution using positive cross-dissipation could not be used to obtain the mean progress variable reaction rate at 7H because the conditional Q_a distribution above $\widetilde{c} = 0.2$ did not have the shape similar to the joint ξ-c distribution from the DNS. Therefore, the independent β-pdf for c provides the best agreement with the empirical joint-pdf for the cross-plane at 7H. Figure 6.14 illustrates the computed age-based pdf using different cross-dissipation and the ξ-c joint distribution at iy = 251 (refer to Fig. 6.13) for the cross-plane 6H. The age-based pdf obtained using negative cross-dissipation is not able to capture the ξ-c distribution with reasonable degree of accuracy as for the zero cross-dissipation. However, the solution using $\langle N_{\xi,c} \mid \eta, \zeta \rangle = 0$ also over predicts the mean reaction rate due to a shift in the peak of Q_a to a region with large reaction rates.

Figure 6.15 shows that the age-based pdf provides an improved prediction of the mean reaction rate compared to the delta function for c for the cross-plane at 12H, however a poor prediction observed for all c-pdf models tested. At around iy = 151 (Fig. 6.15), the reaction rate is over predicted approximately by a factor of 3. Nonetheless, Fig. 6.16 shows that the age-based pdf provides a reasonable prediction of the ξ-c distribution up to $\xi \approx 0.3$ when it sharply drops to $c = 0$ and passes through the region with maximum progress variable reaction rate. Further investigation regarding the model for the conditional scalar dissipation rates is beneficial in order to improve the accuracy of the new approach for the statistically dependent c-pdf.

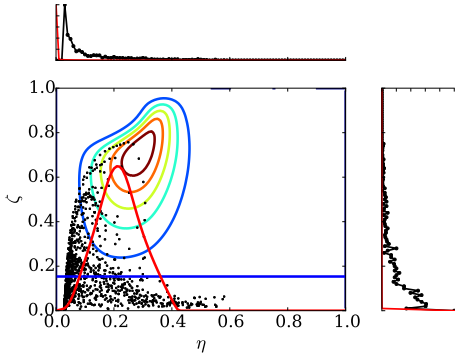

(a) $\langle N_{\xi,c} \mid \eta, \zeta \rangle = -1$

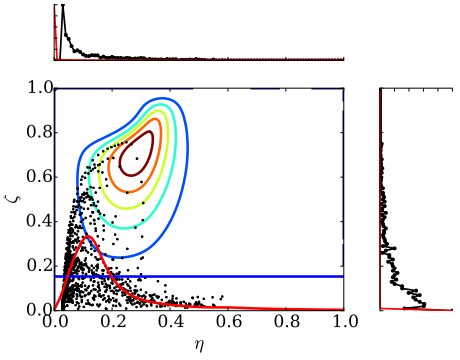

(b) $\langle N_{\xi,c} \mid \eta, \zeta \rangle = 0$

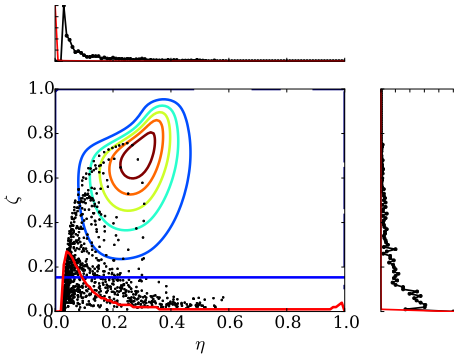

(c) $\langle N_{\xi,c} \mid \eta, \zeta \rangle = 1$

Figure 6.14: Non-premixed lifted flame at iy = 251. Main plot: joint ξ-c distribution (black scatter), progress variable reaction rate (coloured contours), mean progress variable (horizontal blue line), $Q_{\hat{a}} = \hat{a}_{iso}$ (red line). Sub-plots: empirical marginal pdfs (black curves) and fitted β distributions (red) for ξ (top) and c (right).

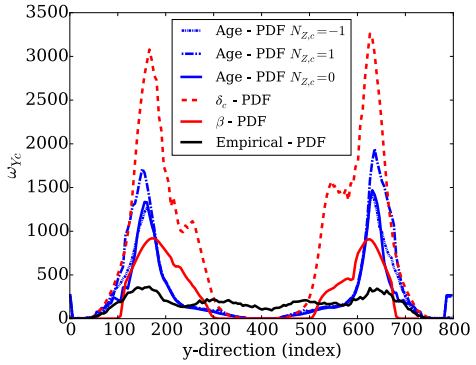

Figure 6.15: Prediction of mean progress variable reaction rate for various c-pdf models at two different cross-planes.

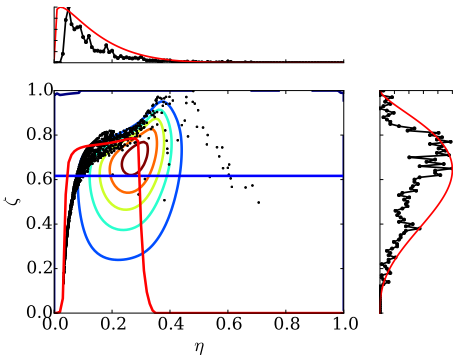

Figure 6.16: Non-premixed lifted flame at iy = 151 and 12H. Main plot: joint ξ-c distribution (black scatter), progress variable reaction rate (coloured contours), mean progress variable (horizontal blue line), $Q_{\hat{a}} = \hat{a}_{iso}$ (red line). Sub-plots: empirical marginal pdfs (black curves) and fitted β distributions (red) for ξ (top) and c (right).

6.5 Conclusion

Mixture fraction and progress variable are statistically-dependent across the spectrum of partially-premixed combustion modes. Qualitatively different 's'-, 'v'- and 'n'-shaped dependence structures appear due to the reaction-diffusion dynamics of the different combustion modes, and these dependence structures cannot be described by the Plackett family of copulas which can only model diagonal dependence structures. A new 'age-based' approach for modelling the joint-pdf is tested, using the DCMC solution to take account of the reaction-diffusion dynamics of the different flame types. A version of the approach that uses only three input moments is tested and compared with results based on the assumption that mixture fraction and scalar dissipation rate are statistically-independent.

While the β-function provides an acceptable model for the mixture fraction marginal distribution, it is not able to capture the range of different progress variable pdf shapes observed. Using the δ-function pdf for progress variable gives a poor approximation to the progress variable marginal pdf. The age-based approach correctly predicts the qualitatively-different dependence structures in each of the DNS cases considered, following the centroid of the DNS scatter across mixture fraction space. Further development of the age-based approach could be made in order to account for the scatter around the centroid, for example by taking a Gaussian or top-hat distribution for the age variable in order to also match the progress variable variance. Even with only three input moments, the age-based approach gives the best reaction rate predictions of any of the

joint-pdf models considered, however it is noted that a priori testing of models can be misleading, since the model for the moments (taken from the DNS) is not consistent with the reaction rate predictions (from the DCMC model and the modelled joint-pdf). Therefore a posteriori testing in LES or RANS is needed to confirm the validity of the age-based approach. However, correct prediction of the dependence structure across a wide range of combustion conditions suggests that the physical basis for the age-based approach is correct and that the improvement in predictions is achieved by considering the reaction-diffusion dynamics particular to each case. While the DCMC solution itself is relatively insensitive to the mixture fraction-progress variable cross dissipation, the predicted joint-pdf shows significant sensitivity to cross dissipation and further investigation of its modelling is recommended.

Chapter 7

Hybrid modelling of dual-fuel combustion

This chapter formulates and tests a hybrid model for dual-fuel combustion. The hybrid model combines Conditional Moment Closure (CMC) modelling, accounting for the autoignition of the n-heptane spray, with the G-equation model describing the subsequent flame propagation. The modelling is tested against previous measurements of dual-fuel methane/n-heptane combustion in a Rapid Compression-Expansion Machine experiment [193]. The CMC/G-equation approach for dual-fuel combustion was first proposed Schlatter [194], where the CMC model was used only to determine the ignition delay time and location. The new implementation, however couples the models to account for the heat release from both fuels and can be used for the full range of fuel substitution, from pure diesel to pure natural gas engines. The new laminar flame speed model developed in Chapter 4 was also implemented within the G-equation model.

7.1 Introduction

Development and validation of advanced simulation methods capable of describing the full range of phenomena in dual-fuel engines has been hindered by the limited availability of fundamental validation data for conditions relevant to pilot-ignited dual-fuel engine operation. A number of experimental studies in recent years focus on dual-fuel engine

performance and emissions [4, 5, 106], however it is difficult to extricate fundamental information about complex dual-fuel combustion processes from such investigations. However, a smaller number of experimental studies have provided more detailed information concerning dual fuel combustion physics, for example using pressure evolution analysis together with optical methods for detecting flame temperature and soot formation in a rapid compression machine (similar to the one described below) [115, 186], or using endoscopic techniques to acquire the luminosity of the combustion [35, 186]. The numerical developments in the present study are validated with respect to recent experimental work by Schlatter et al. [195] that investigated spray autoignition and combustion of an n-heptane pilot spray in a methane-containing atmosphere and the subsequent flame propagation into the premixed charge. The investigation measured high speed imaging of OH chemiluminescence, filtered OH and CH photomultiplier signals and pressure tracer for a wide range of premixed methane in the ambient air/methane mixture. The experiment performed by ETH Zurich uses a rapid compression expansion machine (RCEM) to mimic the engine compression and expansion strokes of a real engine. The RCEM apparatus, presented in Fig. 7.1, comprises an air-driven floating piston compressing a preheated and premixed methane-air charge in an 84mm bore cylinder. The piston has a disk-shaped bowl, with 52 mm diameter and 4 mm depth, with a 52 mm diameter fused silica window in the bowl. The cylinder head is flat and contains a 52 mm diameter sapphire window for optical access. The piston position is recorded with 0.05mm resolution at a frequency of 100 kHz. The piston position and the n-heptane mass flow rate measurements are used in the numerical simulation.

The gas was injected 1.2 s prior the Top Dead Centre in order to ensure a quiescent and homogeneous mixture. A solenoid common-rail diesel fuel injector equipped with a single hole, 136 μm orifice was used in the experiments. The injector was derived from a standard 7-hole injector by means of welding up six holes. The injection rates, hydraulic injection durations and total injected masses of the micro pilot spray were measured with a Bosch tube over 500 injections with a constant rail pressure of 400 bar. The injected mass was 1.36 mg (standard deviation of 0.04 mg), with a measured injection duration of 0.701 ms. The injected mass of n-heptane is kept fixed and the initial temperature, pressure and equivalence ratio of the premixed methane-air charge are varied. The in-cylinder pressure is recorded with a piezoelectric transducer and used along with the measured piston position to infer the apparent heat release rate. The benefits of such an

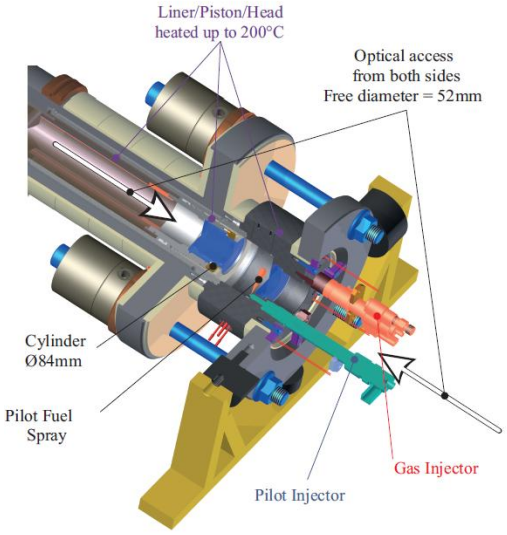

(a) Optical access and injectors position

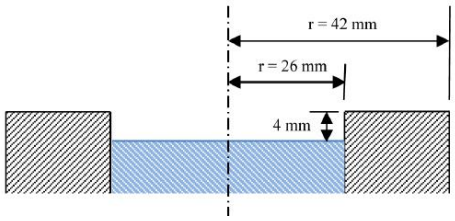

(b) Piston geometry

Figure 7.1: ETH Rapid Compression Machine [194].

experiment comparing to a real engine come from the fact that boundary conditions for the problem, such as cylinder wall temperature and thermochemical conditions of the mixture before combustion, are well defined and reproducible during different measurements. Real engines have a cycle-by-cycle variation of the flow field which is eliminated in the RCEM.

The authors measured five different conditions regarding the methane-air equivalence ratio and temperature at the Start Of Injection (SOI), as presented in Table 7.1. The n-heptane mass injected remained constant throughout the cases. The results for the OP2a and OP3b are selected to be presented in this chapter. The OP2a case has a very lean equivalence ratio close to the flammability limit threshold mentioned by [104], so after methane ignition the experimental heat released has a steady increase mainly driven by flame propagation. The OP3b experimental results show a greater heat released with a fast fuel consumption after the ignition of the premixed charge which can

be related to the autoignition of the premixed charge.

The objective of this chapter is to investigate the performance of a new approach for modelling pilot-ignited dual-fuel combustion systems, and to validate these developments by comparison with high-quality experimental measurements. N-heptane and methane are used as surrogates of diesel and natural gas, respectively. A state-of-art model for autoignition and diffusion flames, Conditional Moment Closure (CMC), is coupled with the level-set G-equation model to account for the flame propagation. The combustion models are coupled in such way, presented later, that the heat released comes from both fuels. The ignition delay time is determined by the turbulence-combustion interaction and the chemical scheme utilized which considers the gas fuel. The G-equation uses an advanced laminar flame speed model to account for mixture inhomogeneity and cool flame effects. Therefore, the new implementation should be able to capture the ignition delay time and heat released for the full range of fuel substitution.

Table 7.1: Operating conditions

Operating condition	OP2a	OP2b	OP2c	OP3a	OP3b
ϕ_{CH4}	0.44	0.57	0.65	0.46	0.60
T[K] at SOI	776			823	
P[bar] at SOI	17.8				

7.2 Formulation

7.2.1 Flow field solver

The flow field is simulated using the Reynolds Averaged Navier Stokes (RANS) equations and a Lagrangian spray model implemented in the Star-CD software [36]. The Star-CD software is a powerful CFD code which was used for engine calculations involving moving grids coupled with the CMC code [53, 240]. The effects of gas-phase turbulence are modelled by the RNG variant of the k–ϵ model [37]. This study focuses on the solution of an industry-like problem where the RANS approach is usually adopted. Spray processes are modelled using sub-models offered within STAR-CD and described in Ref. [37], including: STAR-CDs standard drag, heat and mass transfer correlations; the Reitz atomization model; the Reitz-Diwakar secondary breakup model [172]; the Bai

droplet interaction model; and the ORourke model for droplet-wall collisions. Droplet thermophysical properties (heat capacity, viscosity, latent heat, vapour pressure, density and surface tension) are modelled within STAR-CD as a function of temperature [37]. In order to account for cavitation effects, the nozzle contraction coefficient is adjusted to a value of 0.9 in order to give similar accuracy for pilot spray vapour penetration across all operating points, leading to a nominal orifice diameter of 122μm. The spray modelling is validated in Ref. [194] by comparison against spray penetration observations.

Due to the off-centre location of the pilot injector, a 180deg sector of the combustion chamber was modelled, as shown in Fig. 7.2 close to top dead centre (TDC) with the nozzle position and direction of the pilot injection indicated. The base resolution of the trimmed mesh is 1 mm, and the region surrounding the pilot nozzle and spray are refined with a characteristic cell dimension of 0.5mm, in order to ensure a ratio of cell size/nozzle diameter of 3.7, in accordance with good practice discussed in Refs.[166, 190]. The computational grid consists of 270,000 cells at the start of the simulation and 105,000 cells at TDC. Mesh motion is performed with experimentally-derived piston position files for each operating point, and all initial conditions were set according to the average data obtained from thermodynamic analysis of the respective operating points summarized in Table 7.1.

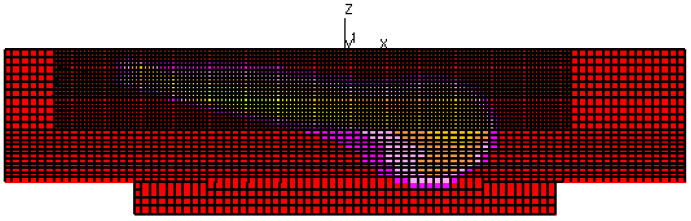

Figure 7.2: Three-dimensional grid in the section plane for a given time close to TDC with contours indicating the pilot injection

7.2.2 G-equation model

Combustion is modelled using the level-set or G-equation approach to describe premixed flame propagation [234]. Ignition of the premixed flame by the pilot spray is modelled using a separate combustion model based on Conditional Moment Closure, described below. The scalar variable G is a distance function from the instantaneous flame position.

The G-equation modelling for turbulent combustion employed in this study is based on the evolution of the modelled Favre mean and variance equations for G [37]:

$$\frac{\partial \bar{\rho}\widetilde{G}}{\partial t} + \frac{\partial \rho \widetilde{u_i}\widetilde{G}}{\partial x_i} = \bar{\rho} s_T \left| \frac{\partial \widetilde{G}}{\partial x_i} \right| \tag{7.1}$$

and

$$\frac{\partial \bar{\rho}\widetilde{G''}}{\partial t} + \frac{\partial \bar{\rho}\widetilde{u_j}\widetilde{G''}}{\partial x_i} - \bar{\rho} S_T \frac{\nabla \widetilde{G''} \nabla \widetilde{G}}{\left|\nabla \widetilde{G}\right|} = 2\frac{\mu_t}{Sc_{\widetilde{G}}} \left[\frac{\partial}{\widetilde{G}} \partial x_i \frac{\partial \widetilde{G}}{\partial x_i} \right] - C_s \bar{\rho} \frac{\epsilon}{k} \widetilde{G''} \tag{7.2}$$

where $c_s = 2$ [37]. S_T is the turbulent flame speed modelled a function of laminar flame properties and local turbulence properties. $Sc_{\widetilde{G}}$ is the turbulent Schmidt number for the moments of the G-field, and μ_T is the turbulent viscosity given by the k-ϵ model. All turbulent Schmidt numbers are set equal to 0.7.

A mean progress variable $\widetilde{c}$ is mapped to the simulated G-moment fields according to

$$\widetilde{C}_G = a_3 \left[erf\left(\frac{a_1 \widetilde{G}}{l_{F,T}} - a_2 \right) + 1 \right] \tag{7.3}$$

where (a_1, a_2, a_3) = (1.8,2.9,0.5) [37] and $l_{F,T}$ is the turbulent flame brush thickness, which is calculated as

$$l_{F,T} = \alpha \frac{\sqrt{\widetilde{G''^2}}}{\left|\nabla \widetilde{G}\right|} \tag{7.4}$$

where α is a model constant with the default value 1.0. The G-equation progress variable $\widetilde{C}_G$ is then used in the coupling as presented in the Section 7.2.8.

7.2.2.1 Turbulent flame speed correlations

Two models for the turbulent flame speed are compared in this study. In the first Simple model, the turbulent flame speed is modelled as a function of the turbulence intensity u' and the laminar flame speed s_l

$$s_T = s_l \left[1 + A \left(\frac{u'}{S_L} \right)^{5/6} \right] \tag{7.5}$$

where u' is calculated from the turbulent kinetic energy $u' = \left(\frac{2}{3}k\right)^{1/2}$ and A is a model constant equal to 0.5. A more sophisticated turbulent flame speed summarised by Peters

[160]

$$s_T = s_l + u'\{\frac{-a_4 b_3^2}{2b_1}Da + \left[\left(\frac{a_4 b_3^2}{2b_1}Da\right)^2 + a_4 b_3^2 Da\right]^{1/2}\} \tag{7.6}$$

where a_4, b_1, b_3 are constants equal to 0.78, 2.0, 1.78, respectively, and u' is the velocity fluctuation. The Damkohler number Da is

$$Da = \frac{s_l L_T}{u' L_F} \tag{7.7}$$

where L_F is the laminar flame thermal thickness estimated by

$$L_F = \frac{(\lambda/Cp)_0}{(\rho s_l)_u}. \tag{7.8}$$

The values for λ and C_p should be evaluated at the inner layer temperature, which according to Ref. [67] can be approximated for different hydrocarbon fuels and conditions by the temperature at the maximum temperature gradient. In the present formulation, ρ λ and C_p are obtained from Star-CD in each CFD cell. The integral scale L_T is computed from the k–ϵmodel [37]

$$L_T = \frac{C_\mu^{3/4}}{\kappa}\frac{k^{3/2}}{\epsilon} \tag{7.9}$$

where κ and C_μ are, respectively, the turbulent viscosity coefficient (0.09) and the von Karman constant (0.419).

7.2.2.2 Methane/n-heptane laminar flame speed model for dual-fuel engines

Two laminar flame speed models are compared in this study. The first is equivalent to the approach adopted by Singh et al. [203], which uses the laminar flame speed given by one-dimensional laminar flame speed calculations with detailed chemical kinetic models for methane fuel only. The second approach uses a new method presented in Chapter 4 that is also based on one-dimensional laminar flame speed calculation data, but which also accounts for the presence of the pilot-injected fuel and uses information about progress variable from the ignition model in order to account for the effects of pre-ignition chemical processes (such as cool flames). The approach given by Singh et al.[203] can be presented as a simplification of the more general model by Soriano

and Richardson [207]. Due to the greater number of independent variables in the more general model, the laminar flame speed is expressed as a correlation, rather than using the look up table approach in Ref. [203]. Since the agreement between the correlation and the database on which it is based is very close, the use of a correlation over a lookup table has negligible influence on simulation results and the correlation approach is preferred due to its slightly shorter computation time.

Due to the lack of experimental measurements for laminar flame speeds of methane/n-heptane mixtures at engine-relevant conditions, the laminar flame speed model is fitted to a database of numerical results for flame speed obtained with a 106 species skeletal mechanism [171] for engine-relevant combustion conditions (unburnt temperatures from 700 to 1000 K, pressure from 20-60 bar, and equivalence ratio from 0.5 to 1.3). It is also verified that the skeletal mechanism is in close agreement with its parent detailed mechanism, and that both mechanisms agree with experimental measurements for n-heptane ignition delays and methane-air flame speeds. First, correlations for the variation of flame speed with temperature, pressure, dilution and equivalence ratio are developed for methane-air and n-heptane-air flames independently. Then the blending rule given in Eq. 4.5 is used to model the flame speed of fuel blends. Last, Eq. 4.8 is applied in order to account for effects of the heat released, the fuel consumed, and the radicals produced by pre-ignition reactions.

The laminar flame speed dependence on equivalence ratio for each individual fuel at a reference unburnt temperature $T_{u,ref}$ and pressure p_{ref} is modelled with a four-parameter Gaussian function

$$s_{r,ref} = A_1 \phi_{tot}^{-A_2} \exp\left(-A_3 \left(\phi_{tot} - A_4\right)^2\right). \tag{7.10}$$

$A = [A_1, A_2, A_3, A_4]$ is a set of fitted coefficients for a particular fuel. At $T_{u,ref} = 850$ K and $p_{ref} = 40$ bar it is obtained $A_{CH4} = 11500, -5.44, 1.20, -1.04$ abd $A_{C7H16} = 344000, -4.80, 0.628, -2.56$.

Metghalchi and Keck [142] provide the following empirical model for the dependence of flame speed on the unburnt temperature , pressure , equivalence ratio and the mass fraction of diluents,

$$s_{r,fuel} = s_{r,ref} \left(\frac{T_u}{T_{u,ref}}\right)^{\alpha} \left(\frac{p}{p_{ref}}\right)^{\beta} \gamma. \tag{7.11}$$

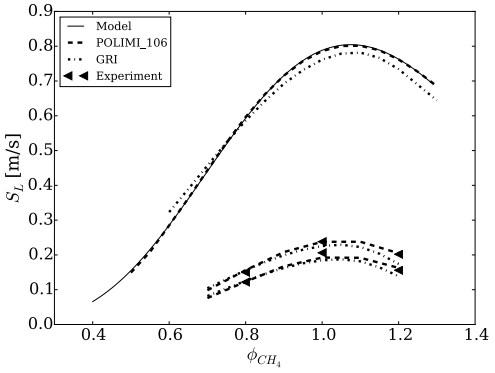

Figure 7.3: Laminar flame speed prediction from POLIMI_106 [171], GRI 3.0[206] and the flame speed correlation for 40 bar and 850 K (upper curve) and comparison against experimental data [69] at 10 bar and 360 K and 400 K (lower two curves).

α, β and γ are model parameters given by expressions of the form:

$$\begin{aligned} \alpha &= B_1 - B_2\,(\phi_{tot} - 1) \\ \beta &= B_3 - B_4\,(\phi_{tot} - 1) \\ \gamma &= 1 - B_5\xi \end{aligned} \tag{7.12}$$

in which $B_{fuel} = B_1, B_2, B_3, B_4, B_5$ is a set of fitted constants and ξ is the mass fraction of diluent, such as recirculated combustion products. For methane and n-heptane it is obtained, respectively, $B_{CH4} = 3.04, 0.70, 0.40, 0.10, 2.49$ and $B_{C7H16} = 2.79, -0.05, 0.26, 0.02, 3.02$ by least-squares fitting to the laminar flame speed database.

The first approach for modelling the flame speed, analogous to Singh et al. [203], lumps the methane and n-heptane fuels together into a single equivalence ratio and uses to obtain a prediction of laminar flame speed. Figure 7.3 shows the close agreement between this laminar flame speed correlation and the flame speed data on which the correlation is based, at 850K and 40 bar. The predictions of the GRI 3.0 [206] detailed mechanism for natural gas/air combustion are also presented, demonstrating the good agreement given by the POLIMI_106 [171] skeletal n-heptane scheme at 850 K/40 bar and also considering experimental data for 360 K and 400 K at 10 bar [69].

The second approach for modelling the flame speed was developed in Chapter 4, employing Eqs. 4.5 and 4.8 in order to account for fuel blending and pre-ignition chemistry. The new model was validated for a range of fuel blends adequately capturing the effects of pre-ignition chemistry on flame speed across the full range of conditions considered.

Figure 4.8 presents the model prediction of laminar flame speed and the solution obtained with POLIMI_106 for stoichiometric mixtures of methane/n-heptane approaching the ignition delay time.

7.2.3 Conditional Moment Closure Ignition Model

Pilot spray ignition is modelled by a two-dimensional single Conditional Moment Closure (CMC) model. According to Ref. [99], the conditional averages have a weak dependence of the cross-stream direction and the third dimension can be neglected. Tests using 2D-CMC and 3D-CMC in diesel engines have shown no difference in terms of pressure trace [53]. The CMC approach presented here considers mixing between two streams: premixed methane-air, corresponding to mixture fraction $\xi = 0$; and pure n-heptane corresponding to $\xi = 1$. The conditional mass fractions are initialised assuming linear mixing between the streams, whereas the temperature is obtained from linear mixing of enthalpy. The initial temperatures at the boundaries $\xi = 1$ and $\xi = 0$ are, respectively, 363 K and the mean temperature of the cylinder. The CMC formulation and implementation adopted are based on the work of Wright et al. [237]. Essential details of the CMC implementation are presented here and the reader is referred to Ref. [240] for further information.

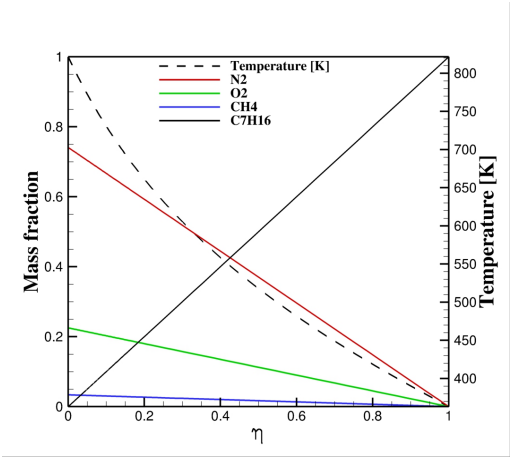

Figure 7.4: Initial profiles in conditional space.

The CMC approach assumes that the thermochemical state in the turbulent flow can be represented adequately by conditional averages –in this study, conditional on the mixture fraction of n-heptane. Following previous CMC compression-ignition engine studies

by Wright et al. [239], radiation, droplet evaporation and wall heat transfer effects are neglected in this formulation, however models for these effects are available, for example from Borghesi et al. [22]. Radiation effects are important in cases with large soot production, which is small in dual-fuel engines. The droplet evaporation is neglected in the CMC equations and mixture fraction variance equation because the liquid fuel evaporates earlier than then start of autoignition due to the increase in ignition delay time with the methane addition, as mentioned in [55].

7.2.4 Numerical implementation of CMC

The CMC equations are discretized with finite difference, using second order central differences for diffusive terms and first order upwind differencing for convective terms. The complex chemistry involves reactions with different timescales spanning many orders of magnitude. The system of equations are integrated with the stiff implicit solver VODPK [27, 28, 31]. It has been successfully used for CMC calculations of autoigniting flames as shown in [53, 237, 239, 240]. However, VODPK has a considerable increase in computational time for large number of ODEs of equations which is overcome by using fractional steps.

The solution of the system of equations is obtained with the Operator Splitting method (OS) in order to reduce the computational time. The method computes separately the transport terms in physical space, reaction source term and diffusion in conditional space. In this implementation, Strang splitting is employed, involving the following five

substeps,

$$
\begin{aligned}
1: \frac{\partial Q_k}{\partial t} &= \langle u_i|\eta\rangle \frac{\partial Q_k}{\partial x_i} + \frac{1}{\langle\rho\rangle P(\eta)} \frac{\partial}{\partial x_i}\left(\left\langle u_i'' Y_k''|\eta\right\rangle \langle\rho\rangle P(\eta)\right) \\
& \quad t \in [t_0, t_0 + \alpha_{xyz}\Delta t] \\
2: \frac{\partial Q_k}{\partial t} &= \frac{\langle\chi_\xi|\eta\rangle}{2} \frac{\partial^2 Q_k}{\partial \eta^2} \\
& \quad t \in \left[t_0 + \Delta t \frac{n-1}{n_{tot}}, t_0 + \Delta t \frac{n-1+\alpha_\eta}{n_{tot}}\right] \\
3: \frac{\partial Q_k}{\partial t} &= \frac{\langle\dot{\omega}_k|\eta\rangle}{\langle\rho|\eta\rangle} \\
& \quad t \in \left[t_0 + \Delta t \frac{n-1}{n_{tot}}, t_0 + \Delta t \frac{n-1+\alpha_\eta}{n_{tot}}\right] \\
4: \frac{\partial Q_k}{\partial t} &= \frac{\langle\chi_\xi|\eta\rangle}{2} \frac{\partial^2 Q_k}{\partial \eta^2} \\
& \quad t \in \left[t_0 + \Delta t \frac{n-1+\alpha_\eta}{n_{tot}}, t_0 + \Delta t \frac{n}{n_{tot}}\right] \\
5: \frac{\partial Q_k}{\partial t} &= \langle u_i|\eta\rangle \frac{\partial Q_k}{\partial x_i} + \frac{1}{\langle\rho\rangle P(\eta)} \frac{\partial}{\partial x_i}\left(\left\langle u_i'' Y_k''|\eta\right\rangle \langle\rho\rangle P(\eta)\right) \\
& \quad t \in [t_0 + \alpha_{xyz}\Delta t, t_0 + \Delta t]\,,
\end{aligned}
\tag{7.13}
$$

where n and n_{tot} correspond respectively to the number of internal steps between diffusion and reaction in conditional space. Δt is the CMC time-step which can be less or equal to the CFD time-step. The coefficient α_{xyz} defines how much the transport in physical space is computed prior to the conditional space calculation. Similarly, α_η weights how much of the diffusion term is solved before the reaction rate. Both coefficients range from 0 to 1 and are set to be 0.5. The advantage of the Operator Splitting is the reduction of the ODE system size and memory requirements. The transport terms of Eq. 7.13 are computed with the non-stiff version of VODPK. The chemical source term in Eq. 7.13 is the most expensive term to be evaluated, and since it is computed alone in this OS technique, a look-up table could be used to speed up the solution. The time-step of fractional stepping must be kept small to avoid errors.

The accuracy of the OS method was assessed in Ref. [237] for a high-pressure autoignition n-heptane spray. The authors tested two different solver: VODPK, described earlier, and CHEMEQ2. The results were compared with the solution from the Method of Lines. The temperature profile in conditional space presented a good agreement during ignition for the different solvers and time-steps used, as seen in Fig.7.5. Small deviations can be observed for the OH mass fraction profile, however considering the CPU time, Fig. 7.6

shows gains of about one order of magnitude compared to the Method of Lines.

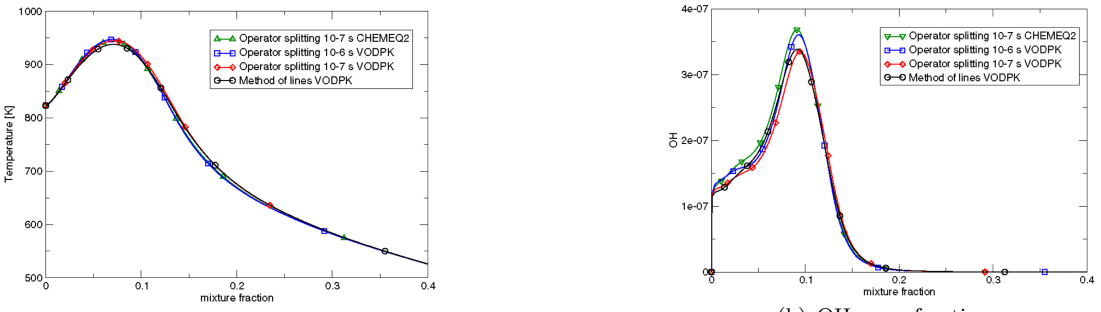

(a) Temperature

(b) OH mass fraction

Figure 7.5: Profiles in mixture fraction space during ignition using different solution methods and timesteps as per the legend [237]

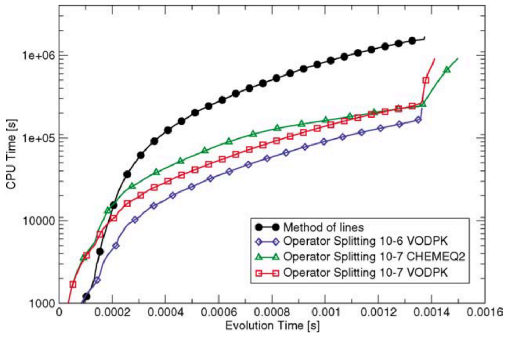

Figure 7.6: Comparison of CPU time using different solution methods [237].

Noting that conditional moments show weak spatial variation compared to unconditional moments, the spatial CMC grid is less refined than the CFD grid and, following several previous studies involving spray auto ignition [19, 20, 22, 239, 240], the conditional statistics are assumed to be homogeneous in the y-direction normal to the injector centreline, according to the coordinate system shown in Fig. 7.2. The Cartesian CMC grid has two spatial dimensions, with 30 cells evenly spaced in the cross-section of the jet, x-direction, and 13 cells in the direction of the cylinder axis which change the size in accordance with the moving CFD grid [51]. The two-dimensional spatial discretization of the conditional variables was already performed for spray autoignition in Refs. [22, 29, 52, 53, 146, 210, 224]

7.2.5 CMC sub-models

The local rate of change of pressure is obtained from the CFD solution. The conditional turbulent fluxes of species mass fractions $\langle u_i'' Y_\alpha'' \rangle$ and temperature $\langle u_i'' T'' \rangle$ are closed assuming gradient transport and employing the unconditional turbulent diffusivity μ_T / Sc_ξ,

$$\left\langle u_i'' Y_k'' | \eta \right\rangle = -D_t \nabla Q_i. \tag{7.14}$$

The conditional velocity is approximated with a linear expression [99] and has an additional term to accounts for the moving grid

$$\langle u_i | \eta \rangle = \widetilde{u}_i + \widetilde{u}_{irel} + \frac{\widetilde{u_i'' \xi''}}{\widetilde{\xi''^2}} \left(\eta - \widetilde{\xi} \right) \tag{7.15}$$

where $\widetilde{u}_{irel}$ is the relative velocity of the grid computed considering different iterations i as $x_p^i - x_p^{i-1} / \Delta T_{CFD}$ [53]. the term $\widetilde{u_i'' \xi''}$ is modelled as an unconditional scalar flux: $\widetilde{u_i'' \xi''} = -D_t \nabla \widetilde{\xi}$. D_t corresponds to the turbulent diffusivity. The conditionally-averaged reaction rates are closed at first order as a function of the conditionally averaged thermochemical state. Local pressure fluctuations are neglected.

The conditional scalar dissipation rate in each CFD cell $\langle N | \eta \rangle_{CFD}$ is modelled using the amplitude mapping closure [149]

$$\langle N | \eta \rangle_{CFD} = N_0 G(\eta) \tag{7.16}$$

where $G(\eta)$ is a bell-shaped function with unity amplitude,

$$G(\eta) = exp\left(-2 \left[erf^{-1}(2\eta - 1) \right]^2 \right), \tag{7.17}$$

and the amplitude of the conditional scalar dissipation rate profile is obtained from the unconditional scalar dissipation rate and the mixture fraction PDF modelled based on the CFD solution,

$$N_0 = \frac{\tilde{\chi}}{2 \int_0^1 G(\eta) \tilde{P}(\eta) d\eta} \tag{7.18}$$

where $\tilde{\chi}$ is computed from the RANS solution variables,

$$\tilde{\chi} = c_{\chi} \frac{\widetilde{\epsilon}}{\widetilde{k}} \widetilde{\xi''^2}. \tag{7.19}$$

c_{χ} is a constant set equal to 2 according to Ref. [237]. The Favre probability density function for the mixture fraction, $\tilde{P}(\eta)$, is modelled by a beta-function, using the Favre mean and variance of mixture fraction in each CFD cell given by Eqs. 8.1 and 8.2. The CFD and CMC grids are not necessarily the same, and a pdf-weighted averaging procedure is used to obtain the conditional scalar dissipation rate for each CMC cell,

$$\langle N|\eta\rangle = \frac{\sum \left(\bar{\rho}\tilde{P}(\eta)\,\langle N|\eta\rangle_{CFD}\,V\right)}{\sum \left(\bar{\rho}\tilde{P}(\eta)V\right)} \tag{7.20}$$

where the summation is over all of the CFD cells contained within that CMC cell and V is the volume of the respective CFD cells.

7.2.6 Ignition chemistry

The 44-species skeletal n-heptane mechanism by Liu et al. [121] is used in the ignition model. As shown on Section 4.3.1, the Liu *et al.* mechanism provides predictions in reasonable agreement with more detailed schemes concerning ignition delay times of n-heptane/methane blends. The fact that it performs less well in relation to flame propagation through n-heptane/methane blends is not a concern in this instance since the CMC model is only used for the ignition prediction and flame speeds are based on empirical formulae, rather than depending on the kinetic mechanism used for the CMC. However, the over prediction of flame speed seen in Fig. 4.6 is usually related to an over prediction of the burnt temperature which can have an effect on heat release rate. The thermodynamic state is modelled using the ideal gas equation and temperature-dependent specific heats in accordance with Liu et al. [121].

7.2.7 Ignition criteria

The hybrid modelling approach requires an ignition criterion in order to determine where and when to initiate the flame propagation process. Ignition in the CMC solution is used

to initiate burning locally in the G-equation model when the unconditional average state predicted by the CMC exceeds a threshold criterion. Two ignition criteria are compared in this study. The first uses a temperature-based criterion, similar to the approach in Ref. [203], and the second uses a criterion based on the hydroxyl (OH) radical mass fraction. Ref. [55] suggests that OH mass fraction provides an effective indication of ignition and is used for this purpose in Ref. [194]. When the unconditional average of either temperature or OH mass fraction obtained in the CMC solution passes the threshold of 1200 K for temperature or $4 \cdot 10^{-04}$ for OH mass fraction in a CFD cell, that cell is considered to have ignited, and a burnt condition is imposed in the G-equation solution for that cell. The predictions of the initial ignition timing are found to be insensitive to the value chosen for the OH and temperature threshold, likely because thermal runaway occurs rapidly following the start of high-temperature ignition, however the spatial distribution of the ignition region is affected, warranting further investigation.

Temperature and hydroxyl radical provide different measures of ignition progress in a non-premixed fuel-air flow. This difference is illustrated by performing stand-alone ignition simulations using the CMC model, keeping the pressure and scalar dissipation constant. The fuel temperature is 373 K, the initial temperature of the $\phi = 0.44$ methane-air mixture in the oxidizer stream is 850 K, and the amplitude of the conditional scalar dissipation rate used in the AMC closure is 10 s^{-1}. Figure 7.2.8 presents the conditional average temperature and OH mass fraction evolution in mixture fraction space with the respective threshold values indicated by dashed lines. The conditional average temperature passes the threshold value at 1.46 ms, whereas the conditional average OH mass fraction passes its threshold at 1.51 ms. The time taken for the unconditional average mass fraction or temperature in the CFD to pass the threshold condition is generally longer than the time taken for the unconditional values to pass the threshold, however Figure 7.2.8 illustrates differences in the timing and overall evolution of the respective properties. Although the time at which the threshold is first passed by the temperature is only marginally shorter than for OH, the rate of spread through mixture fraction space is substantially faster for temperature, which can be expected to influence which regions of the engine get ignited. The CMC ignition model provides mixture fraction-dependent information about the evolution of the ignition process, and this information could be used to develop more advanced ignition criteria if necessary.

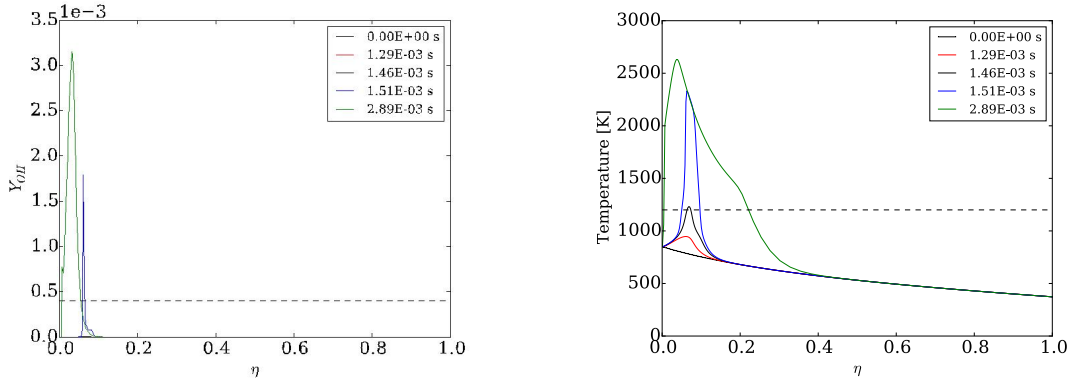

Figure 7.7: Evolution in mixture fraction space of conditional average (a) OH mass fraction; (b) temperature.

7.2.8 Model coupling

The composition used in the CFD simulation is based on a progress variable $\widetilde{C}_{max}$, taken as the greater of the two progress variables from either the CMC or G-equation solutions. The CMC progress variable $\widetilde{C}_{CMC}$ is based on temperature, whereas the mean G-eq progress variable $\widetilde{C}_G$ is obtained by solution of Eq. 7.1,

$$\widetilde{C}_{max} = max|\widetilde{C}_{CMC}, \widetilde{C}_G|. \tag{7.21}$$

The unconditional mean composition in each CFD cell is computed by weighting the burnt and unburnt unconditional mean compositions considering $\widetilde{C}_{max}$,

$$\widetilde{Y}_i = \left(1 - \widetilde{C}_{max}\right) \widetilde{Y}_{i,u} + \widetilde{C}_{max} \widetilde{Y}_{i,b}. \tag{7.22}$$

The unburnt $\widetilde{Y}_{i,u}$, burnt $\widetilde{Y}_{i,b}$ and $\widetilde{C}_{max}$ are obtained by integration of the conditional quantities over the PDF, as presented in Eq. 7.23 for a generic scalar θ.

$$\widetilde{\theta} = \int_0^1 \langle \theta|\eta \rangle \, \widetilde{P}(\eta) d\eta \tag{7.23}$$

The conditional unburnt composition remains constant over the simulation and corresponds to the initial condition. The conditional burnt composition is obtained from an equilibrium solver and updated every time step due to the pressure change caused by the piston motion and combustion. The unconditional average temperature used in the

CFD solution is computed by Star-CD considering the enthalpy of the mixture and the composition given by Eq. 7.23. The coupling scheme ignites the G-equation solution based on the evolution of the CMC solution, and the CMC solution in turn responds to the pressure rise caused by the flame propagation and heat release predicted using the G-equation model.

7.3 Assessment of numerical accuracy

This section describes a grid convergence study for the mixture fraction space grid in the CMC. A series of cases with different time-steps and grid spacing were tested in a standalone version of the CMC code with the following conditions: 42bar; T_{Fu} = 373K; T_{ox} = 1000K; $\phi_{ox,CH4} = 0.6$. $\xi = 1$ corresponds pure n-heptane and $\xi = 0$ is the methane-air mixture with the specified equivalence ratio. The standalone code computes only the terms which are solved in conditional space

$$\frac{\partial Q_k}{\partial t} = \frac{\langle \chi_\xi | \eta \rangle}{2} \frac{\partial^2 Q_k}{\partial \eta^2} + \frac{\dot{\omega}_k}{\rho}, \tag{7.24}$$

keeping the scalar dissipation rate $\langle \chi_\xi | \eta \rangle$ constant.

The solution of Eq. 7.24 is obtained by the operator splitting method described previously. Tight residual tolerances are used in VODPK for all terms: 1.0×10^{-14} for the absolute residual and 1.0×10^{-6} for the relative tolerance.

The reactions are computed with a smaller version of the 44-species skeletal mechanism, the reduced 18-species Liu et al. [121]. Both chemical schemes present similar results of ignition delay time under high pressure and temperature [121], and have already been applied in CFD of diesel engines conditions [17, 18, 51]. It is assumed that for the numerical accuracy study the 44-species and the 18-species chemistries will behave similarly, leading to the same grid requirements.

The conditional space is discretized with a non-equally spaced grid refined around the stoichiometric mixture fraction ξ_{stoich}, and $\xi = 0$ and $\xi = 1$, where $\Delta\xi = 0.0001$. For the conditions used in this test and using Eq. 3.28, the stoichiometric mixture fraction is: $\xi_{stoich} = 0.00251$. According to Ref. [55], the most reactive mixture fraction ξ_{MR} is around 0.18, using the same chemical mechanism and similar conditions to those used in this section. This value of ξ_{MR} is far from the refined stoichiometric region and the

solution may be deteriorated during the early stages of ignition. A different refinement location of $\xi_{stoich} = 0.0603$ was also tested in order to focus refinement closer to the location of the most-reactive mixture fraction.

7.3.0.1 Reference solutions

The effect of the scalar dissipation rate $\langle\chi_\xi|\eta\rangle$ on ignition delay time τ is studied in order to determine the critical value for ignition. The diffusion and reaction terms have opposite effects on the solution, more reactive fuels need more diffusion to prevent ignition. In other words, the chemical time scale needs to the smaller than the diffusion time scale for the mixture to ignite. The methane addition increases τ and may decrease the maximum value of dissipation for which ignition can occur $\langle\chi_\xi|\eta\rangle_{ign}$. Figure 7.8 presents τ sensitivity to the scalar dissipation rate sampled at the ξ_{stoich} computed with the mass fraction definition. The solution is obtained with a refined non-equally spaced grid with 301 points and OS time-step of $1.0 \cdot 10^{-7}$ s. Wright et al. [239] presented an exponential increase in τ with $\langle\chi_\xi|\eta\rangle$ until a certain level where ignition can no longer occur. The presence of fuel in the oxidizer changes the behaviour of ignition delay time for high scalar dissipation rates. The exponential increase is observed, however further increase in scalar dissipation rate does not prevent ignition. In fact, the conditional dissipation rate tends to zero at $\eta \to 0$, so ignition always occurs in the oxidizer boundary. The plateau after $\langle\chi_\xi|\eta_{stoich}\rangle > 100s^{-1}$ corresponds to the methane/air ignition delay time. The maximum scalar dissipation rate where autoignition occurs in a nonpremixed mode $\langle\chi_\xi|\eta\rangle_{ign}$ is defined as the value which ignition delay time tends to infinity. Since τ never goes to infinity, it is considered the value where $(d\tau/d\chi_{\xi,stoich})$ is maximum. For the conditions tested, $\langle\chi_\xi|\eta_{stoich}\rangle_{ign}$ is 21.35.

The numerical accuracy is assessed by considering first the time and η-space location that first reaches 1500 K. This evolution is expected to be more sensitive to the choice of time-step, and to become independent of grid resolution as $\langle\chi_\xi|\eta\rangle \to 0$. In order to assess also the influence of $\Delta\eta$ on the transport in η-space, the evolution of the solution at $\xi_{stoich} - \xi_{stoich}/2$ and $\xi_{stoich} + \xi_{stoich}/2$ are also investigated.

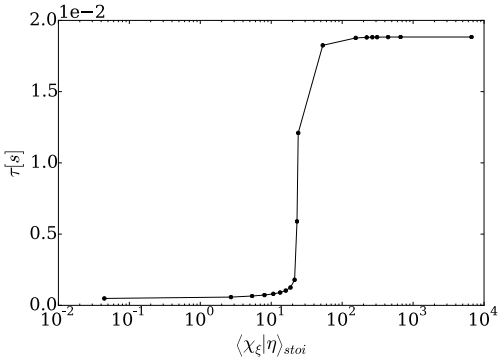

Figure 7.8: Scalar dissipation rate effect on ignition delay time.

7.3.0.2 Time step sensitivity

Different time-steps are tested with a constant scalar dissipation rate $\langle\chi_\xi|\eta_{stoich}\rangle$ / $\langle\chi_\xi|\eta_{stoich}\rangle_{ign}$ = 2.0×10^{-2} and a fixed mixture fraction grid. The ignition process has a small dependence on the time-step, as seen in Fig. 7.9. The other two points will follow the same trend with a small deviation for $\Delta t = 10^{-5}$s. The solution obtained with $\Delta t = 1.0 \cdot 10^{-6}$s is a good balance between accuracy and computational time and will be used in the spatial discretization study.

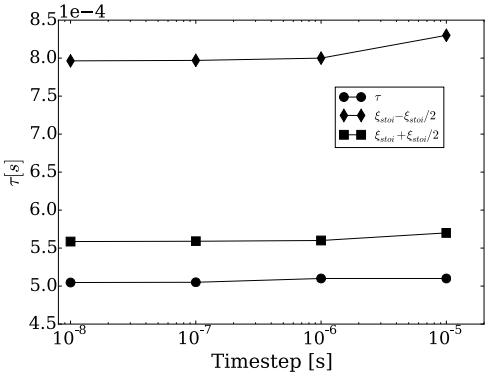

Figure 7.9: Sensitivity of ignition delay to OS time step for the overall ignition delay τ, and the ignition delays at $\eta = \xi_{stoich}/2$ and $\eta = 3\xi_{stoich}/2$.

7.3.0.3 Mixture fraction grid-dependence

The discretization of the η-space was tested for different values of scalar dissipation rate. Figure 7.10 presents the results for the two extreme cases, low and high $\langle\chi_\xi|\eta_{stoich}\rangle$. The lines in the figure correspond to the grid clustered around the stoichiometric mixture

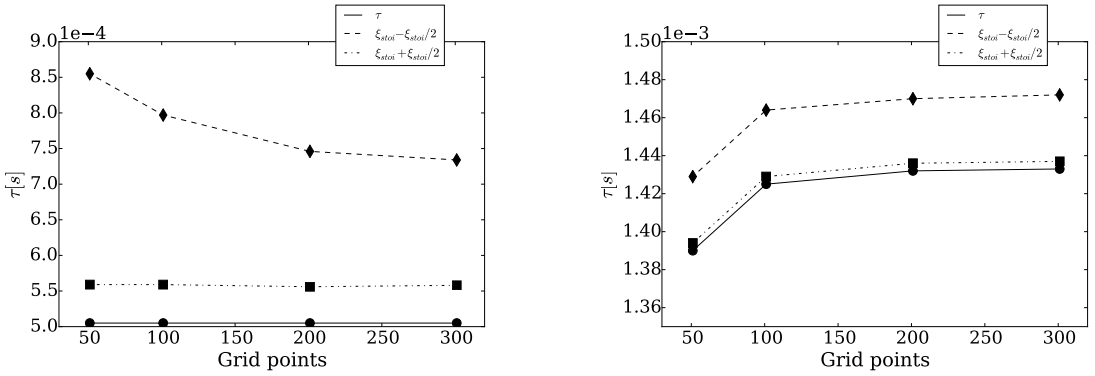

(a) $\langle \chi_\xi | \eta \rangle \,/\, \langle \chi_\xi | \eta \rangle_{ign} = 2.0 \cdot 10^{-2}$

(b) $\langle \chi_\xi | \eta \rangle \,/\, \langle \chi_\xi | \eta \rangle_{ign} = 0.93$

Figure 7.10: Solution dependence on the number of grid points in conditional space.

fraction based mass fraction, whereas the symbols are the results for the correct stoichiometric value based on species elements (Eq. 3.28). No differences are observed between the two clustering strategies. The change in the number of grid points does not affect the prediction of ignition delay time, as expected. However, the solution starts to deteriorate in the propagation towards the oxidizer stream when the number of grid points is reduced. The increase in grid requirements is related to the correct prediction of the steep gradient present after ignition as seen in Fig. 7.11, which can be related to a flame propagation in η-space. Further investigation is necessary in order to find a refinement strategy that can produce accurate results with minimal grid refinement. The number of ODEs to be solved in each CMC cell is a function of number of species and points in η-space. In a multi-dimensional CMC the increase in the number of points in conditional space affects considerably the computational time. The following calculations in the RCEM case use 101 points in η-space, which is a compromise due to computational time.

A snapshot when the temperature at $\xi_{stoich} - \xi_{stoich}/2$ reaches 1500 K for the first time in the case with various numbers of grid points (up to 301) and low scalar dissipation rate is presented in Fig. 7.11. By the time oxidizer region starts to react, the rich mixture is already burning and no difference can be seen in that region.

7.4 Summary of cases

The experimental operating points OP2 and OP3 are simulated using various combinations of modelling options. Table 7.2 summarises the numerical tests performed in this study. The baseline model configuration, Case A, employs the more detailed correlation for S_T from Ref. [160] and the temperature-based threshold, as in Ref. [203], and the advanced flame speed model by Soriano and Richardson [207]. Cases B-D each change one modelling option, compared to Case A. Case B tests the use of an OH mass fraction ignition criterion. Case C compares the laminar flame speed model by Soriano and Richardson [207] with the methane-only approach analogous to Ref. [203]. Case D compares the effect of the S_T alternative correlations. A further case, Case E, considers only the progress variable from the CMC model in order to distinguish the heat release contributed by the two combustion models.

Table 7.2: Numerical test cases

Case name	s_l model	s_t correlation	Ignition threshold
A	Soriano and Richardson [207]	Peters (Eq. 7.6)	$\widetilde{T} \geqslant 1200$ K
B	Soriano and Richardson [207]	Peters (Eq. 7.6)	$\widetilde{Y}_{OH} \geqslant 4 \cdot 10^{-04}$
C	CH4 kinetics [207]	Peters (Eq. 7.6)	$\widetilde{T} \geqslant 1200$ K
D	Soriano and Richardson [207]	Simple (Eq. 7.5)	$\widetilde{T} \geqslant 1200$ K
E	CMC only		

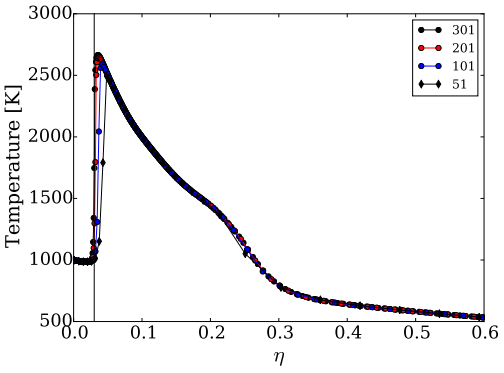

Figure 7.11: Temperature evolution for different grid tested. The plot is the instant which $T_{\xi_{stoich}-\xi_{stoich}/2}$ reaches 1500 K for the first time for 301 points and low scalar dissipation rate.

7.5 Results

The results are presented in terms of cumulative heat release, defined as the integral of the heat release rate from the start of injection. The heat release rate is computed in Eq. 7.25 as the difference between the internal energy due to combustion ΔU, the wall heat transfer $\dot{Q}_{wall}$ and the heat from the droplets $\dot{Q}_{droplets}$ [240],

$$\text{Heat release rate} = \frac{\Delta U}{\Delta t} - \dot{Q}_{wall} - \dot{Q}_{droplets}. \tag{7.25}$$

ΔU is computed by an isentropic compression and the actual internal energy subject to combustion as

$$\Delta U = \frac{c_v}{R} V_n \left[P_n - P_{n-1} \left(\frac{V_{n-1}}{V_n} \right)^{\gamma} \right] \tag{7.26}$$

The same methodology was applied in both numerical and experimental data.

Simulation of the ignition process by the CMC model is illustrated by the unconditional mean OH mass fraction and temperature fields for OP2 Case E in Fig. 7.12. The maximum values in the colour scales correspond to the respective thresholds. The first appearance of OH mass fraction at the threshold value is predicted in the lean fluid at the outer region of the jet, whereas the temperature field passes the 1200 K threshold across the whole jet, including richer mixtures similar to the behaviour seen in Fig. 7.7. At 2.3 ms the ignited region spans across the centre of the fuel jet in both cases, but extends further downstream in the case of the temperature threshold.

The contribution to the overall burning rate from the premixed flame propagation phase is demonstrated by comparison of the apparent heat release rate and the cumulative apparent heat release, based on the pressure and volume traces from measurement and simulation. The apparent heat release reported is evaluated in a manner for both the simulation and experimental data.

Figure 7.13 presents the experimental heat release rate and cumulative heat release, and simulation predictions of Cases A and E for both operating points (OP2 and OP3). The dotted line corresponds to the total calorific value of the n-heptane fuel injected into the cylinder. Compared against the experimental results, the ignition delay time is over predicted by the numerical simulation in both conditions tested. Given the success of the CMC ignition model in previous studies of diesel engine combustion, the over-prediction

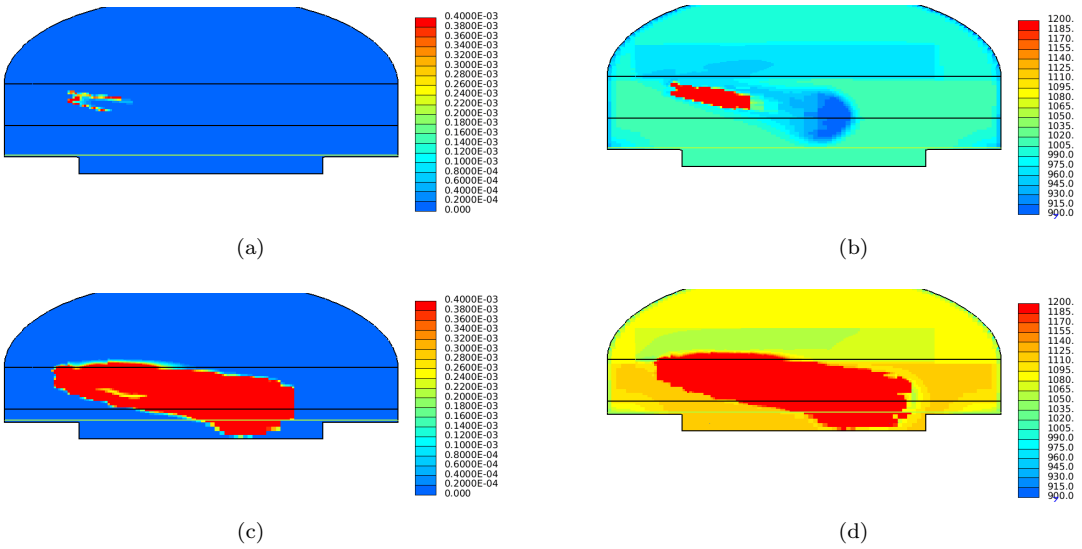

Figure 7.12: $\widetilde{Y}_{OH}$ (left) and mean temperature (right) for Case E at 1.3 ms (top) and 2.3 ms (bottom) after SOI.

of the ignition delay time may be due in part to uncertainty concerning kinetic modelling of ignition of n-heptane/methane fuel mixtures and uncertainty in the initial conditions of the experimental run. The peak magnitude of the heat release rate predicted is lower than the experimental measurement, contrary to the usual observation in diesel engines that increased ignition delay tends to increase the peak heat release rate of the so-called premixed phase. There is no simple explanation for this observation, however it may be affected by over-leaning of the pilot fuel in some regions, and retardation of the premixed combustion progress due to the presence of methane fuel.

Including the premixed flame propagation model (Case A) makes a significant contribution to heat release rate even during the main ignition process (before 2 ms). The premixed flame propagation contribution modelled by the G-equation contributes to a greater heat release rate throughout the entire simulation. While the CMC model does not explicitly account for the small-scale mixing associated with flame propagation, combustion continues to spread through the CMC solution in Case E by spatial convection and turbulent diffusion of the conditional average solution. In the OP2 condition, the CMC-only simulation (Case E) under-predicts the apparent rate of heat release compared to the experiment, while the baseline model (Case A) over-predicts the rate of heat release, compared to the experiment. The initial condition in OP3 eventually results in autoignition of the end-gas, seen in Fig. 7.13 by the sharp increase in experimental cumulative heat release after 4 ms. The CMC is able to capture the autoignition of

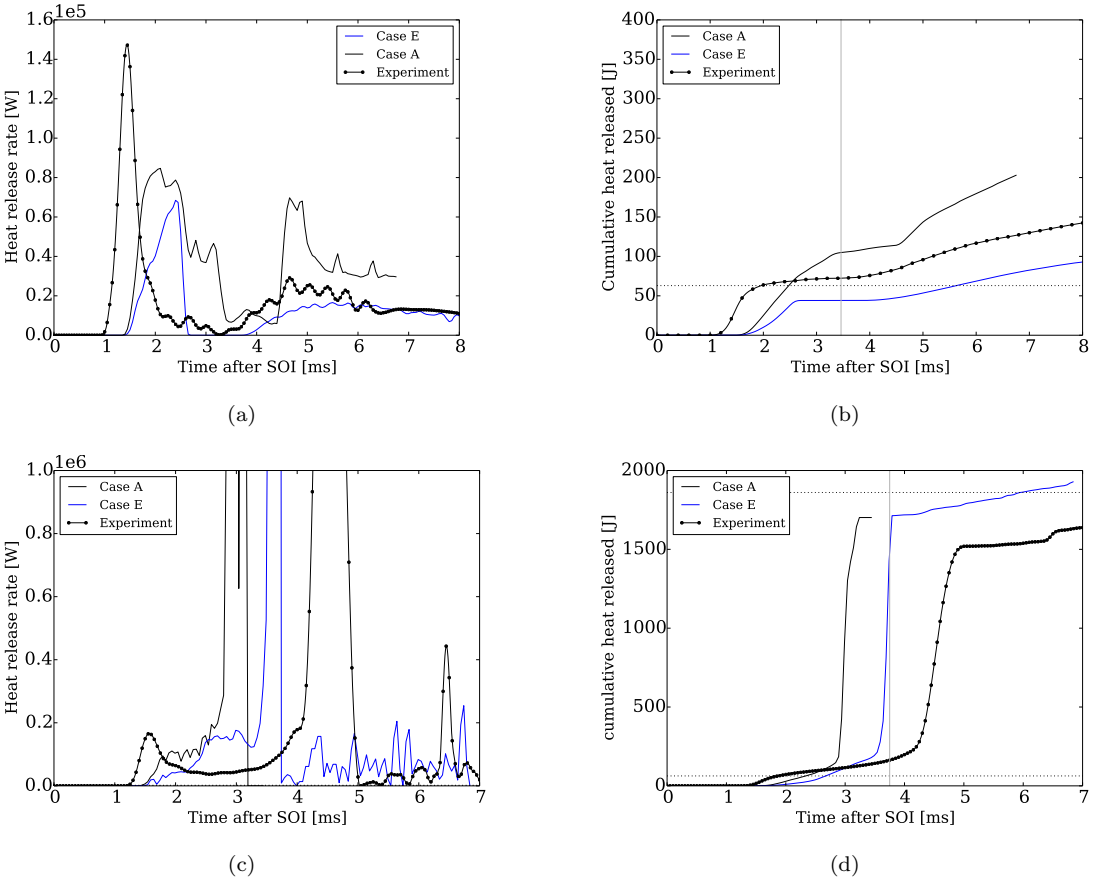

Figure 7.13: Heat release rate (left) and cumulative heat release (right) for experiment and Cases A and E for OP2 (top) and OP3 (bottom). Vertical grey line corresponds to TDC.

the premixed charge, although the ignition delay for the methane-air mixture is under-predicted.

The modelling options affecting the prediction of the premixed phase are: the threshold used to ignite G-equation; the laminar flame speed model; and the turbulent flame speed correlation. The sensitivity of the solution to those three parameters is investigated in the following subsections.

7.5.1 Ignition criteria

Heat release results showing the difference caused by use of the temperature threshold ignition criterion (Case A) and the OH mass fraction threshold ignition criterion (Case B) are presented in Fig. 7.14. The choice of ignition criterion has a small effect on heat release rate during initial ignition, with the solution being similar to the heat release

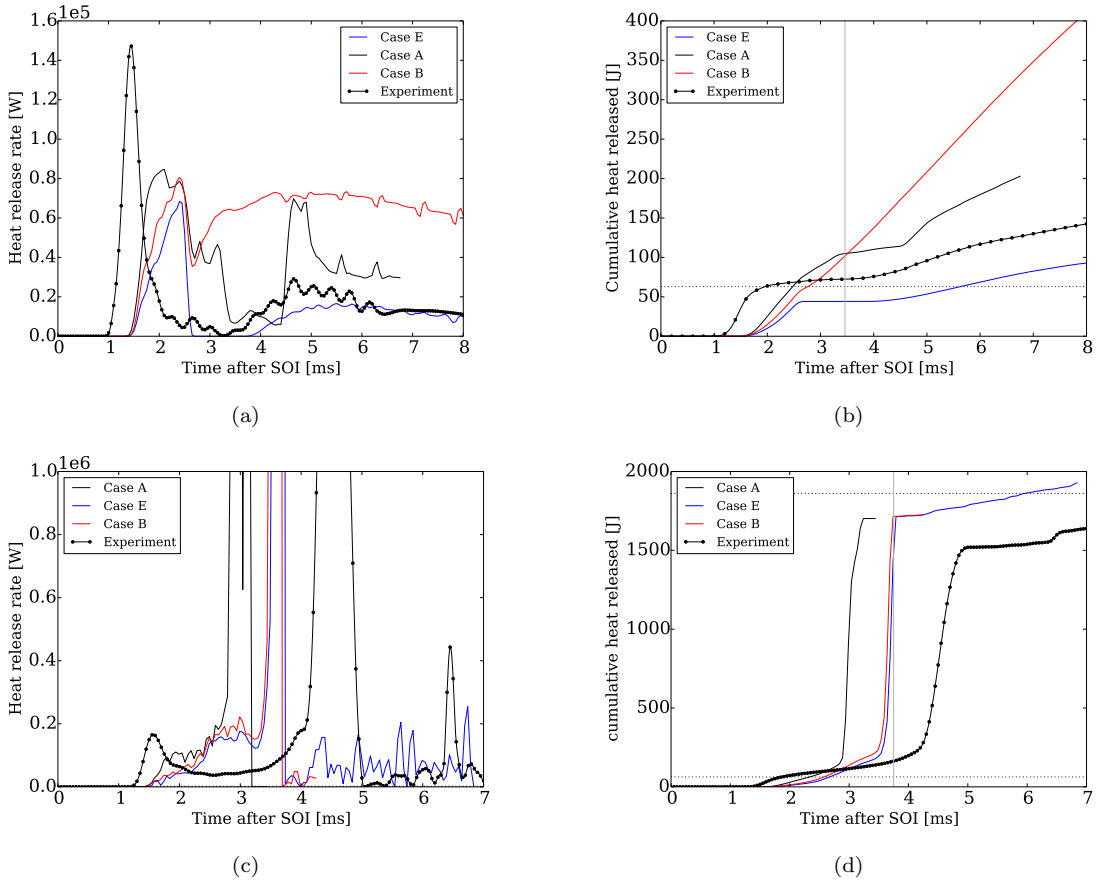

Figure 7.14: Heat release rate (left) and cumulative heat release (right) for Cases A, B, E and experiment for OP2 (top) and OP3 (bottom). Vertical grey line corresponds to TDC.

rate computed only by the CMC model. After 2.5 ms, the different initialisation of the G-equation field due to the different ignition criteria result in persistent differences in the heat release rate associated with the flame propagation phase and, for OP3, in the timing of the end-gas ignition.

The threshold used to ignite the G-equation model changes the location of the premixed flame, as observed in Fig. 7.7. The propagation of the premixed flame is also affected by the threshold. Figure 7.15 presents the contours $\widetilde{Y}_{OH,CMC}$ and the $\widetilde{C}_G = 0.5$ isoline for simulations A (left) and B (right) of case OP2. The temperature threshold is reached earlier than the OH mass fraction and the premixed flame for case A propagates ahead of the flame in case B.

The greater difference between simulations A and B of OP2 occur at around 3.5 ms, when the CMC model is not contributing to the heat release rate. Small differences are observed for the temperature contours in the direction of the pilot jet as presented in

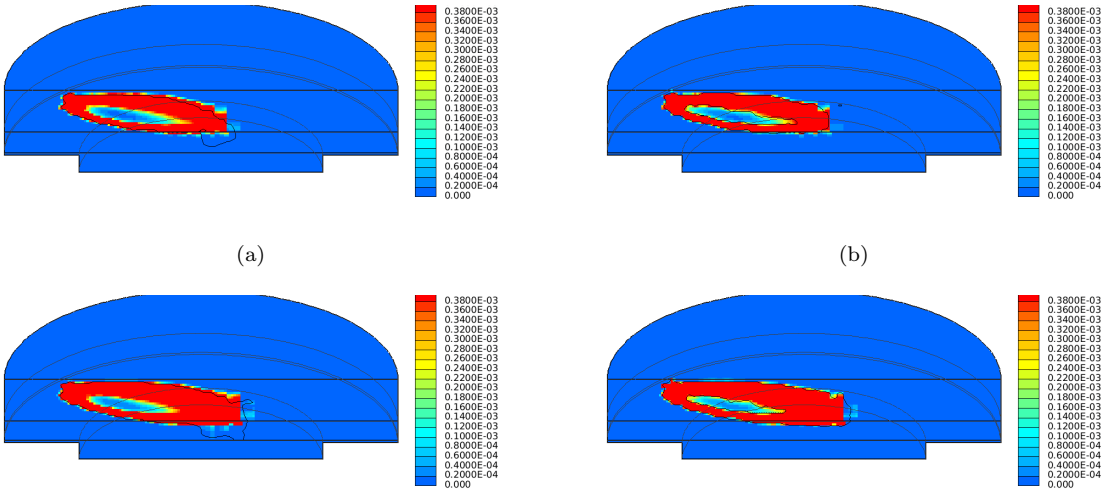

Figure 7.15: $\widetilde{Y}_{OH,CMC}$ contour with $\widetilde{C}_G = 0.5$ iso-line at 1.7 and 1.8ms after SOI in case OP2: left column uses $\widetilde{T} \geqslant 1200$ K as threshold and right column uses $\widetilde{Y}_{OH} \geqslant 4 \cdot 10^{-04}$.

Fig. 7.16 for 3.7 ms after start of injection. The difference in the temperature field does not reflect the great difference in heat release rate. In fact, the difference comes from the direction radial to the n-heptane. The methodology used to ignite G-equation changes the distribution of mixture fraction in the physical domain. Figures 7.17a and b present the mean mixture fraction iso-surface at 3.7 ms for the simulations A (Fig.7.17a) and B (Fig.7.17b) of OP2. A greater distribution of mixture fraction is observed for the case B, which enhances the laminar flame speed. The correlation between the mixture fraction and flame distributions are observed in Figures 7.17c and d, where the iso-surface corresponds to $\widetilde{C}_G = 0.5$. The high sensitivity of the predictions to the choice of the two ignition criteria considered here is a limitation of the hybrid modelling approach, however, since the CMC provides detailed information about the evolution of ignition in mixture-fraction space, it may be possible to develop more robust ignition criteria using mixture fraction-conditioned properties.

7.5.2 Laminar flame speed modelling

Two approaches for modelling the laminar flame speed are compared. The baseline simulation A uses the full model by Soriano and Richardson [207] in order to account for the effects of n-heptane fuel properties and pre-ignition reactions on the flame speed.

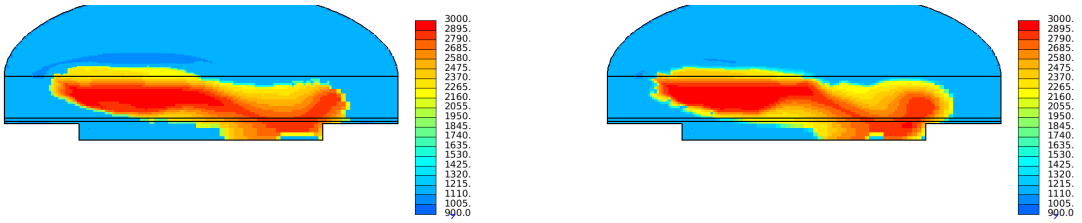

(a) (b)

Figure 7.16: Temperature field of OP2 at 3.7 ms after start of injection. Simulation A (left) and B (right).

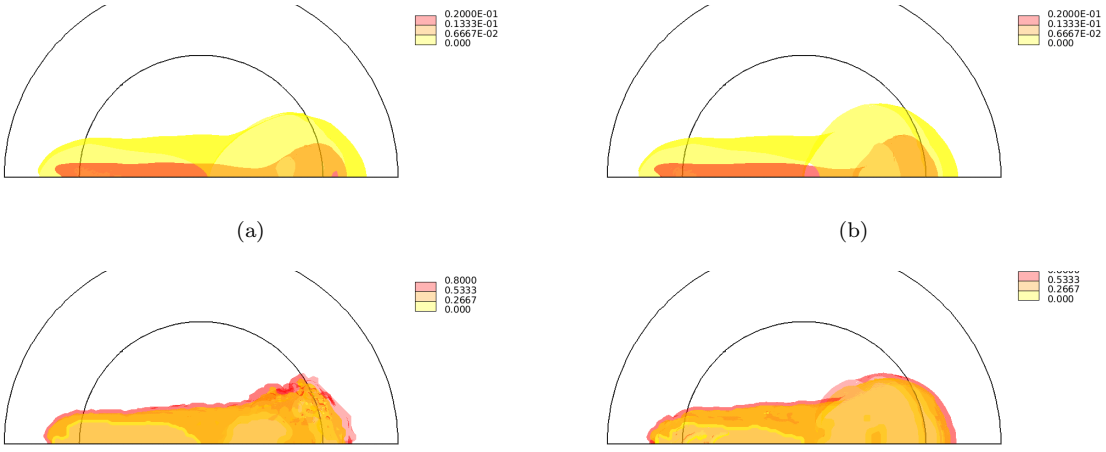

(a) (b)

(c) (d)

Figure 7.17: Iso-surfaces from simulations A (left) and B (right) of OP2 at 3.7 ms after start of injection. On the top: $\widetilde{\xi} = 0.02$ and $\widetilde{\xi} = 0.002$ on the bottom: $\widetilde{C}_G = 0.5$.

Simulation C models the flame speed using the methane-air correlation, based on the overall equivalence ratio including both n-heptane and methane. The predictions for OP2 and OP3 are presented in Fig. 7.18, and show that accounting for n-heptane fuel properties and for pre-ignition reactions contributes to a significant increase in the heat release rate during the ignition and initial flame propagation phase for OP2. After 5 ms, when the contribution of n-heptane is not significant, the heat release rate becomes equal for both sets of models. Operating point OP3 is less influenced by the modelling of the flame propagation due to the higher temperature eventually leading to ignition of the end gas, and overall predictions of models A and C are similar.

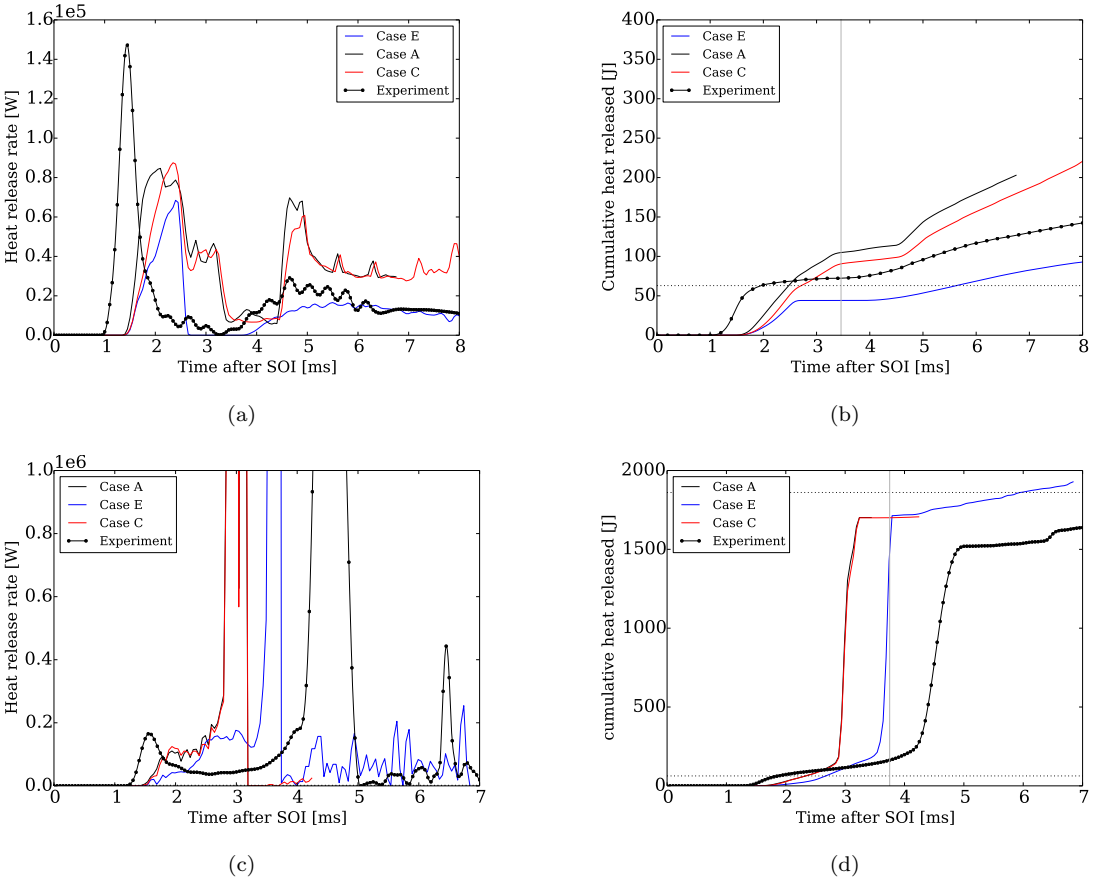

Figure 7.18: Comparison of simulationsA, C and E with experiment for OP2 (top) and OP3 (bottom): (left) Heat release rate; (right) Cumulative heat release. Vertical grey line corresponds to TDC.

7.5.3 Turbulent flame speed correlations

The influence of the turbulent flame speed correlation is illustrated by comparing the heat release results from simulation A with turbulent flame speed modelled by Eq. 7.6, and simulation D with flame speed modelled by Eq. 7.5. Figure 7.19 shows that the predictions for OP2 show substantial sensitivity to the turbulent flame speed correlation used, whereas predictions for OP3 are less sensitive to the modelling of the flame propagation. For OP2, simulation D predicts a slower heat release during ignition when the turbulence levels are higher and it persists in a later stage after 4 ms, see Fig. 7.19a. The slower propagation given by modelling option D gives a better agreement with the experiment in terms cumulative heat release, Fig. 7.19b. The predictions show a greater sensitivity to the selection of turbulent flame speed correlation than to the range of laminar flame speed models considered here, as may be expected from Eqs. 7.5 and 7.6 when . Predictions are therefore expected to depend on the choice of model constants

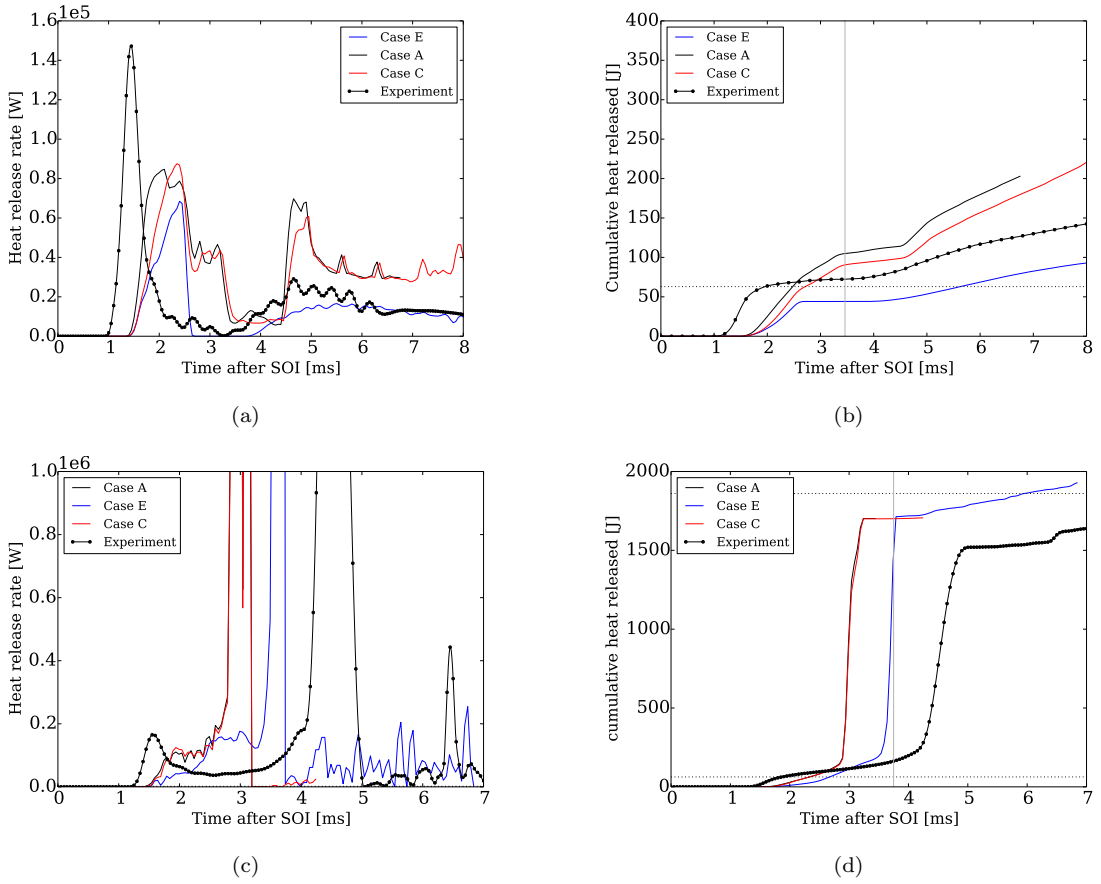

Figure 7.19: Comparison of simulation Cases A, D, and E with experiment for OP2 (top) and OP3 (bottom), showing heat release rate (left), cumulative heat release (right). Vertical grey line corresponds to TDC.

in Eqs. 5 or 6, however no tuning of these constants away from the values proposed by the original authors of the respective models has been pursued here.

7.5.4 Further discussion about the hybrid modelling

The predictions of heat release rate using the hybrid modelling approach presents deviations from the experimental measurements performed at ETH Zurich. The ignition delay time is of great importance in dual-fuel combustion because it dictates the behaviour of the subsequent flame propagation along the evolving pilot spray and ignition of the purely premixed charge. The results in Chapter 5 revealed that the autoignition of the pilot fuel in dual-fuel combustion is affected by the chemical kinetics of the premixed fuel and an additional sensitivity to fluid dynamic strain. The Conditional Moment Closure used in the hybrid model is capable of capturing the complex dual-fuel autoignition process since it accounts for fluid dynamic strain through the scalar dissipation rate

model and for the different chemical kinetics of dissimilar fuels through its capability to incorporate any complex chemistry. CMC has been succesfully applied to single fuel compression ignition combustion, however a deviation of ignition delay time is observed in the numerical results presented here. The deviation is atributted to the inacurracy of the 44-species skeletal n-heptane mechanism by Liu et al. [121] on predicting the ignition delay time at those conditions. In fact, even the detailed mechanisms tailored methane combustion have difficulties on correctly predicting the ignition delay time of methane-air mixtures at elevated pressures and temperatures as those observed during the autoignition of the end-gas in case OP3. However, more complex chemical kinetics could be incorporated in the CMC model to give better predictions of ignition delay time of dual-fuel mixtures, but at greater computational cost. The results show the necessity to develop reduced chemical kinetic models that can reproduce the ignition delay time and propagation speed of n-heptane/methane dual-fuel mixtures.

7.6 Conclusion

A hybrid modelling approach is presented that combines the ability of the Conditional Moment Closure (CMC) approach to describe autoignition of fuel sprays with the ability of the G-equation approach to describe the subsequent flame propagation. The effects of partially-ignited fuel on the flame propagation speed is taken into account by a new laminar flame speed model. The formulation presented takes account of all of the heat released by both the premixed gaseous fuel and the injected liquid fuel. The modelling is evaluated by simulating n-heptane pilot jet-ignited combustion of a premixed methane air charge in a rapid compression-expansion machine apparatus. The results show that the hybrid model adequately captures ignition and transition to premixed flame propagation, and accounts for autoignition of the premixed end gas seen in experiments. The results demonstrate that the new laminar flame speed modelling approach that accounts for the presence of n-heptane and pre-ignition reactions in the reactant mixture leads to a significant increase in burning rate at certain points during combustion, where the flame propagates through pockets of unburned pilot fuel near the head of the fuel injection. The results also show a sensitivity to the choice of the turbulent flame speed correlation and to the choice of the ignition criterion used to couple the CMC and G-equation models. The use of OH- or temperature-based criteria does not change

the timing of ignition significantly, but has a significant effect on the location. The temperature threshold leads to ignition of a larger volume of the pilot fuel, including richer mixture in the centre of the spray and extending further into the head of the pilot fuel injection, with knock-on effects on the heat release rate. The over-prediction of the initial ignition delay time also highlights the importance of developing chemical mechanisms that properly account for dual fuel ignition kinetics, and are reduced using appropriate target flames.

The sensitivity to the criteria for initiating the G-equation motivates development of the multi-mode DCMC approach in Chapter 8 in order to avoid the need for switching criteria.

Chapter 8

Double Conditional Moment Closure modelling of dual-fuel combustion

The hybrid approach presented in Chapter 7 is sensitive to the criteria used to couple the models. The Double Conditional Moment Closure (DCMC) approach seeks to avoid the need for such criteria by describing the entire combustion process within a single modelling framework. Application of the DCMC approach is investigated through simulation of dual-fuel combustion for the conditions of a dodecane-methane dual-fuel Rapid Compression-Expansion Machine experiment. The DCMC model is implemented using a tabulation method assuming statistical homogeneity in space and time. The sensitivity of the DCMC solution to mixing is examined by varying the magnitude of the progress variable dissipation rate. The work reported in this chapter is performed as part of a collaboration with the group of Prof. Boulouchos and Dr Yuri Wright at ETH Zurich, whose experimental data are used as a validation target, and whose CFD simulation set-up is used as the starting point for this investigation.

8.1 Introduction

Numerical modelling of dual-fuel combustion using complex chemistry has focused either on direct chemistry integration, neglecting effects of turbulence chemistry interaction [86], or on hybrid coupling of different combustion models in the attempt to correctly capture autoignition and premixed flame propagation [3, 32, 119, 143, 194, 198, 202, 203, 208, 250]. However, as concluded in Chapter 7 the main limitation of hybridising different models in dual-fuel combustion is related to the coupling strategy. In Ref. [198] a hybrid flamelet generated manifold (FGM) hybrid model was developed to capture the auto-ignition and flame propagation of lean premixed methane-air mixtures and tested in the context of Reynolds-Averaged Navier-Stokes simulation (RANS). The different combustion modes were represented by flamelet tables generated by either a non-premixed counter-flow configuration (Conditional Moment Closure) or a purely premixed laminar flame for different mixture fraction compositions. The model performance was assessed through prediction of dual-fuel combustion in the ETH Zurich Rapid Compression-Expansion Machine (RCEM) experiment [214, 216] for a single temperature and pressure condition. The RCEM features a cylindrical combustion chamber with 84 mm bore and a piston displacement of 249 mm. Methane, used as surrogate for natural gas, is injected prior the start of compression to ensure homgeneity of the premixed charge. A 100 μm single-hole coaxial pilot injector of n-dodecane is mounted at the periphery of the cylinder. The schematic illustration of the RCEM configuration is presented in Fig. 8.1. Further information regarding the experiment can be found in Refs. [214, 216].

The experimental condition assessed in Seddik's study (1000K, 45 bar at Start of Injection (SOI)) results in combustion that is dominated by non-premixed autoignition with reduced influence of two-stage ignition, compared to lower pressure and temperature conditions [214, 216]. Following ignition, the flame propagates into an essentially laminar mixture, for which RANS turbulent combustion model with 0.5 mm grid spacing is not expected to work well. The premixed/non-premixed tabulation approach again depends on coupling criteria and neglects stratification effects in the premixed flames in the pilot region, however the authors reported encouraging performance, given that the tabulated approach is computationally inexpensive. The goal of the present study is to attempt to improve upon this previous work by replacing the choice between non-premixed or

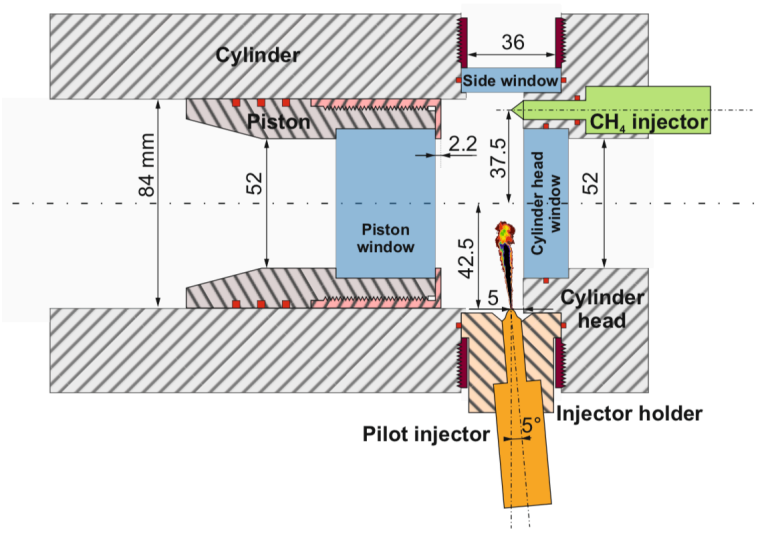

Figure 8.1: Schematic illustration of the RCEM [213].

premixed look-up tables with a partially-premixed look-up tables generated using the mixture fraction-progress variable (ξ-c) DCMC approach. The different characteristics of non-premixed or premixed flames then result from specification of conditional scalar dissipation rates in the DCMC. This Chapter considers a lower-temperature and lower-pressure operating condition (850 K, 25 bar and background methane equivalence ratio of 0.59) that is expected to exhibit increased influence of two-stage ignition and subsequently of deflagrative combustion, presenting increased modelling challenges.

Differently from Chapter 7, the results presented here use n-dodecane as surrogate for diesel. It corresponds to the second measurement campaign on the investigation of pilot-ignited methane/air combustion at ETH Zurich, and due to modifications on the experimental setup and test conditions the results cannot be directly compared with Chapter 7.

8.2 Formulation

DCMC modelling of the dual-fuel combustion process is investigated by performing stand-alone DCMC simulations for the experimental conditions (850 K, 25 bar, ϕ_{CH_4}=0.59 at SOI) for a range of scalar dissipation rates. These DCMC solutions are subsequently used as a look-up table for three-dimensional RANS simulation of the experimental set-up.

8.2.1 Double Conditional Moment Closure

The DCMC equations and solution process are introduced in Chapter 3. Steady-state DCMC solutions are calculated for a set of different conditional scalar dissipation rate profiles in order to show the sensitivity of the solution. As in Ref. [198], the dodecane chemistry is modelled employing a mechanism of 130 species and 2399 reactions reported to give good predictions for ignition delay time and flame propagation [171]. This chemical mechanism is both large and numerically stiff making solution of the DCMC by the method of lines computationally prohibitive. Therefore an operator splitting approach is employed as set out below.

Progress variable is defined as a combination of three chemical species, $Y_c = Y_{CO2}+Y_{CO}+Y_{CH2O}$, in consistency with previous work [198] although the resolution of autoignition chemistry close to $c = 0$ could be optimised further with a different definition of Y_c. The compositions of the two reactant streams correspond to the initial condition taken from the experiment. Mixture fraction is defined, at $c = 0$, by the lean methane-air mixture and 850 K at $Z = 0$ and by pure n-dodecane gaseous fuel at 373 K for $Z = 1$, in agreement with Ref. [198].

The unburnt condition at $c = 0$ is specified according to linear mixing of species mass fractions and enthalpy between the two reactant streams at $Z = 0$ and 1. The corresponding burnt condition at c = 1 is given by the chemical equilibrium state given by constant pressure evolution of the chemical mechanism. Radiative heat losses, differential diffusion and pressure change in conditional space were neglected, therefore total enthalpy remains a constant linear function of mixture fraction for all ζ and temperature is retrieved from composition and enthalpy at each grid point.

The conditional scalar dissipation rate for mixture fraction and progress variable is modelled using the Amplitude Mapping Closure (AMC) [149]. The maximum scalar dissipation rate in mixture fraction $\langle N_\xi^0 \mid \eta = 0.5\rangle = 60s^{-1}$ is the same as presented in Seddik et al. [198], whereas the magnitude of progress variable scalar dissipation rate $\langle N_c^0 \mid \zeta = 0.5\rangle$ varies for different solutions. The cross-dissipation term is set to zero for all DCMC calculations.

The solution of the conditional age distribution, similarly Chapter 6, is computed for the dual-fuel conditions presented here. The age solution is obtained as a post-processing

step based on a steady-state solution for the 130-species chemistry with prescribed amplitudes for the scalar dissipation rate AMC model. The age transport equation is solved using the progress variable scalar dissipation rate model introduced in Eq. 6.4. The new approach for N_c can have a better description for the scalar dissipation rate compared to the AMC model, however dual-fuel DCMC tables do not use the approach yet.

The DCMC equations given in Chapter 3 are implemented in a parallel in-house Fortran code. The composition is integrated in time until a steady-state solution is achieved. Convergence to steady state is by verified by evaluating the relative difference of progress variable source term at different timesteps. Strang operator splitting is employed [218], alternating between time advancement of the chemical source terms and time advancement of transport in $\eta-\zeta$ space. The transport terms are integrated using a fourth-order Runge-Kutta method, whereas the chemistry is integrated with a stiff LSODE solver using sparse analytical approach for the Jacobian matrix [159, 169]. Derivatives in $\eta-\zeta$ space are evaluated using finite differences: central second-order difference for diffusive terms, and first-order upwind differences for convective terms. The term in Eq. 3.40 involving the first derivative in ζ-direction and the chemical source term is not integrated in time but implemented by mapping the composition back to the linear relation between Y_c and c every time step using linear interpolation.

In order to achieve grid-independent solutions, 101 non-uniformly spaced grid lines in η-space are clustered around the stoichiometric mixture fraction value. The prediction of first- and second-stage ignition delay times are sensitive to grid resolution close to the unburned boundary at $c = 0$, due to steep gradients of species involved in ignition with respect to the overall progress variable. The calculations performed here required 151 points clustered around c = 0.01 in order to achieve grid independence. The splitting time step is 10-8 s, yielding time-step-independent steady-state solutions.

8.2.2 Computational Fluid Dynamics

The CFD solver is coupled with the turbulent combustion model using a pre-computed lookup table for unconditionally averaged state variables and source terms required in the RANS solution. The lookup table is generated by convolution of the DCMC steady-state solutions with a presumed joint-pdf for mixture fraction and progress variable. The ξ-c joint-pdf is modelled by assuming that ξ and c are statistically-independent,

$\widetilde{P}_{\xi,c}(\eta,\zeta) = \widetilde{P}_{\xi}(\eta)\widetilde{P}_{c}(\zeta)$, with the marginal pdfs $\widetilde{P}_{\xi}$ and $\widetilde{P}_{c}$ modelled by the β-function distribution. The table generation is performed as a pre-processing step, yielding four-dimensional tables in terms of $\tilde{\xi}$, $\widetilde{\xi''^2}$, $\tilde{c}$ and $\widetilde{c''^2}$ axes for each set of scalar dissipation rates considered.

There is a one-way coupling of the DCMC model into the CFD through the lookup table. The CFD set-up was developed by ETH Zurich in OpenFOAM, where momentum, turbulence, mass and energy equations are solved in physical space. Turbulence is modelled using a standard $k-\epsilon$ model with a tuned ϵ_1 constant in order to correct for the round jet anomaly as previously used in diesel spray problems [151]. The liquid spray injection is characterized using the blob injection model [174] and the Reitz-Diwakar model for the secondary break-up [172]. The spray was validated with the experiment in terms of vapour penetration. Pressure-velocity coupling is performed using PISO, spatial derivatives computed with second order accuracy and the solution is advanced by implicit second order time integration.

The mixture fraction and progress variable moments used as inputs to the lookup table are given by Reynolds-Averaged transport equations solved in the CFD. The transport equations are modelled assuming gradient-type turbulent transport, unity Lewis number, and a simple treatment of spray evaporation (the spray evaporation source term is only retained in the mean mixture fraction equation).

The mean mixture fraction is modelled by

$$\frac{\partial \bar{\rho}\widetilde{\xi}}{\partial t} + \nabla \cdot \left(\bar{\rho}\tilde{\mathbf{u}}\tilde{\xi}\right) = \nabla \cdot \left[\bar{\rho}\left(\bar{D} + \bar{D}_t\right)\nabla\tilde{\xi}\right] + \bar{\rho}\Pi_{\xi} \tag{8.1}$$

and the mixture fraction variance is modelled by

$$\frac{\partial \bar{\rho}\widetilde{\xi''^2}}{\partial t} + \nabla \cdot \left(\bar{\rho}\tilde{\mathbf{u}}\tilde{\xi''^2}\right) = \nabla \cdot \left[\bar{\rho}\left(\bar{D} + D_t\right)\nabla\tilde{\xi''^2}\right] + 2\bar{\rho}\left(\bar{D} + D_t\right)\nabla\tilde{\xi}\cdot\nabla\tilde{\xi} - 2\bar{\rho}\widetilde{N_{\xi}}, \tag{8.2}$$

where the molecular and turbulent diffusivities are computed as $\bar{D} = \bar{\mu}/\left(\bar{\rho}Sc\right)$ and $D_t = \mu_t/\left(\bar{\rho}Sc_t\right)$ respectively and μ_t is the turbulent viscosity given by the k-ϵ model. The unconditional mean mixture fraction scalar dissipation rate is modelled as $\widetilde{N_{\xi}} = \frac{1}{2}C_{\chi}\widetilde{\epsilon}/k\widetilde{\xi''^2}$ [198, 237], where the model coefficient is set as $C_{\chi} = 2$ [202, 215].

Considering that progress variable is dependent on mixture fraction, the transport equations for its mean and variance are given by

$$\frac{\partial \bar{\rho}\widetilde{c}}{\partial t} + \nabla \cdot \left(\bar{\rho}\tilde{\mathbf{u}}\tilde{c}\right) = \nabla \cdot \left[\bar{\rho}\left(\bar{D} + D_t\right)\nabla\tilde{c}\right] + \bar{\rho}\widetilde{\dot{\omega}_{c^*}} \tag{8.3}$$

and the mixture fraction variance is modelled by

$$\begin{aligned}\frac{\partial \bar{\rho}\widetilde{c''^2}}{\partial t} + \nabla \cdot \left(\bar{\rho}\tilde{\mathbf{u}}\widetilde{c''^2}\right) = \nabla \cdot \left[\bar{\rho}\left(\bar{D} + D_t\right)\nabla\tilde{c}\cdot\nabla\tilde{c}\right] \\ + 2\left(\bar{D} + D_t\right)\nabla\tilde{c}\cdot\nabla\tilde{c} - 2\bar{\rho}\widetilde{N_c} \\ + 2\bar{\rho}\left(\widetilde{c\dot{\omega}_{c^*}} - \tilde{c}\widetilde{\dot{\omega}_{c^*}}\right).\end{aligned} \tag{8.4}$$

where the effective progress variable reaction rate $\dot{\omega}_{c^*}$ is given by,

$$\dot{\omega}_{c^*} = \frac{1}{\partial Y_c/\partial c}\left[\dot{\omega}_{Y_c} + N_\xi\frac{\partial^2 Y_c}{\partial \xi^2} + 2N_{\xi,c}\frac{\partial^2 Y_c}{\partial \xi \partial c} + N_c\frac{\partial^2 Y_c}{\partial c^2}\right]. \tag{8.5}$$

Terms in Eqs. 8.3 and 8.4 involving $\dot{\omega}_{c^*}$ are closed by convolution of the joint-pdf with the relevant quantities from the DCMC solution. The mean progress variable scalar dissipation rate $\widetilde{N_c}$ is closed using the model presented in Kolla et al. [103] as

$$\widetilde{N_c} = \frac{1}{2\beta_c}\left[\left(2K_c^* - \tau C_4\right)\frac{s_l^0}{\delta_l^0} + C_3\frac{\widetilde{\epsilon}}{k}\right]\widetilde{c''^2} \tag{8.6}$$

where τ is a heat release parameter approximated by the burnt and unburnt temperatures $\tau = \left(T_b - T_u\right)/T_u$. s_l^0 and δ_l^0 are, respectively, the laminar flame speed and thermal thickness. The remaining model parameters are defined as: $\beta_c = 6.7$, $K_c^* = 0.85\tau$, $C_3 = 1.5\sqrt{Ka}/\left(1+\sqrt{Ka}\right)$ and $C_4 = 1.1/\left(1+Ka\right)^{0.4}$. Ka is the Karlovitz number defined as $Ka = \sqrt{\left(u'/s_l^0\right)^3\left(\delta_l^0/L\right)}$, where L is the integral length scale. The term K_c^* is related to dilatation, whereas C_3 and C_4 account for the interaction between turbulent strain and scalar gradient [103].

The CFD solver computes all the transport equations in physical space, i.e. momentum, energy, turbulence and first two moments for ξ and c, and obtains the source terms for Eqs. 8.3 and 8.4 from the look-up table. The process is performed within the timestep until convergence is achieved. Figure 8.2 illustrates the coupling between the CFD solver and the turbulent combustion model presented in Ref. [198].

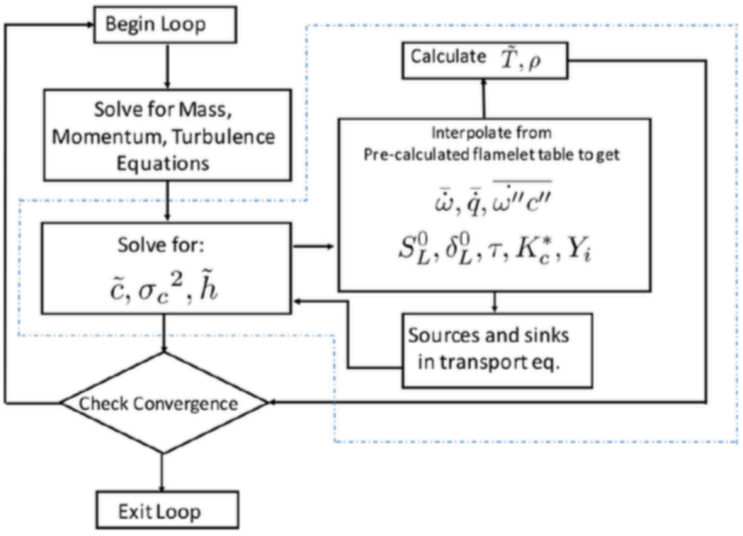

Figure 8.2: Schematic illustration of the coupling between CFD and turbulent combustion model [198].

8.2.3 Numerical setup

The CFD grid used hexahedral cells of 0.5 mm. The simulation is initialised with the pressure and temperature from the experiment corresponding to the start of injection 3.7 ms before Top Dead Centre. Temperature and composition are assumed to be uniform throughout the cylinder. The combustion chamber is initialised with a quiescent velocity field and turbulence is generated during the spray injection. The flow field conditions do not correspond to a real engine condition where high turbulence is expected prior fuel injection. The implication of the flow conditions in the RCEM is that the flow and the flame propagation outside of the pilot region are laminar. Since the grid resolution here is not sufficient to accurately solve laminar premixed flames and the target for dual-fuel modelling is turbulent combustion, the simulation was stopped as the flame approached the boundary of the pilot region.

In order to test the effects of molecular transport on the DCMC solutions, the results presented here used different scalar dissipation rates based on the magnitude provided for the Amplitude Mapping Closure as presented in Table 8.1. $N_{0,Z}$ was obtained based on non-reactive calculations of the fuel spray, whereas the maximum magnitude in progress variable direction was computed considering the timescale of a methane-air laminar premixed flame at the conditions used for the CFD. Cross-dissipation is neglected. The matrix presented in Table 8.1 goes from zero transport in c experienced pior to ignition, which corresponds to a single conditioned solution in mixture fraction, to a case with

Table 8.1: Peak scalar dissipation rates used in the DCMC solutions.

Case	$\left\langle N_{\xi}^{0} \middle\vert \eta,\zeta \right\rangle$	$\langle N_{c}^{0} \vert \eta,\zeta \rangle$	$\left\langle N_{\xi,c}^{0} \middle\vert \eta,\zeta \right\rangle$
N_60_0_0	60	0	0
N_60_30_0	60	30	0
N_60_300_0	60	300	0
N_60_3000_0	60	3000	0

scalar dissipation rate magnitude similar to the expected for a partially premixed flame at those conditions.

8.3 Results

Figure 8.3 presents the predictions of conditional mean progress variable reaction rate $\langle \dot{\omega}_c \mid \eta,\zeta \rangle = \langle \omega_{\dot{Y}_c} \mid \eta,\zeta \rangle / \left(\partial Q_{Y_c}/\partial\zeta\right)$ for the four cases introduced in Table 8.1. The high reaction rate observed in Fig. 8.3a for the range $0.0 < \xi < 0.4$ and $0 < c < 0.5$ correspond to the first-stage ignition process associated with the low temperature chemistry of n-dodecane combustion. The results reveal sensitivity of reaction rate to progress variable scalar dissipation rate, which is more pronounced at rich mixtures ($\xi_{st} = 0.026$). The rate of transport in the ζ-direction wipes out the low temperature chemistry for $\langle N_c^0 \mid \eta,\zeta \rangle = 3000$.

A separate simulation of the RCEM experiment is performed using each of the DCMC-generated lookup tables listed in Table 8.1. The predictions of heat release rate using table N_60_0_0, presented in Fig. 8.4, show a very good agreement with the experimental data. As expected, the ignition delay time was retarded for the tables with $\langle N_c^0 \mid \eta,\zeta \rangle > 0$. For the manifolds with progress variable scalar dissipation amplitude higher than 30 s^{-1}, no ignition was observed. Nonetheless, the solutions for N_60_0_0 and N_60_30_0 presented a similar first-stage ignition delay time. The case N_60_3000_0 approximates the solution of a premixed laminar flame front and therefore molecular transport plays a much greater role than during autoignition. Tests performed on a simple one-dimensional reaction-diffusion solver for progress variable revealed that the case case N_60_3000_0 reproduces the laminar flame speed obtained with a freely-propagating flame, whereas N_60_0_0 considerable under-predicts flame propagation.

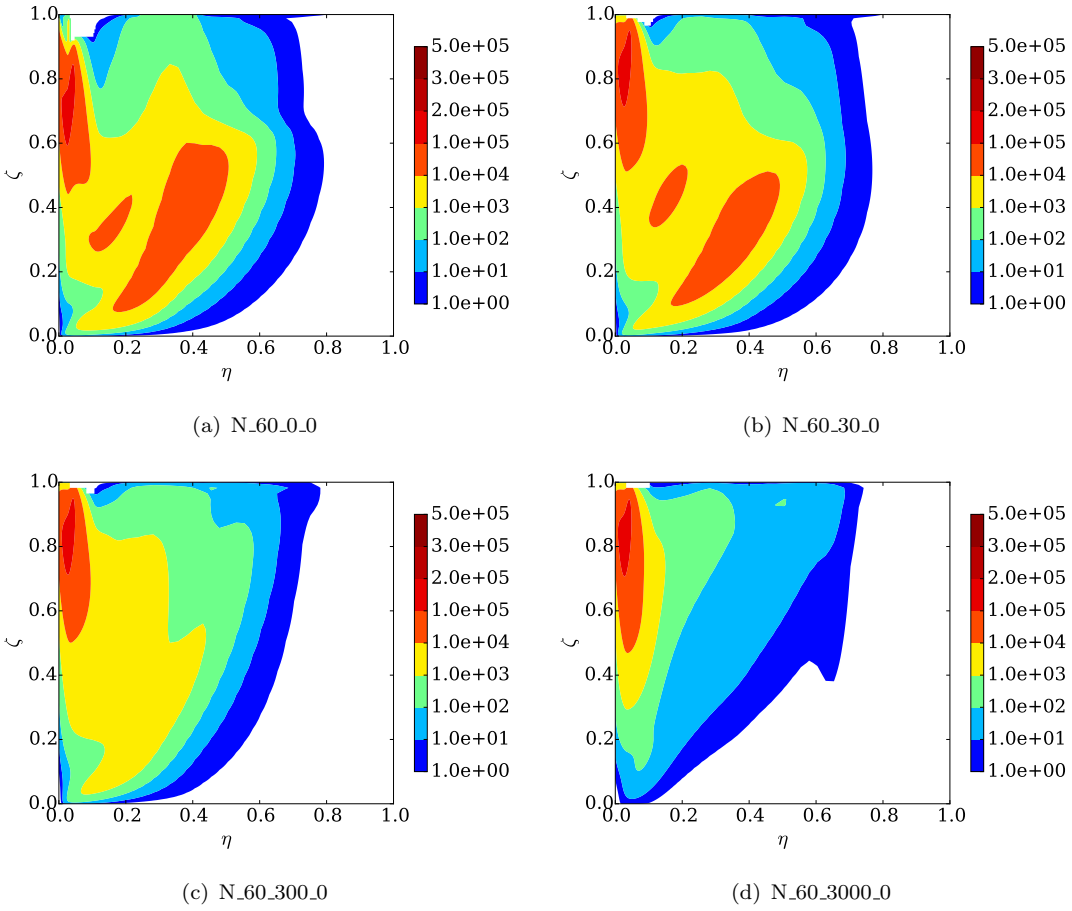

(a) N_60_0_0

(b) N_60_30_0

(c) N_60_300_0

(d) N_60_3000_0

Figure 8.3: Predictions of conditional mean progress variable reaction rate for various scalar dissipation rates.

Figure 8.5 presents the evolution of mixture fraction and temperature in physical space at different timesteps using table N_60_0_0. At 0.735 ms, the simulation shows the low temperature region due to evaporation of the pilot fuel and first-stage ignition occuring at the spray tip. The low temperature chemistry region is convected with the spray and is the precursor to autoignition. Prior second-stage igntion, the pilot spray occupies a great volume in the combustion chamber, what highlight the importance of correctly predicting partially premixed flames at dual-fuel conditions. Part of the inhomogeneous mixture in the region of the injector nozzle remains unburnt by the time the simulation was stopped.

The sensitivity to progress variable scalar dissipation rate implies that it is not possible to model the entire ignition and propagation process with a single DCMC solution with constant conditional scalar dissipation rate profiles. In the context of the lookup table approach, the table could be extended using additional DCMC solutions for a range

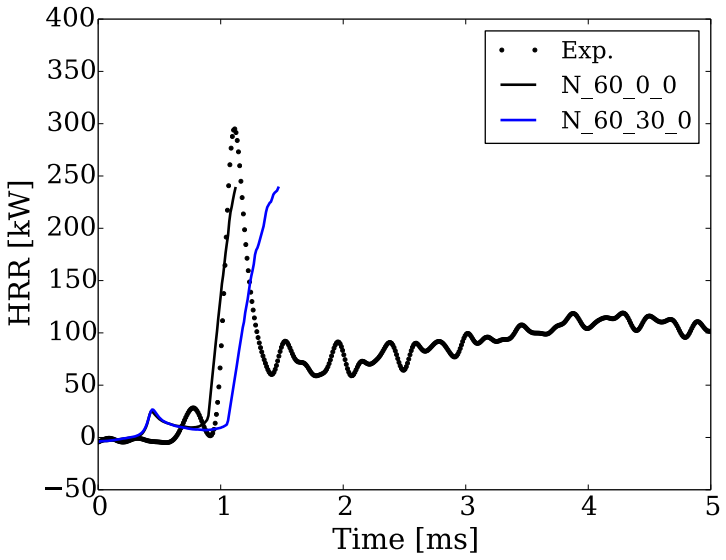

Figure 8.4: Comparison of measured heat release rate with DCMC prediction.

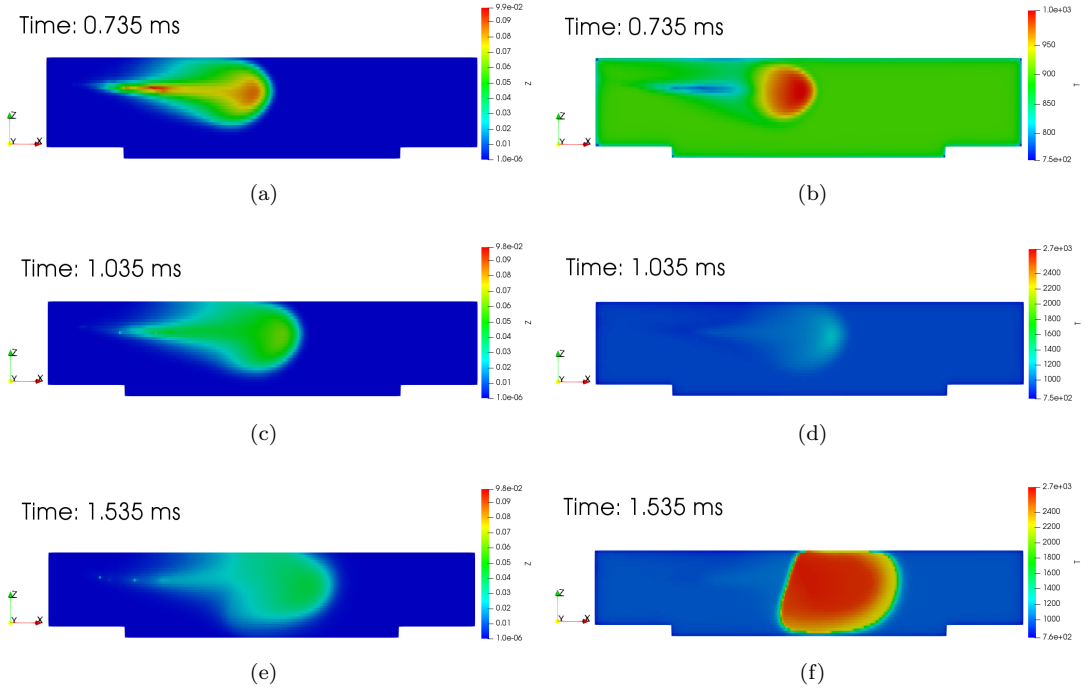

Figure 8.5: Combustion evolution in physical space: Mixture fraction on the left; and temperature on the right

of scalar dissipation rates in order to include the amplitudes of mixture fraction and progress variable conditional scalar dissipation rates as look-up variables. This would allow solutions with different combinations of scalar dissipation rate amplitudes to be used in different regions of the domain. However it is not just the amplitude but also modelling for the shape of the progress variable dissipation rate profile that may be

important for autoignitive flames.

The modelling so far in this Chapter and in previous DCMC [205] and multi-dimensional flamelet [147] has employed a simple bell-shaped curve for the profile of the conditionally-averaged progress variable dissipation rate. This may be appropriate in classical deflagrative combustion where a single thin reaction front spans the entire range of progress variable. However the situation in fuels exhibiting two-stage ignition is significantly more complex, and modelling of conditional scalar dissipation rates associated with, for example, polybrachial flame structures is an undeveloped subject. In an autoignitive premixed system involving both cool-flames and hot-flames two distinct peaks of conditional scalar dissipation rate can be expected in the low- and high-temperature regions of composition space, with a region of relatively low scalar dissipation in between. The challenge of modelling conditional scalar dissipation rates therefore presents a significant barrier to application of DCMC-like methods for problems combining multi-stage ignition and flame propagation: It is necessary for the progress variable conditional scalar dissipation rate model to account for the reaction-diffusion dynamics of the particular combustion problem.

The new age-based approach to modelling of progress variable conditional scalar dissipation rate given by Eq. 6.4 in Chapter 6 provides a possible approach for addressing this problem. In order to illustrate the age-based approach in this context, a DCMC solution for the relative age, $Q_{\hat{a}}$, is computed from the N_60_30_0 DCMC solution as a post processing step keeping the $\dot{\omega}_{c^*}$ and $\langle N_\xi \mid \eta \rangle$ fields fixed, yielding the age-contour plot in Fig. 8.3a. The corresponding conditional progress variable scalar dissipation rate given by Eq. 6.4 is plotted in Fig. 8.3b. Equation 6.4 predicts a complex structure entirely different from the bell-shaped Amplitude Mapping Closure, containing distinct peaks corresponding to low and high-temperature chemistry fronts expected in this case. The new modelling approach provides a means to take account of the reaction-diffusion dynamics of any particular combustion case. The different scalar dissipation rate structure is expected to significantly modify the sensitivity of the ignition process to the unconditional progress variable scalar dissipation rate imposed.

The prediction of the conditional progress variable scalar dissipation rate given by Eq.

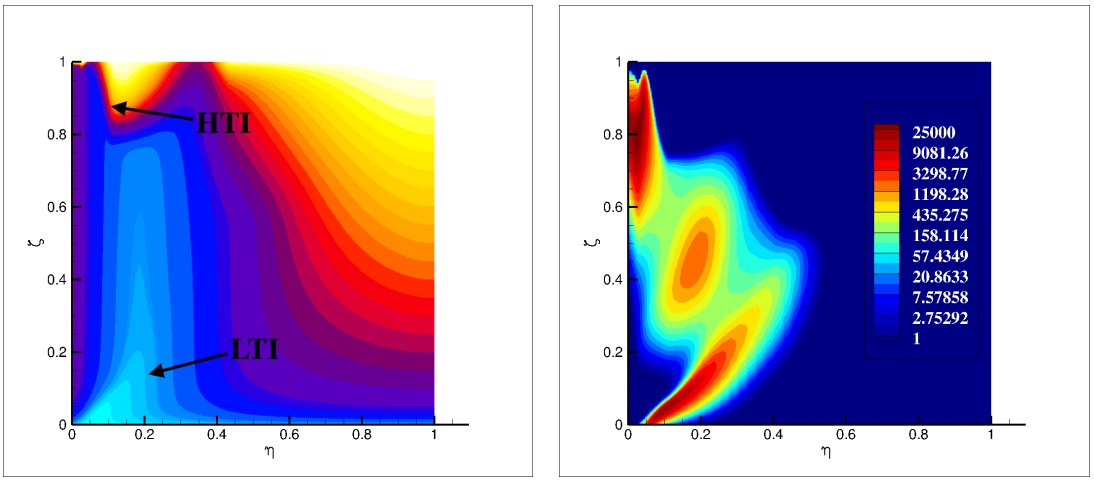

(a) $\langle Q_{\hat{a}} | \eta, \zeta \rangle$ (b) $\langle N_c | \eta, \zeta \rangle$

Figure 8.6: Multi-dimensional flamelet solution of relative age. (a) conditional distribution of relative age: LTI corresponds to Low-Temperature Ignition, and HTI to High-Temperature Ignition ; (b) progress variable scalar dissipation rate using model from Eq. 6.4.

6.4 remains to be validated for combustion processes involving two-stage ignition combustion processes. The impact of this alternative model on predictions of ignition processes also needs to be established.

8.4 Conclusion

The Rapid Compression and Expansion Machine experiment from Refs. [214, 216] was modelled using Double Conditional Moment Closure based on mixture fraction and progress variable. The DCMC model was implemented into CFD simulation using a lookup table approach, modelling the joint mixture fraction-progress variable pdf with independent β-function distributions and the conditional scalar dissipation rates with bell-shaped profiles.

For low progress variable dissipation rates, the DCMC solution exhibits two-stage ignition. The magnitude of the first-stage reaction rates are attenuated as the progress variable dissipation rate increases, resulting in extension of ignition delay beyond that observed in the experiment. This behaviour is a feature of the simplistic 'amplitude mapping closure' modelling employed for progress variable conditional scalar dissipation rates. The amplitude mapping closure is built on an assumption that the progress variable coordinate spans a single mixing structure characterised by single length scale. Due

to the time interval that separates first and second stage ignition processes and their differing chemical kinetic rates, the analysis shows that more sophisticated modelling of the conditional reaction rates is required for DCMC in flow regions involving two-stage ignition, or containing both ignition and flame propagation. This indicates that, for successful DCMC modelling of dual-fuel combustion, it is important to account for the spatio-temporal variation of scalar dissipation rate levels, either by adding spatial dimensions to the DCMC approach or, for the present uncoupled/tabulated DCMC implementation, by including scalar dissipation rate coordinates in the look-up table. The age-based approach developed for modelling the joint-pdf in Chapter 6 also suggests new possibilities for modelling the progress variable conditional scalar dissipation rate, and this is a subject that warrants further investigation.

Chapter 9

Conclusion

Pilot-ignited dual-fuel combustion is an attractive strategy for utilising lean mixtures of alternative fuels such as natural gas in internal combustion engines, promising high thermal efficiency and low exhaust emissions. The combustion process is fundamentally different from classical compression ignition and spark ignition engines. The dual-fuel combustion process involves competition between deflagration, diffusion and autoignition combustion modes. *Theory and modelling of dual-fuel combustion* develops modelling appraoches for dual-fuel engine simulation, addressing three fundamental questions that arise in dual-fuel engines, in addition to the challenges of the better-understood single fuel diesel engine: (a) the combined influence of the two fuels on the ignition process; (b) the effect of the inhomogeneous and reactive conditions on the flame structure; (c) and the effect of both fuels on flame propagation speed. These challenges are addressed in fundamental investigations of laminar and then turbulent flows, with this understanding contributing to development of two modelling strategies for duel-fuel combustion: a hybrid non-premixed/premixed approach, and a more general approach describing multiple combustion modes.

9.1 Dual-fuel flame propagation in laminar flow

The influence of pre-ignition chemical processes on flame propagation is investigated first in laminar flow in Chapter 4. It is found that fuel-blends that exhibit two-stage ignition undergo a significant increase in the laminar flame speed before ignition. The

production of intermediate species and the heat released during first-stage ignition both make significant contributions to the increase of the laminar flame speed. Methane addition in the fuel blend reduces the contribution of first-stage ignition to flame speed enhancement because of dilution of the more reactive fuel and consumption of radicals by the CH_4 chemical kinetics. The flame can be classified as deflagrative or ignitive depending on the magnitude of the diffusion contribution in the flame front, and it is shown that the nature of the reaction front can alternatively be characterised by considering the scaling of the flame thickness with respect to thermal diffusivity and flame speed. Despite significant increase in flame speed, the reaction fronts remain deflagrative until the residence time in the mixture approaches the ignition delay time. A new flame speed model is developed to account for the contributions of heat release, reactant consumption, and enhanced reactivity ahead of the flame. The model correctly captures the variation of flame speed for the full range of methane/n-heptane fuel blends at relevant engine conditions up to the transition to ignition.

9.2 Ignition processes, flame propagation and flame structure in turbulent flow

The ignition process in turbulent and laminar dual-fuel combustion is investigated in Chapter 5. The chemical contribution of methane to the early stages of dual-fuel combustion are analysed in DNS calculations of a dimethyl-ether/methane-air mixing layer using multi-step chemistry. The chemical contribution of the premixed fuel was isolated by comparing the ignition process with a simulation in which methane was treated as inert. The retarded ignition delay time for dual-fuel combustion has been observed in the literature and was captured in the calculation. The analysis revealed an increased sensitivity to fluid dynamic strain associated with methane addition due to chemical interaction involving CH_4, and this is the leading cause of the DME-methane mixture's increased ignition delay time when subject to turbulent mixing. The heat released during first-stage ignition is significantly reduced by the methane chemistry, nonetheless it still shifts the ignition to richer mixtures as previously observed in diesel-like autoignition.

The first application of Chemical Explosive Mode Analysis to dual-fuel combustion reveals a complex combustion process in which the majority of the inhomogeneous mixture

is consumed by diffusion-assisted ignition, i.e. deflagration. Therefore, the correct description of flame propagation in inhomogeneous and partially reacted mixtures present in the early stages of dual-fuel combustion is key to the modelling of dual-fuel combustion. The consumption of the stoichiometric mixture occurs through the propagation of a *polybrachial* flame structure with a cool-flame forming the additional branch of the classical triple flame. The lean methane-air flame is observed to be initiated by the lean branch of the *polybrachial* structure.

During the early stages of lean flame propagation the displacement speed is highly affected by mixture reactivity, stratification and unsteadiness. Curvature is also observed to play an important role in flame speed enhancement. The flame speed model developed in Chapter 4 is used to quantify the low-temperature chemistry effects on displacement speed. It is shown that in the region with large/moderate gradients of mixture fraction the combined effects of back-support and unsteadiness increase the displacement speed by a similar amount to the effect of pre-ignition chemistry. The mean displacement speed of flames approaching the premixed methane/air at the edge of the pilot region is observed to be greater than the laminar flame speed for that mixture, highlighting the importance of accounting for effects of pre-ignition chemistry on the deflagration speed.

9.3 Duel-fuel combustion modelling

A combination of different approaches is identified for modelling the premixed and non-premixed phases of dual-fuel combustion. Two different modelling approaches are developed: a hybrid mixture fraction Conditional Moment Closure (CMC)/G-equation approach; and a mixture fraction-progress variable Double Conditional Moment Closure (DCMC). These approaches are tested considering experimental data for a dual-fuel Rapid Compression-Expansion Machine in Chapters 7 and 8.

Hybrid modelling: The hybrid approach developed in Chapter 7 uses Conditional Moment Closure (CMC) to model the autoigniting diffusion flame and G-equation to capture the premixed phase. The effects of partially reacted fuel and mixture inhomogeneity are taken into account by the laminar flame speed model developed in Chapter 4. The model adequately captures ignition and the transition to flame propagation of

the n-heptane pilot-ignited methane-air experiment used for validation. Predictions of heat release rate presented sensitivity to the turbulence flame speed correlation and the ignition criterion used to couple the CMC and G-equation models. Even though the ignition time remains similar, the criterion had a major impact on the ignition location. The presence of n-heptane and pre-ignition reactions on the laminar flame speed model was demonstrated to increase the burning rate at certain locations of the combustion chamber. The over-prediction of ignition delay time is associated with the limitation of the reduced n-heptane chemical mechanism to properly account for dual-fuel ignition kinetics. Sensitivity to the criteria used for transitioning between the CMC ignition model and the G-equation flame propagation model motivates development of more general double-conditional moment closure (DCMC) modelling that can be applied to the entire combustion process.

DCMC modelling for partially premixed combustion: An implementation of the DCMC approach is developed and initial application for dual-fuel combustion is presented in Chapter 8. Use of DCMC relies on modelling for the joint-pdf of mixture fraction and progress variable. Chapter 6 examines their joint-pdf in three DNS cases corresponding to different partially-premixed combustion modes that may arise in dual-fuel engines. It is observed that each case exhibits statistical dependence between mixture fraction and progress variable, and that the nature of the statistical dependence is qualitatively different during autoignition, local extinction, re-ignition, and in equivalence ratio-stratified flame propagation due to different reaction-diffusion dynamics. It is shown that the common approximation of neglecting this dependence can lead to substantial errors in closure of reaction rates. A new 'age-based' approach for modelling the joint-pdf is tested, using the DCMC solution in order to take account of the effect of the reaction-diffusion dynamics on the shape of the joint-pdf. The age-based approach correctly predicts the qualitatively-different dependence structures in each of the DNS cases considered. Even with only three input moments, the age-based approach gives the best reaction rate predictions of any of the joint-pdf models considered, however it is noted that a priori testing of models can be misleading, since the model for the moments (taken from the DNS) is not consistent with the reaction rate predictions (from the DCMC model and the modelled joint-pdf). Therefore a posteriori testing in LES or RANS is needed to confirm the validity of the age-based approach. However,

correct prediction of the dependence structure across a wide range of combustion conditions suggests that the physical basis for the age-based approach is correct and that the improvement in predictions is achieved for the right reasons.

Application of DCMC modelling to duel-fuel combustion: The DCMC approach is applied to dual-fuel combustions in Chapter 8 for the conditions of a dodecane-methane dual-fuel Rapid Compression-Expansion Machine experiment. The sensitivity of the DCMC solution to mixing is examined by varying the magnitude of the progress variable dissipation rate. For low progress variable dissipation rates, the solution exhibits two-stage ignition. The magnitude of the first-stage reaction rates is attenuated as the progress variable dissipation rate increases, resulting in extension of ignition delay beyond that observed in the experiment. This behaviour is a feature of the simplistic 'amplitude mapping closure' modelling employed for progress variable conditional scalar dissipation rates. The amplitude mapping closure is built on an assumption that the progress variable coordinate spans a single mixing structure characterised by single length scale. Due to the time interval that separates first and second stage ignition processes and their differing chemical kinetic rates, the analysis shows that more sophisticated modelling of the conditional reaction rates is required for DCMC in flow regions involving two-stage ignition, or containing both ignition and flame propagation. This indicates that, for successful DCMC modelling of dual-fuel combustion, it is important to account for the spatio-temporal variation of scalar dissipation rate levels, either by adding spatial dimensions to the DCMC approach or, for the present uncoupled/tabulated DCMC implementation, by including scalar dissipation rate coordinates in the look-up table. The age-based approach developed for modelling the joint-pdf in Chapter 6 also suggests new possibilities for modelling the progress variable conditional scalar dissipation rate, and this is a subject that warrants further investigation.

9.4 Future work

This section provides insights of future work regarding the different aspects of dual-fuel combustion modelling addressed in this thesis.

The application of DCMC modelling to dual-fuel combustion could be investigated using the DNS simulation presented in Chapter 5. The assumptions regarding the two conditioning variables and the models for conditional scalar dissipation rates can be evaluated *a posteriori* by running the DNS with additional transport equations for mixture fraction and progress variable and obtaining reaction source term from the DCMC.

The model presented in Chapter 6 for the conditional progress variable dissipation rate based on the distribution of age is a promissing possibility to overcome the difficulties of having one single conditional state to model the two-stage autoigniting process and the subsequent flame propagation observed in dual-fuel combustion. However, the proposed model requires further investigation at those conditions. DNS or well-resolved LES simulations at relevant thermochemical conditions can provide the information necessary to verify the validity and predictions of the scalar dissipation rate model.

The application of the DCMC model on a dual-fuel engine-like simulation was presented in Chapter 8. Nonetheless, the model validation still requires a more realistic experiment where the entire combustion process can be succesfully compared with the simulation. A direct comparison of the DCMC and hybrid modelling approaches for the same test case can highlight the implications of using each of the models.

Appendix A

Procedure for removing intermediate species ahead of the flame

The modified flame simulation involves two steps illustrated in Fig. A.1.

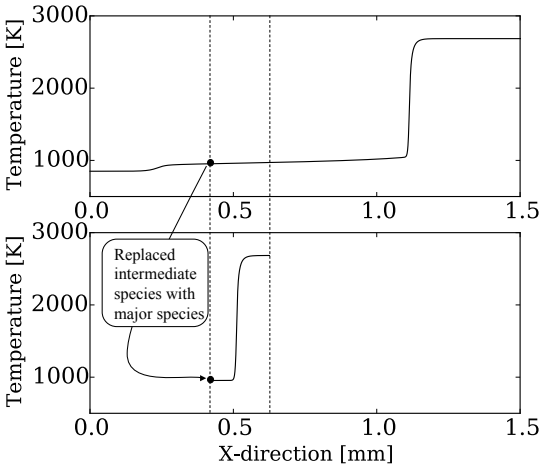

Figure A.1: Illustration of the reduced-domain simulation procedure: temperature field from a full-domain simulation of a stoichiometric n-heptane–air flame with $\tau_f = 0.95\tau_{ign}$ (top); temperature field from the reduced-domain simulation.

Step 1

The first step determines the modified composition ahead of the flame. A single precursor flame simulation (Fig. A.1 top) is used to determine the variation of the reactant composition with residence time upstream of the flame front. The composition recorded for each residence time is then modified by replacing the intermediate species with a mixture of reactants and major products of stoichiometric combustion, while keeping the temperature and total enthalpy unchanged. The replacement mixture consists of CH_4, C_7H_{16}, O_2, N_2, CO_2, and H_2O. The modified mass fraction vector $\mathbf{Y}'$ is calculated by weighting the unburnt and burnt composition of complete combustion, $\mathbf{Y}_u$ and $\mathbf{Y}_b$ respectively, with an enthalpy-based progress variable c_h

$$\mathbf{Y}' = \mathbf{Y}_b c_h + \mathbf{Y}_u(1 - c_h). \tag{A.1}$$

The burnt composition is taken as the products of complete stoichiometric combustion, consisting of N_2, CO_2 and H_2O. The progress variable c_Y is given by

$$c_h = \frac{\sum_{\alpha=1}^{nspec} [Y_\alpha h_\alpha(T) - Y_{\alpha,u} h_\alpha(T_u)]}{\sum_{\alpha=1}^{nspec} [Y_{\alpha,b} h_\alpha(T_b) - Y_{\alpha,u} h_\alpha(T_u)]}, \tag{A.2}$$

where $\mathbf{Y}$ and T are the original unmodified mass fraction vector and temperature, and h_α is the specific total enthalpy of each species.

Step 2

The second step produces a flame solution using the modified composition as the inlet condition with the flame positioned 67μm from the inlet (Fig. A.1 bottom). The total domain length is 200 μm. The flame residence time for the modified flame simulation is sufficiently small that the results are not influenced significantly by chemical reaction upstream of the modified flame front, and sufficiently large that the flame speed is not influenced significantly by diffusive flux through the domain inlet. This is confirmed in Fig. 4.9 by applying the two-step procedure without removing intermediate species from the reactant mixture: the flame speeds obtained using this 'reduced' solution domain closely follow the residence time-dependence obtained using a single 'full' solution domain with the same total residence time. The difference due to the use of the reduced domain procedure is negligible compared with the effect of replacing the intermediate

species. This confirms the validity of the modified flame approach for determining the relative influences of intermediate species and thermal effects.

Appendix B

Validation of the DME/CH4 chemical mechanism

Figure B.1 presents the comparison of ignition delay time predictions using the detailed [30] and reduced 25-species mechanisms for the conditions used in the DNS calculations. The reduced mechanism is capable of correctly predicting the first- and second-stage ignition delay times.

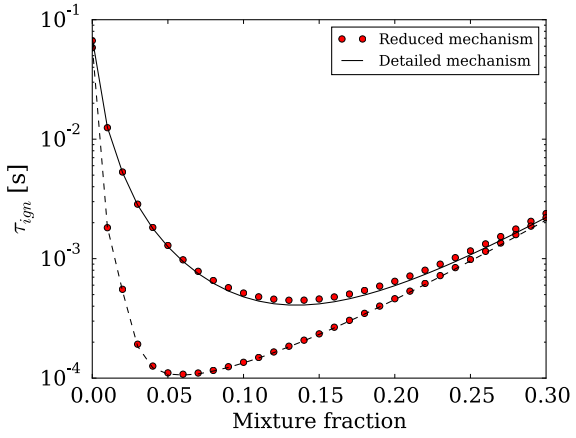

Figure B.1: Ignition delay times using reduced and detailed mechanisms. Dashed-line corresponds to first-stage ignition; Solid line to ignition delay time.

The reduced mechanism also presents high accuracy on predicting the laminar flame speeds for the all fuel blends at high temperatures and pressures, as presented in Fig. B.2.

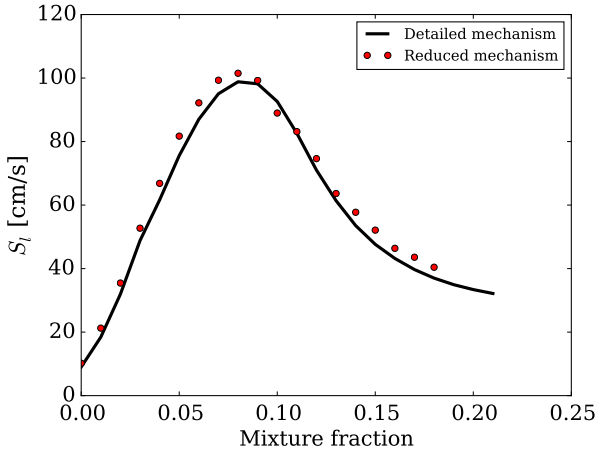

Figure B.2: Laminar flame speed predictions using reduced and detailed mechanisms

References

[1] Chemical-kinetic mechanisms for combustion applications, version 2014-10-04, San Diego. *Mechanism web page, Mechanical and Aerospace Engineering (Combustion Research), University of California at San Diego.*

[2] Cosilab Software. Technical report, Cosilab, Rotexo Software, Bochum, 2011.

[3] C Abagnale, M C Cameretti, L De Simio, M Gambino, S Iannaccone, and R Tuccillo. Numerical simulation and experimental test of dual fuel operated diesel engines. *Applied Thermal Engineering*, 65(1-2):403–417, 2014.

[4] G H Abd Alla, O A Badr, H A Soliman, and M F Abd Rabbo. Exhaust emissions from an indirect injection dual-fuel engine. *Proceedings of the Institution of Mechanical Engineers, Part D: Journal of Automobile Engineering*, 214(3):333–340, 2005.

[5] G H Abd Alla, H A Soliman, O A Badr, and M F Abd Rabbo. Effect of pilot fuel quantity on the performance of a dual fuel engine. *Energy Conversion and Management*, 41(6):559–572, apr 2000.

[6] G H Abd Alla, H A Soliman, O A Badr, and M F Abd Rabbo. Combustion quasi-two zone predictive model for dual fuel engines. *Energy Conversion and Management*, 42(12):1477–1498, aug 2001.

[7] S K Aggarwal, O Awomolo, and K Akber. Ignition characteristics of heptane–hydrogen and heptane–methane fuel blends at elevated pressures. *international journal of hydrogen energy*, 36(23):15392–15402, 2011.

[8] Irufan Ahmed. *Simulation of turbulent flames relevant to spark-ignition engines.* PhD thesis, University of Cambridge, 2014.

[9] S Amzin, N Swaminathan, J W Rogerson, and J H Kent. Conditional moment closure for turbulent premixed flames. *Comb. Sci. Technol.*, 184(10-11):1743–1767, 2012.

[10] Shokri Amzin and Nedunchezhian Swaminathan. Computations of turbulent lean premixed combustion using conditional moment closure. *Combust. Theor. Modell.*, 17(6):1125–1153, 2013.

[11] A. Avdić, G. Kuenne, and J. Janicka. Flow Physics of a Bluff-Body Swirl Stabilized Flame and their Prediction by Means of a Joint Eulerian Stochastic Field and Tabulated Chemistry Approach. *Flow, Turbulence and Combustion*, 97(4):1185–1210, dec 2016.

[12] F Battin-Leclerc. Detailed chemical kinetic models for the low-temperature combustion of hydrocarbons with application to gasoline and diesel fuel surrogates. *Progress in Energy and Combustion Science*, 34(4):440–498, 2008.

[13] Ankit Bhagatwala, Zhaoyu Luo, Han Shen, Jeffrey a. Sutton, Tianfeng Lu, and Jacqueline H Chen. Numerical and experimental investigation of turbulent DME jet flames. *Proceedings of the Combustion Institute*, 35(2):1157–1166, 2014.

[14] Ankit Bhagatwala, Ramanan Sankaran, Sage Kokjohn, and Jacqueline H Chen. Numerical investigation of spontaneous flame propagation under RCCI conditions. *Combustion and Flame*, 162(9):3412–3426, 2014.

[15] R. W. Bilger. The Structure of Diffusion Flames. *Combustion Science and Technology*, 13(1-6):155–170, jul 1976.

[16] R W Bilger. Conditional Moment Closure for Turbulent Reacting Flow. *Physics of Fluids a-Fluid Dynamics*, 5(2):436–444, 1993.

[17] Mi. Bolla, Y M Wright, K Boulouchos, G Borghesi, and E Mastorakos. Soot Formation Modeling of n -Heptane Sprays Under Diesel Engine Conditions Using the Conditional Moment Closure Approach. *Combustion Science and Technology*, 185(5):766–793, 2013.

[18] Michele Bolla. *Modeling Soot Formation in Diesel Engines using Conditional Moment Closure*. PhD thesis, ETH Zürich, 2013.

[19] Michele Bolla, Daniele Farrace, Yuri M Wright, Konstantinos Boulouchos, and Epaminondas Mastorakos. Influence of turbulencechemistry interaction for n - heptane spray combustion under diesel engine conditions with emphasis on soot formation and oxidation. *Combustion Theory and Modelling*, 18(2):330–360, 2014.

[20] Michele Bolla, Thordur Gudmundsson, Yuri M Wright, and Konstantinos Boulouchos. Simulations of Diesel Sprays Using the Conditional Moment Closure Model. *SAE Int. J. Engines*, 6(2):1249–1261, 2013.

[21] S. Bondi and W.P. Jones. A combustion model for premixed flames with varying stoichiometry. *Proceedings of the Combustion Institute*, 29(2):2123–2129, jan 2002.

[22] G Borghesi, E Mastorakos, C B Devaud, and R W Bilger. Modeling evaporation effects in conditional moment closure for spray autoignition. *Combustion Theory and Modelling*, 15(5):725–752, 2011.

[23] K N C Bray and J B Moss. A unified statistical model of the premixed turbulent flame. *Acta Astronautica*, 4(3-4):291–319, mar 1977.

[24] K.N.C. Bray. The challenge of turbulent combustion. *Symposium (International) on Combustion*, 26(1):1–26, jan 1996.

[25] K.N.C. Bray, M. Champion, P.A. Libby, and N. Swaminathan. Finite rate chemistry and presumed PDF models for premixed turbulent combustion. *Combustion and Flame*, 146(4):665–673, sep 2006.

[26] British Petroleum. BP Statistical Review of World Energy, 2015.

[27] Peter N Brown, George D Byrne, and Alan C Hindmarsh. VODE, a variable-coefficient ODE solver. Technical report, Lawrence Livermore National Laboratory, 1988.

[28] Peter N Brown and Alan C Hindmarsh. Reduced storage matrix methods in stiff ODE systems. Technical report, Lawrence Livermore National Laboratory, 1987.

[29] A J M Buckrell and C B Devaud. Investigation of mixing models and conditional moment closure applied to autoignition of hydrogen jets. *Flow, Turbulence and Combustion*, 90(3):621–644, 2013.

[30] Ultan Burke, Kieran P. Somers, Peter O'Toole, Chis M. Zinner, Nicolas Marquet, Gilles Bourque, Eric L. Petersen, Wayne K. Metcalfe, Zeynep Serinyel, and Henry J. Curran. An ignition delay and kinetic modeling study of methane, dimethyl ether, and their mixtures at high pressures. *Combustion and Flame*, 162(2):315–330, feb 2015.

[31] G D Byrne. Pragmatic Experiments with Krylov Methods in the Stiff ODE Setting. In J Cash and I Gladwell, editors, *Computational ordinary differential equations*, pages 323–356. Oxford University, Oxford, 1992.

[32] M C Cameretti, R Tuccillo, L De Simio, S Iannaccone, and U Ciaravola. A numerical and experimental study of dual fuel diesel engine for different injection timings. *Applied Thermal Engineering*, jan 2016.

[33] Shufen Cao and Tarek Echekki. Autoignition in nonhomogeneous mixtures: Conditional statistics and implications for modeling. *Combustion and Flame*, 151(1-2):120–141, oct 2007.

[34] Michael Carlowicz. Nasa Earth Observatory - Global Temperatures, 2010.

[35] A Carlucci, D Laforgia, R Saracino, and G Toto. Study of Combustion Development in Methane-Diesel Dual Fuel Engines, Based on the Analysis of In-Cylinder Luminance. *SAE Technical Paper*, (2010-01-1297), 2010.

[36] CD-adapco. CD-adapco website.

[37] CD-adapco. Star cd ®version 4.24 Methodology, 2015.

[38] By Chong M Cha and George Kos. Doubly-conditional moment closure modeling of turbulent nonpremixed combustion. (1999), 2000.

[39] Chong M Cha, George Kosaly, and Heinz Pitsch. Modeling extinction and reignition in turbulent nonpremixed combustion using a doubly-conditional moment closure approach. *Physics of Fluids*, 13(12):3824–3834, 2001.

[40] Chong M Cha and Heinz Pitsch. Higher-order conditional moment closure modelling of local extinction and reignition in turbulent combustion. *Combustion Theory and Modelling*, 6(3):425–437, sep 2002.

[41] J H Chen, A Choudhary, B de Supinski, M DeVries, E R Hawkes, S Klasky, W K Liao, K L Ma, J Mellor-Crummey, N Podhorszki, R Sankaran, S Shende, and C S Yoo. Terascale direct numerical simulations of turbulent combustion using S3D. *Computational Science & Discovery*, 2(1):15001, 2009.

[42] Jacqueline H Chen, Evatt R Hawkes, Ramanan Sankaran, Scott D Mason, and Hong G Im. Direct numerical simulation of ignition front propagation in a constant volume with temperature inhomogeneities: I. Fundamental analysis and diagnostics. *Combustion and Flame*, 145(1):128–144, 2006.

[43] Haeng Muk Cho and Bang-Quan He. Spark ignition natural gas enginesA review. *Energy Conversion and Management*, 48(2):608–618, feb 2007.

[44] H K Ciezki and G Adomeit. Shock-tube investigation of self-ignition of n-heptane-air mixtures under engine relevant conditions. *Combustion and Flame*, 93(4):421–433, 1993.

[45] O Colin, A Benkenida, and C Angelberger. 3D modeling of mixing, ignition and combustion phenomena in highly stratified gasoline engines. *Oil & gas science and technology*, 58(1):47–62, 2003.

[46] S Cordiner, V Rocco, R Scarcelli, and M Gambino. Experiments and Multi-Dimensional Simulation of Dual-Fuel Diesel/Natural Gas Engines. *SAE Technical paper*, (2007-24-0124):18, 2007.

[47] Cosilab. Manual. Technical report, Rotexo Software, Bochum, 2011.

[48] H J Curran, P Gaffuri, W J Pitz, and C K Westbrook. A Comprehensive Modeling Study of n-Heptane Oxidation. *Combustion and Flame*, 114(1):149–177, 1998.

[49] J Dale. Application of high energy ignition systems to engines. *Progress in Energy and Combustion Science*, 23(5-6):379–398, 1997.

[50] O. R. Darbyshire and N. Swaminathan. A Presumed Joint pdf Model for Turbulent Combustion with Varying Equivalence Ratio. *Combustion Science and Technology*, 184(12):2036–2067, dec 2012.

[51] G de Paola. Conditional Moment Closure for Autoignition in Turbulent flows. *University of Cambridge*, (May), 2007.

[52] G De Paola, I S Kim, and E Mastorakos. Second-order conditional moment closure simulations of autoignition of an n-heptane plume in a turbulent coflow of heated air. *Flow, Turbulence and Combustion*, 82(4):455–475, 2009.

[53] G De Paola, E Mastorakos, Y M Wright, and K Boulouchos. Diesel Engine Simulations with Multi-Dimensional Conditional Moment Closure. *Combustion Science and Technology*, 180(912941598):883–899, 2008.

[54] John E Dec. A conceptual model of DI diesel combustion based on laser-sheet imaging. Technical report, SAE technical paper, 1997.

[55] Elena Demosthenous, Giulio Borghesi, Epaminondas Mastorakos, and Robert Stewart Cant. Direct Numerical Simulations of premixed methane flame initiation by pilot n-heptane spray autoignition. *Combustion and Flame*, 163:122–137, jan 2016.

[56] Elena Demosthenous, Epaminondas Mastorakos, and Robert Stewart Cant. Direct Numerical Simulations of Dual-Fuel Non-Premixed Autoignition. *Combustion Science and Technology*, 188(4-5):542–555, may 2016.

[57] C Devaud. Assessment of the applicability of conditional moment closure to a lifted turbulent flame: first order model. *Combustion and Flame*, 132(1-2):102–114, jan 2003.

[58] V Di Sarli and A Di Benedetto. Laminar burning velocity of hydrogen–methane/air premixed flames. *International Journal of Hydrogen Energy*, 32(5):637–646, 2007.

[59] P. Domingo and L. Vervisch. Triple flames and partially premixed combustion in autoignition of non-premixed turbulent mixtures. *Symposium (International) on Combustion*, 26(1):233–240, jan 2007.

[60] Frederick L Dryer. Chemical kinetic and combustion characteristics of transportation fuels. *Proceedings of the Combustion Institute*, 35(1):117–144, 2015.

[61] Martin A Elliott and Rogers F Davis. Dual-fuel combustion in diesel engines. *Industrial and Engineering Chemistry*, 43(12):2854–2864, 1951.

[62] A Garmory and E Mastorakos. Capturing localised extinction in Sandia Flame F with LES - CMC. *Proceedings of the Combustion Institute*, 33(1):1673–1680, 2011.

[63] B M Gauthier, D F Davidson, and R K Hanson. Shock tube determination of ignition delay times in full-blend and surrogate fuel mixtures. *Combustion and Flame*, 139(4):300–311, 2004.

[64] M. Ghaderi Masouleh, A. Wehrfritz, O. Kaario, H. Kahila, and V. Vuorinen. Comparative study on chemical kinetic schemes for dual-fuel combustion of n-dodecane/methane blends. *Fuel*, 191:62–76, mar 2017.

[65] Federico Ghirelli and Bo Leckner. Transport equation for the local residence time of a fluid. *Chemical Engineering Science*, 59(3):513–523, feb 2004.

[66] A Giusti and Epaminondas Mastorakos. Detailed chemistry LES/CMC simulation of a swirling ethanol spray flame approaching blow-off. *Proceedings of the Combustion Institute*, 36(2):2625–2632, jan 2017.

[67] J Göttgens, F Mauss, and N Peters. Analytic approximations of burning velocities and flame thicknesses of lean hydrogen, methane, ethylene, ethane, acetylene, and propane flames. *Symposium (International) on Combustion*, 24(1):129–135, jan 1992.

[68] J F Griffiths and S K Scott. Thermokinetic interactions: Fundamentals of spontaneous ignition and cool flames. *Progress in Energy and Combustion Science*, 13(3):161–197, 1987.

[69] Xiao Jun Gu, Md Zahurul Haq, Malcolm Lawes, and R Woolley. Laminar burning velocity and Markstein lengths of methane–air mixtures. *Combustion and flame*, 121(1-2):41–58, 2000.

[70] D Gussak, L., Turkish, M., and Siegla. High Chemical Activity of Incomplete Combustion Products and a Method of Prechamber Torch Ignition for Avalanche Activation of Combustion in Internal Combustion Engines. *SAE Technical Paper 750890*, page 25, 1975.

[71] Peter Habisreuther, Flavio Cesar Cunha Galeazzo, Chockalingam Prathap, and Nikolaos Zarzalis. Structure of laminar premixed flames of methane near the auto-ignition limit. *Combustion and Flame*, 160(12):2770–2782, 2013.

[72] M P Halstead, L J Kirsch, and C P Quinn. The autoignition of hydrocarbon fuels at high temperatures and pressuresFitting of a mathematical model. *Combustion and Flame*, 30:45–60, jan 1977.

[73] J Hansen, M Sato, R Ruedy, P Kharecha, A Lacis, R Miller, L Nazarenko, K Lo, G A Schmidt, G Russell, I Aleinov, S Bauer, E Baum, B Cairns, V Canuto, M Chandler, Y Cheng, A Cohen, A Del Genio, G Faluvegi, E Fleming, A Friend, T Hall, C Jackman, J Jonas, M Kelley, N Y Kiang, D Koch, G Labow, J Lerner, S Menon, T Novakov, V Oinas, Ja Perlwitz, Ju Perlwitz, D Rind, A Romanou, R Schmunk, D Shindell, P Stone, S Sun, D Streets, N Tausnev, D Thresher, N Unger, M Yao, and S Zhang. Climate simulations for 1880-2003 with GISS modelE. *Climate Dynamics*, 29(7-8):661–696, 2007.

[74] J Hansen, M Sato, R Ruedy, P Kharecha, A Lacis, R Miller, L Nazarenko, K Lo, G A Schmidt, G Russell, I Aleinov, S Bauer, E Baum, B Cairns, V Canuto, M Chandler, Y Cheng, A Cohen, A Del Genio, G Faluvegi, E Fleming, A Friend, T Hall, C Jackman, J Jonas, M Kelley, N Y Kiang, D Koch, G Labow, J Lerner, S Menon, T Novakov, V Oinas, Ja. Perlwitz, Ju. Perlwitz, D Rind, A Romanou, R Schmunk, D Shindell, P Stone, S Sun, D Streets, N Tausnev, D Thresher, N Unger, M Yao, and S Zhang. Dangerous human-made interference with climate: a GISS modelE study. *Atmos. Chem. Phys.*, 7(9):2287–2312, 2007.

[75] D C Haworth. Progress in probability density function methods for turbulent reacting flows. *Progress in Energy and Combustion Science*, 36(2):168–259, apr 2010.

[76] John B Heywood. *Internal Combustion Engine Fundementals*, volume 21. 1988.

[77] T Hirasawa, C J Sung, A Joshi, Z Yang, H Wang, and C K Law. Determination of laminar flame speeds using digital particle image velocimetry: binary fuel blends of ethylene, n-butane, and toluene. *Proceedings of the Combustion Institute*, 29(2):1427–1434, 2002.

[78] J Huang, W K Bushe, P G Hill, and S R Munshi. Experimental and kinetic study of shock initiated ignition in homogeneous methane–hydrogen–air mixtures at engine-relevant conditions. *International Journal of Chemical Kinetics*, 38(4):221–233, 2006.

[79] Matthias Ihme and Heinz Pitsch. Prediction of extinction and reignition in non-premixed turbulent flames using a flamelet/progress variable model: 2. Application in LES of Sandia flames D and E. *Combustion and Flame*, 155(1-2):90–107, oct 2008.

[80] Matthias Ihme, Lee Shunn, and Jian Zhang. Regularization of reaction progress variable for application to flamelet-based combustion models. *Journal of Computational Physics*, 231(23):7715–7721, 2012.

[81] Hong G Im, Laxminarayan L Raja, Robert J Kee, and Linda R Petzold. A Numerical Study of Transient Ignition in a Counterflow Nonpremixed Methane-Air Flame Using Adaptive Time Integration. *Combustion Science and Technology*, 158(1):341–363, 2000.

[82] S Imran, D R Emberson, B Ihracska, D S Wen, R J Crookes, and T Korakianitis. Effect of pilot fuel quantity and type on performance and emissions of natural gas and hydrogen based combustion in a compression ignition engine. *International Journal of Hydrogen Energy*, 39(10):5163–5175, mar 2014.

[83] B. Jin, R. Grout, and W. K. Bushe. Conditional Source-Term Estimation as a Method for Chemical Closure in Premixed Turbulent Reacting Flow. *Flow, Turbulence and Combustion*, 81(4):563–582, dec 2008.

[84] Tai Jin, Xujiang Wang, Kai H Luo, Kun Luo, and Jianren Fan. Structure of tetrabrachial flames in non-premixed autoigniting dimethyl ether/air mixtures. *Fuel*, 232:90–98, 2018.

[85] Yiguang Ju, Christopher B Reuter, and Sang Hee Won. Numerical simulations of premixed cool flames of dimethyl ether/oxygen mixtures. *Combustion and Flame*, 162(10):3580–3588, 2015.

[86] Heikki Kahila, Armin Wehrfritz, Ossi Kaario, and Ville Vuorinen. Large-eddy simulation of dual-fuel ignition: Diesel spray injection into a lean methane-air mixture. *Combustion and Flame*, 199:131–151, jan 2019.

[87] G A Karim. Combustion in Gas Fueled Compression: Ignition Engines of the Dual Fuel Type. *Journal of Engineering for Gas Turbines and Power*, 125(3):827, 2003.

[88] Ghazi A Karim. A review of combustion processes in the dual fuel engineThe gas diesel engine. *Progress in Energy and Combustion Science*, 6(3):277–285, jan 1980.

[89] Ghazi A. Karim. *Dual-fuel diesel engines*. CRC Press, Boca Raton, 1st edition, 2015.

[90] Kichiro Kato, Kohei Igarashi, and Michihiko Masuda. Development of Engine for Natural Gas Vehicle. *SAE Technical*, (724), 1999.

[91] R J Kee, J F Grcar, M D Smooke, J A Miller, and E Meeks. PREMIX : A FORTRAN Program for Modeling Steady Laminar One-Dimensional Premixed Flames. *Design*, (April):1–87, 1998.

[92] R.J. Kee, F.M. Rupley, E. Meeks, and J.A. Miller. CHEMKIN-III: A FORTRAN chemical kinetics package for the analysis of gas-phase chemical and plasma kinetics. Technical report, Sandia National Laboratories (SNL), Albuquerque, NM, and Livermore, CA (United States), may 1996.

[93] Robert J. Kee, G. Dixon-Lewis, Jurgen Warnatz, M.E. Coltrin, and James A. Miller. A FORTRAN computer code package for the evaluation of gas-phase multicomponent transport properties. *Sandia report*, SAND86-824(December):3–39, 1986.

[94] Christopher A. Kennedy and Mark H. Carpenter. Several new numerical methods for compressible shear-layer simulations. *Applied Numerical Mathematics*, 14(4):397–433, jun 1994.

[95] Christopher A Kennedy, Mark H Carpenter, and R.Michael Lewis. Low-storage, explicit RungeKutta schemes for the compressible NavierStokes equations. *Applied Numerical Mathematics*, 35(3):177–219, nov 2000.

[96] G Kim, S Kang, Y Kim, R W Bilger, and M J Cleary. Conditional moment closure and transient flamelet modelling for detailed structure and NOx formation characteristics of turbulent nonpremixed jet and recirculating flames. *Combustion Theory and Modelling*, 11(4):527–552, 2007.

[97] S H Kim and K Y Huh. Second-Order Conditional Moment Closure Modeling of Turbulent Piloted Jet Diffusion Flames. *Comb. and Flame*, 138(4):336–352, 2004.

[98] T Kitamura, T Ito, J Senda, and H Fujimoto. Mechanism of smokeless diesel combustion with oxygenated fuels based on the dependence of the equivalence ration and temperature on soot particle formation. *International Journal of Engine Research*, 3(4):223–248, 2005.

[99] A Y Klimenko and R W Bilger. Conditional moment closure for turbulent combustion. *Progress in Energy and Combustion Science*, 25(6):595–687, 1999.

[100] A Yu Klimenko. Multicomponent diffusion of various admixtures in turbulent flow. *Fluid Dynamics*, 25(3):327–334, 1990.

[101] E. Knudsen, E. S. Richardson, E. M. Doran, H. Pitsch, and J. H. Chen. Modeling scalar dissipation and scalar variance in large eddy simulation: Algebraic and transport equation closures. *Physics of Fluids*, 24(5):055103, may 2012.

[102] Sage L Kokjohn and Rolf D Reitz. Reactivity controlled compression ignition and conventional diesel combustion: A comparison of methods to meet light-duty NOx and fuel economy targets. *International Journal of Engine Research*, 14(5):452–468, 2013.

[103] H. Kolla, J. W. Rogerson, N. Chakraborty, and N. Swaminathan. Scalar Dissipation Rate Modeling and its Validation. *Combustion Science and Technology*, 181(3):518–535, feb 2009.

[104] T Korakianitis, A M Namasivayam, and R J Crookes. Natural-gas fueled spark-ignition ({SI}) and compression-ignition ({CI}) engine performance and emissions. *Progress in Energy and Combustion Science*, 37(1):89–112, 2011.

[105] T. Korakianitis, A.M. Namasivayam, and R.J. Crookes. Diesel and rapeseed methyl ester (RME) pilot fuels for hydrogen and natural gas dual-fuel combustion in compressionignition engines. *Fuel*, 90(7):2384–2395, jul 2011.

[106] S R Krishnan, K K Srinivasan, S Singh, S R Bell, K C Midkiff, W Gong, S B Fiveland, and M Willi. Strategies for Reduced NOx Emissions in Pilot-Ignited Natural Gas Engines. *Journal of Engineering for Gas Turbines and Power*, 126(3):665, 2004.

[107] Alex Krisman, Evatt R Hawkes, and Jacqueline H Chen. The structure and propagation of laminar flames under autoignitive conditions. *Combustion and Flame*, 188:399–411, 2018.

[108] Alex Krisman, Evatt R Hawkes, Mohsen Talei, Ankit Bhagatwala, and Jacqueline H Chen. Polybrachial structures in dimethyl ether edge-flames at negative temperature coefficient conditions. *Proceedings of the Combustion Institute*, 35(1):999–1006, jan 2015.

[109] Alex Krisman, Evatt R Hawkes, Mohsen Talei, Ankit Bhagatwala, and Jacqueline H Chen. A direct numerical simulation of cool-flame affected autoignition in diesel engine-relevant conditions. *Proceedings of the Combustion Institute*, 000(3):1–9, 2016.

[110] Alex Krisman, Evatt R Hawkes, Mohsen Talei, Ankit Bhagatwala, and Jacqueline H Chen. Characterisation of two-stage ignition in diesel engine-relevant thermochemical conditions using direct numerical simulation. *Combustion and Flame*, 172:326–341, 2016.

[111] A Kronenburg. Double conditioning of reactive scalar transport equations in turbulent nonpremixed flames. *Physics of Fluids*, 16(7):2640–2648, 2004.

[112] Prithwish Kundu, Muhsin M Ameen, and Sibendu Som. Importance of turbulence-chemistry interactions at low temperature engine conditions. *Combustion and Flame*, 183:283–298, sep 2017.

[113] T. Landenfeld, A. Sadiki, and J. Janicka. A turbulence-chemistry interaction model based on a multivariate presumed beta-PDF method for turbulent flames. *Flow, Turbulence and Combustion*, 68(2):111–135, 2002.

[114] Jing Li, Wenming Yang, and Dezhi Zhou. Review on the management of RCCI engines. *Renewable and Sustainable Energy Reviews*, 69:65–79, mar 2017.

[115] N Lida, M Nakamura, and H Ohashi. Study of Diesel Spray Combustion in An Ambient Gas Containing Hydrocarbon Using a Rapid Compression Machine. *SAE Technical Paper*, (970899), 1997.

[116] David O. Lignell, Jacqueline H. Chen, and Hans A. Schmutz. Effects of Damköhler number on flame extinction and reignition in turbulent non-premixed flames using DNS. *Combustion and Flame*, 158(5):949–963, may 2011.

[117] J B Liu and G A Karim. Simulation of combustion processes in gas-fuelled diesel engines. *Proc Instn Mech Engrs*, 211:A, 1997.

[118] Jie Liu, Fuyuan Yang, Hewu Wang, Minggao Ouyang, and Shougang Hao. Effects of pilot fuel quantity on the emissions characteristics of a CNG/diesel dual fuel engine with optimized pilot injection timing. *Applied Energy*, 110:201–206, oct 2013.

[119] Jie Liu, Xin Zhang, Tao Wang, Jibao Zhang, and Hewu Wang. Experimental and numerical study of the pollution formation in a diesel/CNG dual fuel engine. *Fuel*, 159:418–429, 2015.

[120] Shiling Liu, John C Hewson, and Jacqueline H Chen. Nonpremixed n-heptane autoignition in unsteady counterflow. *Combustion and Flame*, 145(4):730–739, 2006.

[121] Shiling Liu, John C Hewson, Jacqueline H Chen, and Heinz Pitsch. Effects of strain rate on high-pressure nonpremixed n-heptane autoignition in counterflow. *Combustion and flame*, 137(3):320–339, 2004.

[122] J C Livengood and P C Wu. Correlation of autoignition phenomena in internal combustion engines and rapid compression machines. In *Symposium (International) on Combustion*, volume 5, pages 347–356, 1955.

[123] Mohand Said Lounici, Khaled Loubar, Lyes Tarabet, Mourad Balistrou, Dan-Catalin Niculescu, and Mohand Tazerout. Towards improvement of natural gas-diesel dual fuel mode: An experimental investigation on performance and exhaust emissions. *Energy*, 64:200–211, jan 2014.

[124] T. F. Lu, C. S. Yoo, J. H. Chen, and C. K. Law. Three-dimensional direct numerical simulation of a turbulent lifted hydrogen jet flame in heated coflow: a chemical explosive mode analysis. *Journal of Fluid Mechanics*, 652:45–64, jun 2010.

[125] Tianfeng Lu, Chung K Law, Chun Sang Yoo, and Jacqueline H Chen. Dynamic stiffness removal for direct numerical simulations. *Combustion and Flame*, 156(8):1542–1551, 2009.

[126] Noud Maes, Maarten Meijer, Nico Dam, Bart Somers, Hubert Baya Toda, Gilles Bruneaux, Scott A. Skeen, Lyle M. Pickett, and Julien Manin. Characterization of Spray A flame structure for parametric variations in ECN constant-volume vessels using chemiluminescence and laser-induced fluorescence. *Combustion and Flame*, 174:138–151, 2016.

[127] Amin Maghbouli, Rahim Khoshbakhti Saray, Sina Shafee, and Jafar Ghafouri. Numerical study of combustion and emission characteristics of dual-fuel engines using 3D-CFD models coupled with chemical kinetics. *Fuel*, 106:98–105, 2013.

[128] a Manivannan, P Tamil, and S Chandrasekaran. Lean Burn Natural Gas Spark Ignition Engine An Overview Reprinted From: SI Combustion. *SAE International*, (724), 2003.

[129] Cheikh Mansour, Abdelhamid Bounif, Abdelkader Aris, and Françoise Gaillard. GasDiesel (dual-fuel) modeling in diesel engine environment. *International Journal of Thermal Sciences*, 40(4):409–424, apr 2001.

[130] T Mantel and R W Bilger. Some conditional statistics in a turbulent premixed flame derived from direct numerical simulations. *Combust. Sci. Technol.*, 111(October):393–417, 1995.

[131] Frank E Marble and James Broadwell. The coherent flame model for turbulent chemical reactions. Technical report, Purdue University, West Lafayette, Indiana, 1977.

[132] C.N. Markides, G. De Paola, and E. Mastorakos. Measurements and simulations of mixing and autoignition of an n-heptane plume in a turbulent flow of heated air. *Experimental Thermal and Fluid Science*, 31(5):393–401, apr 2007.

[133] J B Martz, H Kwak, H G Im, G A Lavoie, and D N Assanis. Combustion regime of a reacting front propagating into an auto-igniting mixture. *Proceedings of the Combustion Institute*, 33(2):3001–3006, 2011.

[134] Scott D Mason, J H Chen, and Hong G Im. Effects of unsteady scalar dissipation rate on ignition of non-premixed hydrogen/air mixtures in counterflow. *Proc. Comb. Inst.*, 29:1629–1636, 2002.

[135] E Mastorakos, T A Baritaud, and T J Poinsot. Numerical simulations of autoignition in turbulent mixing flows. *Combustion and Flame*, 109(1-2):198–223, apr 1997.

[136] Epaminondas Mastorakos. Ignition of turbulent non-premixed flames. *Progress in Energy and Combustion Science*, 35(1):57–97, feb 2009.

[137] Tomas Matheson. *Presumed pdf modelling for turbulent spray combustion.* PhD thesis, University of Southampton, 2016.

[138] M Mbarawa, B E Milton, R T Casey, and H Miao. Fuel injection characteristics of diesel-stimulated natural gas combustion. *International Journal of Energy Research*, 23(15):1359–1371, 1999.

[139] Makame Mbarawa, Brain Edward Milton, and Robert Thomas Casey. Experiments and modelling of natural gas combustion ignited by a pilot diesel fuel spray. *International Journal of Thermal Sciences*, 40(10):927–936, 2001.

[140] Nabil Haque Meah. *Modelling for turbulent autoignition with split fuel injection.* PhD thesis, University of Southampton, 2016.

[141] Marco Mehl, William J Pitz, Charles K Westbrook, and Henry J Curran. Kinetic modeling of gasoline surrogate components and mixtures under engine conditions. *Proceedings of the Combustion Institute*, 33(1):193–200, 2011.

[142] Mohamad Metghalchi and James C Keck. Burning velocities of mixtures of air with methanol, isooctane, and indolene at high pressure and temperature. *Combustion and flame*, 48:191–210, 1982.

[143] Seyed Mohammad Mousavi, Rahim Khoshbakhti Saray, Kamran Poorghasemi, and Amin Maghbouli. A numerical investigation on combustion and emission characteristics of a dual fuel engine at part load condition. *Fuel*, 166:309–319, feb 2016.

[144] Natural & Bio gas Vehicle Association. CO2 & AIR QUALITY.

[145] S Navarro-Martinez and A Kronenburg. LES-CMC simulations of a turbulent bluff-body flame. *Proceedings of the Combustion Institute*, 31 II:1721–1728, 2007.

[146] S Navarro-Martinez and A Kronenburg. LESCMC simulations of a lifted methane flame. *Proceedings of the Combustion Institute*, 32(1):1509–1516, 2009.

[147] Phuc-Danh Nguyen, Luc Vervisch, Vallinayagam Subramanian, and Pascale Domingo. Multidimensional flamelet-generated manifolds for partially premixed combustion. *Combustion and Flame*, 157(1):43–61, jan 2010.

[148] NOAA - National Centers for Environmental Information. State of the Climate: Global Analysis for Annual 2016.

[149] Edward E O'Brien and Tai-Lun Jiang. The conditional dissipation rate of an initially binary scalar in homogeneous turbulence. *Physics of Fluids A: Fluid Dynamics*, 3(12):3121, 1991.

[150] Jiaying Pan, Haiqiao Wei, Gequn Shu, Zheng Chen, and Peng Zhao. The role of low temperature chemistry in combustion mode development under elevated pressures. *Combustion and Flame*, 174:179–193, 2016.

[151] Sushant S Pandurangi, Michele Bolla, Yuri M Wright, Konstantinos Boulouchos, Scott A Skeen, Julien Manin, and Lyle M Pickett. Onset and progression of soot in high-pressure n - dodecane sprays under diesel engine conditions. *International Journal of Engine Research*, 18(5-6):436–452, aug 2017.

[152] R G Papagiannakis and D T Hountalas. Experimental investigation concerning the effect of natural gas percentage on performance and emissions of a DI dual fuel diesel engine. *Applied Thermal Engineering*, 23(3):353–365, feb 2003.

[153] R G Papagiannakis and D T Hountalas. Combustion and exhaust emission characteristics of a dual fuel compression ignition engine operated with pilot Diesel fuel and natural gas. *Energy Conversion and Management*, 45(18-19):2971–2987, nov 2004.

[154] T. Passot and A. Pouquet. Numerical Simulation of Compressible Homogeneous Flows in the Turbulent Regime. *Journal of Fluid Mechanics*, 181:441–466, 1987.

[155] Yuanjiang Pei, Evatt R. Hawkes, Michele Bolla, Sanghoon Kook, Graham M. Goldin, Yue Yang, Stephen B. Pope, and Sibendu Som. An analysis of the structure

of an n-dodecane spray flame using TPDF modelling. *Combustion and Flame*, 168:420–435, jun 2016.

[156] Yuanjiang Pei, Evatt R Hawkes, Michele Bolla, Sanghoon Kook, Graham M Goldin, Yue Yang, Stephen B Pope, and Sibendu Som. An analysis of the structure of an n-dodecane spray flame using TPDF modelling. *Combustion and Flame*, 168:420–435, 2016.

[157] Yuanjiang Pei, Bing Hu, and Sibendu Som. Large-Eddy Simulation of an n-Dodecane Spray Flame Under Different Ambient Oxygen Conditions. *Journal of Energy Resources Technology*, 138(3):032205, 2016.

[158] Yuanjiang Pei, Sibendu Som, Eric Pomraning, Peter K. Senecal, Scott A. Skeen, Julien Manin, and Lyle M. Pickett. Large eddy simulation of a reacting spray flame with multiple realizations under compression ignition engine conditions. *Combustion and Flame*, 162(12):4442–4455, 2015.

[159] Federico Perini, Emanuele Galligani, and Rolf D. Reitz. An analytical Jacobian approach to sparse reaction kinetics for computationally efficient combustion modeling with large reaction mechanisms. *Energy and Fuels*, 26(8):4804–4822, 2012.

[160] N Peters. *Turbulent combustion*, volume 53. Cambrudge University Press, Cambridge, 2004.

[161] Norbert Peters. *Turbulent Combustion*. Cambridge Monographs on Mechanics. Cambridge University Press, 2000.

[162] L Pickett, G Bruneaux, and R Payri. Engine Combustion Network.

[163] Lyle M. Pickett, Jesper Schramm, Caspar Christiansen, Caroline L. Genzale, Louis-Marie Malbec, Gilles Bruneaux, and Laurent Hermant. Comparison of Diesel Spray Combustion in Different High-Temperature, High-Pressure Facilities. *SAE International Journal of Engines*, 3(2):156–181, 2010.

[164] V Pirouzpanah, R Khoshbakhti Saray, A Sohrabi, and A Niaei. Comparison of thermal and radical effects of EGR gases on combustion process in dual fuel engines at part loads. *Energy Conversion and Management*, 48(7):1909–1918, 2007.

[165] H Pitsch. Extended flamelet model for LES of non-premixed. *Annual Research Briefs-2000*, pages 149–158, 2000.

[166] Gianmarco Pizza, Yuri Martin Wright, German Weisser, and Konstantinos Boulouchos. Evaporating and non-evaporating diesel spray simulation : comparison between the ETAB and wave breakup model. *International Journal of Vehicle Design*, 45:80–99, 2007.

[167] T.J Poinsot and S.K Lelef. Boundary conditions for direct simulations of compressible viscous flows. *Journal of Computational Physics*, 101(1):104–129, jul 1992.

[168] Stephen B. Pope. Small scales, many species and the manifold challenges of turbulent combustion. *Proceedings of the Combustion Institute*, 34(1):1–31, jan 2013.

[169] K Radhakrishnan and A C Hindmarsh. Description and use of LSODE, the Livemore Solver for Ordinary Differential Equations. Technical report, Lawrence Livermore National Laboratory (LLNL), Livermore, CA, dec 1993.

[170] E Ranzi, A Frassoldati, R Grana, A Cuoci, T Faravelli, A P Kelley, and C K Law. Hierarchical and comparative kinetic modeling of laminar flame speeds of hydrocarbon and oxygenated fuels. *Progress in Energy and Combustion Science*, 38(4):468–501, 2012.

[171] Eliseo Ranzi, Alessio Frassoldati, Alessandro Stagni, Matteo Pelucchi, Alberto Cuoci, and Tiziano Faravelli. Reduced kinetic schemes of complex reaction systems: fossil and biomass-derived transportation fuels. *International Journal of Chemical Kinetics*, 46(9):512–542, 2014.

[172] R Reitz and R Diwakar. Effect of Drop Breakup on Fuel Sprays. *SAE Technical paper*, (860469), 1986.

[173] Rolf D Reitz and Ganesh Duraisamy. Review of high efficiency and clean reactivity controlled compression ignition (RCCI) combustion in internal combustion engines. *Progress in Energy and Combustion Science*, 46:12–71, 2015.

[174] Reitz R. D. Modeling atomization processes in high-pressure vaporizing sprays. *Atomisation and Spray Technology*, 3:309–337, 1988.

[175] Christopher B Reuter, Sang Hee Won, and Yiguang Ju. Flame structure and ignition limit of partially premixed cool flames in a counterflow burner. *Proceedings of the Combustion Institute*, 2016.

[176] Christopher B. Reuter, Rui Zhang, Omar R. Yehia, Yacine Rezgui, and Yiguang Ju. Counterflow flame experiments and chemical kinetic modeling of dimethyl ether/methane mixtures. *Combustion and Flame*, 196:1–10, oct 2018.

[177] E. S. Richardson, V. E. Granet, A. Eyssartier, and J. H. Chen. Effects of equivalence ratio variation on lean, stratified methaneair laminar counterflow flames. *Combustion Theory and Modelling*, 14(6):775–792, nov 2010.

[178] E S Richardson and E Mastorakos. Conditional Moment Closure Modelling for Spark Ignition in a Turbulent N-Heptane Spray. *Proceeding of the Mediterranean Combustion Symposium*, 5, 2007.

[179] E S Richardson, C S Yoo, and J H Chen. Analysis of second-order conditional moment closure applied to an autoignitive lifted hydrogen jet flame. *Proceedings of the Combustion Institute*, 32(2):1695–1703, 2009.

[180] Edward S. Richardson and Jacqueline H. Chen. Analysis of turbulent flame propagation in equivalence ratio-stratified flow. *Proceedings of the Combustion Institute*, 36(2):1729–1736, jan 2017.

[181] Jeremy Rochussen and Patrick Kirchen. Characterization of reaction zone growth in an optically accessible heavy-duty diesel/methane dual-fuel engine. *International Journal of Engine Research*, page 146808741875653, 2018.

[182] Shaohong Ruan, Nedunchezhian Swaminathan, and Oliver Darbyshire. Modelling of turbulent lifted jet flames using flamelets: a priori assessment and a posteriori validation. *Combustion Theory and Modelling*, 18(2):295–329, mar 2014.

[183] G. R. Ruetsch, L. Vervisch, and A. Liñán. Effects of heat release on triple flames. *Physics of Fluids*, 7(6):1447–1454, jun 1995.

[184] S R Bell S. Singh, S.R. Krishnan, K.K. Srinivasan, K.C. Midkiff. Singh et al 2004, Effects of pilot injection timing, pilot quantity and intake charge conditions, 2004.

[185] B B Sahoo, N Sahoo, and U K Saha. Effect of engine parameters and type of gaseous fuel on the performance of dual-fuel gas diesel enginesA critical review. *Renewable and Sustainable Energy Reviews*, 13(6-7):1151–1184, aug 2009.

[186] H Saito, T Sakurai, T Sakonji, and T Hirashima. Study on Lean Burn Gas Engine Using Pilot Oil as the Ignition Source. *SAE Technical Paper*, (2001-01-0143), 2001.

[187] Fatemeh Salehi, Mohsen Talei, Evatt R Hawkes, Ankit Bhagatwala, Jacqueline H Chen, Chun Sang Yoo, and Sanghoon Kook. Doubly conditional moment closure modelling for HCCI with temperature inhomogeneities. *Proceedings of the Combustion Institute*, 36(3):3677–3685, 2017.

[188] Fatemeh Salehi, Mohsen Talei, Evatt R Hawkes, Chun Sang Yoo, Tommaso Lucchini, Gianluca D'Errico, and Sanghoon Kook. A Comparative Study of Conditional Moment Closure Modelling for Ignition of iso-octane and n-heptane in Thermally Stratified Mixtures. *Flow, Turbulence and Combustion*, 95(1):1–28, 2015.

[189] Fatemeh Salehi, Mohsen Talei, Evatt R Hawkes, Chun Sang Yoo, Tommaso Lucchini, Gianluca D'Errico, and Sanghoon Kook. Conditional moment closure modelling for HCCI with temperature inhomogeneities. *Proceedings of the Combustion Institute*, 35(3):3087–3095, 2015.

[190] Sandia National Laboratory. Engine Combustion Network, 2014.

[191] A El Sayed and C B Devaud. Conditional Moment Closure (CMC) applied to autoignition of high pressure methane jets in a shock tube. *Combustion Theory and Modelling*, 12(5):943–972, oct 2008.

[192] Kong SC and Reitz RD. Multidimensional Modeling of Diesel Ignition and Combustion Using a Multistep Kinetics Model. *ASME. J. Eng. Gas Turbines Power*, 115:781–789, 1993.

[193] S Schlatter. *Experimental and Numerical Characterization of Enhanced Ignition Systems for Large Bore Gas Engines*. PhD thesis, ETH-Zürich, Switzerland, 2015.

[194] Stéphanie Schlatter. *Experimental and Numerical Characterization of Enhanced Ignition Systems for Large Bore Gas Engines*. PhD thesis, ETH-Zürich, 2015.

[195] Stéphanie Schlatter and B Schneider. Ignition and Combustion Characteristics of a Diesel Pilot Spray in a Lean Premixed Methane/Air Charge using a Rapid Compression Expansion Machine. *SAE Technical paper*, pages 1–21, 2012.

[196] Gavin A. Schmidt, Reto Ruedy, James E. Hansen, Igor Aleinov, Nadine Bell, Mike Bauer, Susanne Bauer, Brian Cairns, Vittorio Canuto, Ye Cheng, Anthony Del Genio, Greg Faluvegi, Andrew D. Friend, Tim M. Hall, Yongyun Hu, Max

Kelley, Nancy Y. Kiang, Dorothy Koch, Andy A. Lacis, Jean Lerner, Ken K. Lo, Ron L. Miller, Larissa Nazarenko, Valdar Oinas, Jan Perlwitz, Judith Perlwitz, David Rind, Anastasia Romanou, Gary L. Russell, Makiko Sato, Drew T. Shindell, Peter H. Stone, Shan Sun, Nick Tausnev, Duane Thresher, and Mao-Sung Yao. Present-Day Atmospheric Simulations Using GISS ModelE: Comparison to In Situ, Satellite, and Reanalysis Data. *Journal of Climate*, 19(2):153–192, jan 2006.

[197] E. Schneider, A. Maltsev, A. Sadiki, and J. Janicka. Study on the potential of BML-approach and G-equation concept-based models for predicting swirling partially premixed combustion systems: URANS computations. *Combustion and Flame*, 152(4):548–572, mar 2008.

[198] Omar Seddik, Sushant S. Pandurangi, Michele Bolla, Konstantinos Boulouchos, Aleš Srna, and Yuri M. Wright. Flamelet Generated Manifolds Applied to Dual-Fuel Combustion of Lean Methane/Air Mixtures at Engine Relevant Conditions Ignited by n-Dodecane Micro Pilot Sprays. *WCX SAE World Congress Experience*, (2019-01-1163), 2019.

[199] Dong-Hyuk Shin, Edward S Richardson, Vlad Aparece-Scutariu, Yuki Minamoto, and Jacqueline H Chen. Fluid age-based analysis of a lifted turbulent DME jet flame DNS. *Proceedings of the Combustion Institute*, 2018.

[200] Dong-Hyuk Shin, Edward S. Richardson, Vlad Aparece-Scutariu, Yuki Minamoto, and Jacqueline H. Chen. Fluid age-based analysis of a lifted turbulent DME jet flame DNS. *Proceedings of the Combustion Institute*, 37(2):2215–2222, jan 2019.

[201] Donghyuk Shin, R D Sandberg, and E S Richardson. Self-similarity of fluid residence time statistics in a turbulent round jet. *Journal of Fluid Mechanics*, 823:1–25, 2017.

[202] S Singh, L Liang, S-C Kong, and R D Reitz. Development of a Flame Propagation Model for Dual-Fuel Partially Premixed Compression Ignition Engines. *International Journal of Engine Research*, 7(1):65–75, 2006.

[203] Satbir Singh, Sc Kong, Rd Reitz, Sr Krishnan, and Kc Midkiff. Modeling and experiments of dual-fuel engine combustion and emissions. (724), 2004.

[204] Michael Philip Sitte and Epaminondas Mastorakos. Modelling of Spray Flames with Doubly Conditional Moment Closure. *Flow, Turbulence and Combustion*, 99(3-4):933–954, dec 2017.

[205] Michael Philip Sitte and Epaminondas Mastorakos. Large Eddy Simulation of a spray jet flame using Doubly Conditional Moment Closure. *Combustion and Flame*, 199:309–323, jan 2019.

[206] Gregory P Smith, David M Golden, Michael Frenklach, Nigel W Moriarty, Boris Eiteneer, Mikhail Goldenberg, C Thomas Bowman, Ronald K Hanson, Soonho Song, William C Gardiner Jr, and Others. GRI 3.0 Mechanism. *Gas Research Institute, Des Plaines, IL, accessed Aug*, 21:2017, 1999.

[207] B S Soriano. *Theory and modelling of dual-fuel combustion*. PhD thesis, University of Southampton, 2019.

[208] B.S. Soriano, E.S. Richardson, S. Schlatter, and Y.M. Wright. Conditional Moment Closure Modelling for Dual-Fuel Combustion Engines with Pilot-Assisted Compression Ignition. *SAE Technical Papers*, 2017-Octob, 2017.

[209] D B Spalding. *Combustion and Mass Transfer*. Pergamon Press, 1979.

[210] S Sreedhara and Kang Y Huh. Modeling of turbulent, two-dimensional non-premixed CH4/H 2 flame over a bluffbody using first- and second-order elliptic conditional moment closures. *Combustion and Flame*, 143(1-2):119–134, 2005.

[211] S Sreedhara and K N Lakshmisha. Assessment of conditional moment closure models of turbulent autoignition using DNS data. *Proceedings of the Combustion Institute*, 29(2):2069–2077, jan 2002.

[212] Paiboon Sripakagorn, Satoshi Mitarai, George Kosaly, and Heinz Pitsch. Extinction and reignition in a diffusion flame: a direct numerical simulation study. *Journal of Fluid Mechanics*, 518:231–259, nov 2004.

[213] Aleš Srna. *Experimental Characterization of Pilot-Fuel Ignition, Combustion, and Soot Formation in Dual-Fuel Combustion Systems*. PhD thesis, ETH Zurich, 2018.

[214] Aleš Srna, Michele Bolla, Yuri M Wright, Kai Herrmann, Rolf Bombach, Sushant S Pandurangi, Konstantinos Boulouchos, and Gilles Bruneaux. Effect of methane

on pilot-fuel auto-ignition in dual-fuel engines. *Proceedings of the Combustion Institute*, 2018.

[215] Aleš Srna, Michele Bolla, Yuri M. Wright, Kai Herrmann, Rolf Bombach, Sushant S. Pandurangi, Konstantinos Boulouchos, and Gilles Bruneaux. Effect of methane on pilot-fuel auto-ignition in dual-fuel engines. *Proceedings of the Combustion Institute*, 37(4):4741–4749, 2019.

[216] Aleš Srna, Gilles Bruneaux, Beat von Rotz, Rolf Bombach, Kai Herrmann, and Konstantinos Boulouchos. Optical Investigation of Sooting Propensity of n- Dodecane Pilot/Lean-Premixed Methane Dual-Fuel Combustion in a Rapid Compression-Expansion Machine. *SAE International Journal of Engines*, 11(6):2018–01–0258, apr 2018.

[217] Stephen R. Turns. *An Introduction to Combustion: Concepts and Applications*. McGraw-Hill, 1996.

[218] Gilbert Strang. On the Construction and Comparison of Difference Schemes. *SIAM Journal on Numerical Analysis*, 5(3):506–517, sep 1968.

[219] L Sun, Y Liu, K Zeng, R Yang, and Z Hang. Combustion performance and stability of a dual-fuel diesel-natural-gas engine. *Proceedings of the Institution of Mechanical Engineers, Part D: Journal of Automobile Engineering*, 229(2):235–246, 2014.

[220] N Swaminathan and R W Bilger. Analyses of conditional moment closure for turbulent premixed flames. *Combustion Theory and Modelling*, 5(2):241–260, 2001.

[221] Zhichao Tan and Rolf D Reitz. An ignition and combustion model based on the level-set method for spark ignition engine multidimensional modeling. *Combustion and Flame*, 145(1-2):1–15, apr 2006.

[222] Denis Veynante Thierry Poinsot. *Combustion ModellingTheoretical and Numerical Combustion*. illustrate edition, 2005.

[223] B Thornber, R W Bilger, a.R. Masri, and E R Hawkes. An algorithm for LES of premixed compressible flows using the Conditional Moment Closure model. *Journal of Computational Physics*, 230(20):7687–7705, 2011.

[224] A Triantafyllidis and E Mastorakos. Implementation Issues of the Conditional Moment Closure Model in Large Eddy Simulations. *Flow Turbulence and Combustion*, 84(3):481–512, 2010.

[225] H. P. Tsui and W. K. Bushe. Linear-Eddy Model Formulated Probability Density Function and Scalar Dissipation Rate Models for Premixed Combustion. *Flow, Turbulence and Combustion*, 93(3):487–503, oct 2014.

[226] Stephen R Turns. An introduction to combustion, 2000. *MacGraw Hill, Boston, Massachusetts, US*, 2000.

[227] Denis Veynante and Luc Vervisch. Turbulent combustion modeling. *Progress in Energy and Combustion Science*, 28(3):193–266, mar 2002.

[228] A Vreman, B Albrecht, J Vanoijen, L Degoey, and R Bastiaans. Premixed and nonpremixed generated manifolds in large-eddy simulation of Sandia flame D and F. *Combustion and Flame*, 153(3):394–416, may 2008.

[229] Daniel H. Wacks and Nilanjan Chakraborty. Statistical Analysis of the Reaction Progress Variable and Mixture Fraction Gradients in Flames Propagating into Droplet Mist: A Direct Numerical Simulation Analysis. *Combustion Science and Technology*, 188(11-12):2149–2177, dec 2016.

[230] Zhiyan Wang and John Abraham. Fundamental physics of flame development in an autoigniting dual fuel mixture. *Proceedings of the Combustion Institute*, 35(1):1041–1048, 2015.

[231] Krisada Wannatong, Nirod Akarapanyavit, Somchai Siengsanorh, and Somchai Chanchaona. Combustion and Knock Characteristics of Natural Gas Diesel Dual Fuel Engine. *SAE Technical Paper*, 01(JULY 2007):1894–1899, 2007.

[232] Lijiang Wei and Peng Geng. A review on natural gas/diesel dual fuel combustion, emissions and performance. *Fuel Processing Technology*, 142:264–278, feb 2016.

[233] H G Weller, S Uslu, a D Gosman, R R Maly, R Herweg, and B Heel. Prediction of Combustion in Homogeneous-Charge Spark-Ignition Engines, 1994.

[234] F A Williams. The mathematics of combustion. *SIAM, Philadelphia*, 97, 1985.

[235] Bret Windom, Sang Hee Won, Christopher B Reuter, Bo Jiang, Yiguang Ju, Stephen Hammack, Timothy Ombrello, and Campbell Carter. Study of ignition chemistry on turbulent premixed flames of n-heptane/air by using a reactor assisted turbulent slot burner. *Combustion and Flame*, 169:19–29, 2016.

[236] Sang Hee Won, Bret Windom, Bo Jiang, and Yiguang Ju. The role of low temperature fuel chemistry on turbulent flame propagation. *Combustion and Flame*, 161(2):475–483, 2014.

[237] Y Wright, G De Paola, K Boulouchos, and E Mastorakos. Simulations of spray autoignition and flame establishment with two-dimensional CMC. *Combustion and Flame*, 143(4):402–419, dec 2005.

[238] Y M Wright, K Boulouchos, G De Paola, and E Mastorakos. Multi-dimensional Conditional Moment Closure Modelling Applied to a Heavy-duty Common-rail Diesel Engine. *SAE International Journal of Engines*, 2(1):717–2009, 2009.

[239] Yuri M Wright, Ourania Nektaria Margari, Konstantinos Boulouchos, Giorgio De Paola, and Epaminondas Mastorakos. Experiments and simulations of n-heptane spray auto-ignition in a closed combustion chamber at diesel engine conditions. *Flow, Turbulence and Combustion*, 84(1):49–78, 2010.

[240] Yuri Martin Wright. Numerical investigation of turbulent spray combustion with Conditional Moment Closure. (16386), 2005.

[241] Chao Xu, Ji-Woong Park, Chun Sang Yoo, Jacqueline H. Chen, and Tianfeng Lu. Identification of premixed flame propagation modes using chemical explosive mode analysis. *Proceedings of the Combustion Institute*, 37(2):2407–2415, jan 2019.

[242] Shigeki Yamaguchi, Norio Ohiwa, and Tatsuya Hasegawa. Ignition and burning process in a divided chamber bomb. *Combustion and Flame*, 59(2):177–187, feb 1985.

[243] Bo Yang, Xing Wei, Chengxun Xi, Yifu Liu, Ke Zeng, and Ming Chia Lai. Experimental study of the effects of natural gas injection timing on the combustion performance and emissions of a turbocharged common rail dual-fuel engine. *Energy Conversion and Management*, 87:297–304, 2014.

[244] Shiyou Yang and Rolf D Reitz. Integration of a continuous multi-component fuel evaporation model with an improved G-equation combustion and detailed chemical kinetics model with application to GDI engines. Technical report, SAE Technical Paper, 2009.

[245] C. S. Yoo and H. G. Im. Characteristic boundary conditions for simulations of compressible reacting flows with multi-dimensional, viscous and reaction effects. *Combustion Theory and Modelling*, 11(2):259–286, apr 2007.

[246] Chun Sang Yoo, Tianfeng Lu, Jacqueline H Chen, and Chung K Law. Direct numerical simulations of ignition of a lean n-heptane/air mixture with temperature inhomogeneities at constant volume: Parametric study. *Combustion and Flame*, 158(9):1727–1741, 2011.

[247] Chun Sang Yoo, Edward S. Richardson, Ramanan Sankaran, and Jacqueline H. Chen. A DNS study on the stabilization mechanism of a turbulent lifted ethylene jet flame in highly-heated coflow. *Proceedings of the Combustion Institute*, 33(1):1619–1627, jan 2011.

[248] Ya. B Zeldovich. Regime classification of an exothermic reaction with nonuniform initial conditions. *Combustion and Flame*, 39(2):211–214, 1980.

[249] Qiang Zhang, Na Li, and Menghan Li. Combustion and emission characteristics of an electronically-controlled common-rail dual-fuel engine. *Journal of the Energy Institute*, pages 1–16, 2015.

[250] Youtong Zhang, Song-charng Kong, and Rolf D Reitz. Modeling and Simulation of a Dual Fuel (Diesel / Natural Gas) Engine With Multidimensional CFD. *SAE Technical Paper 2003-01-0755*, (724):1–14, 2003.

[251] Peng Zhao, Wenkai Liang, Sili Deng, and Chung K Law. Initiation and propagation of laminar premixed cool flames. *Fuel*, 166:477–487, 2016.